

Old Dominion University Research Foundation

DEPARTMENT OF MECHANICAL ENGINEERING & MECHANICS
COLLEGE OF ENGINEERING & TECHNOLOGY
OLD DOMINION UNIVERSITY
NORFOLK, VIRGINIA 23529

11/11/92
IN-34-CR
13/11/92
P-127

ANALYSIS AND CONTROL OF ASYMMETRIC VORTEX FLOWS
AND SUPERSONIC VORTEX BREAKDOWN

By

Osama A. Kandil, Principal Investigator

Final Report
For the period December 1, 1991 to November 30, 1992

Prepared for
National Aeronautics and Space Administration
Langley Research Center
Hampton, Virginia 23665

92-14007
--1180--
92-14007
UNCLAS

Under
Research Grant NAG-1-994
Dr. C. H. Liu, Technical Monitor
Computational Aerodynamics Branch

ANALYSIS AND CONTROL OF ASYMMETRIC VORTEX FLOWS AND SUPERSONIC VORTEX BREAKDOWN
Final Report, 1 Dec. 1991 - 30 Nov. 1992 (Old Dominion Univ.)
dhp

November 1992

48/1992

DEPARTMENT OF MECHANICAL ENGINEERING & MECHANICS
COLLEGE OF ENGINEERING & TECHNOLOGY
OLD DOMINION UNIVERSITY
NORFOLK, VIRGINIA 23529

**ANALYSIS AND CONTROL OF ASYMMETRIC VORTEX FLOWS
AND SUPERSONIC VORTEX BREAKDOWN**

By

Osama A. Kandil, Principal Investigator

Final Report
For the period December 1, 1991 to November 30, 1992

Prepared for
National Aeronautics and Space Administration
Langley Research Center
Hampton, Virginia 23665

Under
Research Grant NAG-1-994
Dr. C. H. Liu, Technical Monitor
Computational Aerodynamics Branch

Submitted by the
Old Dominion University Research Foundation
P.O. Box 6369
Norfolk, Virginia 23508-0369

November 1992

ANALYSIS AND CONTROL OF ASYMMETRIC VORTEX FLOWS AND SUPERSONIC VORTEX BREAKDOWN

Osama A. Kandil*

Accomplishments (Dec. 1, 1991–Nov. 30, 1992)

The accomplishments which have been achieved in the present year covering the period from Dec. 1, 1991 until Nov. 30, 1992 are given. These accomplishments include publications, national and international presentations, NASA Research Highlights and presentations, and the research group supported under this grant.

I. Conference Papers, Proceedings and Journal Publications:

1. Kandil, O. A., Kandil, H. A. and Liu, C. H., "Shock/Vortex Interaction and Vortex Breakdown Modes," IUTAM Symposium on Fluid Dynamics of High Angle of Attack, Paper No. T.1.2, University of Tokyo, Tokyo, Japan, September 13-17, 1992 (Invited), (a copy is enclosed).
2. Kandil, O. A., Wong, T. C., Sharaf, H. H. and Liu, C. H., "Recent Advances in Numerical Simulation and Control of Asymmetric Flows Around Slender Bodies," IUTAM Symposium on Fluid Dynamics of High Angle of Attack, Paper No. W.1.2, University of Tokyo, Tokyo, Japan, September 13-17, 1992 (Invited), (a copy is enclosed).
3. Wong, T. C., Kandil, O. A., and Liu, C. H., "Computation of Wake Vortex Flows and Control of Their Effects on Trailing Wings," AIAA 4429-92-CP, AIAA Atmospheric Flight Mechanics Conference, South Carolina, August 1992, Vol. 1, pp. 280–292, (a copy is enclosed).
4. Kandil, O. A., Sharaf, H. H. and Liu, C. H., "Active Control of Asymmetric Vortical Flows Around Cones Using Injection and Heating," AIAA 92-4426-CP, AIAA Atmospheric Flight Mechanics Conference, South Carolina, August 1992, Vol. 1, pp. 244–253, (a copy is enclosed).
5. Kandil, O. A., Kandil, H. A. and Liu, C. H., "Critical Effect of Downstream Boundary Conditions on Vortex Breakdown," AIAA 92-2601-CP, 10th Applied Aerodynamics Conference, Palo Alto, CA, June 22-24, 1992, pp. 12–26, (a copy is enclosed).
6. Kandil, O. A. and Liu, C. H., "Unsteady Vortex Flows and Flow Control Around Slender Bodies and Delta Wings," Workshop on Supermaneuverability, AFOSR, Lehigh University, April 9–10, 1992, pp. 383–417.
7. Kandil, O. A. and Sharaf, H. H., "Recent Advances in Computational Active Control of Asymmetric Vortex Flows," Fourth International Conference for Fluid Mechanics, Alexandria, Egypt, April 28–30, 1992, Vol. I, pp. 237–249.

8. Wong, T. C., Kandil, O. A. and Liu, C. H., "Three-Dimensional Computational Study of Asymmetric Flows Using Navier-Stokes Equations," Proceedings of Asian Pacific Conference on Computational Mechanics, Hong Kong, December 11–13, 1991, pp. 1365–1371, (a copy is enclosed).
9. Liu, C. H., Kandil, O. A. and Wong, T. C., "Computational Study for Passive Control of Supersonic Asymmetric Vortical Flows around Cones," Impact Journal of Computing in Science and Engineering, Academic Press, Inc., Vol. 4, pp. 80–96, March, 1992, (a copy is enclosed).
10. Kandil, O. A., Wong, T. C. and Liu, C. H., "Numerical Simulation of Unsteady Asymmetric Flows around Cones," Journal of Fluids and Structures, Academic Press, Vol. 6, pp. 249–265, February 1992, (a copy is enclosed).
11. Kandil, O. A., Wong, T. C. and Liu, C. H., "Prediction of Steady and Unsteady Asymmetric Vortical Flow Around Cones," AIAA Journal, Vol. 29, No. 12, December 1991, pp. 1269–1278, (a copy is enclosed).
12. Kandil, O. A., Wong, T. C., Kandil, H. A. and Liu, C. H., "Thin-Layer and Full Navier-Stokes Locally-Conical Asymmetric Solutions," Accepted for Publication to the ASME Journal of Fluids Engineering, December 17, 1991, log. No. 3303-RKA, to appear in April 1993.
13. Kandil, O. A., Kandil, H. A. and Liu, C. H., "Supersonic Quasi-Axisymmetric Vortex Breakdown," Accepted for Publication to the ASME Journal of Fluids Engineering, December 17, 1991, Log. No. 3302-RKA, to appear in April 1993.
14. Kandil, O. A., Wong, T. C. and Liu, C. H., "Three-Dimensional Navier-Stokes Asymmetric Solutions for Cones and Cone-Cylinder Configurations," Accepted for Publication to the AIAA Journal, November 1991, to appear in December 1993.
15. Liu, C. H., Wong, T. C. and Kandil, O. A., "Prediction of Asymmetric Vortical Flows Around Slender Bodies Using Navier-Stokes Equations," Japanese Journal of Fluid Dynamics Research, to appear January 1993.

II. National and International Presentations:

1. "Unsteady High- α Computational Prediction and Control," Institute for Space and Astronautical Sciences (ISAS), Tokyo, Japan, September 17, 1992. (Invited)
2. "Shock/Vortex Interaction and Vortex-Breakdown Modes," IUTAM Symposium of Fluid Dynamics of High Angle of Attack, Tokyo, Japan, September 13–17, 1992.
3. "Recent Advances in Numerical Simulation and Control of Asymmetric Flows Around Slender Bodies," IUTAM Symposium of Fluid Dynamics of High Angle of Attack, Tokyo, Japan, September 13–17, 1992.

4. "Computational High- α Aerodynamics," Presentation given to General John Loh (4 star-general) of Langley Air Force Base, ODU, August 31, 1992.
5. "Computation of Vortex Wake Flows and Control of Their Effects on Trailing Wings," AIAA Atmospheric Flight Mechanics Conference, Hilton Head, SC, August 10-12, 1992.
6. "Active Control of Asymmetric Vortical Flows Around Cones Using Injection and Heating," AIAA Atmospheric Flight Mechanics Conference, Hilton Head, SC, August 10-12, 1992.
7. "Computation and Control of Vortex Wake Flows," Directorate Review of Theoretical Flow Physics Branch, NASA Langley Research Center, Hampton, VA, July 16, 1992.
8. "Critical Effects of Downstream Boundary Conditions on Vortex Breakdown," AIAA 10th Applied Aerodynamics Conference, Palo Alto, CA, June 22-25, 1992.
9. "Vortex-Wake Flows," Division Review of Theoretical Flow Physics Branch, NASA-Langley Research Center, Hampton, VA, June 5, 1992.
10. "Recent Advances in Computational Active Control of Asymmetric Vortex Flows," Fourth International Conference for Fluid Mechanics, Alexandria, Egypt, April 28-30, 1992.
11. "Prediction and Control of Unsteady Flows for Supermanuverability," Taiwan Aeronautical Research Center — ODU Symposium, MEM Dept., ODU, April 20-21, 1992.
12. "Physical Issues and Numerical Simulation of Supersonic Vortex Breakdown," MEM Dept. Televised Seminars, ODU, Norfolk, VA, April 17, 1992.
13. "Unsteady Vortex Flows and Flow Control Around Slender Bodies and Delta Wings," AFOSR Workshop on Supermanueverability, Lehigh Univ., PA, April 9-10, 1992. Also Unsteady Aerodynamics Branch Briefing to the Canadian Air Force, NASA Langley, May 26, 1992.
14. "Vortex Research Work" Briefing to AFOSR Program Manager, NASA Langley Research Center, Hampton, VA, Feb. 12, 1992.

III. Papers Submitted or Accepted for Presentation:

1. Kandil, O. A., Kandil, H. A. and Liu, C. H., "Three-Dimensional Supersonic Vortex Breakdown," AIAA 93-0526, AIAA 31st Aerospace Sciences Meeting, Reno, Nevada, January 11-14, 1993.
2. Kandil, O. A., Kandil, H. A. and Liu, C. H., "Vortex/Shock Interaction on a 65°-Delta Wing in Transonic Flow," Submitted to the AIAA Fluids and Plasma Dynamics, Orlando, Florida, July 6-9, 1993.

3. Kandil, O. A., Sharaf, H. H. and Liu, C. H., "Active Control of Asymmetric Conical Flow Using Spinning and Oscillation," submitted to the AIAA Fluids and Plasma Dynamics, Orlando, Florida, July 6-9, 1993.

IV. NASA Research Highlights:

1. "Three-Dimensional Shock/Vortex Interaction and Vortex Breakdown Modes," Kandil, O. A., Kandil, H. A. and Liu, C. H., NASA RTOP, July 1992.
2. "Active and Passive Control of Asymmetric Vortical Flows Around Conical Forebodies," Kandil, O. A., Sharaf, H. H., and Liu, C. H., NASA RTOP, July 1992.

V. Research Group:

This Principal Investigator is assisted by the following persons in the research group:

1. Dr. T. C. Wong, Research Associate, MEM Dept., Old Dominion University; Prediction and Control of Wake-Vortex Flows.
2. Mr. Hamdy A. Kandil, Ph.D. Candidate, MEM Dept., Old Dominion University; Internal and External Shock/Vortex Interaction and Vortex-Breakdown Modes.
3. Mr. Hazem H. Sharaf El-Din, Ph.D. Student, MEM Dept., Old Dominion University; Passive and Active Control Methods for Asymmetric Flows around Conical Forebodies.

Paper No. W.1.2

27-34
12011
483100
1682
N93-14688

**RECENT ADVANCES IN NUMERICAL SIMULATION
AND CONTROL OF ASYMMETRIC FLOWS
AROUND SLENDER BODIES**

O. A. Kandil, T.-C. Wong, H. H. Sharaf
Old Dominion University, Norfolk, VA, USA

C. H. Liu
NASA Langley Research Center, Hampton, VA, USA



**IUTAM SYMPOSIUM ON FLUID
DYNAMICS OF HIGH ANGLE OF ATTACK**
Tokyo, Japan — September 13-17, 1992

RECENT ADVANCES IN NUMERICAL SIMULATION AND CONTROL OF ASYMMETRIC FLOWS AROUND SLENDER BODIES

O. A. Kandil. T.-C. Wong, H. H. Sharaf El-Din
Dept. of Mechanical Engineering and Mechanics
Old Dominion University, Norfolk, VA

C. H. Liu
Theoretical Flow Physics Br.
NASA Langley, Hampton, VA

Summary

The problems of asymmetric flow around slender bodies and its control are formulated using the unsteady, compressible, thin-layer or full Navier-Stokes equations which are solved using an implicit, flux-difference splitting, finite-volume scheme. The problem is numerically simulated for both locally-conical and three-dimensional flows. The numerical applications include studies of the effects of relative incidence, Mach number and Reynolds number on the flow asymmetry. For the control of flow asymmetry, the numerical simulation cover passive and active control methods. For the passive control, the effectiveness of vertical fins placed in the leeward plane of geometric symmetry and side strakes with different orientations is studied. For the active control, the effectiveness of normal and tangential flow injection and surface heating and a combination of these methods is studied.

Introduction

Flow asymmetry around pointed slender cones develops at critical values of relative incidence (ratio of angle of attack to nose semiapex angle) due to short-duration transient disturbances or forced disturbances. The origin of the transient disturbances may be a transient side slip, an acoustic disturbance, or similar disturbances of short duration. The origin of forced disturbances is geometric imperfections in the nose or similar disturbances of permanent nature. Flow asymmetry produces side forces, asymmetric lifting forces and corresponding yawing, rolling and pitching moments that might be larger than those available by the control system of the vehicle. Currently, research efforts are devoted for eliminating or alleviating flow asymmetry and its corresponding asymmetric loads. Various methods of passive and active control are being studied to learn about their control effectiveness.

In several recent papers by Kandil, et al. [1]-[4], the unsteady, thin-layer, compressible Navier-Stokes equations have been used to simulate steady and unsteady, asymmetric vortex flows, including their passive control, around cones with different cross-sectional shapes. The emphasis of these papers was extensive computational studies of the parameters which influence the asymmetric flow phenomenon and its passive control. Since the computational cost associated with the solution of three-dimensional-flow problems at reasonable flow resolution is very expensive, all the computational solutions were obtained using a locally-conical flow assumption. Such an assumption reduces the problem solution to that on

two conical planes, which are in close proximity of each other, and hence it reduces the computational cost by an order of magnitude. Moreover, such solutions still provide extensive understanding of the flow physics since one can use very fine grids for reasonable flow resolution.

In a later paper, by Kandil, et al. [5], the full Navier-Stokes solutions were compared with the thin-layer Navier-Stokes solutions. It was shown that the full Navier-Stokes solutions produced thicker free-shear layers and more vortex-core resolution as compared with those of the thin-layer Navier-Stokes equations. In reference [5], a few tentative three-dimensional flow solutions were also presented.

Substantial research efforts have recently been devoted for eliminating or alleviating flow asymmetry and its corresponding side force. In the experimental area, several passive-control methods [6]–[8] and active-control methods [9]–[13] have been investigated. Computational simulations have also been used to investigate the effectiveness of several passive-control methods [1]–[5] and active-control methods [12], [14], [15]. Various methods of passive control were demonstrated in the above references which include the use of vertical fins along the leeward plane of geometric symmetry, thin and thick side strakes with different orientations, and rotatable forebody tips which have variable cross section (from a circular shape at its base to an elliptic shape at its tip). It was shown by Kandil, et al. [4] that side-strakes control is more practical than the vertical-fin control since the former was more effective over a wide range of angle of attack than the former. Moreover, side-strake control provided an additional lifting force. However, the effectiveness of the side-strake control terminates at very high angles of attack for the considered strake geometry and flow conditions.

Various active-control methods have been used which include forebody blowing and movable forebody strakes. The forebody blowing methods include forward blowing, normal blowing, aft blowing and tangential blowing. The main concept of forebody blowing is to control flow separation on the forebody and to create yawing forces and moments which can be utilized in controlling the body.

In this paper, we present samples of simulating asymmetric locally-conical and three-dimensional flows around cones. Next, we present samples of simulation for passive control using a vertical fin and a side strake. Samples of simulating active control using normal and tangential flow injection, surface heating and hybrid methods are also presented.

Highlights for Formulation and Computational Schemes

Formulation: The asymmetric-flow problems including their passive and active controls are formulated using the conservative form of the unsteady, compressible, thin or full Navier-

Stokes equations in terms of time-independent, body-conforming coordinates. The equations are given in Ref. [5] and hence, they are not repeated here.

The boundary and initial conditions vary according to the problem under consideration. The boundary conditions are explicitly satisfied. In general, they include inflow-outflow conditions and solid-boundary conditions. For problems of flow asymmetry, where the flow is solved throughout the whole computational domain, periodic boundary conditions are used at the plane of geometric symmetry of the problem.

For the asymmetric flow problems around slender bodies and for supersonic inflow-outflow boundary, the Riemann-invariant boundary conditions are used. They require that the inflow variables be at the freestream conditions, and the conical shock enclosing the body be captured as part of the solution. For supersonic outflow boundary, the Riemann-invariant boundary conditions require that all flow variables be extrapolated from the interior cells. On the solid boundary, without injection or heating, the no-slip and no-penetration conditions are enforced. Moreover, the zero normal-pressure gradient and adiabatic boundary conditions are enforced. For the active control problems, the mass-flow rate is specified at the body surface for the normal injection control and the temperature distribution is specified at the surface for the heating control. For the tangential flow injection, the mass flow rate and velocity profile are specified at the lip exit.

The initial conditions correspond to the uniform flow conditions with $u_1 = u_2 = u_3 = 0$ on the solid boundary. These conditions are used to obtain the asymmetric flow solution. Next, the flow control conditions are enforced and the previously obtained asymmetric solution is used for the initial conditions of the active control problem.

Computational Scheme: The implicit, upwind, flux-difference splitting, finite-volume scheme is used to solve the unsteady, compressible, full Navier-Stokes equations. The scheme uses the flux-difference splitting scheme of Roe which is based on the solution of the approximate Riemann problem. In the Roe scheme, the inviscid flux difference at the interface of computational cells is split into two parts; left and right flux differences. The splitting is accomplished according to the signs of the eigenvalues of the Roe averaged-Jacobian matrix of the inviscid fluxes at the cell interface. The smooth flux limiter is used to eliminate oscillations at locations of large flow gradients. The viscous-and heat-flux terms are linearized and the cross-derivative terms are eliminated in the implicit operator. The viscous terms are differenced using a second-order accurate central differencing. The resulting difference equation is approximately factored and is solved in three sweeps in the ξ^1 , ξ^2 , and ξ^3 directions. The computational scheme is coded in the computer program "FTNS3D".

For the locally-conical flow solutions, an axial station of $x_1 = 1.0$ is selected and the components of the flowfield vector are forced to be equal between this axial station and

another axial station in close proximity to $x_1 = 1.0$. This ensures that the flow variables are locally independent of the axial direction at $x_1 = 1.0$ (Kandil, et al. [5]).

Computational Applications and Discussion

Asymmetric Steady Flow (locally-conical solution): Figure 1 shows the residual error versus the number of iterations, surface-pressure (SP) coefficient, cross-flow velocity and total-pressure-loss (TPL) contour for the solution around a 5° -semiapex circular cone. Two computer codes (CFL3D and ICF3D) which solve the thin-layer Navier-Stokes equations are used to validate the asymmetric flow solution. The logarithmic-residual-error curve shows the stages through which the solution goes until a stable asymmetric steady solution is obtained. A grid of $161 \times 81 \times 2$ points in the wrap-around, normal and axial directions, respectively, with minimum spacing of 10^{-4} , has been used. The computational domain extends around the body to $21 r$ where r is the local radius of the cone. For these critical conditions, the asymmetry is developed due to random disturbances; such as the machine round-off-error for the CFL3D solution.

Asymmetric Unsteady Flow (locally-conical solution): Figure 2 shows the results for the solution of the flow around the same cone using the same grid, where $\alpha = 30^\circ$. Here, the solution is validated by using the thin-layer and full, Navier-Stokes equations using the flux-difference splitting (FDS) scheme and the flux-vector splitting (FVS) scheme. All the solutions show asymmetric, periodic flow with vortex shedding. The figures show snapshots of TPL contours over a half cycle of periodic response. The periodicity is substantiated by the first and last snapshot in each row. It is clearly observed that they are mirror image of each other over the half cycle.

Asymmetric Steady Flow (three-dimensional solutions): Figures 3 and 4 show the asymmetric flow results for the flows around a 5° -semiapex cone and a 5° -semiapex cone with cylindrical after-body configuration. A grid of $161 \times 81 \times 65$ points in the wrap-around, normal and axial directions, respectively, with minimum spacing of 10^{-6} has been used. For the cone solution, the spatial flow asymmetry is qualitatively similar to that of the temporal flow asymmetry of the locally-conical flow solution of Fig. 2. For the cone-cylinder configuration at the same angle of attack and Mach number as those of the cone case, it is concluded that the cylindrical afterbody enhances the flow asymmetry at lower Reynolds number. These solutions are obtained using the thin-layer Navier-Stokes equations.

Passive Control Using Fins and Strakes (locally-conical solutions): Figures 5 and 6 show the solutions using passive flow controls through a vertical fin placed in the leeward plane of geometric symmetry (Fig. 5) or side strakes (Fig. 6). It is concluded that the fin height, h , must be at least equal to or greater than the height of the free-shear layers in order

to yield a symmetric flow. The side-stroke control is more practical than the fin control since it is more effective for high angles of attack than the fin, and moreover it provides additional lifting force. These solutions are obtained using the thin-layer Navier-Stokes equations.

Active-Control Using Normal Flow Injection: Figure 7 shows the history of the locally-conically full Navier-Stokes solutions for active control around a 5° -semiapex cone. The control is achieved by injecting flow from circumferential ports in the circumferential angle range of $\theta = \pm 67.5^\circ$. A variable mass-flow-rate injection of maximum rate of 0.03 is used. The mass flow rate is proportional to the difference in the surface pressure between the left and right sides of the cone. Figure 8 shows the effectiveness of this flow injection as the angle of attack is increased up to 30° , where flow asymmetry develops again. The solution is obtained using the full Navier-Stokes solver, FTNS-3D code, on a grid of $241 \times 81 \times 2$.

Hybrid Active Control Using Heating and Injection: Since normal flow injection failed to yield asymmetric solutions at angles of attack as high as 30° , hybrid methods of active control are investigated. Figure 9 shows the effectiveness of hybrid surface heating and variable mass flow normal injection for the same cone as the angle of attack is increased. It is seen that this method is very promising at high angles of attack. Here, symmetric surface pressure and not symmetric flow is obtained at $\alpha = 38^\circ$ and 42° . The surface temperature is taken as $T_s = 5T_\infty$ and the maximum mass flow rate is 0.05. The solution is obtained using the full Navier-Stokes solver, FTNS-3D code, on the same grid as that of Fig. 8.

Active Control Using Tangential Flow Injection: Figure 10 shows the results for active control using injection of flow from side lips. The radius of the lower portion is 1.05 that of the upper portion. The maximum mass flow rate is 0.2 and a parabolic velocity profile is assumed at the lip exit. The solution is obtained by using the full Navier-Stokes solver, FTNS-3D, code and a multi-block scheme to grid the lip-flow exit and the upper and lower flow regions. It is seen that this method is effective up to 30° angle of attack.

Concluding Remarks

The unsteady, compressible, thin-layer and full Navier-Stokes equations have been used to solve for asymmetric steady and unsteady, locally-conical and three-dimensional flows around circular cones at high angles of attack. Passive and active control methods have been applied to study their effectiveness to yield either a symmetric flow or a symmetric surface pressure distribution and hence removing the side forces. Work is underway to use other active control methods as well as hybrid passive-active control methods.

Acknowledgement

For the first three authors, this research work has been supported by the NASA Langley Research Center under Grant No. NAG-1-994. The computational resources provided by the NASA Langley Research are appreciated.

References

1. Kandil, O. A.; Wong, T-C.; Liu, C. H.: Prediction of Steady and Unsteady Asymmetric Vortical Flow Around Cones. AIAA 90-0598, 1990. Also in AIAA Journal, Vol. 29. No. 12, pp. 1269-1278, 1991.
2. Kandil, O. A.; Wong, T-C.; Liu, C. H.: Asymmetric Flow Around Cones with Noncircular Sections. AGARD Symposium on Missile Aerodynamics, AGARD CP No. 493, Friedrichshafen, Germany, pp. 16.1-16.11, 1990.
3. Kandil, O. A.; Wong, T-C.; Liu, C. H.: Numerical Simulation of Steady and Unsteady Asymmetric Vortical Flows. ASME Symposium on Non-Steady Fluid Dynamics, FED-Vol. 92, Toronto, Canada, pp. 99-108, 1990. Also in the Journal of Fluids and Structures, Vol. 6, pp. 249-265, 1992.
4. Kandil, O. A.; Wong, T-C.; Kandil, H., A.; Liu, C. H.: Computation and Control of Asymmetric Vortex Flow Around Circular Cones Using Navier-Stokes Equations. ICAS Paper No. 3.5.3, Vol. 2, Stockholm, Sweden, pp. 883-893, 1990.
5. Kandil, O. A.; Wong, T-C.; Kandil, H. A.; Liu, C. H.: Thin-Layer and Full Navier-Stokes, Locally-Conical and Three-Dimensional Asymmetric Solutions. AIAA 91-0547, 1991.
6. Stahl, W.: Suppression of Asymmetry of Vortex Flow Behind a Circular Cone at High Incidence. Proceedings of the AIAA Atmospheric Flight Mechanics Conference, Boston, MA, AIAA 39-3372-CP, pp. 231-236, 1989.
7. Ng, T. T.: On Leading Edge Vortex and Its Control. Proceedings of the AIAA Atmospheric Flight Mechanics Conference, Boston, MA, AIAA 89-3346-CP, pp. 1-15, 1989.
8. Moskovitz, C., Hall, R.: DeJarnette; Experimental Investigation of a New Device to Control the Asymmetric Flowfield on Forebodies at Large Angles of Attack. AIAA 90-0069, 1990.
9. Skow, A. M.; Peake, D. J.: Control of the Forebody Vortex Orientation by Asymmetric Air Injection, (Part B) — Details of the Flow Structure. AGARD-LS-121, High Angle-of-Attack Aerodynamics, pp. 10.1-10.22, 1982.
10. Ng, T. T.; Suarez, C. J.; Malcolm, N.; Forebody Vortex Control Using Slot Blowing. Proceedings of the AIAA 9th Applied Aerodynamics Conference, Baltimore, Maryland, AIAA 91-3254-CP, pp. 412-421, 1991.
11. Gittner, M. N.; Chokani, N.: An Experimental Study of the Effects of Aft Blowing on a 3.0 Caliber Tangent Ogive Body at High Angles of Attack. Proceedings of the AIAA 9th Applied Aerodynamics Conference, Baltimore, Maryland, AIAA 91-3252-CP, pp. 390-399, 1991.

12. Font, G. I.; Celik, Z. Z.; Roberts, L.: A Numerical and Experimental Study of Tangential Jet Blowing Applied to Bodies at High Angles of Attack. Proceedings of the AIAA 9th Applied Aerodynamics Conference, Baltimore, Maryland, AIAA 91-3253-CP, pp. 400-411, 1991.
13. Ng, T. T.: Aerodynamic Control of NASP-Type Vehicles Through Vortex Manipulation. AIAA 90-0594, 1990.
14. Tavella, D. A.; Schiff, L. B.; Cummings, R. M.; Pneumatic Vortical Flow Control at High Angles of Attack. AIAA 90-0098, 1990.
15. Gee, K.; Tavella, D.; Schiff, L. S.: Computational Optimization of a Pneumatic Forebody Flow Control Concept. Proceedings of the AIAA 9th Applied Aerodynamics Conference, Baltimore, Maryland, AIAA 91-3249-CP, pp. 370-380, 1991.

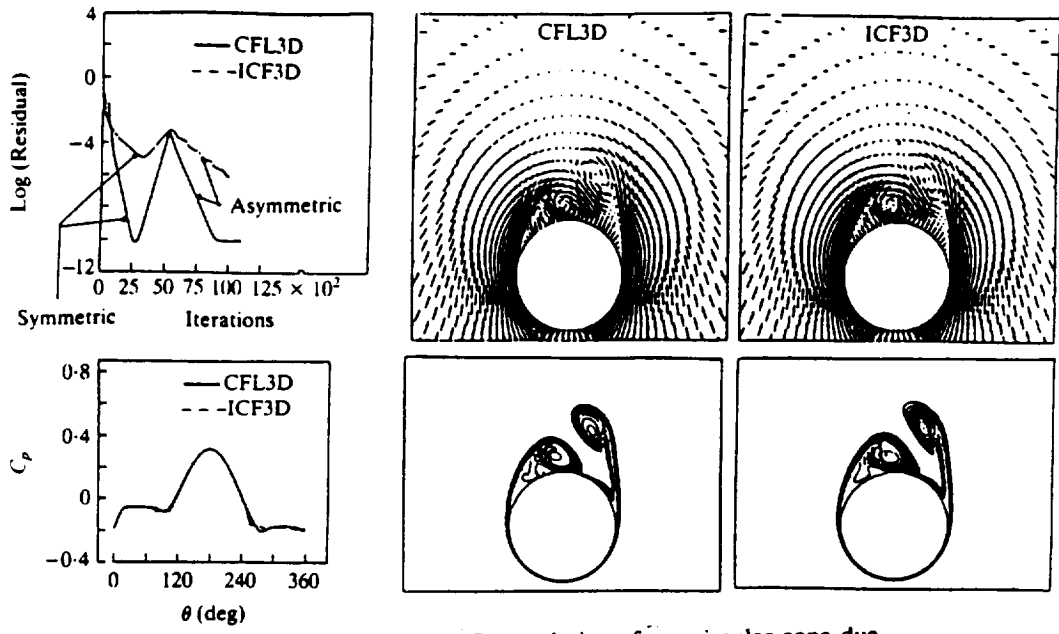


Figure 1. Steady asymmetric flow solutions for a circular cone due to random disturbances, $\alpha = 20$ deg, $M_\infty = 1.8$, $R_e = 10^5$

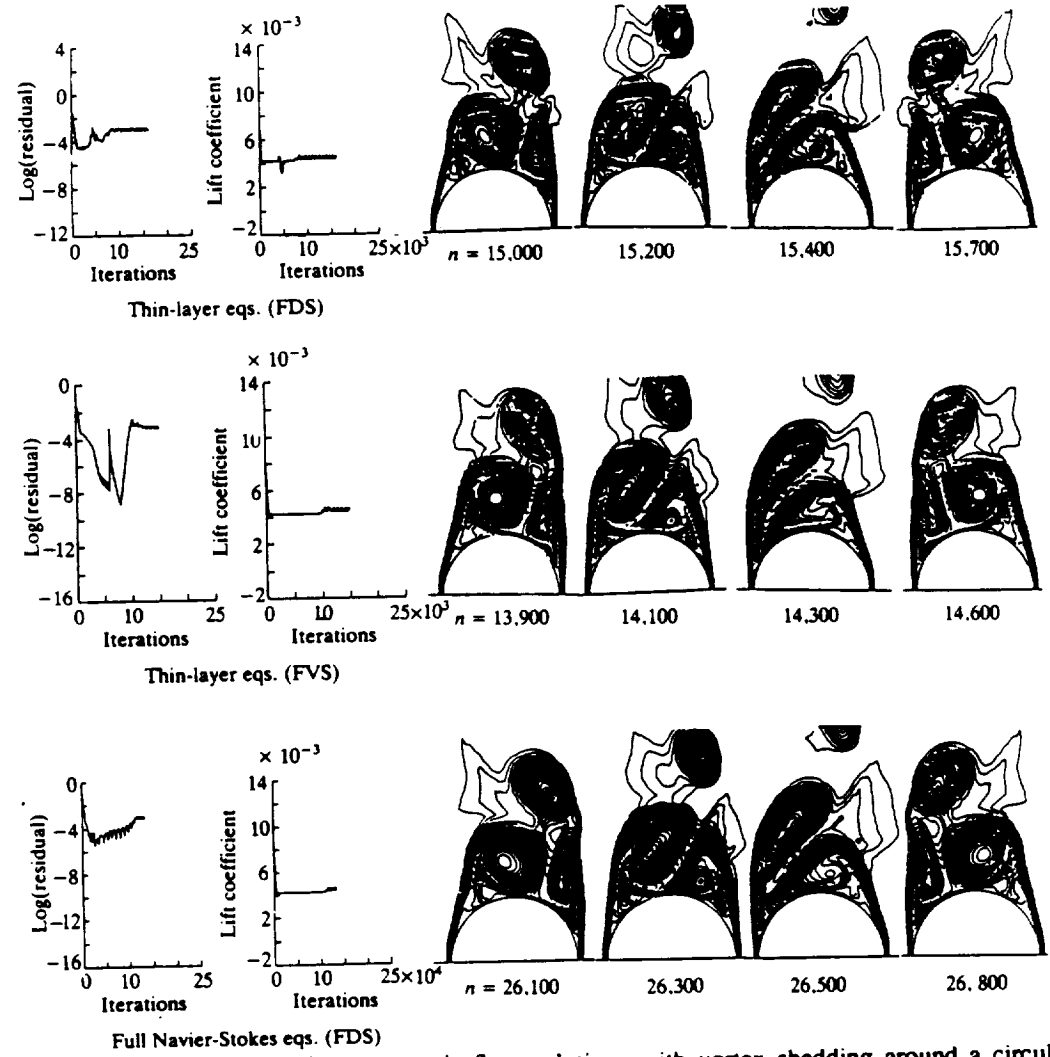


Figure 2. Comparison of unsteady asymmetric flow solutions with vortex shedding around a circular cone; periodic flow response; $\alpha = 30^\circ$, $M_\infty = 1.8$, $R_e = 10^5$, $\Delta t = 10^{-3}$.

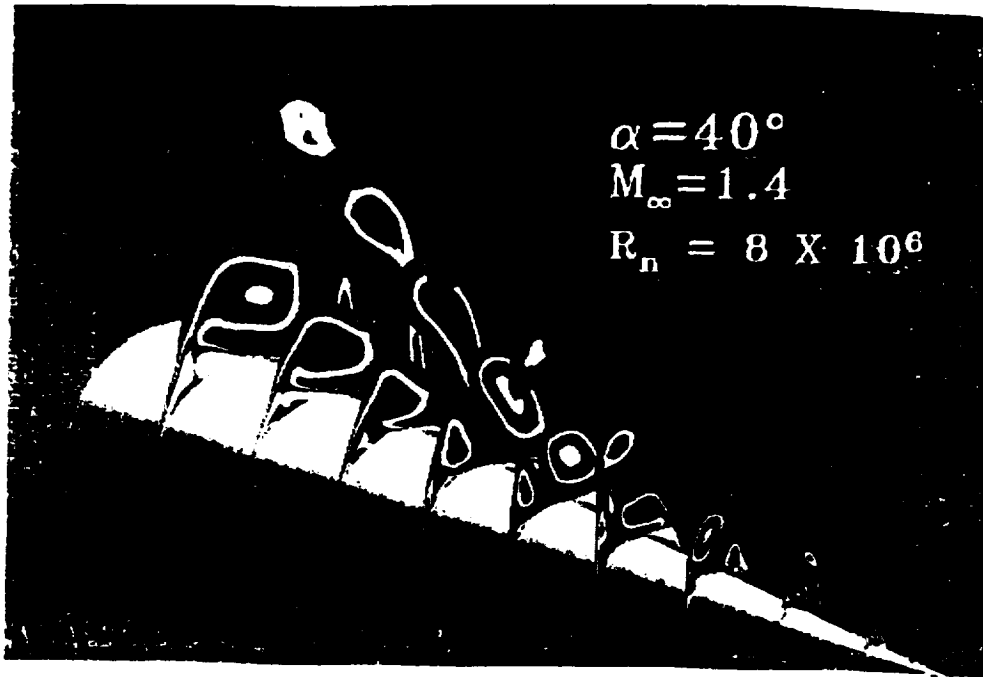


Figure 3. Asymmetric flow solution around a cone of unit length, short-duration side slip.

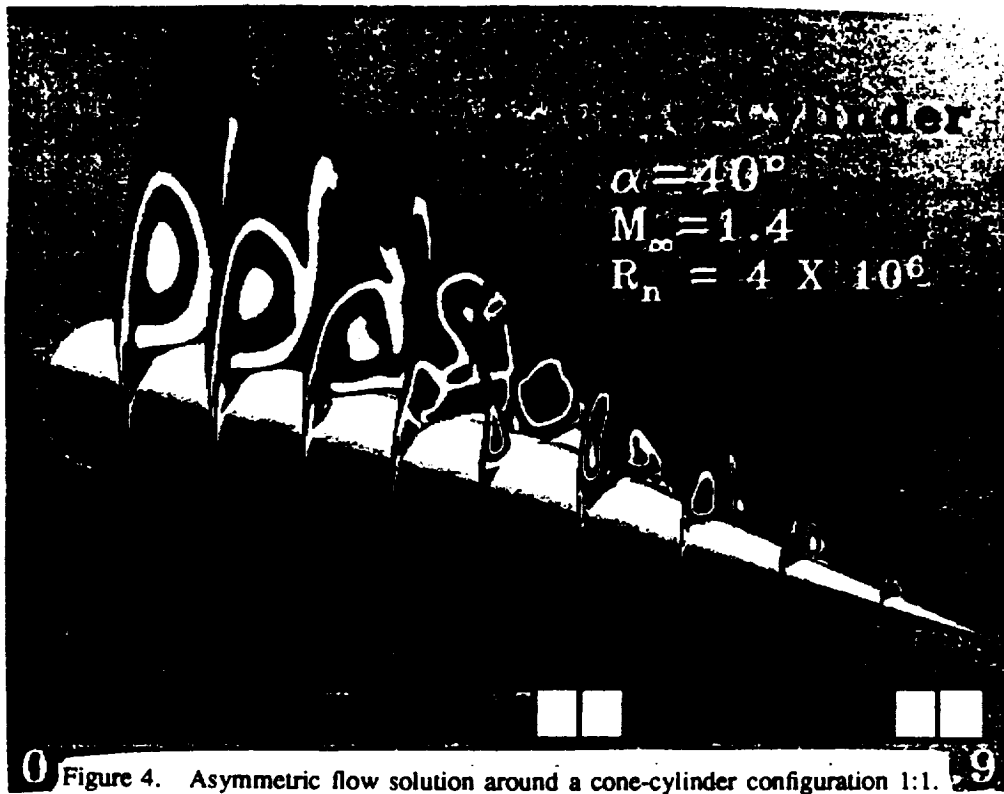


Figure 4. Asymmetric flow solution around a cone-cylinder configuration 1:1.

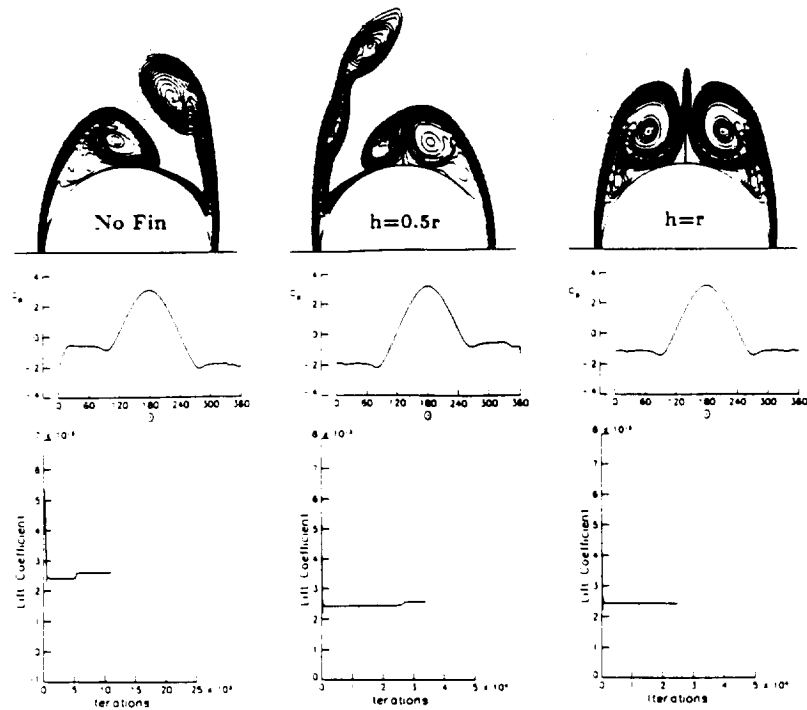


Figure 5. Passive control of asymmetric flow around a circular cone using a vertical fin. $\alpha = 20^\circ$, $M_\infty = 1.8$, $R_e = 10^5$, $h = 0.5r$ and r ($r \equiv$ cone local radius).

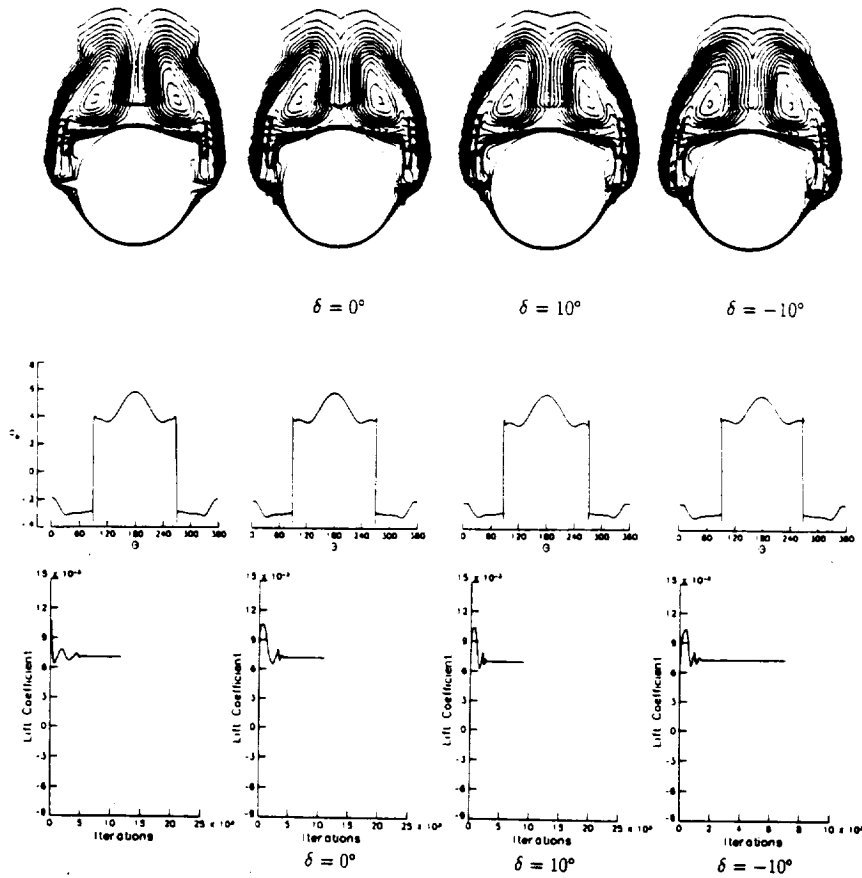


Figure 6. Passive control of asymmetric flow around a circular cone using sharp-edged thick strakes and flat-plate strakes with different orientations. $\alpha = 30^\circ$, $M_\infty = 1.8$, $R_e = 10^5$, $h = 0.3r$.

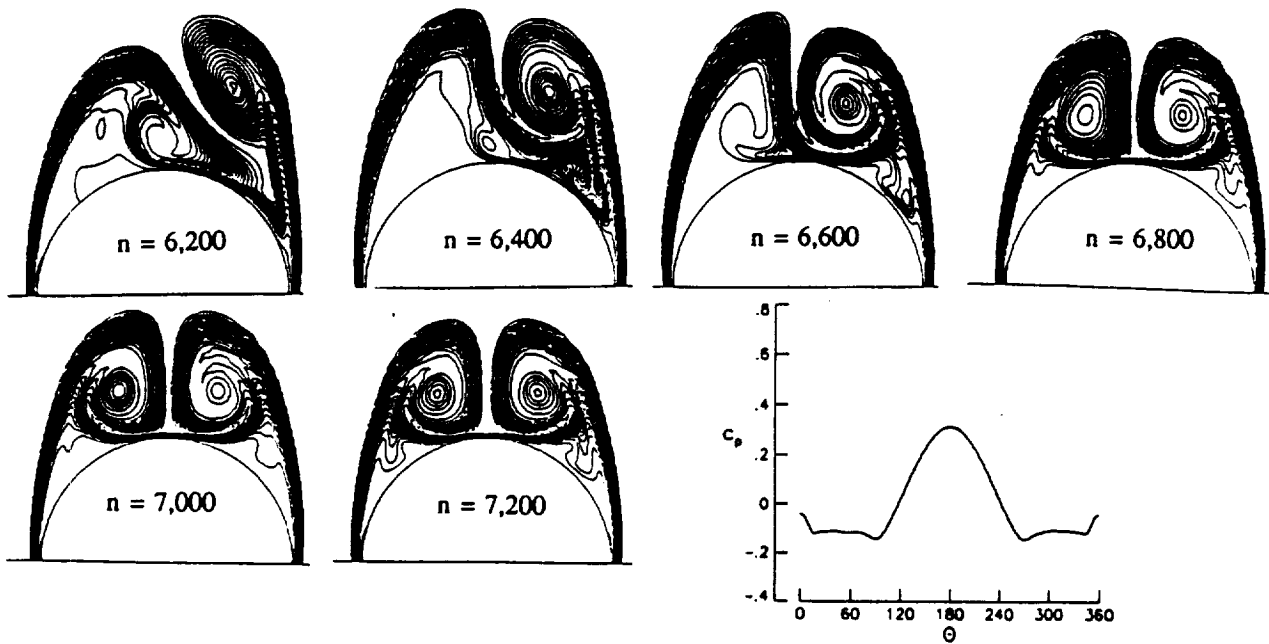


Figure 7. Normal-injection control; history of TPL contours and SP coefficient; $\alpha = 20^\circ$, $M_\infty = 1.8$, $R_e = 10^5$, variable \dot{m} , $\dot{m}_{\max} = 0.03$, $\theta = -67.5^\circ \rightarrow +67.5^\circ$.

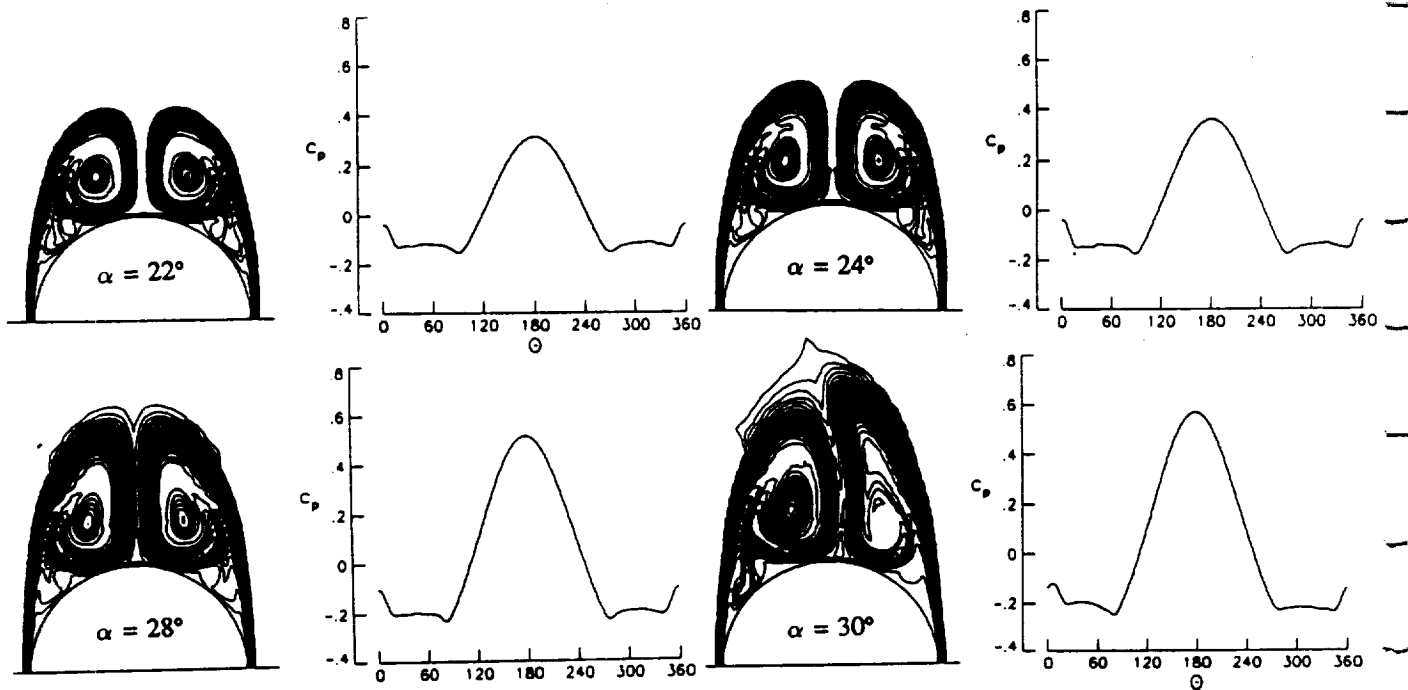


Figure 8. Normal-injection control; TPL contours and SP coefficient; $\alpha = 22^\circ - 30^\circ$, $M_\infty = 1.8$, $R_e = 10^5$, variable \dot{m} , $\dot{m}_{\max} = 0.03$, $\theta = -67.5^\circ - +67.5^\circ$.

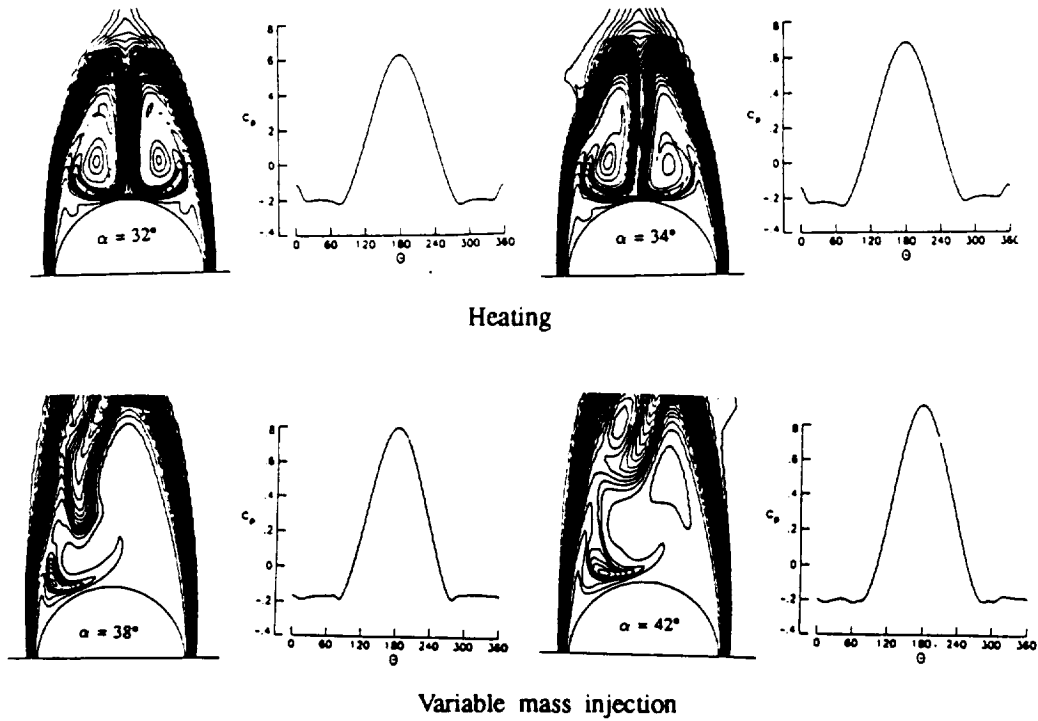


Figure 9. Hybrid heating-injection control; TPL contours and SP coefficient; $\alpha = 20^\circ - 42^\circ$, $M_\infty = 1.8$, $R_e = 10^5$, $\dot{m} = 0.05$, $T_s = 5T_\infty$ on whole surface.

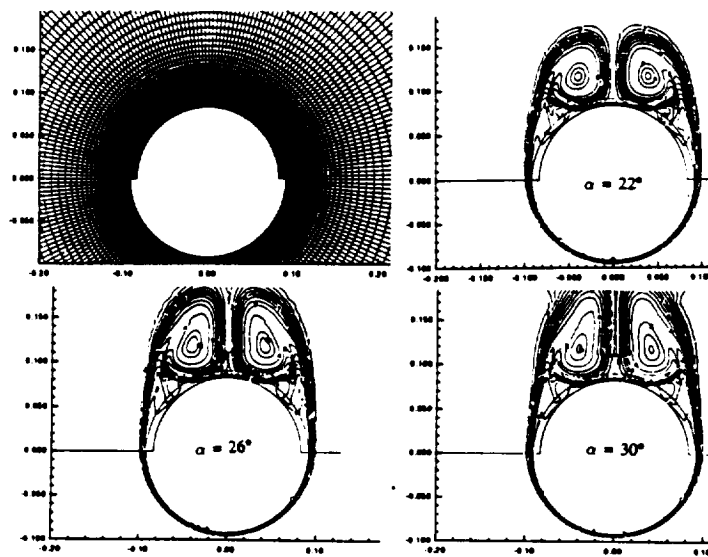


Figure 10. Typical multi-block grid and total pressure-loss contours for the tangential-flow injection control; $\alpha = 22^\circ, 26^\circ, 30^\circ$; $M_\infty = 1.8$, $R_e = 10^5$, parabolic velocity profile at lip exit, $\dot{m}_{\max} = 0.2$.

483004

Paper No. T.1.3

53 34
N93-14689
130112

**SHOCK/VORTEX INTERACTION AND
VORTEX-BREAKDOWN MODES**

P. 13

O. A. Kandil and H. A. Kandil
Old Dominion University, Norfolk, VA, USA

C. H. Liu
NASA Langley Research Center, Hampton, VA, USA



**IUTAM SYMPOSIUM OF FLUID
DYNAMICS OF HIGH ANGLE OF ATTACK
Tokyo, Japan — September 13-17, 1992**

SHOCK/VORTEX INTERACTION AND VORTEX-BREAKDOWN MODES

O. A. Kandil and H. A. Kandil
Dept. of Mechanical Engineering and Mechanics
Old Dominion University, Norfolk, VA

C. H. Liu
Theoretical Flow Physics Br.
NASA Langley, Hampton, VA

Summary

Computational simulation and study of shock/vortex interaction and vortex-breakdown modes are considered for bound (internal) and unbound (external) flow domains. The problem is formulated using the unsteady, compressible, full Navier-Stokes (NS) equations which are solved using an implicit, flux-difference splitting, finite-volume scheme. For the bound flow domain, a supersonic swirling flow is considered in a configured circular duct and the problem is solved for quasi-axisymmetric and three-dimensional flows. For the unbound domain, a supersonic swirling flow issued from a nozzle into a uniform supersonic flow of lower Mach number is considered for quasi-axisymmetric and three-dimensional flows. The results show several modes of breakdown; e.g., no-breakdown, transient single-bubble breakdown, transient multi-bubble breakdown, periodic multi-bubble multi-frequency breakdown and helical breakdown.

Introduction

Longitudinal vortex/transverse shock-wave interactions are typical applications which appear in transonic and supersonic flows over a strake-wing configuration at moderate-high angles of attack, at a supersonic inlet injecting a vortex and inside a supersonic combustor where fuel is injected in a swirling jet to enhance fuel-air mixing [1]-[3]. For the strake-wing configuration, vortex breakdown is undesirable since it results in the stall phenomenon, and hence its occurrence need to be delayed. On the other hand, vortex breakdown for the other two applications is desirable since it enhances mixing and stability of the flame [4]-[5], and hence its occurrence need to be controlled for the optimum performance. Unfortunately, the literature lacks this type of analysis with the exception of the preliminary work of Liu, Krause and Menne [6], Copening and Anderson [7], Delery, et al. [1], Kandil and Kandil [8] and Meadows, Kumer and Hussaini [9].

The first time-accurate NS solution for a supersonic vortex breakdown was developed by the present authors in Ref. [10]. We considered a supersonic quasi-axisymmetric vortex flow in a configured circular duct. The time-accurate solution of the unsteady, compressible NS equations was obtained using an implicit, upwind, flux-difference splitting finite-volume scheme. A shock wave has been generated near the duct inlet and unsteady vortex breakdown has been predicted behind the shock. The predicted flow was characterized by the evolution, convection merging and shedding of vortex breakdown bubbles. The Euler equations were

also used to solve the same problem. The Euler solution showed larger size and number of vortex-breakdown bubbles in comparison with those of the NS solutions. The time-accurate solution was carried out for 3,200 time steps which are equivalent to a dimensionless time of 16. Only one value of Reynolds number of 10,000 was considered in Ref. [10].

In a later paper [11], we expanded our study of this flow using time-accurate computations of the NS equations with a fine grid in the shock-vortex interaction region and for longer computational times. Several issues were addressed in that study. First, we showed the effect of Reynolds number on the temporal evolution and persistence of vortex-breakdown bubbles behind the shock. In that stage of computations, the conditions at the downstream exit were obtained by extrapolating the components of the flowfield vector from the interior cell centers. Although the flow was supersonic over a large portion of the duct exit, subsonic flow existed over a small portion of the exit around the duct centerline. Therefore, selected flow cases were computed using a Riemann-invariant-type boundary conditions as well as other boundary conditions at subsonic points of the duct exit [12].

In the present paper, we consider shock/vortex interaction and the resulting vortex breakdown modes for quasi-axisymmetric and three-dimensional flows. This study covers bound and unbound flow domains. For the bound domain, supersonic swirling flow is considered in a configured duct, and for the unbound domain supersonic swirling flow that is issued from a nozzle into a uniform supersonic flow of lower Mach number is considered.

Highlights of Formulation and Computational Scheme

Formulation: The conservative, unsteady, compressible, full Navier-Stokes equations in terms of time-independent, body-conformed coordinates ξ^1 , ξ^2 and ξ^3 are used to solve the problem. The equations are given in Ref. [11] and hence they are not presented here. Along with these equations, boundary conditions are specified at the computational-domain inlet, side wall and downstream exit. The downstream exit boundary conditions will be presented and discussed in the next section of the computational results. The initial conditions are also presented in the next section.

Computational Scheme: The computational scheme used to solve the unsteady, compressible full NS equations is an implicit, upwind, flux-difference splitting, finite-volume scheme. It employs the flux-difference splitting scheme of Roe which is based on the solution of the approximate one-dimensional Riemann problem in each of the three directions. In the Roe scheme, the inviscid flux difference at the interface of a computational cell is split into left and right flux differences. The splitting is accomplished according to the signs of the eigenvalues of the Roe averaged-Jacobian matrix of the inviscid flux at the cell interface. The smooth limiter is used to eliminate oscillations in the shock region. The viscous and heat-flux terms are differenced using second-order spatially accurate central differencing. The resulting

difference equation is approximately factored and is solved in three sweeps in the ξ^1 , ξ^2 and ξ^3 directions. The scheme is coded in the computer program which is called "FTNS3D".

The quasi-axisymmetric solutions are obtained using the three-dimensional code by forcing the flowfield vector to be equal on two axial planes, which are in close proximity of each other.

Computational Results and Discussion

a. Quasi-axisymmetric Vortex Breakdown Modes in a Configured Duct: Figure 1 shows an axial plane of a configured circular duct. The design of the duct configuration is intended to ensure that the supersonic inflow becomes supersonic at the exit. However, as the computation will show, a small portion of the duct exit becomes subsonic at certain times for the specified inflow conditions. A grid of $221 \times 51 \times 2$ in the axial, radial and circumferential directions, respectively, is used for the quasi-axisymmetric flow. For the three-dimensional flow, a grid of $221 \times 51 \times 49$ in the axial, radial and circumferential directions, respectively, is used. The minimum grid length is 0.002. The upstream Mach number is kept at 1.75.

The initial profile for the tangential velocity is given by

$$\frac{w}{U_\infty} = \frac{k_e}{r} \left[1 - \exp\left(-\frac{r^2}{r_m^2}\right) \right] \quad (1)$$

where $U_\infty = 1.74$, $r_m = 0.2$ and $k_e = 0.1$. The maximum $\frac{w}{U_\infty}$, swirl ratio β , is at $r = 0.224$ and its value is kept at 0.32. The radial velocity, v , at the initial station is set equal to zero and the radial momentum equation is integrated to obtain the initial pressure profile. Finally, the density ρ is obtained from the definition of the speed of sound for the inlet flow. With these compatible set of profiles, the computations are carried out accurately in time with $\Delta t = 0.0025$. The wall boundary conditions follow the typical Navier-Stokes solid-boundary conditions.

Reynolds number, $Re = 4,000$: Figure 2 shows snapshots of the streamlines and Mach contours for the flow case of $Re = 4,000$. For this value of Reynolds number, a single breakdown bubble is seen at $t = 5$ and it is convected downstreams as time passes. This breakdown bubble is formed during the downstream motion of the inlet shock, which reaches its maximum downstream displacement at $t = 5$. Later on, the shock moves upstream, as it is seen at $t = 8$, while the breakdown bubble is convected in the downstream direction. Thereafter, the shock stays stationary at the inlet. This swirling flow case shows a transient single-bubble breakdown flow. The conditions at the exit are obtained by extrapolation from the interior cell centers.

Reynolds number, $Re = 20,000$: Figure 3 shows snapshots of the streamlines and Mach contours for this case. These snapshots show a vortex breakdown mechanism of evolution,

convection, merging and shedding of bubbles while the inlet shock is moving downstreams, then upstreams and finally downstreams. The inlet shock becomes stationary and no more bubbles are developed. This swirling flow case shows a transient multi-bubble breakdown flow.

Reynolds number, $Re = 100,000$: Figure 4 shows snapshots of the streamlines and Mach contours for this case. The downstream boundary conditions are obtained by extrapolating all the flow variables from the cell centers at the exit. The streamlines snapshots show multi-bubble vortex breakdown evolution, convection, merging and shedding. The time-accurate integration was carried out up to $t = 200$ and the solution showed periodic multi-frequency cycles of vortex-breakdown bubbles [21]. An example of the merging of vortex breakdown bubbles of same sign of vorticity is shown at $t = 17$. An example of convection and shedding of vortex breakdown bubbles is shown at $t = 25$. Comparing the streamlines solutions at $t = 25$ and $t = 89$, it is seen that the solutions are almost the same which conclusively show that the breakdown process is periodic. The Mach-contours show the dynamics of inlet shock motion. In the time range of $t = 3-8$, the inlet shock moves upstream toward the inlet and its central portion exists outside the inlet section at $t = 8$. In the time range of $t = 8-25$, the inlet shock moves downstream with corresponding evolution, convection, merging and shedding of breakdown bubbles. In the time range of $t = 25-45$, the inlet shock maintains its motion in the downstream direction at a slower rate than before, while another shock, which is downstream of the inlet shock, appears and also moves in the downstream direction. The evolution, convection and shedding slowly continues until $t = 66$. In the time range of $t = 66-78$, the downstream shock disappears and a large vortex-breakdown bubble appears and moves upstream. This motion of the bubble is accompanied by upstream motion of the inlet shock ($t = 78$). Later the inlet shock again moves in the downstream direction and the process is repeated. An animation movie has been produced for the total dimensionless time of $t = 200$.

Exit Riemann Invariant Condition, $p_b = 2p_\infty$: In this case, the back pressure at the subsonic points of the duct exit is specified to be $p_b = 2p_\infty$ and the other four variables are extrapolated from the interior cell centers. Figure 5 shows snapshots of the streamlines and Mach contours of the solution. Comparing the present solution with the solution of the previous case (Fig. 4), it is seen that the two solutions are similar with the exception that the present solution lags that of the first case in time. The reason behind this behavior is that the back pressure p_b is larger than that of the first case. Moreover, the Riemann invariant type conditions at subsonic points let the downstream effects propagate upstream as time increases. The existence of the large back pressure which is felt upstream supports the inlet shock and keeps it in the inlet region.

b. Three-Dimensional Vortex-Breakdown in a Configured Duct: Figure 6 shows the streamlines and Mach contours for the three-dimensional vortex breakdown modes in a con-

figured duct with the same inflow conditions as those of Fig. 4. At the downstream exit, flow conditions are extrapolated from the interior cell centers. It is observed from the vertical, axial planes that the vortex breakdown is a three-dimensional phenomenon. The breakdown changes from a two-bubble type ($t = 2-5$) to a multi-bubble type ($t = 7-34$). At certain times, $t = 11$ and 19 , it is observed that the multi-bubble breakdown is followed by a spiral breakdown. Beyond $t = 46$, the breakdown becomes a single-bubble type.

c. Quasi-axisymmetric Vortex-Breakdown of a Supersonic Flow from a Nozzle: Here, a supersonic swirling jet at $M_j = 3.0$, which is issued from a nozzle into a supersonic uniform flow of $M_\infty = 2.0$, is considered. A grid of $221 \times 51 \times 2$ in the axial, radial and tangential directions, respectively is considered. The computational domain in an axial plane has the dimensions of 7.0×3.5 in the axial and radial directions, respectively, where the nozzle exit radius $r = 1$. The freestream Reynolds number is 296,000. The inflow profiles are taken from the experimental data of Ref. [2] and they are used as quasi-axisymmetric profiles [12]. Figure 7 shows snapshots of the streamlines and Mach contours at selected time steps. The streamline figures show multi-bubble breakdown at the early levels of time. These bubbles develop due to the shock system existing at the nozzle exit. The shock system consists of two oblique shocks; one is weak and the other is strong. For $t > 55$, the shock system and the breakdown bubble move upstreams and remain there with low frequency oscillation.

d. Three-Dimensional Vortex-Breakdown of a Supersonic Flow from a Nozzle: The flow of the previous case is considered for three-dimensional computations using a square-cross flow computational domain and a circular cross-flow computational domain. For the first case, one-half the square side is 3.5 units and for the second case, the radius is 3.5 units. Three types of grid are used for the first case (Grid types 1, 2 and 3) and one type of grid is used for the second case (Grid type 4), see Fig. 8. This study shows the dominant effect of the grid shape and distribution on the vortex breakdown solutions. While grid type 1 shows two large breakdown bubbles, Grids 2, 3 and 4 show substantially smaller breakdown bubbles. Moreover, the conical shock system ahead of the breakdown bubbles shows substantial difference in size, location and shape. This study gives an alarming conclusion to the researchers who use substantially coarse grids with a rectangular cross-flow domain and a rectangular grid, and still claim capturing of physical vortex-breakdown flows. In the present study, the vortex breakdown bubbles of grid type 4 are of the same size order as those of grid type 3, although the shock system is somewhat different in shape.

Concluding Remarks

Computational simulation and study of shock/vortex interaction and vortex breakdown have been considered for internal and external supersonic swirling flow. The time-accurate computation for full Navier-Stokes equations is used to produce all the present cases.

Numerous modes of vortex breakdown flows have been captured. The results show the effects of Reynolds number, downstream exit conditions, and grid shape, fineness and distribution. Three-dimensional vortex breakdown computations show somewhat different results from the quasi-axisymmetric counter parts since the three-dimensional flow provides a flow relieving effect in the circumferential direction.

Acknowledgement

For the first two authors, this research work has been supported by NASA Langley Research Center under Grant No. NAG-1-994.

References

1. Delery, J.; Horowitz, E.; Leuchter, O.; Solignac, J. L.: Fundamental Studies of Vortex Flows. *La Recherche Aéronautique*, No. 1984-2, 1984, pp. 1-24.
2. Metwally, O.; Settles, G.; Horstman, C.: An Experimentally Study of Shock Wave/Vortex Interaction. AIAA 89-0082, January 1989.
3. Cutler, A. D.; Levey, B. S.: Vortex Breakdown in a Supersonic Jet. AIAA 91-1815, June 1991.
- 4* Rhode, D. L.; Lilley, D. G.; McLaughlin, D. K.: On the Prediction of Swirling Flowfields Found in Axisymmetric Combustor Geometries. Transactions of ASME, Vol. 104, September 1982, pp. 378-384.
5. Altegeld, H.; Jones, W. P.; Wilhelmi: Velocity Measurements in a Confined Swirl Driven Recirculating Flow. *Experiments in Fluids*, Springer Verlag, Vol. 1, 1983, pp. 73-78.
6. Liu, C. H.; Krause, E.; Menne, S.: Admissible Upstream Conditions for Slender Compressible Vortices. AIAA 86-1093, 1986.
7. Copening, G.; Anderson, J.: Numerical Solutions to Three-Dimensional Shock/Vortex Interaction at Hypersonic Speeds. AIAA 89-0674, January 1989.
8. Kandil, O. A.; Kandil, H. A.: Computation of Compressible Quasi-Axisymmetric Slender Vortex Flow and Breakdown. IMACS 1st International Conference on Computational Physics, University of Colorado, Boulder, June 1990, pp. 46-51. Also in Computer Physics Communications, Vol. 65, North-Holland, March 1991, pp. 164-172.
9. Meadows, K.; Kumar, A.; Hussaini, M.: A Computational Study on the Interaction Between a Vortex and a Shock Wave. AIAA 89-1043, April 1989.
10. Kandil, O. A.; Kandil, H. A.; Liu, C. H.: Computation of Steady and Unsteady Compressible Quasi-Axisymmetric Vortex Flow and Breakdown. AIAA 91-0752, January 1991.
11. Kandil, O. A.; Kandil, H. A.; Liu, C. H.: Supersonic Quasi-Axisymmetric Vortex Breakdown. AIAA 91-3311-CP, September 1991, pp. 851-863.
12. Kandil, O. A.; Kandil, H. A.; Liu, C. H.: Critical Effects of Downstream Boundary Conditions on Vortex Breakdown. AIAA 92-2601-CP, June 1992.

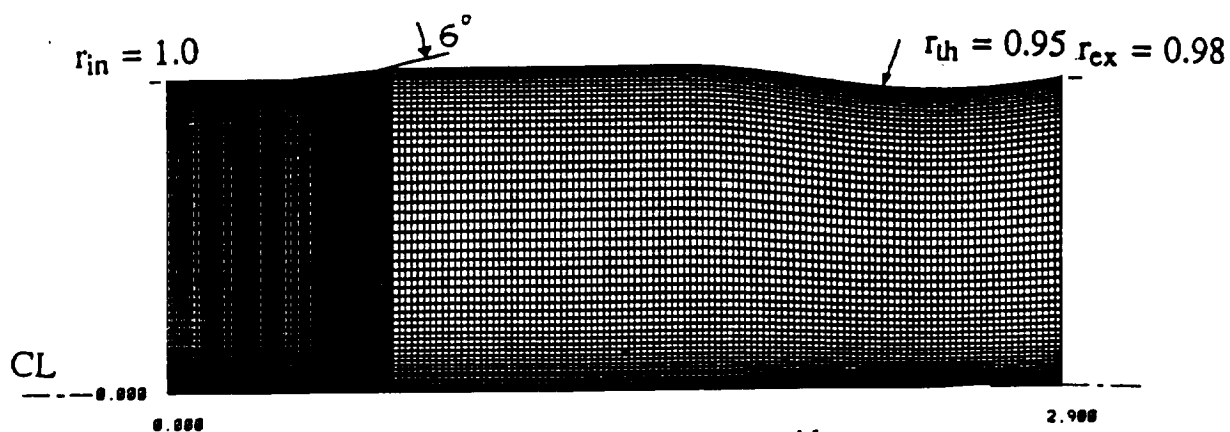


Figure 1. Configured duct grid

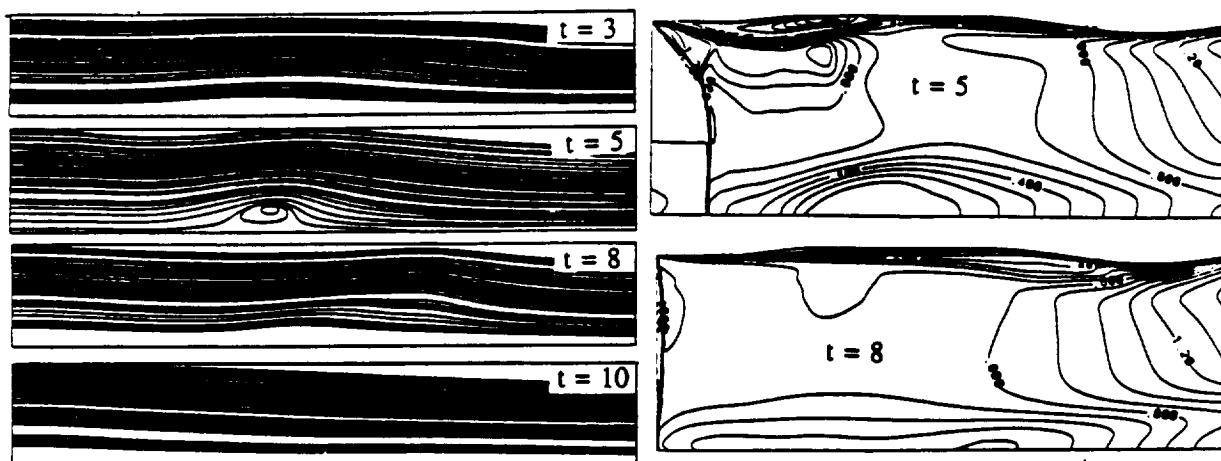


Figure 2. Streamlines and Mach contours for a swirling flow with a transient single-bubble breakdown, $M_\infty = 1.75$, $\beta = 0.32$, $Re = 4,000$.

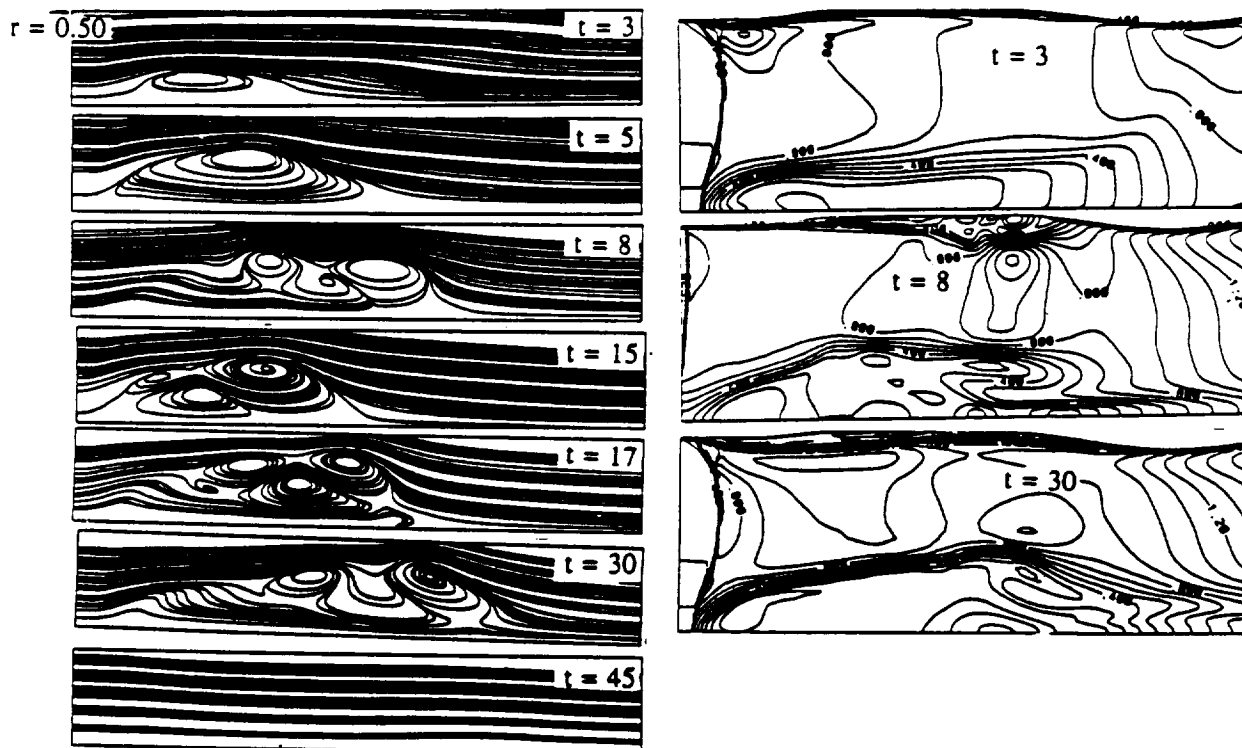


Figure 3. Streamlines for a swirling flow with transient multi-bubble breakdown, $M_\infty = 1.75$, $\beta = 0.32$, $Re = 20,000$

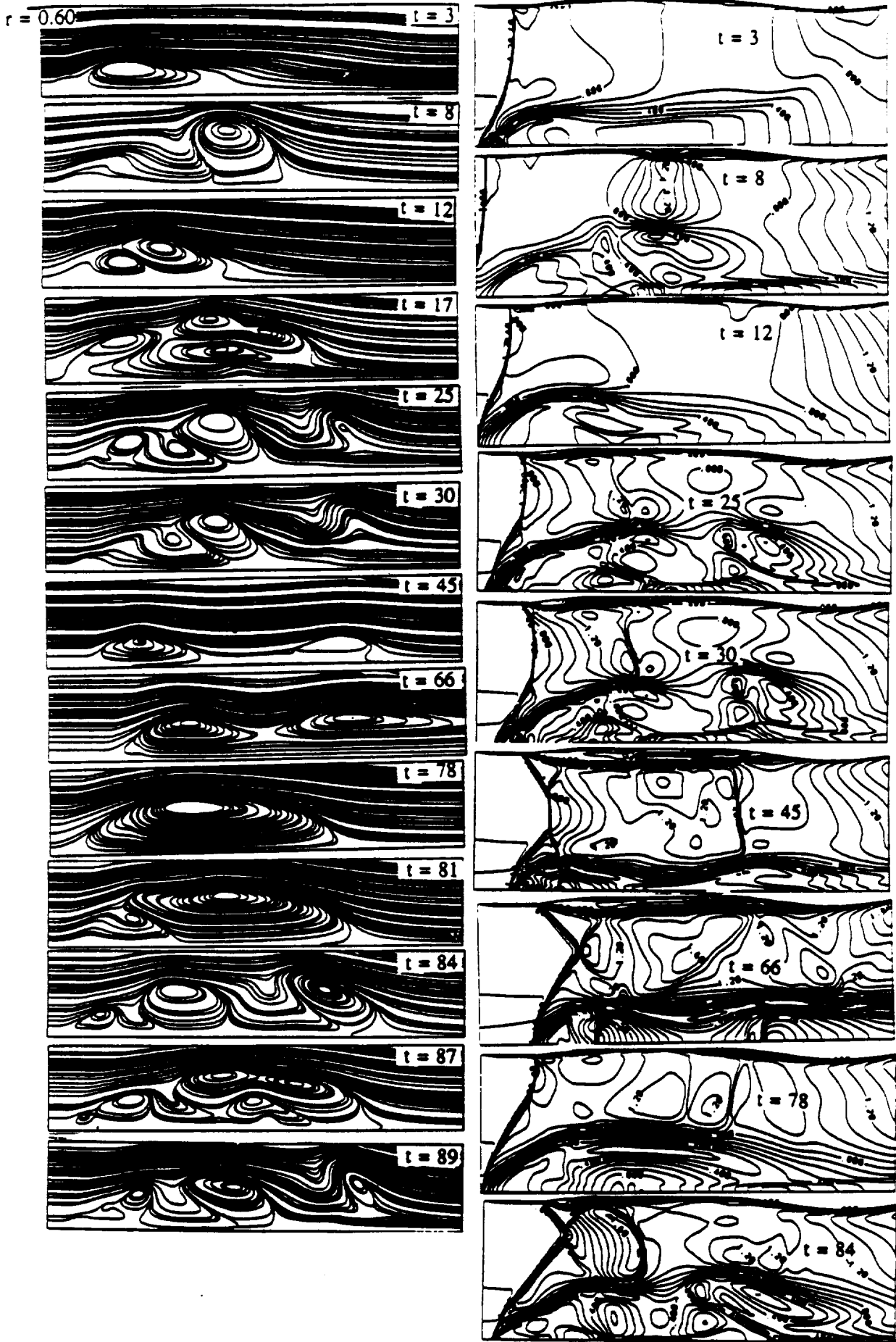


Figure 4. Streamlines and Mach contours for a swirling flow with periodic multibubble, multi-frequency vortex breakdown, extrapolation from interior

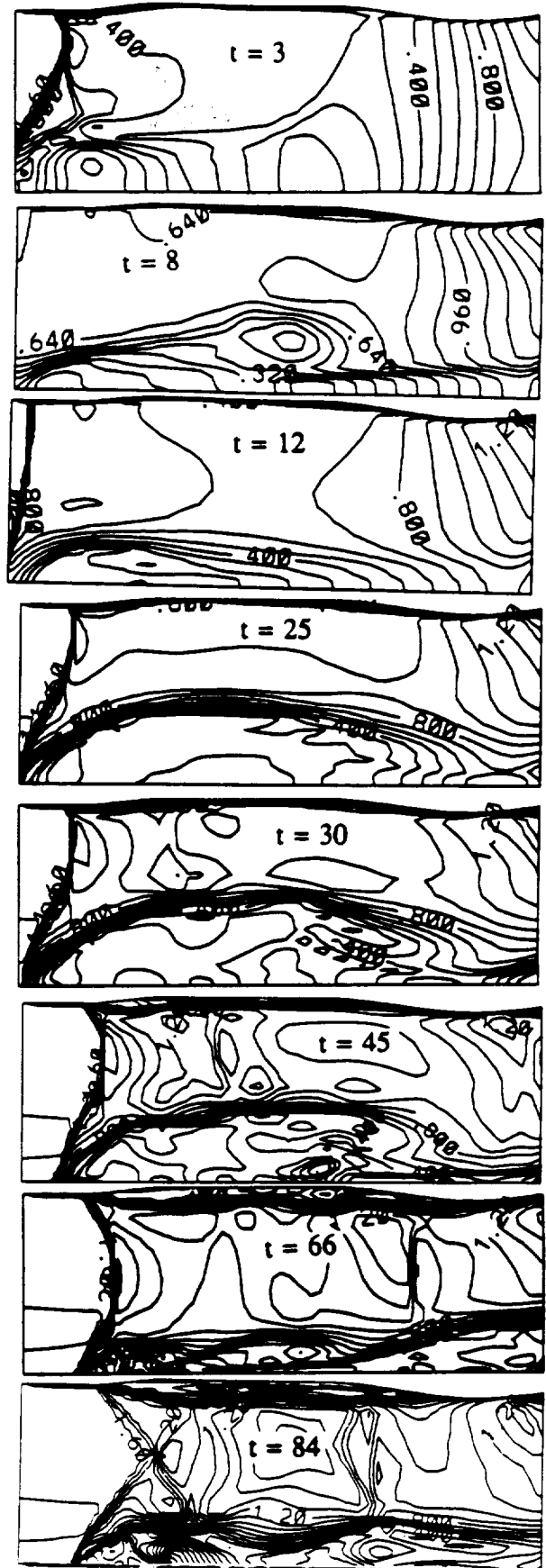
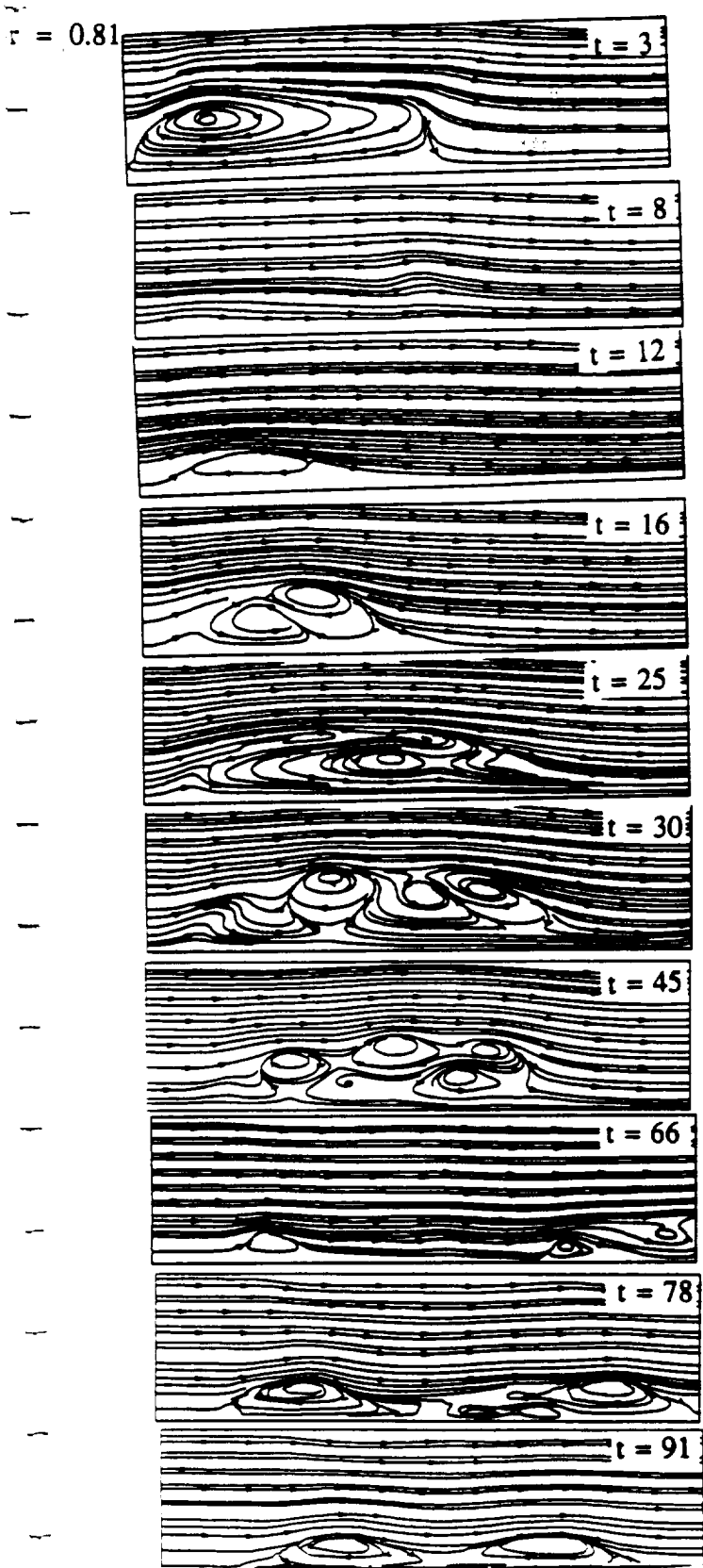


Figure 5. Streamlines and Mach contours for a swirling flow with periodic multibubble, multi-frequency vortex breakdown, $P_b = 2P_\infty$, Riemann invariant B.C.

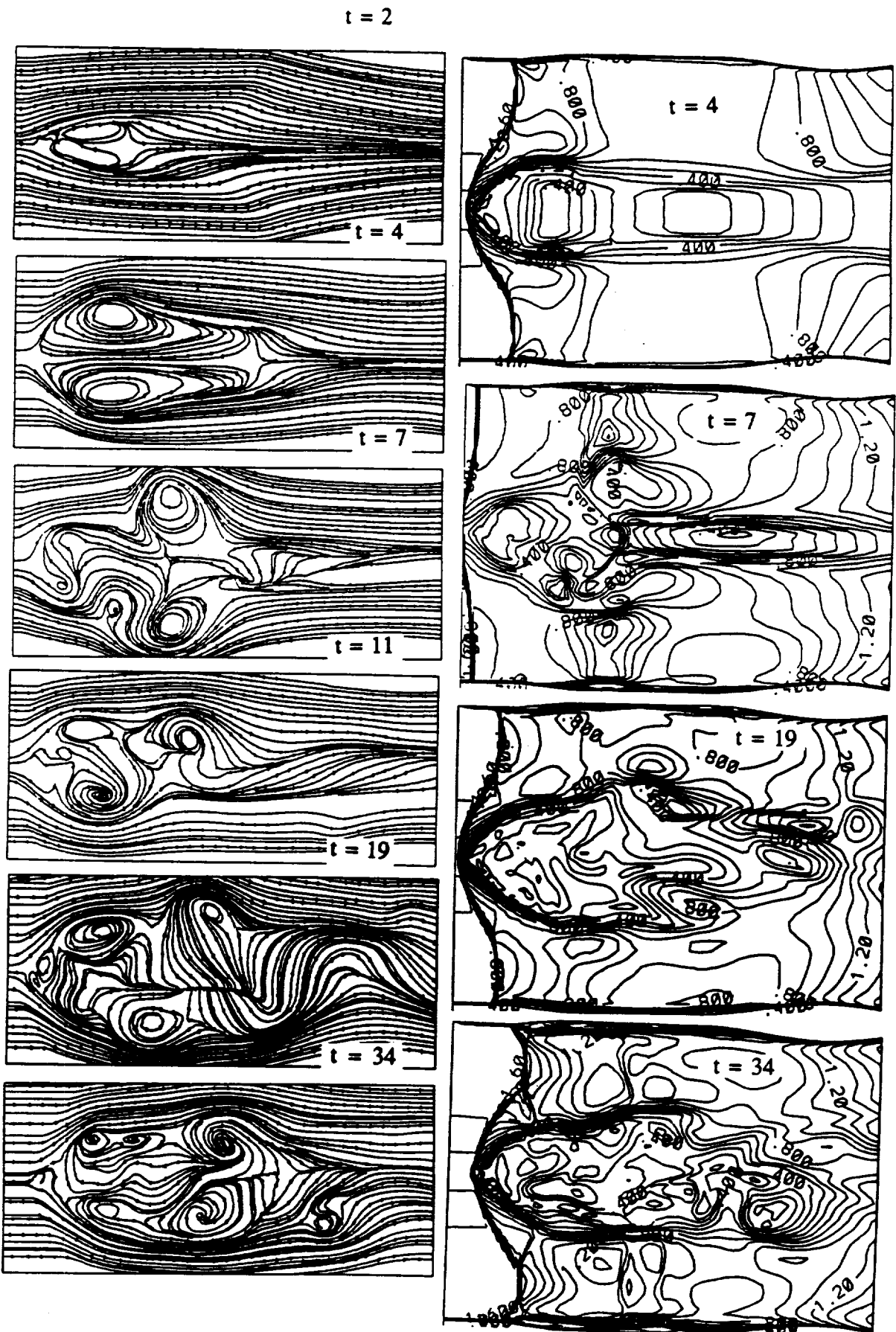
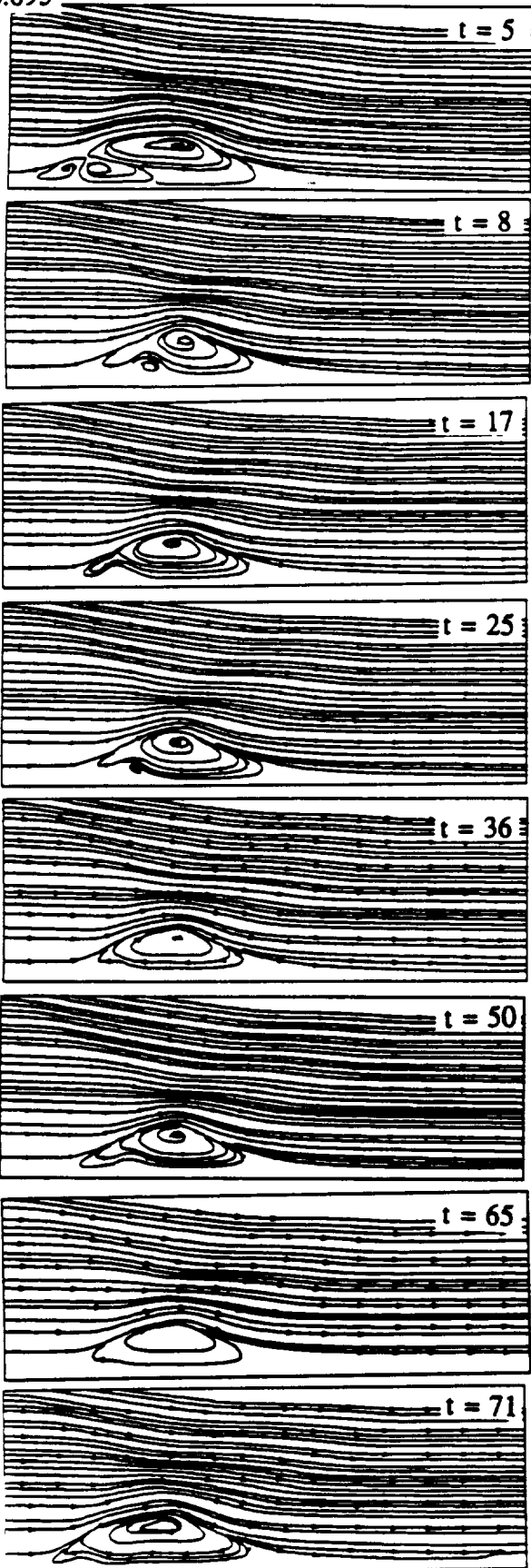


Figure 6. Mach contours and streamlines for a swirling three-dimensional flow in a configured circular duct, $M_\infty = 1.75$, $Re = 100,000$, $\beta = 0.32$

$r = 0.695$



$r = 1.1$

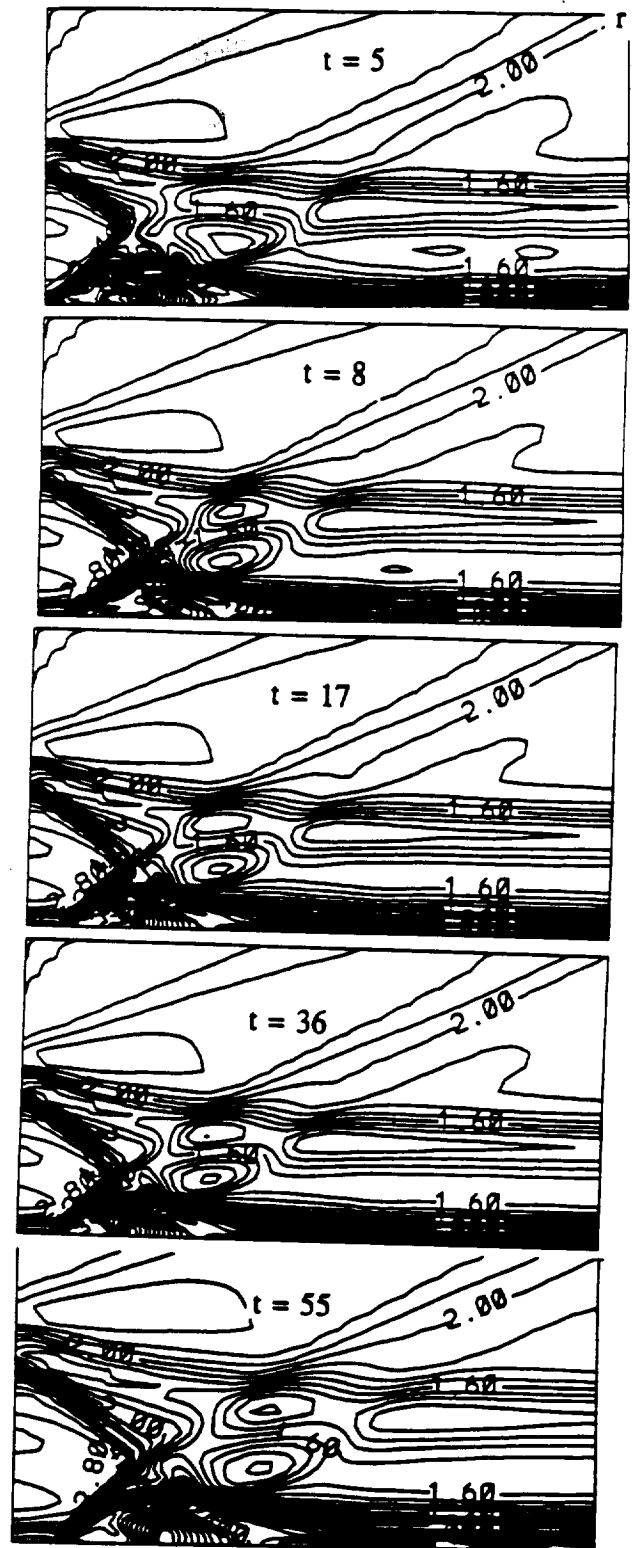


Figure 7. Streamlines and Mach contours for supersonic swirling jet from a nozzle with low-frequency almost single bubble vortex breakdown, extrapolation from interior B.C.

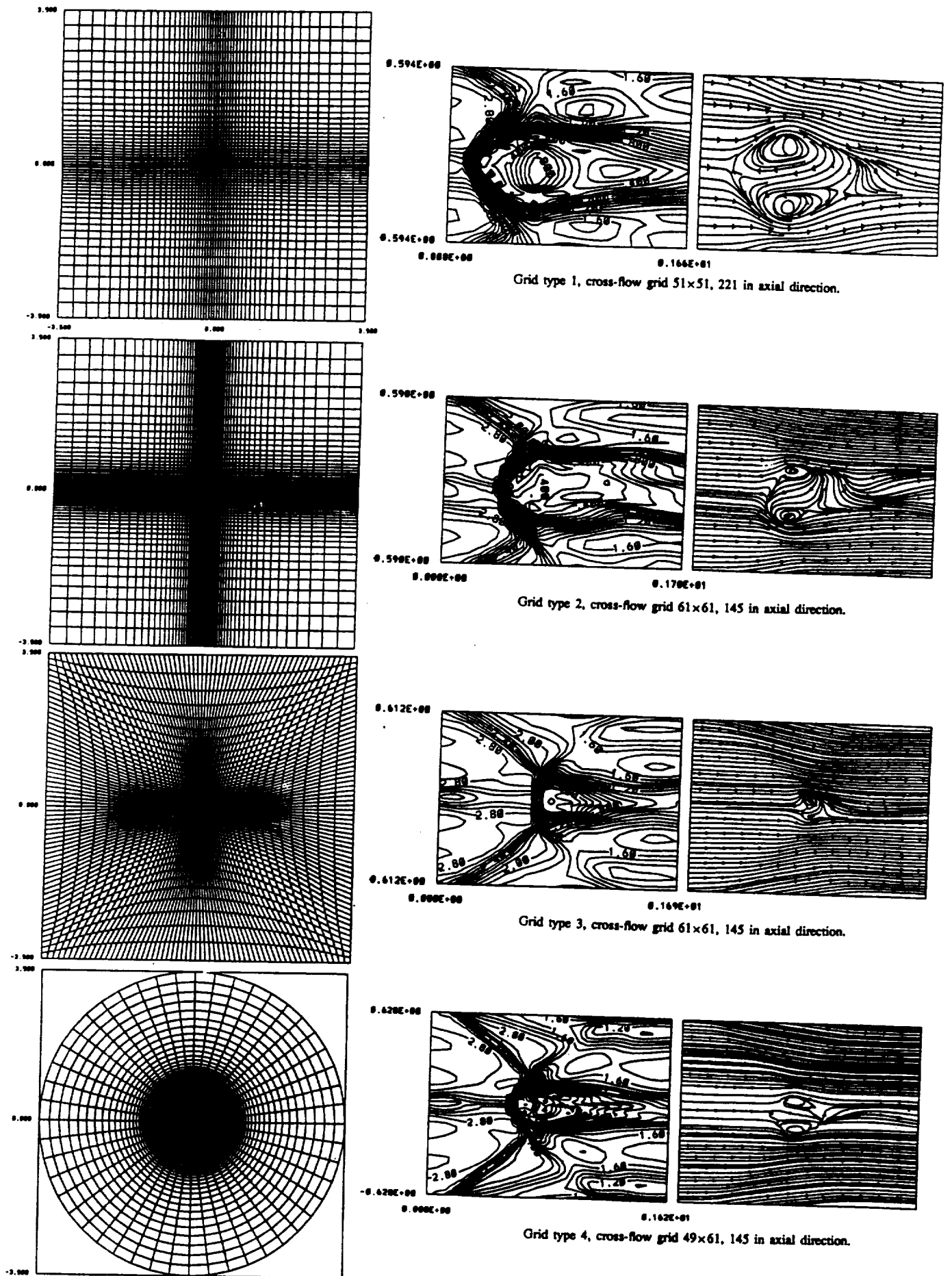


Figure 8. Mach contours and streamlines for vortex breakdown in a vertical axial plane for a supersonic swirling flow from a nozzle, $t = 10$, $M_j = 3.0$, $M_\infty = 2.0$, $Re = 296,000$



AIAA-92-4429-CP

**COMPUTATION OF VORTEX WAKE
FLOWS AND CONTROL OF THEIR
EFFECTS ON TRAILING WINGS**

**Tin-Chee Wong and Osama A. Kandil
Old Dominion University, Norfolk, VA 23529**

**C. H. Liu
NASA Langley Research Center, Hampton, VA 23665**

**AIAA Atmospheric Flight
Mechanics Conference
Hilton Head, SC, August 10-12, 1992**



COMPUTATION OF VORTEX WAKE FLOWS AND CONTROL OF THEIR EFFECTS ON TRAILING WINGS

Tin-Chee Wong* and Osama A. Kandil**
Old Dominion University, Norfolk, VA 23529

and
C.H. Liu***

NASA Langley Research Center, Hampton VA 23665

ABSTRACT

The near-vortex-wake flow of a large aspect-ratio rectangular wing is accurately computed by using the thin-layer and full Navier-Stokes (NS) equations. The chordwise section of the wing is a NACA-0012 airfoil and its tip is round. The computations have been carried out on a fine C-O grid using an implicit, upwind, flux-difference splitting, finite-volume scheme. The thin-layer NS results have been obtained with and without flux limiters and the full NS results have been obtained without flux limiters. Flow transition from laminar to turbulent is mimicked by turning-on the Baldwin-Lomax algebraic model at an experimentally prescribed chord-station location of 0.05. Comparison of the computed results with each other and with the experimental data shows that the full NS results give the best resolution of the near-vortex-wake flow. Next, the strength of the wing-tip vortex has been reduced substantially without reducing the lift coefficient by using flow-injection from a slot along a portion of the wing tip. The flow injection is directed in the wing plane at 45° with the wing-tip chord.

INTRODUCTION

Recently, there has been an alarming rate of increase of the volume of air civil transport at many airports. With this status of air traffic congestion, the hazardous effect of wake vortices emanating from large aircraft on light aircraft, which pass through these vortices during landing and take-off operations, is becoming a vital concern for operations safety. These vortices are characterized with high intensity and turbulence, and may produce high rolling moments on trailing aircraft which could exceed the available roll control of the trailing aircraft. Moreover, the trailing aircraft, under the influence of these vortex trails, could suffer a loss of altitude or climb rate in addition to structural damages. These vortices may persist up to several miles and for long periods of time before their decay, and therefore they play a major role in sequencing landing and take-off operations at busy airports. For example, a minimum safe-separation distance between aircraft is dictated depending on the vortex intensity, wind shear, atmospheric turbulence and temperature gradient; among others.

* Research Associate, Dept. of Mechanical Engineering and Mechanics, Member AIAA.

** Professor and Eminent Scholar, Dept. of Mechanical Engineering and Mechanics, Associate Fellow AIAA.

*** Group Leader, Theoretical Flow Physics Branch, Associate Fellow AIAA.

The literature shows a few experimental and computational investigations that attempt to model and analyze wake vortex interaction, merging, decay and their hazardous effects on trailing aircraft. Hallock and Eberle¹ presented a review of the state of the art of aircraft wake vortices covering the research efforts in the United States until the mid-seventies. Experimental wind tunnel and airport measurements of the vortex wakes were conducted by Dee and Nicholas² Harvey and Perry³, El-Ramly⁴, Wood and McWilliams⁵, Gardoz⁶, Cliffone and Lonzo⁷, Olwi and Ghazi⁸, Liu⁹ and Liu et al¹⁰.

Mathematical models and computational schemes were developed using inviscid analysis by Chorin and Bernard¹¹, Hacket and Evans¹², Yates¹³, Iversen and Bernstein¹⁴, and Rossow¹⁵. Although an inviscid model cannot describe the wake aging including its diffusion, it is still capable of producing the wake shape and its dynamics. The mathematical modeling used in the above references were based on the use of the point vortex method to compute the motion of a finite number of point vortices which model the vorticity behind a wing. The first three-dimensional inviscid model was introduced by Kandil, et. al¹⁶, where the nonlinear vortex-lattice, which was also developed by Kandil, et. al¹⁷, was used to compute the interference flow between wings and the vortex wake hazardous effects.

Viscous modeling of trailing vortices was first introduced by McCormick, et. al¹⁸. Viscous interactions in vortex wakes and the effects of background turbulence, wind shear and ground on two-dimensional vortex pairs were presented by Bilanin, et. al^{19,20}. Liu and his co-workers²¹⁻²⁴ studied the interaction, merging and decay of vortices in two-dimensional space and of three-dimensional vortex filaments. To estimate the effects of density stratification, turbulence and Reynolds number on vortex wakes, an approximate model was recently developed by Greene²⁵. Later on, Greene and his co-workers²⁶ presented selected results of aircraft vortices which include a juncture vortex, a lifting-wing vortex and a wake vortex.

It is concluded from the above brief literature survey that the problem contains several vortex flow regions along with several critical parameters influencing the vortex wake flows. The vortex wake flow of interacting-wing problems can be divided into three regions. The first region includes the leading wing and its near-vortex-wake flow. The second region includes the interacting vortices in the wake. The third region includes the far-wake flow along with the trailing-wing flow. In Ref. 27, Kandil,

Wong and Liu presented results of the near-vortex-wake flow for a large-aspect-ratio rectangular wing using the thin-layer, Reynolds averaged, NS equations on a C-O grid. Next, a small aspect-ratio rectangular wing was introduced in the near-wake of the leading wing and the problem was recomputed to demonstrate the hazardous effects of the vortex wake flow. Two interference cases were considered. The first was called the "along-track penetration through vortex center" and the second was called the "along-track penetration between vortices", see Fig. 1. It was demonstrated that in the first case, the trailing wing experienced large rolling moments and in the second case the trailing wing experienced loss of lift.

In the present paper, the near-vortex-wake flow is recomputed using a finer grid than the grid used in Ref. 27. Moreover, the thin-layer and full NS equations are used along with an upwind scheme, wherein the flux limiter of the solver is turned on and off. The goal of this part of the paper is to accurately compute the vortex wake flow and to study the effect of the numerical dissipation of the flux limiter on the computed results. In the second part of the paper, alleviation of the strength of the tip vortex without reducing the lift force is demonstrated by using directed flow injection from a slot along a certain length of the wing tip.

FORMULATION

Full and Thin-Layer Navier-Stokes Equations

The conservative form of the dimensionless, unsteady, compressible, full Navier-Stokes equations in terms of time-independent, body-conformed coordinates ξ^1 , ξ^2 and ξ^3 is given by

$$\frac{\partial \bar{Q}}{\partial t} + \frac{\partial \bar{E}_m}{\partial \xi^m} - \frac{\partial (\bar{E}_v)_s}{\partial \xi^s} = 0; \quad m = 1-3, \quad s = 1-3 \quad (1)$$

where

$$\xi^m = \xi^m(x_1, x_2, x_3) \quad (2)$$

$$\bar{Q} = \frac{\bar{q}}{J} = \frac{1}{J}[\rho, \rho u_1, \rho u_2, \rho u_3, \rho e]^t \quad (3)$$

$$\begin{aligned} \bar{E}_m &\equiv \text{inviscid flux} \\ &= \frac{1}{J} [\partial_k \xi^m \hat{E}_k]^t \\ &= \frac{1}{J} [\rho U_m, \rho u_1 U_m + \partial_1 \xi^m p, \rho u_2 U_m \\ &\quad + \partial_2 \xi^m p, \rho u_3 U_m + \partial_3 \xi^m p, (\rho e + p) U_m]^t \end{aligned} \quad (4)$$

$$\begin{aligned} (\bar{E}_v)_s &\equiv \text{viscous and heat - conduction flux in } \xi^s \\ &\quad \text{direction} \\ &= \frac{1}{J} [0, \partial_k \xi^s \tau_{k1}, \partial_k \xi^s \tau_{k2}, \partial_k \xi^s \tau_{k3}, \\ &\quad \partial_k \xi^s (u_n \tau_{kn} - q_k)]^t; \quad k = 1-3, \quad n = 1-3 \end{aligned} \quad (5)$$

$$U_m = \partial_k \xi^m u_k \quad (6)$$

The three momentum elements of Eq. (5) are given by

$$\begin{aligned} \partial_k \xi^s \tau_{kj} &\equiv \frac{M_\infty \mu}{Re} \left[\left(\partial_k \xi^s \partial_j \xi^n - \frac{2}{3} \partial_j \xi^s \partial_k \xi^n \right) \frac{\partial u_k}{\partial \xi^n} \right. \\ &\quad \left. + \partial_k \xi^s \partial_k \xi^n \frac{\partial u_j}{\partial \xi^n} \right]; \quad j = 1-3 \end{aligned} \quad (7)$$

The last element of Eq. (5) is given by

$$\begin{aligned} \partial_k \xi^s (u_p \tau_{kp} - q_k) &\equiv \frac{M_\infty \mu}{Re} \left[\left(\partial_k \xi^s \partial_p \xi^n \right. \right. \\ &\quad \left. \left. - \frac{2}{3} \partial_p \xi^s \partial_k \xi^n \right) u_p \frac{\partial u_k}{\partial \xi^n} \right. \\ &\quad \left. + \partial_k \xi^s \partial_k \xi^n u_p \frac{\partial u_p}{\partial \xi^n} \right. \\ &\quad \left. + \frac{1}{(\gamma-1)P_r} \partial_k \xi^s \frac{\partial (a^2)}{\partial \xi^n} \right]; \quad p = 1-3 \end{aligned} \quad (8)$$

The single thin-layer approximations of the full Navier-Stokes equations demand that we only keep the derivatives in the normal direction to the body, ξ^2 , in the viscous and heat flux terms in Eqs. (1), (7) and (8). Thus, we let $s = 2$ for the term $\frac{\partial (\bar{E}_v)_s}{\partial \xi^s}$ in Eq. (1) and $s = 2$ and $n = 2$ in Eqs. (7) and (8). These equations reduce to

$$\frac{\partial \bar{Q}}{\partial t} + \frac{\partial \bar{E}_m}{\partial \xi^m} - \frac{\partial (\bar{E}_v)_2}{\partial \xi^2} = 0 \quad (9)$$

$$\partial_k \xi^2 \tau_{k1} \equiv \frac{M_\infty \mu}{Re} \left(\psi \partial_1 \xi^2 + \phi \frac{\partial u_1}{\partial \xi^2} \right) \quad (10)$$

$$\begin{aligned} \partial_k \xi^2 (u_p \tau_{kp} - q_k) &\equiv \frac{M_\infty \mu}{Re} \left\{ \psi W \right. \\ &\quad \left. + \phi \left[\frac{1}{2} \frac{\partial}{\partial \xi^2} (u_1^2 + u_2^2 + u_3^2) \right. \right. \\ &\quad \left. \left. + \frac{1}{(\gamma-1)P_r} \frac{\partial (a^2)}{\partial \xi^2} \right] \right\} \end{aligned} \quad (11)$$

where

$$\phi_1 = \partial_k \xi^2 \partial_k \xi^2, \quad \psi = \frac{1}{3} \partial_k \xi^2 \frac{\partial u_k}{\partial \xi^2}, \quad W = \partial_p \xi^2 u_p \quad (12)$$

In Eqs. (1)-(12), the dimensionless variables are referenced to their appropriate freestream values. The dimensionless density ρ , cartesian velocity components u_1 , u_2 and u_3 , total energy per unit mass, e , dynamic viscosity, μ and speed of sound, a , are defined as the ratio of the corresponding physical quantities to those of the freestream; namely, ρ_∞ , a_∞ , $\rho_\infty a_\infty^2$, μ_∞ and a_∞ ; respectively. The pressure, p , is non-dimensionalized by $\rho_\infty a_\infty^2$, and is related to the total energy for a perfect gas by the equation of state

$$p = (\gamma-1)\rho \left(e - \frac{1}{2} u_j u_j \right); \quad j = 1-3 \quad (13)$$

where γ is the ratio of specific heats and its value is 1.4. The viscosity, μ , is calculated from the Sutherland law

$$\mu = T^{3/2} \left(\frac{1+c}{T+c} \right), c = 0.4317 \quad (14)$$

where T is the temperature which is non-dimensionalized by T_∞ . The Prandtl number, P_r is fixed at 0.72. The Reynolds number is defined as $R_e = \rho_\infty U_\infty L / \mu_\infty$ and the characteristic length, L , is chosen as the root chord of the wing.

In Eqs. (1)-(13), the indicial notation is used for convenience. The subscripts k, n, p and j are summation indices, the superscript or subscript s is a summation index and the superscript or subscript m is a free index. The partial derivative $\frac{\partial}{\partial x_k}$ is referred to by ∂_k .

Turbulent Flow

For the turbulent flow, the Navier-Stokes equations are transformed to the Reynolds-averaged equations by replacing the coefficient of molecular viscosity, μ , and the coefficient of thermal conductivity k with

$$\mu_t = \mu + \mu_t = \mu(1 + \mu_t/\mu) \quad (15)$$

$$k_e = k + k_t = \frac{\mu C_p}{P_r} \left(1 + \frac{\mu_t P_r}{\mu P_r} \right) \quad (16)$$

where μ_e is the effective viscosity, k_e the effective thermal conductivity, μ_t the turbulent viscosity, P_r the laminar Prandtl number, P_r the turbulent Prandtl number and C_p the specific heat under constant pressure. The turbulent viscosity μ_t is obtained by using the two-layer algebraic eddy viscosity model which was first developed by Cebeci²⁸ for the boundary-layer equations and modified later by Baldwin and Lomax²⁹ for the Navier-Stokes equations. The details of the turbulent model is given in Ref. (30) by Wong, Kandil and Liu.

Boundary and Initial Conditions

Boundary conditions are explicitly implemented. They include the inflow-outflow conditions and the solid-boundary conditions. At the plane of geometric symmetry, periodic conditions are used. The inflow-outflow boundary conditions are implemented using the one-dimensional Riemann-invariant conditions normal to these boundaries. On the solid boundaries, the no-slip and no-penetration conditions are enforced; $u_1 = u_2 = u_3 = 0$, and the normal pressure gradient is set equal to zero. For the temperature, the adiabatic boundary condition is enforced at the solid boundaries.

The initial conditions correspond to the freestream conditions with $u_1 = u_2 = u_3 = 0$ on the solid boundaries.

The freestream conditions are given by

$$\begin{aligned} \rho_\infty &= a_\infty = T_\infty = 1, \\ u_{1\infty} &= M_\infty \cos \alpha, \\ u_{2\infty} &= M_\infty \sin \alpha, \\ u_{3\infty} &= 0, \\ p_\infty &= 1/\gamma, e_\infty = \frac{1}{\gamma(\gamma-1)} + \frac{M_\infty^2}{2} \end{aligned} \quad (17)$$

where α is the angle of attack.

COMPUTATIONAL SCHEME

The implicit, upwind, flux-difference splitting, finite-volume scheme is used to solve the unsteady, compressible, thin-layer and Full Reynolds-averaged, Navier-Stokes equations. The scheme uses the flux-difference splitting scheme of Roe which is based on the solution of the approximate Riemann problem. In the Roe scheme, the inviscid flux difference at the interface of computational cells is split into two parts; left and right flux differences. The splitting is accomplished according to the signs of the eigenvalues of the Roe averaged-Jacobian matrix of the inviscid fluxes at the cell interface. The smooth flux limiter is used to eliminate oscillations at locations of large flow gradients. The viscous and heat-flux terms are linearized and the cross-derivative terms are eliminated in the implicit operator. The viscous terms are differenced using a second-order accurate central differencing. The resulting difference equation is approximately factored and is solved in three sweeps in the ξ^1 , ξ^2 , and ξ^3 directions. The computational scheme is coded in the computer program "FTNS-3D"³¹.

COMPUTATIONAL RESULTS AND DISCUSSIONS

We consider a rectangular wing of aspect ratio, $AR = 5.9$ and a NACA 0012 chordal section, at an angle of attack of $\alpha=4.64^\circ$. The flow Reynolds number, R_e is 3.2×10^6 (based on the root-chord length) and the Mach number, M_∞ is taken as 0.3 for low speed flows. The computational domain consists of a hemispherical boundary which is followed by a cylindrical boundary. The hemisphere center is located at the intersection of the wing root-chord and its trailing edge. Its radius is 15 chords and the cylindrical boundary extends 14 chords in the downstream direction beyond the trailing edge. A C-O grid of $231 \times 65 \times 65$ grid points in the streamwise wrap-around, spanwise and normal directions, respectively, is generated by using transfinite interpolation. The minimum grid spacings normal to the wing surface at the leading-edge and tip regions are chosen to be 10^{-5} . The grid points close to the trailing edge are clustered up to 5 chords in the downstream direction. The reason is that for the present work our interest is focused on the resolution of the near-vortex-wake flow. Figure 2 shows a typical grid for the wing and its near wake. The flow is considered to be laminar until the chord station of 0.05 from the wing leading edge. Thereafter, the turbulent model is

turned on to mimic the transition to turbulent flow. This location of the transitional flow has been experimentally determined by Yip and Shubert³².

Thin-Layer and Full Navier-Stokes Solutions

The flow around the rectangular wing is solved using the thin-layer NS equations and the full NS equations. The computations are carried out three times using the same grid described above and the implicit upwind scheme. In the first and second times, the thin-layer NS equations are solved using the implicit upwind scheme with and without the smooth flux limiter. In the third time, the full NS equations are solved using the implicit upwind scheme without the smooth flux limiter. Next, we compare the results of these three computations with each other and with the experimental data of Ref. 32.

Figure 3 shows a comparison of the history of the logarithmic residual error and the lift coefficient of these computations. The thin-layer computation with a flux limiter (TL-limiter) shows a drop of the residual error of about five orders of magnitude after 8000 iteration steps. The thin-layer computation without a flux limiter (TL-no limiter) shows a drop of the residual error of the same order of magnitude as that of the TL-limiter computation after 10,800 iteration steps. The full Navier-Stokes computation without a flux limiter (FNS-no limiter) shows a drop of the same order of magnitude as that of the TL-limiter computation after 8,900 iteration steps. The lift coefficient of the three computations is 0.34090 (TL-limiter), 0.35354 (TL-no limiter) and 0.35250 (FNS-no limiter). In the next table, we show comparison of the three computations and the experimental data for the normal force coefficient, C_N , the pitching-moment coefficient about the leading edge, C_M , and the drag coefficient, C_D . The results of the case of next section for the tip-jet control are also included in the table. The results show that

	C_N	C_M	C_D
TL-limiter	0.34128	-0.07581	0.01857
TL-no limiter	0.35374	-0.08161	0.01682
FNS-no limiter	0.35272	-0.08137	0.01702
Experiment ³²	0.35	-0.0825	N/A
FNS-no limiter (tip jet control)	0.3682	-0.08667	0.01732

the C_N of the FNS-no limiter computation is the closest to the experimental C_N with an error of +0.78%. The corresponding error for the TL-no limiter computation is +1.07% and for the TL-limiter computation is -2.49%. The error in the computed C_M in comparison with the experimental value is -1.37% for the NS-no limiter computation, -1.08% for the TL-no limiter computation and -8.11% for the TL-limiter computation.

Figure 4 shows a comparison of the computed surface-pressure-coefficient distribution in the chordwise direction at different spanwise stations with the same experimental

data. The present computed results are in good agreement with those of the experimental data with the exception of the peak suction pressure at the wing leading edge. This is attributed to the simple modeling of the transitional flow at this location, wherein a simple algebraic turbulent model is turned on. At the spanwise station of 0.9883 in the tip region, it is noticed that the computed C_p using the TL-no limiter and FNS-no limiter computations are in excellent agreement with the experimental data than that of the TL-limiter computation, particularly in the chordwise direction as of $X/C=0.3$.

Figure 5 shows a comparison of the spanwise variation of the total pressure-loss contours at chord-stations range of $X/C=0.9-5.0$ covering the evolution of vortex wake. The range of the total pressure-loss contours shows that the tip vortex reaches its maximum strength very close to the downstream side of the trailing edge. Thereafter, the tip-vortex core expands due to the viscous diffusion and moves inboards while growing in size. It is also observed that the wake thickness increases and moves upwards. The TL-no limiter results of the vortex core and wake shear layer show less viscous diffusion and more inboard motion than those of the TL-limiter results. The FNS-no limiter results show a little better resolution of the vortex core and wake shear layer than that of the TL-no limiter results. However, the inboard motion of the vortex core and wake shear layer is the same as that of the TL-no limiter results. Hence, it is concluded that the flux limiter is responsible for the vortex-core and wake shear-layer diffusions and their small inboard motions. In Fig. 6, the particle traces for the wing tip flow and the vortex wake flow are shown for the TL-limiter and FNS-no limiter computations. Again, the TL-limiter results show the larger diffusion of the tip vortex than that of the FNS-no limiter results.

Active Injection Control of Tip Vortex

The hazardous effects of the tip vortex on trailing aircraft is very significant as it has been demonstrated in Ref. 27. Several ideas exist for passive and active control of the tip vortex in order to alleviate its hazardous effects. The challenging issue here is to diffuse the tip vortex without decreasing the lifting force of the leading aircraft. Our first attempt to accomplish these objectives is to use active injection from a slot along the wing tip. The slot is located on the wing-tip surface and extends from the chord station $X/C=0.2$ to the chord station $X/C=0.6$. The direction of the jet blowing is downstream at 45° which is measured from the x -axis. A constant mass-flow-rate coefficient of 0.015 is used for the jet blowing through the wing-tip slot. The solution of this case is obtained by using the FNS-no limiter computation. Two types of initial conditions have been used. In the first, the control starts from the uniform flow conditions while in the second, the control starts from the FNS-no limiter solution of the preceding section. The final steady flow

solution for both cases showed the same results. Here, only the results of the first case are shown.

Figure 7 shows the history of the residual error and lift coefficient for 16,000 iteration steps. The spikes shown in the residual error graph are due to the step increases of the mass-flow rate from 0.005 to 0.01 and finally to 0.015. The residual error drops three orders of magnitude and the lift coefficient shows a value of 0.3680. The lift coefficient is 4.4% higher than that of the FNS-no limiter computation without injection. The values of C_N , C_M and C_D are included in the table of the preceding section. The C_D coefficient shows 1.76% increase than that of the FNS-no limiter computation without injection. In Fig. 8, the pressure coefficient is shown at the spanwise stations near the wing tip for comparison with the experimental data of the case without injection. It is observed that only the tip-section C_p near the trailing edge shows a slight decrease from that of the experimental data.

Figure 9 shows the spanwise variation of the total pressure-loss contours at chord stations from $X/C=0.95$ to $X/C=5.0$. A comparison of these results with those of Fig. 5 reveals the excellent effect of the tip-injection control in dissipating the tip vortex. This is also seen in Fig. 10 of the particle traces in comparison with those of Fig. 6.

Figure 11 shows a blow-up of the total pressure-loss contours at the wing tip covering chord stations from $X/C=0.2$ to $X/C=0.9$. It is observed that the tip vortex existing at $X/C=0.2$ (at the starting location of the slot) is quickly diffused by the blown jet. However, by the end of the slot length at $X/C=0.6$, the tip vortex is recovering but with small strength. It is concluded that tip-injection control is effective in diffusing the tip vortex and moreover it is very important to study the effect of the injection-slot length in the future. Other parameters need to be included in the future study such as the direction of injection, the mass-flow rate and the width of injection.

CONCLUDING REMARKS

The thin-layer and full NS equations have been used to accurately solve for the near-vortex-wake flow around a large-aspect-ratio rectangular wing. The flow has been computed by using the thin-layer equations with and without flux limiters and the NS equations without flux limiters, all on the same grid. The results show the substantial effects of the flux limiter in diffusing the tip vortex and the trailing-edge shear layer and in their small in-board motions. The full Navier-Stokes computation without flux limiters show the best results in comparison with the experimental data. Also, it has been demonstrated that tip-injection control is substantially effective in diffusing the tip vortex without reduction of the wing lift coefficient. Although the drag coefficient slightly increased the lift to drag ratio increased. Currently, work is underway to conduct an extensive parametric study on the tip-injection control and to study its effect on a trailing wing. Passive-control methods are also being investigated.

ACKNOWLEDGEMENT

For the first two authors, this research work has been supported by the NASA Langley Research Center under Grant No. NAG-1-994. The computational resources provided by the NASA Langley Research Center and the National Aerodynamics Simulation (NAS) Center also are appreciated.

REFERENCES

1. Hallock, J. N. and Eberle, W. R., "Aircraft Wake Vortices: A State-of-the-Art Review of the United States R&D Program," FAA Rept. FAA-RD-77-23, February 1977.
2. Dee, F. W. and Nicholas, O. P., "Flight Measurements of Wing tip Vortex Motion Near the Ground," CP 1065, British Aeronautical Research Council, London, 1968.
3. Harvey, J. K. and Perry, F. J., "Flowfield Produced by Trailing Vortices in the Vicinity of the Ground," AIAA Journal, Vol. 9, Aug. 1977, pp. 1659-1660.
4. El-Ramly, Z., "Induced Rolling Moment on Trailing Wings," AIAA 10th Fluid & Plasma-dynamics Conference, Albuquerque, NM, June 1977.
5. Wood, W. D. and McWilliams, T. G., "Wake Turbulence Detection and Economic Impact of Proposed Improvements," SAE Air Transportation Meeting, Washington, D.C., May 1977.
6. Gardoz, L. J., "Federal Aviation Administration Full-Scale Aircraft Vortex Wake Turbulence Flight Test Investigations: Past, Present, Future," AIAA Paper No. 71-97, January 1971.
7. Cliffone, D. L. and Lonzo, C., Jr., "Flow Visualization of Vortex Interactions in Multiple vortex Wakes Behind Aircraft," NASA TMX 62, 459, June 1975.
8. Olwi, I. A. and Ghazi, M. A., "An Experimental Investigation of the Turbulence Effect of a Leading Wing on a Trailing Aircraft," AIAA 91-3309-CP, AIAA 10th Applied Aerodynamics Conference, September 1991, pp. 830-837.
9. Liu, H.-T., "Effects of Ambient Turbulence on the Lifespan of a Trailing Vortex Wake," Quest Integrated, Inc., Technical paper No. 268, Kent, Washington, October 1991.
10. Liu, H.-T., Hwang, P.A. and Srnsky, R.A., "Physical Modeling of Ground Effects on Vortex Wakes," Quest Integrated, Inc., Technical paper No. 274, Kent, Washington, October 1991.
11. Chorin, A. J. and Bernard, P. S., "Discretization of a Vortex Sheet, with an Example of Roll-up," Journal of Computational Physics, Vol. 13, November 1973, pp. 423-429.

12. Hackett, J. E. and Evans, M. R., "Vortex Wakes Behind High Lift Wings," *Journal of Aircraft*, Vol. 8, May 1971, pp. 334-340.
13. Yates, J. E., "Calculation of Initial Vortex Roll-Up in Aircraft Wakes," *Journal of Aircraft*, Vol. 11, July 1974, pp. 397-400.
14. Iversen, J. D. and Bernstein, S., "Trailing Vortex Effects on Following Aircraft," *Journal of Aircraft*, Vol. 11, January 1974, pp. 60-61.
15. Rossow, V. J., "Inviscid Modeling of Aircraft Trailing Vortices," *Proceedings of NASA Symposium on Wake Vortex Minimization*, Washington, D.C., February 1976, pp. 4-54.
16. Kandil, O. A., Mook, D. T. and Nayfeh, A. H., "Application of the Nonlinear vortex-Lattice Concept to aircraft-Interference Problems," *Advances in Engineering Science, NASA CP-2001*, Vol. 4, November 1976, pp. 1321-1326.
17. Kandil, O. A., Mook, D. T. and Nayfeh, A. H., "Nonlinear Prediction of the Aerodynamics Loads on Lifting Surface," *Journal of Aircraft*, Vol. 13, No. 1, January 1976, pp. 22-28.
18. McCormick, B. W., Tangler, J. L. and Sherrieb, H. E., "Structure of Trailing vortices," *Journal of Aircraft*, Vol. 5, No. 3, May-June 1968, pp. 260-267.
19. Bilanin, A. J., Teske, M. E. and Williamson, G. G., "Vortex Interactions and Decay in Aircraft Wakes," *AIAA Journal*, Vol. 15, No. 2, Feb. 1977, pp. 250-260.
20. Bilanin, A. J., Teske, M. E. and Hirsh, J. E., "Neutral Atmospheric Effects on the Dissipation of Aircraft Vortex Wakes," *AIAA Journal*, Vol. 16, No. 9, September 1978, pp. 956-961.
21. Liu, C. H. and Ting, L., "Interaction of Decaying Trailing vortices in spanwise Shear Flow," *Computer and Fluids*, Vol. 15, No. 1, 1987, pp. 77-92.
22. Weston, R. P., Ting, L. and Liu, C. H., "Numerical Studies of the Merging Vortices," *AIAA 86-0557*, January 1986.
23. Liu, C. H., Tavantzis, J. and Ting, L., "Numerical Studies of Motion and Decay of vortex Filaments," *AIAA Journal*, Vol. 24, No. 8, August 1986, pp. 1290-1297.
24. Liu, C. H., Krause, E. and Ting, L., "Vortex-Dominated Flow with Viscous Core Structure," *AIAA 85-1556*, invited paper, July 1985.
25. Greene, G. C., "An Approximate Model of Vortex Decay in the Atmosphere," *Journal of Aircraft*, Vol. 23, No. 7, July 1986, pp. 566-573.
26. Greene, G. C., Lamar, J. E. and Kubendran, L. R., "Aircraft Vortices: Juncture, Wing and Wake," *AIAA 88-3743*, July 1988.
27. Kandil, O. A., Wong, T. C. and Liu, C. H., "Analysis and Computations of Trailing Vortices and their Hazardous Effects," *WAKE VORTEX SYMPOSIUM*, FAA, Washington, D.C., October 1991.
28. Cebeci, T., "Calculation of Compressible Turbulent Boundary Layers with heat and Mass Transfer," *AIAA Paper 70-741*, June 1970.
29. Baldwin, B. S. and Lomax, H., "Thin-Layer Approximation and Algebraic Model for Separated Turbulent Flows," *AIAA Paper 78-257*, January 1978.
30. Wong, T. C. Kandil, O. A. and Liu, C. H., "Navier-Stokes Computations of Separated Vortical Flows Past Prolate Spheroid at Incidence," *AIAA 89-0553*, January 1989.
31. Kandil, O. A., Kandil, H. A. and Liu, C. H., "Supersonic Quasi-Axisymmetric Vortex Breakdown," *AIAA 91-3311-CP*, Sept. 1991, Vol. II, pp. 851-863.
32. Yip, L. P. and Shubert, G. L., "Pressure Distributions on a 1-By 3-Meter Semispan Wing at Sweep Angles from 0°-40° in Subsonic Flow," *NASA TN D-8307*, December 1976.

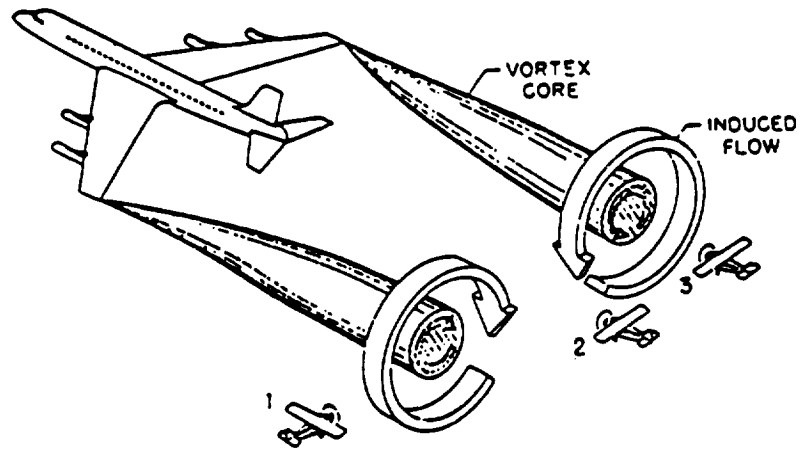


Figure 1. Types of interference of Trailing Vortex Wake; (1) cross-track penetration, (2) along-track penetration between tip vortices, and (3) along-track penetration through tip vortex center.

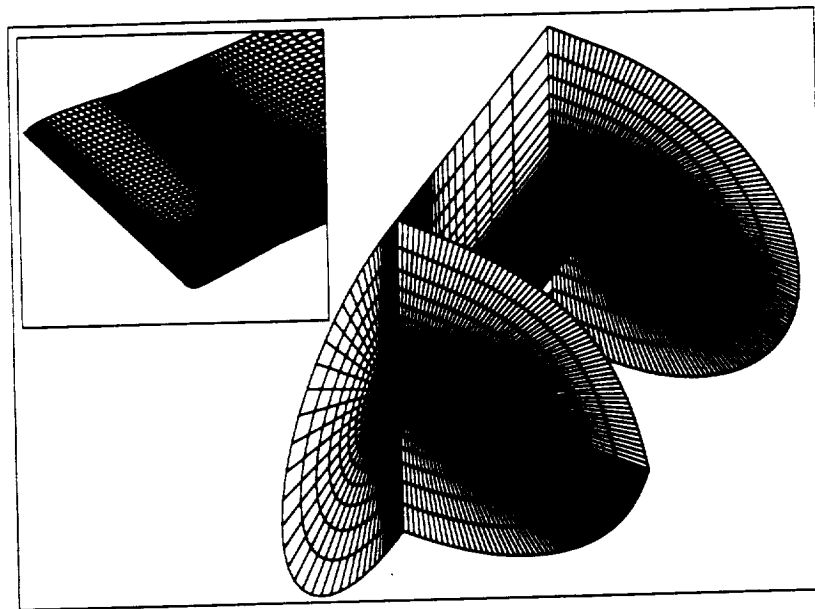


Figure 2. Typical computational grid for the wing

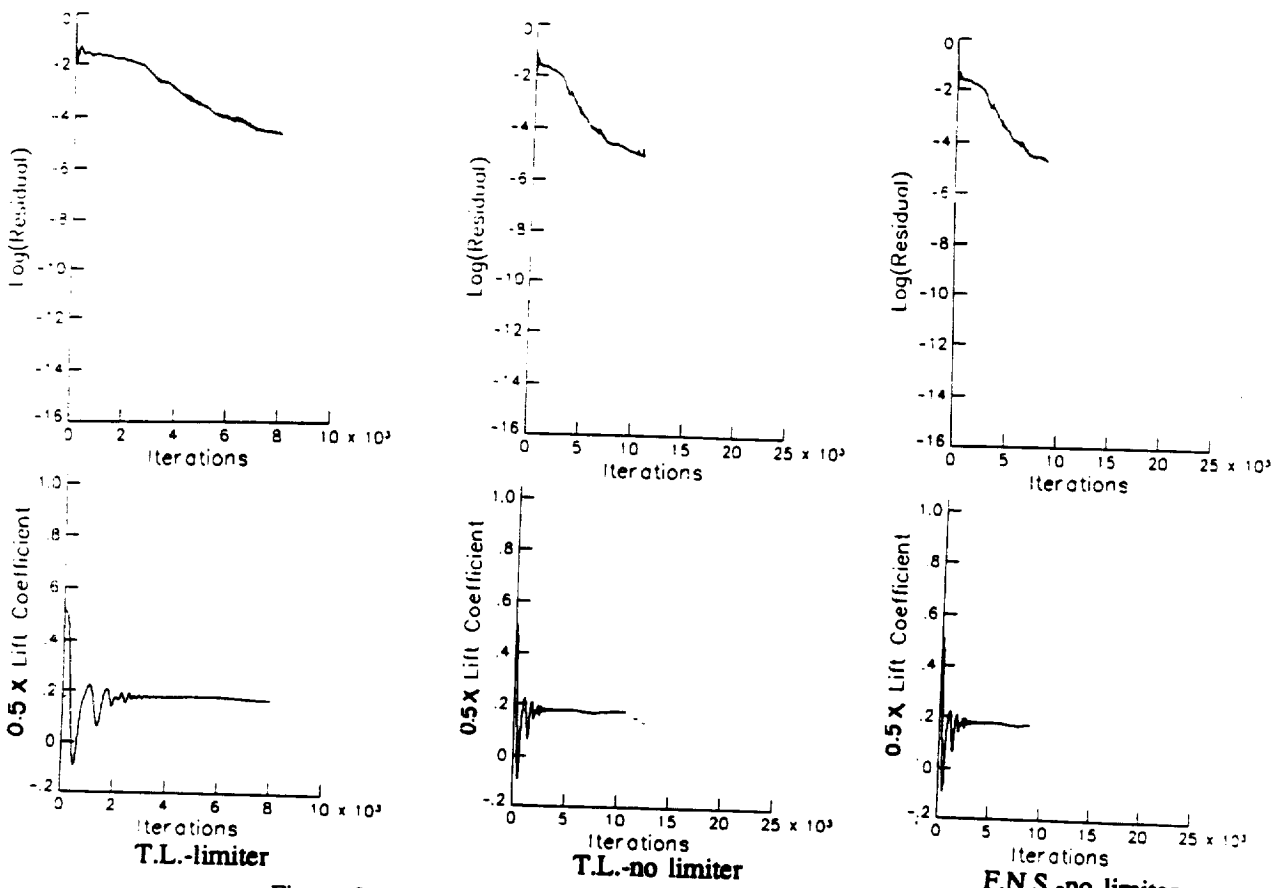
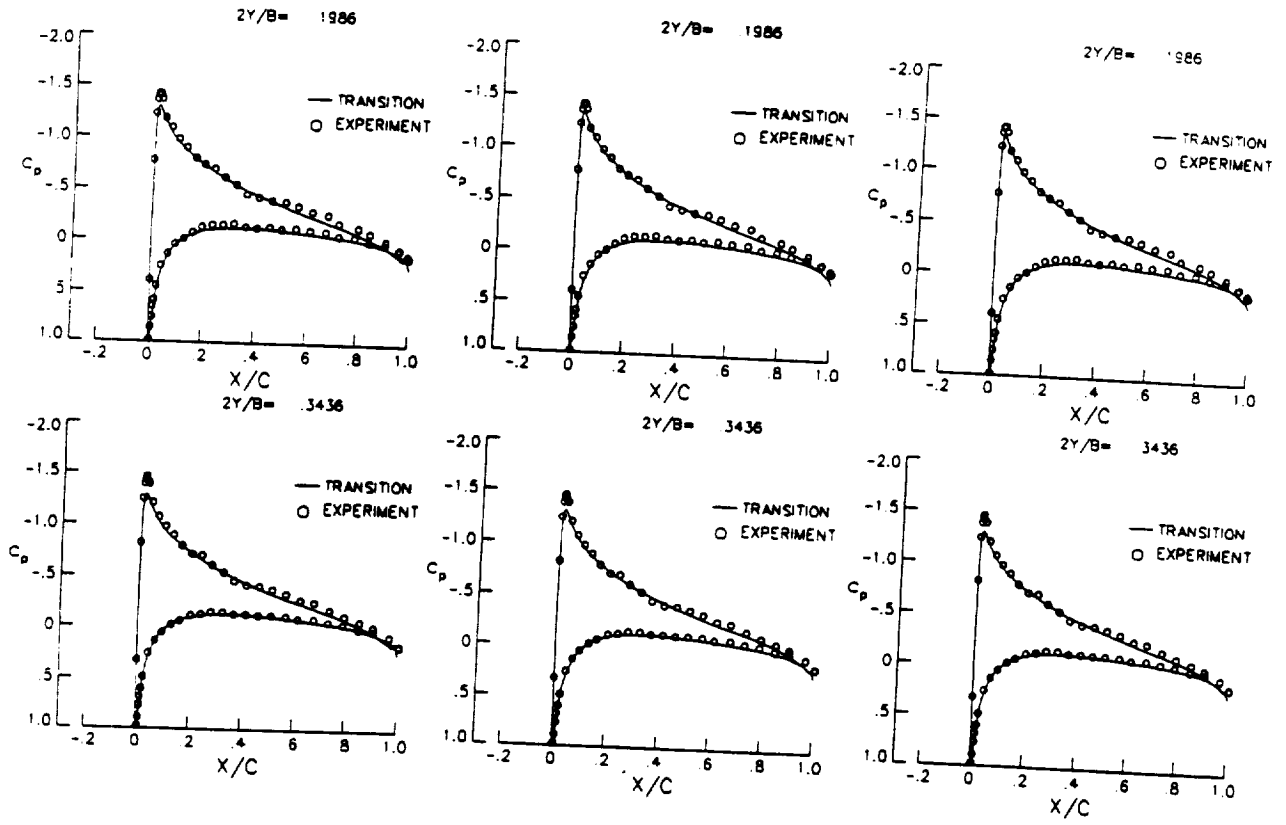


Figure 3. Iteration history of residual error and lift coefficient.



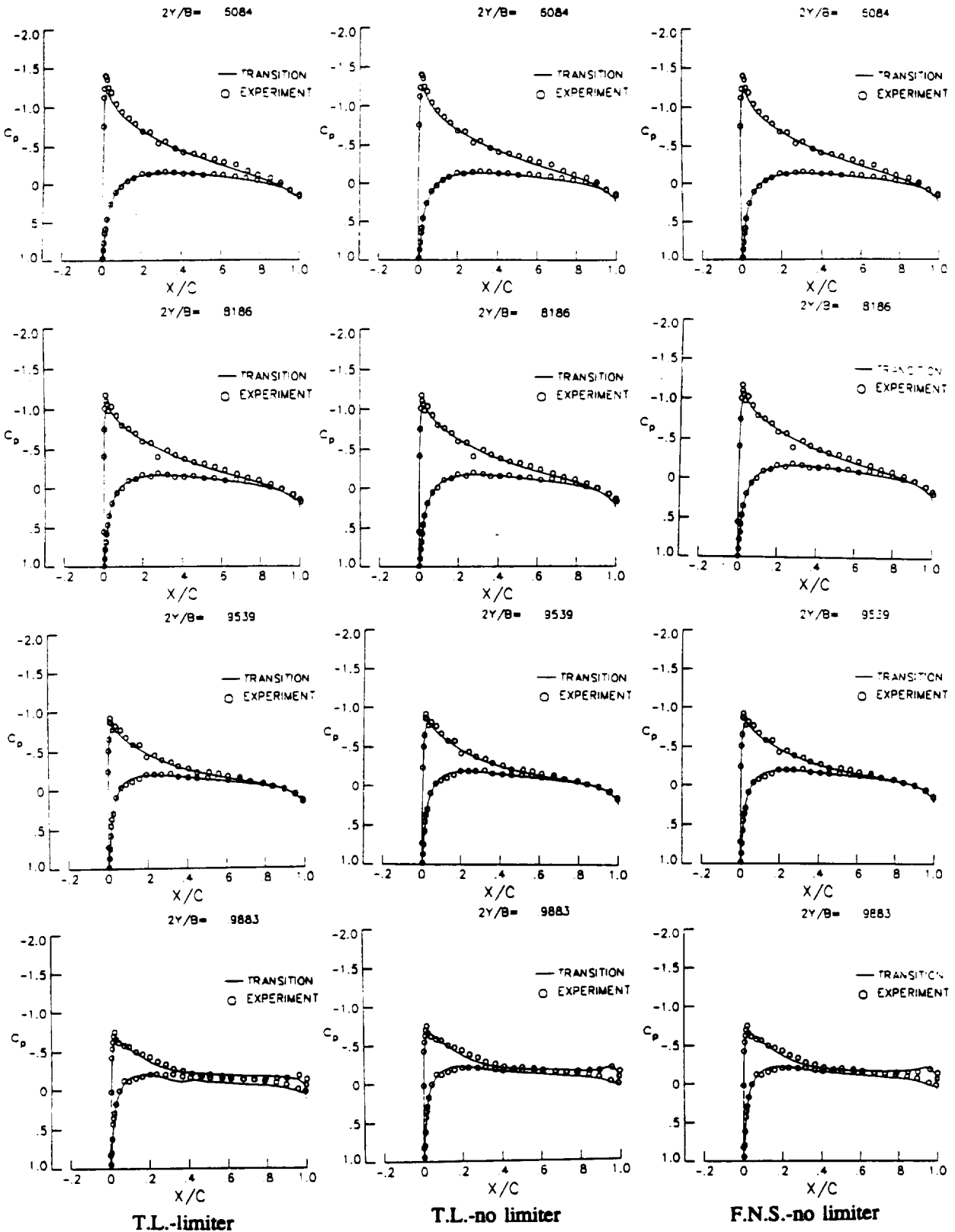


Figure 4. Chordwise surface-pressure distribution at spanwise stations for an isolated wing and comparison with experimental data.

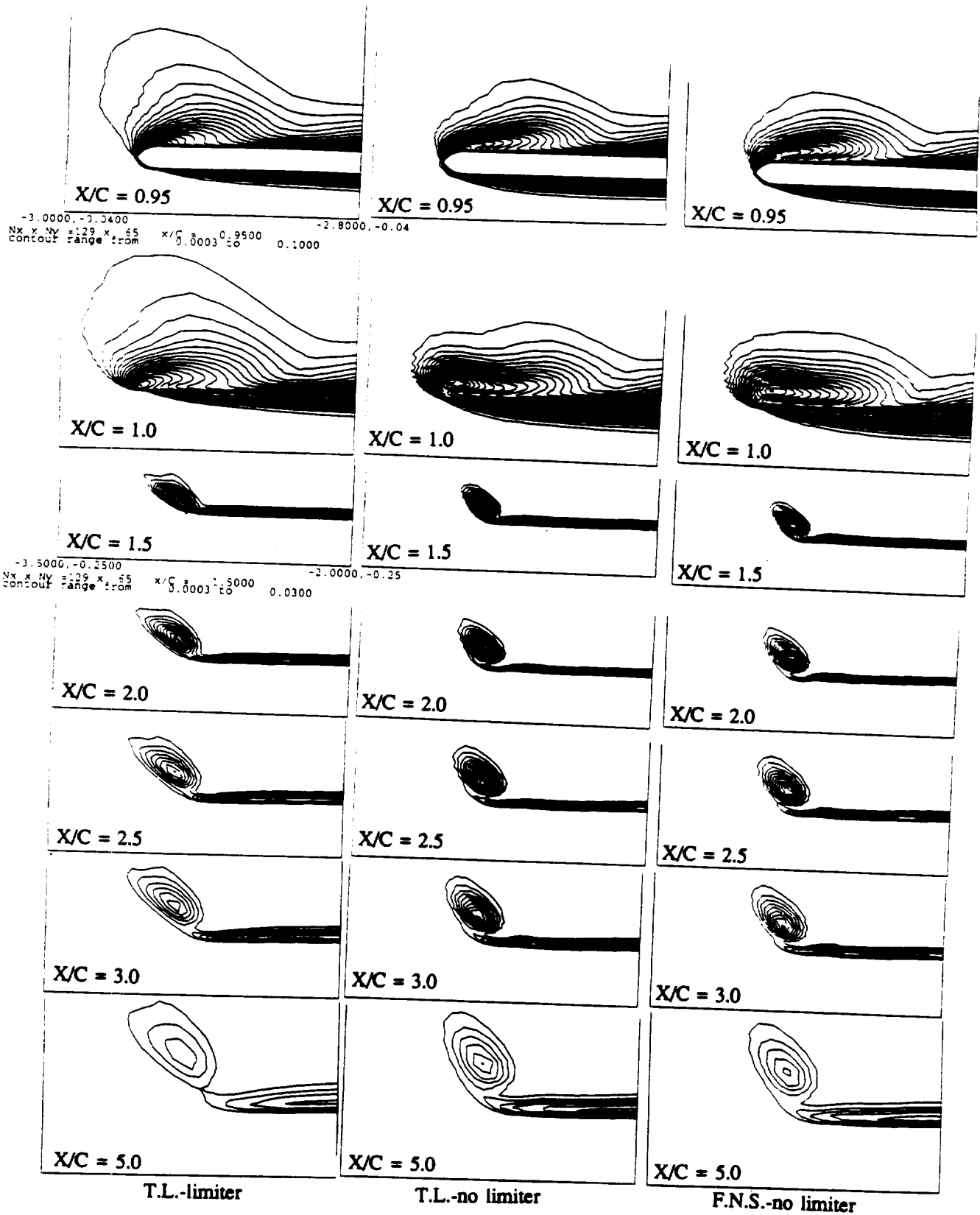


Figure 5. Spanwise variation of total pressure-loss contours at chordwise stations on the wing and its vortex wake.

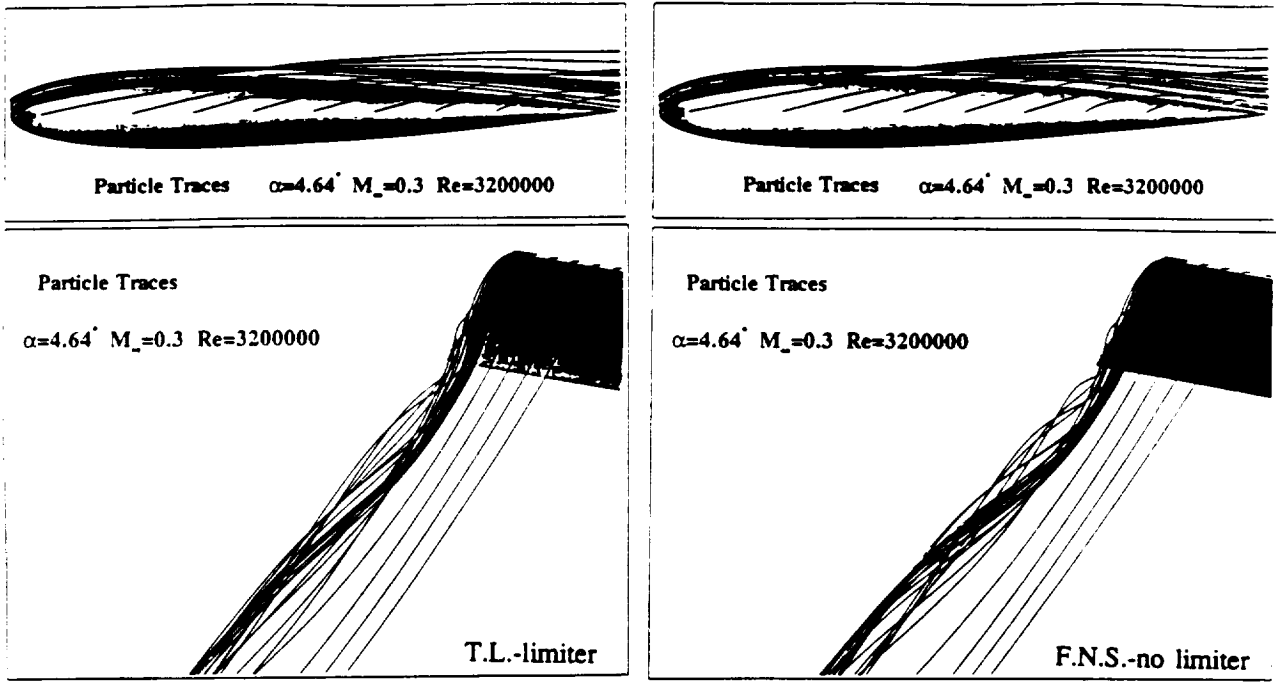


Figure 6. Particle traces for the wing tip and its vortex wake.

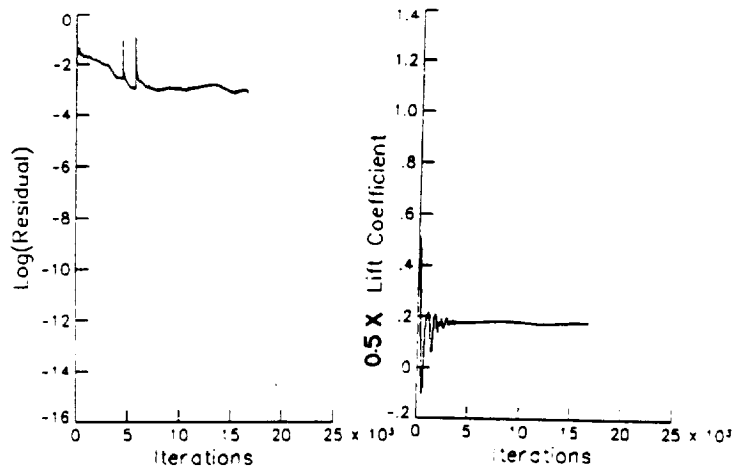


Figure 7. Iteration history of residual error and lift coefficient for the wing with tip-injection control (F.N.S. no limiter).

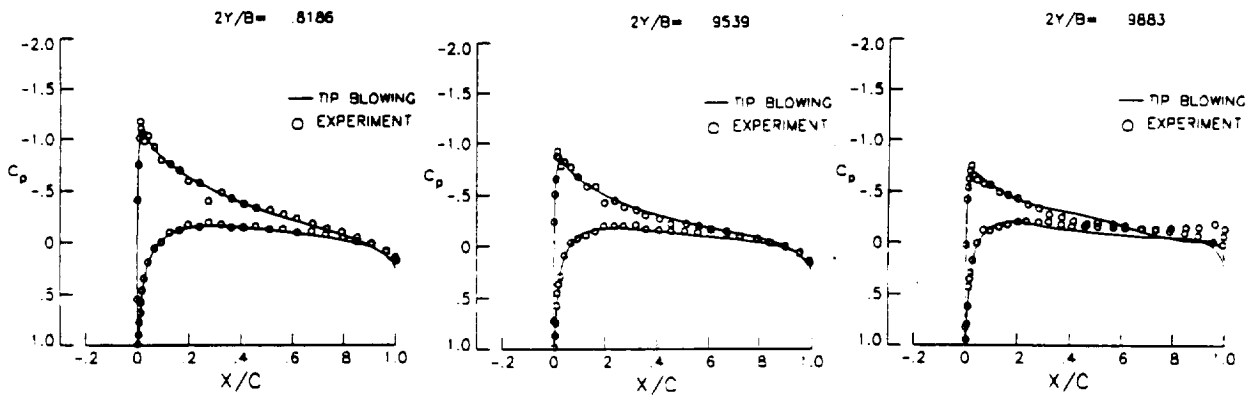


Figure 8. Chordwise surface-pressure distribution at spanwise stations for an isolated wing with tip-injection control (F.N.S. no limiter).

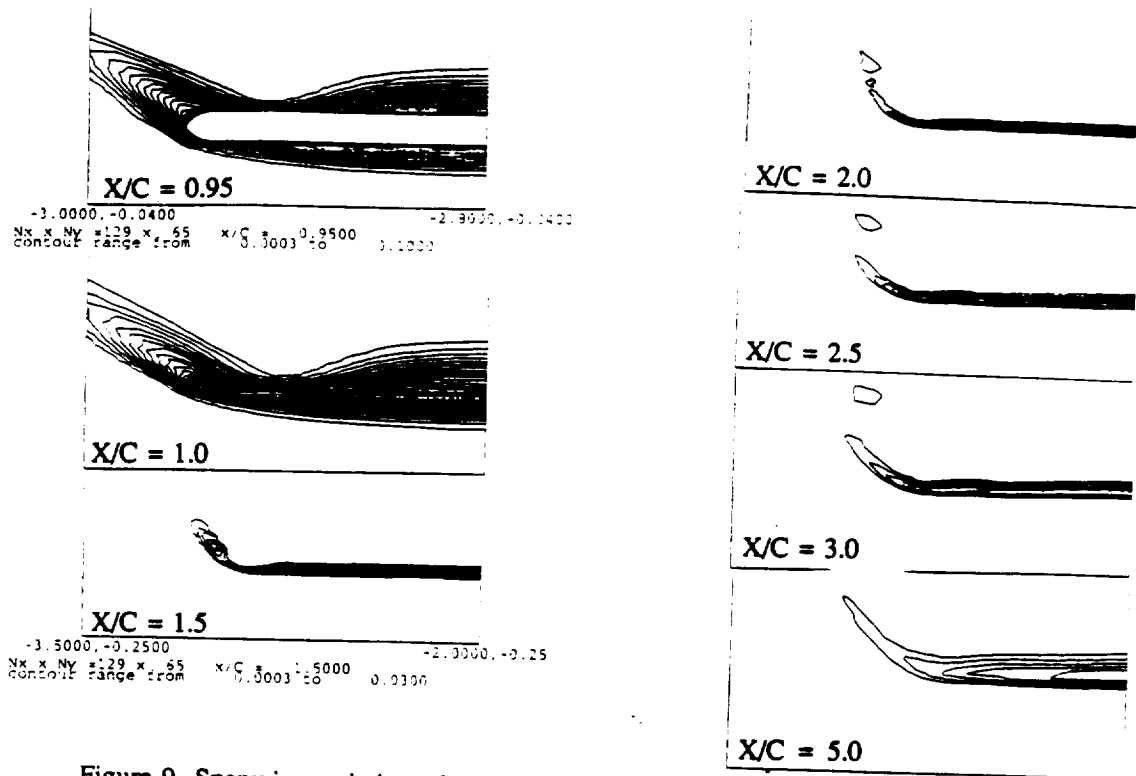


Figure 9. Spanwise variation of total pressure-loss contours at chordwise stations on the wing with tip-injection control and its vortex wake (F.N.S.-no limiter).

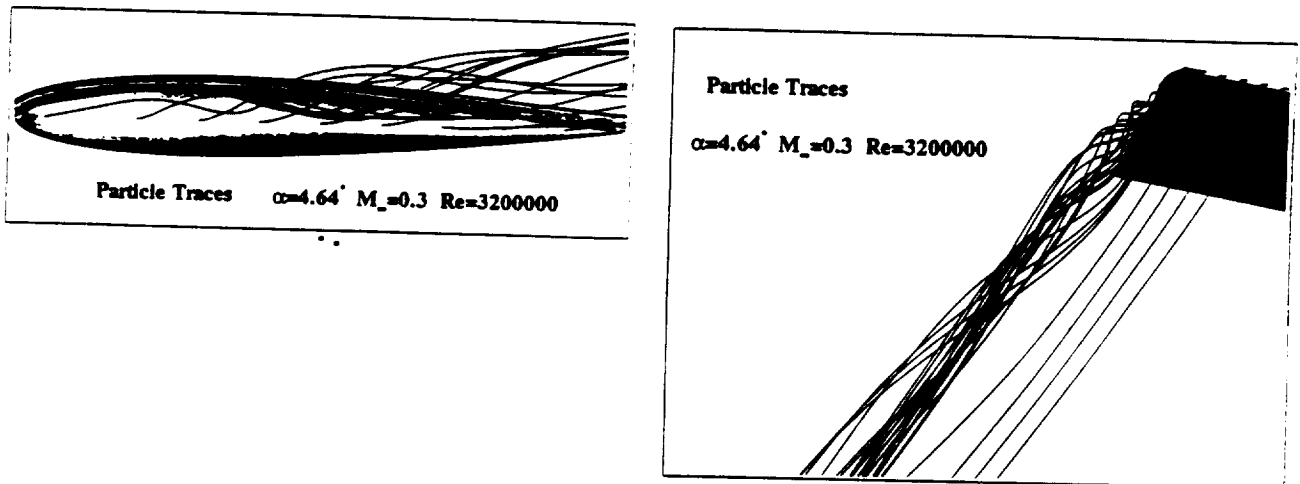


Figure 10. Particle traces for the wing tip with tip-injection control and its vortex wake (F.N.S.-no limiter).

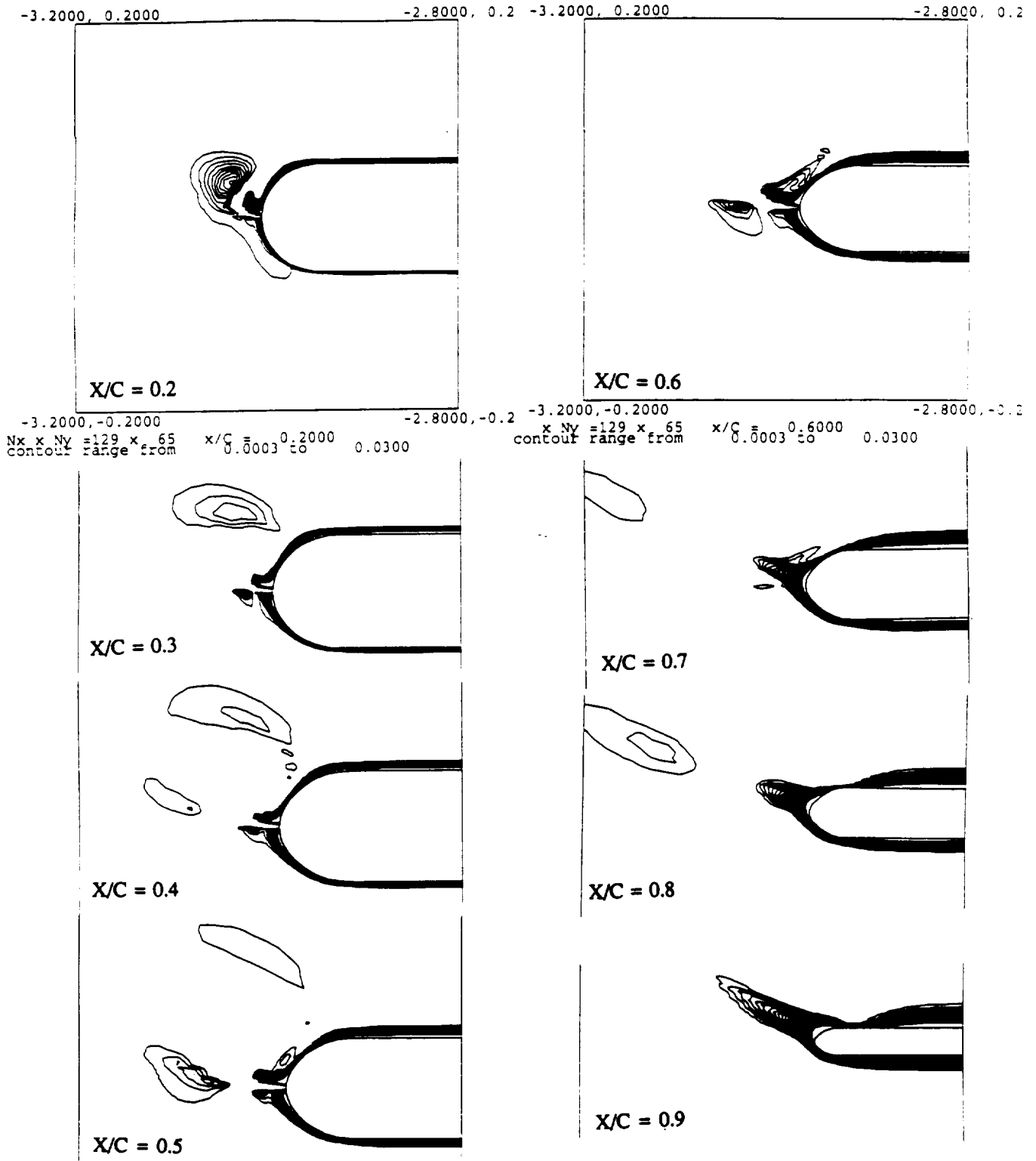
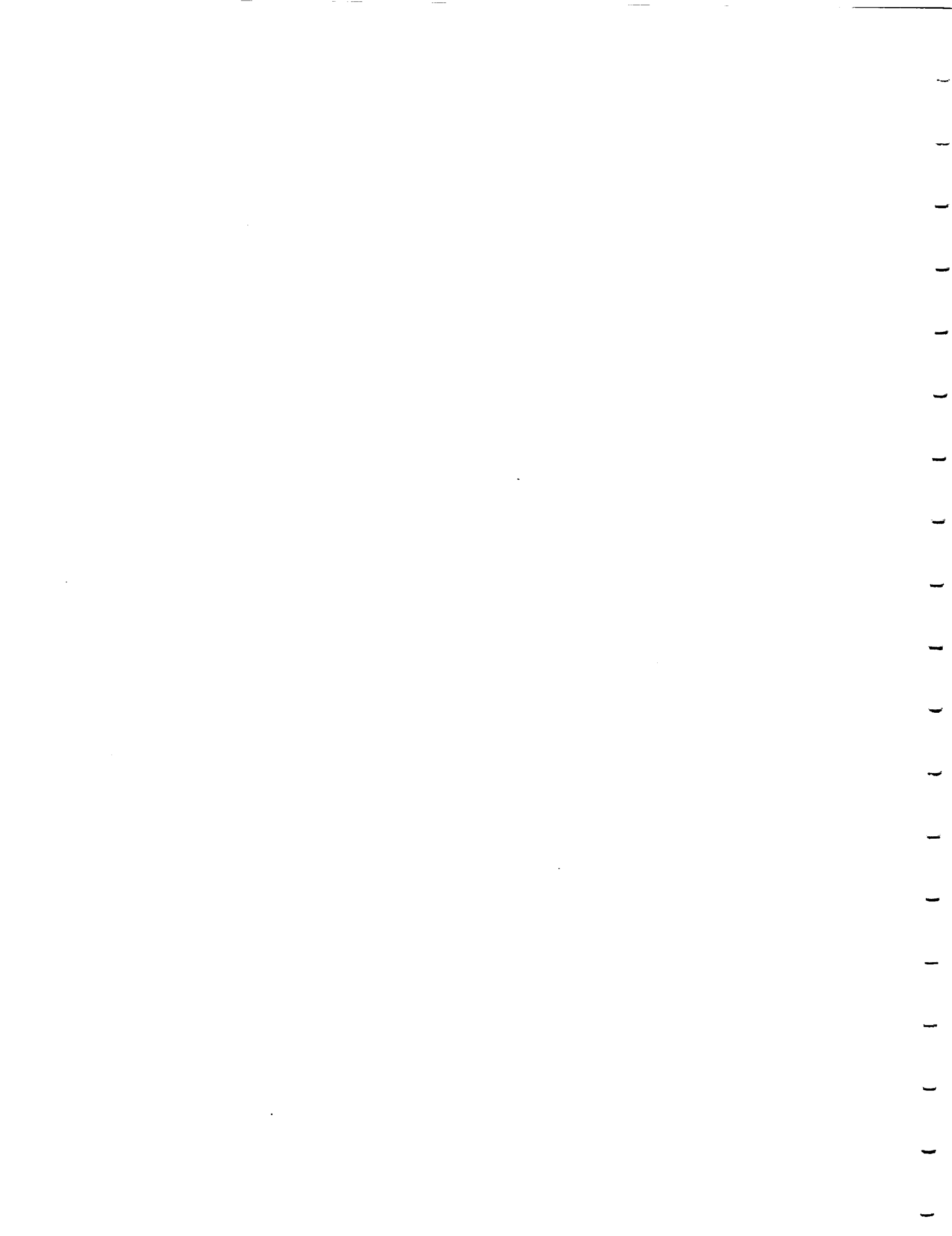


Figure 11. Spanwise variation of total pressure-loss contours at chordwise stations on the wing with tip-injection control (F.N.S.-no limiter).





1992-11-0
10-11-92

AIAA-92-4426-CP

**ACTIVE CONTROL OF ASYMMETRIC
VORTICAL FLOWS AROUND CONES
USING INJECTION AND HEATING**

**Osama A. Kandil and Hazem H. Sharaf
Old Dominion University, Norfolk, VA 23529**

**C. H. Liu
NASA Langley Research Center, Hampton, VA 23665**

**AIAA Atmospheric Flight
Mechanics Conference
Hilton Head, SC, August 10-12, 1992**



ACTIVE CONTROL OF ASYMMETRIC VORTICAL FLOWS AROUND CONES USING INJECTION AND HEATING

Osama A. Kandil* and Hazem H. Sharaf**
Old Dominion University, Norfolk, VA 23529

and

C.H. Liu***

NASA Langley Research Center, Hampton VA 23665

ABSTRACT

The effectiveness of certain active-control methods for asymmetric flows around circular cones is investigated by using computational solution of the unsteady, compressible full Navier-Stokes equations. Two main methods of active control which include flow injection and surface heating are used. For the flow-injection-control method, flow injection is used either in the normal direction to the surface or in the tangential direction to the surface. For the surface-heating-control method, the temperature of the cone surface is increased. The effectiveness of a hybrid method of flow control which combines normal injection with surface heating has also been studied. The Navier-Stokes equations, subjected to various surface boundary conditions, are solved by using an implicit, upwind, flux-difference splitting, finite-volume scheme for locally-conical flow solutions.

INTRODUCTION

The problems of prediction, analysis and control of asymmetric vortical flows around slender pointed bodies are of vital importance to the dynamic stability and controllability of missiles and fighter aircraft. The onset of flow asymmetry occurs when the relative incidence (ratio of angle of attack to nose semi-apex angle) of pointed forebodies exceeds certain critical values. At these critical values of relative incidence, flow asymmetry develops due to natural and/or forced disturbances. The origin of natural disturbances may be a transient side slip, an acoustic disturbance, or similar disturbance of short duration. The origin of forced disturbances is geometric perturbations due to imperfections in the nose geometric symmetry or similar disturbances of permanent nature. In addition to the relative incidence as one of the influential parameters for the onset of flow asymmetry, the freestream Mach number, Reynolds number and shape of the body-cross sectional area are also important parameters.

In several recent papers by Kandil et al.¹⁻⁴, the unsteady, thin-layer, compressible Navier-Stokes equations have been used to simulate steady and unsteady, asymmetric vortex flows, including their passive control,

around cones with different cross-sectional shapes. The emphasis of these papers was extensive computational studies of the parameters which influence the asymmetric flow phenomenon and its passive control. Since the computational cost associated with the solution of three-dimensional-flow problems at reasonable flow resolution is very expensive, all the computational solutions were obtained using a locally-conical flow assumption. Such an assumption reduces the problem solution to that on two conical planes, which are in close proximity of each other, and hence it reduces the computational cost by an order of magnitude. Moreover, such solutions still provide extensive understanding of the flow physics since one can use very fine grids for reasonable flow resolution. These studies showed that asymmetric flow solutions were unique irrespective of the type of flow disturbance; a random disturbance in the form of a machine round-off error or a controlled disturbance in the form of a short-duration side-slip disturbance. Unsteady asymmetric flow solutions with perfectly periodic vortex shedding were successfully simulated, and the solutions were unique irrespective of the computational scheme used. It has also been shown that as the Mach number was increased, the flow asymmetry was decreased, and as the Reynolds number was increased the flow asymmetry was increased. Moreover, the cross-sectional shape of the cone has been shown to be a very influential parameter on the flow asymmetry. Circular sections produced very strong flow asymmetry and diamond sections produced relatively-weaker flow asymmetry.

In a later paper, by Kandil et al.⁵, the full Navier-Stokes solutions were compared with the thin-layer Navier-Stokes solutions. It was shown that the full Navier-Stokes solutions produced thicker free-shear layers and more vortex-core resolution as compared with those of the thin-layer Navier-Stokes equations. In Ref. 5, a few tentative three-dimensional flow solutions were also presented.

Substantial research efforts have recently been devoted for eliminating or alleviating flow asymmetry and its corresponding side force. In the experimental area, several passive-control methods⁶⁻⁸ and active-control methods⁹⁻¹³ have been investigated. Computational simulations have also been used to investigate the effectiveness of several passive-control methods¹⁻⁵ and active-control methods^{12, 14, 15}. Various methods of passive control were demonstrated in the above references which include the use of vertical fins along the leeward plane of geometric symmetry, thin and thick side strakes

* Professor and Eminent Scholar, Dept. of Mechanical Engineering and Mechanics, Associate Fellow AIAA.

** Graduate Research Assistant, Member AIAA.

*** Group Leader, Theoretical Flow Physics Branch, Associate Fellow AIAA.

with different orientations, and rotatable forebody tips which have variable cross section (from a circular shape at its base to an elliptic shape at its tip). It was shown by Kandil et al.⁴ that side-strakes control is more practical than the vertical-fin control since the former was more effective over a wide range of angle of attack than the latter. Moreover, side-strake control provided an additional lifting force. However, the effectiveness of the side-strake control terminates at very high angles of attack for the considered strake geometry and flow conditions.

Various active-control methods have been used which include forebody blowing and movable forebody strakes. The forebody blowing methods include forward blowing, normal blowing, aft blowing and tangential blowing. The main concept of forebody blowing is to control flow separation on the forebody and to create yawing forces and moments which can be utilized in controlling the body.

In the present paper, we investigate the effectiveness of two main methods of active control which include flow injection and surface heating. The study of flow-injection control covers normal and tangential injection. Moreover, a hybrid method of flow control which combines surface heating and normal injection methods is also investigated. At this stage of research, the flow control is aiming at either rendering the vortical asymmetric flow symmetric or rendering the surface-pressure distribution symmetric. Computational solution of the unsteady, compressible, full Navier-Stokes equations is used for the present work with the exception of the tangential injection. For the tangential injection, the thin-layer NS equations are used. The computational applications are focused on circular-section cones, and locally-conical flow assumptions are used to substantially reduce the computational cost.

FORMULATION AND COMPUTATIONAL SCHEME

Full Navier-Stokes Equations

The conservative form of the dimensionless, unsteady, compressible, full Navier-Stokes equations in terms of time-independent, body-conformed coordinates ξ^1, ξ^2 and ξ^3 is given by

$$\frac{\partial \bar{Q}}{\partial t} + \frac{\partial \bar{E}_m}{\partial \xi^m} - \frac{\partial (\bar{E}_v)_s}{\partial \xi^s} = 0; \quad m = 1 - 3, \quad s = 1 - 3 \quad (1)$$

where

$$\xi^m = \xi^m(x_1, x_2, x_3) \quad (2)$$

$$\bar{Q} = \frac{\hat{q}}{J} = \frac{1}{J} [\rho, \rho u_1, \rho u_2, \rho u_3, \rho e]^t \quad (3)$$

$$\begin{aligned} \bar{E}_m &\equiv \text{inviscid flux} \\ &= \frac{1}{J} [\partial_k \xi^m \hat{E}_k]^t \\ &= \frac{1}{J} [\rho U_m, \rho u_1 U_m + \partial_1 \xi^m p, \rho u_2 U_m \\ &\quad + \partial_2 \xi^m p, \rho u_3 U_m + \partial_3 \xi^m p, (\rho e + p) U_m]^t \end{aligned} \quad (4)$$

$$\begin{aligned} (\bar{E}_v)_s &\equiv \text{viscous and heat-conduction flux in } \xi^s \\ &\text{direction} \\ &= \frac{1}{J} [0, \partial_k \xi^s \tau_{k1}, \partial_k \xi^s \tau_{k2}, \partial_k \xi^s \tau_{k3}, \\ &\quad \partial_k \xi^s (u_n \tau_{kn} - q_k)]^t; \quad k = 1 - 3, \quad n = 1 - 3 \end{aligned} \quad (5)$$

$$U_m = \partial_k \xi^m u_k \quad (6)$$

The three momentum elements of Eq. (5) are given by

$$\begin{aligned} \partial_k \xi^s \tau_{kj} &\equiv \frac{M_\infty \mu}{Re} \left[\left(\partial_k \xi^s \partial_j \xi^n - \frac{2}{3} \partial_j \xi^s \partial_k \xi^n \right) \frac{\partial u_k}{\partial \xi^n} \right. \\ &\quad \left. + \partial_k \xi^s \partial_k \xi^n \frac{\partial u_j}{\partial \xi^n} \right] \end{aligned} \quad (7)$$

The last element of Eq. (5) is given by

$$\begin{aligned} \partial_k \xi^s (u_p \tau_{kp} - q_k) &\equiv \frac{M_\infty \mu}{Re} \left[\left(\partial_k \xi^s \partial_p \xi^n - \frac{2}{3} \partial_p \xi^s \partial_k \xi^n \right) u_p \frac{\partial u_k}{\partial \xi^n} \right. \\ &\quad \left. + \partial_k \xi^s \partial_k \xi^n u_p \frac{\partial u_p}{\partial \xi^n} + \frac{1}{(\gamma - 1) Pr} \partial_k \xi^s \frac{\partial (a^2)}{\partial \xi^n} \right]; \quad p = 1 - 3 \end{aligned} \quad (8)$$

The reference parameters for the dimensionless form of the equations are $L, a_\infty, L/a_\infty, \rho_\infty$ and μ_∞ for the length, velocity, time, density and molecular viscosity, respectively. The Reynolds number is defined as $Re = \rho_\infty V_\infty L / \mu_\infty$, where the characteristic length, L , is the body length. The pressure, p , is related to the total energy per unit mass and density by the gas equation

$$p = (\gamma - 1) \rho \left[e - \frac{1}{2} (u_1^2 + u_2^2 + u_3^2) \right] \quad (9)$$

The viscosity is calculated from the Sutherland law

$$\mu = T^{3/2} \left(\frac{1 + C}{T + C} \right), \quad C = 0.4317 \quad (10)$$

and the Prandtl number $Pr = 0.72$. In Eqs. (1)-(10), the indicial notation is used for convenience.

Boundary and Initial Conditions

The boundary and initial conditions vary according to the problem under consideration. The boundary conditions are explicitly satisfied. In general, they include inflow-outflow conditions and solid-boundary conditions. For problems of flow asymmetry, where the flow is solved throughout the whole computational domain, periodic boundary conditions are used at the plane of geometric symmetry of the problem.

For the asymmetric flow problems around slender bodies and for supersonic inflow-outflow boundary, the Riemann-invariant boundary conditions are used. They require that the inflow variables be at the freestream conditions, and the conical shock enclosing the body be

captured as part of the solution. For supersonic outflow boundary, the Riemann-invariant boundary conditions require that all flow variables be extrapolated from the interior cells. On the solid boundary, without injection or heating, the no-slip and no-penetration conditions are enforced. Moreover, the zero normal-pressure gradient and adiabatic boundary conditions are enforced. For the present active control problems, the mass-flow rate is specified at the body surface for the normal injection control and the temperature distribution is specified at the surface for the heating control. For the tangential flow injection the mass flow rate and velocity profile are specified at the lip exit (shown in Fig. 10 of next section).

The initial conditions correspond to the uniform flow conditions with $u_1 = u_2 = u_3 = 0$ on the solid boundary. These conditions are used to obtain the asymmetric flow solution. Next, the flow control conditions are enforced and the previously obtained asymmetric solution is used for the initial conditions of the active control problem.

Computational Scheme

The implicit, upwind, flux-difference splitting, finite-volume scheme is used to solve the unsteady, compressible, full Navier-Stokes equations. The scheme uses the flux-difference splitting scheme of Roe which is based on the solution of the approximate Riemann problem. In the Roe scheme, the inviscid flux difference at the interface of computational cells is split into two parts; left and right flux differences. The splitting is accomplished according to the signs of the eigenvalues of the Roe averaged-Jacobian matrix of the inviscid fluxes at the cell interface. The smooth flux limiter is used to eliminate oscillations at locations of large flow gradients. The viscous and heat-flux terms are linearized and the cross-derivative terms are eliminated in the implicit operator. The viscous terms are differenced using a second-order accurate central differencing. The resulting difference equation is approximately factored and is solved in three sweeps in the ξ^1 , ξ^2 , and ξ^3 directions. The computational scheme is coded in the computer program "FTNS3D".

For the locally-conical flow solutions, an axial station of $x_1 = 1.0$ is selected and the components of the flowfield vector are forced to be equal between this axial station and another axial station in close proximity to $x_1 = 1.0$. This ensures that the flow variables are locally independent of the axial direction at $x_1 = 1.0$ (Kandil et al.⁵).

COMPUTATIONAL APPLICATIONS AND DISCUSSION

For all the computational applications shown in this section, a 5° -semiapex angle circular cone at 1.8 Mach number and 10^5 Reynolds number is considered. These flow conditions were considered earlier (Kandil et al.^{4,5}) for the same cone for asymmetric-flow prediction and passive-control methods. The grid is $241 \times 81 \times 2$ points in the wrap around, normal directions and axial direction, respectively. The grid is generated using a modified

Joukowski transformation with a minimum grid size of 10^{-4} in the ξ^2 direction at the body surface. For the tangential flow injection a multi-block grid has been used and it is explained later on.

Asymmetric Flow, $\alpha = 20^\circ$

Figure 1 shows the locally-conical flow solution without any control around the cone at an angle of attack of 20° . The figure shows the total-pressure-loss (TPL) contours and the surface-pressure (SP) coefficient. The surface pressure is presented versus the angle θ , which is measured in the clockwise direction from the leeward plane of geometric symmetry. This stable asymmetric flow solution is obtained after 6,000 iteration steps. The source of flow disturbance at these critical flow conditions is the truncation error. As it has been shown earlier (Kandil et al.¹), this solution is unique irrespective of the type of source of the flow disturbance.

Normal Injection Control, $\theta = -22.5^\circ \rightarrow -67.5^\circ$, $m = \text{constant} = 0.03$, $\alpha = 20^\circ$

Next, a constant mass-flow injection of $m = 0.03$ is applied normal to the cone surface. The circumferential range of injection ports extends over $\theta = -22.5^\circ \rightarrow -67.5^\circ$. The solution of the previous asymmetric flow case is used as initial conditions along with modified surface boundary conditions. Figure 2 shows the TPL contours and the SP coefficient from the solution of the controlled flow. Although the vortical flow is still asymmetric, as it is seen from the TPL contours, the SP curve shows a symmetric distribution resulting in a zero side force. The TPL contours show that a primary vortex of smaller height (in comparison to the case of Fig. 1) is still existing on the right side and it is connected through a free-shear layer with the left side of the body surface. The injection flow on the left side of the body decreases the suction pressure on that side making its distribution equal to that on the right side.

Normal Injection Control, $\theta = 0^\circ \rightarrow -67.5^\circ$, $m = \text{constant} = 0.03$, $\alpha = 20^\circ$

In this case, the constant mass-flow injection of $m = 0.03$ is kept fixed while the circumferential range of injection ports is extended to cover the range of $\theta = 0^\circ \rightarrow -67.5^\circ$. Figure 3 shows the TPL contours and SP coefficient of the solution of the controlled flow. The vortical flow is still asymmetric but the SP curve shows a symmetric distribution, which results in a zero side force. It is also noticed that the primary vortex on the right side moves to a larger height (in comparison with the cases of Figs. 1 and 2) and the left-side free-shear layer also moves to the same height level. The SP coefficient curve shows less negative pressure coefficient on the leeward side in comparison with the case of Fig. 2, which produces smaller lifting force.

Normal Injection Control, $\theta = -67.5^\circ \rightarrow +67.5^\circ$,
Variable Mass-Flow Rate, $m_{\max} = 0.03$, $\alpha = 20^\circ$

In this case, the circumferential range of injection ports is extended to cover a symmetric range of $\theta = -67.5^\circ \rightarrow +67.5^\circ$. Moreover, the injected mass-flow rate is made proportional to the difference in the surface pressure between corresponding points on the right and left side of the body (within $\theta = -67.5^\circ \rightarrow +67.5^\circ$). The maximum injected mass-flow rate, m_{\max} , which corresponds to the maximum pressure difference is restricted to $m_{\max} = 0.03$. Practically, this control method can be achieved by sensing the pressure difference between the right and left ports and using it as a feedback control in order to inject a mass-flow rate which is proportional to that pressure difference. Figure 4 shows the results of this controlled flow. The history of the residual error versus the number of iterations shows the asymmetric solution up to 6,000 iterations and the evolution of the symmetric controlled-flow solution up to 7,200 iterations. The corresponding curve of the history of the side force shows that the side force becomes zero at the end of 7,200 iterations. Snapshots of the evolution of the symmetric controlled flow solution, in terms of the TPL contours, are given at the 6,200; 6,400; 6,600; 6,800; 7,000 and 7,200 iteration step. The vortical flow is rendered symmetric using the present method and the SP coefficient curve shows a symmetric distribution.

Surface Heating Control, $\theta = 0 \rightarrow -180^\circ$,
 $T_s = 7 T_\infty$, $\alpha = 20^\circ$

For the heating control, the left surface temperature of the cone, in the circumferential range of $\theta = 0^\circ \rightarrow -180^\circ$, has been changed from the adiabatic condition to a constant temperature condition of surface temperature, $T_s = 7 T_\infty$, where T_∞ is the freestream temperature. Starting from the stable asymmetric flow solution at the 12,000 iteration step, the left surface temperature is raised to $T_s = 5T_\infty$ and then it is raised further to $T_s = 7 T_\infty$. Figure 5 shows the results of this case which include the history of the residual error and the corresponding history of the side force along with the TPL contours after 24,000 iterations. The side-force curve shows that the side force decreases as the temperature increases until it vanishes for $T_s = 7 T_\infty$. Although the side force is zero, the vortical flow is still asymmetric. This case shows the effect of increasing the gas viscosity with heating in order to equalize the surface pressure distribution on the right and left sides of the body. This is the first time, we know of, that such an active control method has been applied to control asymmetric flows.

Injection Flow Control, Variable Mass-Flow
Rate, $\alpha = 20^\circ - 30^\circ$

In this case, the effectiveness of the normal injection control of the case of Fig. 4 ($m_{\max} = 0.03$, $\alpha = 20^\circ$, $\theta = -67.5^\circ \rightarrow 67.5^\circ$) is studied for higher angles of attack. Figure 6 shows the results of this study which includes the history of the residual error versus the number of iterations, the corresponding history of the side force and the TPL contours along with the SP-coefficient curves for $\alpha = 22^\circ, 24^\circ, 26^\circ, 28^\circ$ and 30° . The residual error and the side-force curves show the responses for the following history: First, no control is applied until the 12,000 iteration step; second, injection is applied at $\alpha = 20^\circ$ for 2,000 iterations; third, the angle of attack is increased 2° each 500 iterations until $\alpha = 28^\circ$; fourth, at $\alpha = 30^\circ$ injection is continued for 2,000 iterations. The side-force curve shows zero value in the angle of attack range of $\alpha = 20^\circ - 28^\circ$ (corresponding to the iterations range of 14,000 - 16,000). When the angle of attack reaches 30° , the normal injection control becomes incapable of achieving flow symmetry. It is interesting to study the snapshots of the TPL contours at these angles of attack. It is noticed that the primary vortices increase in size in the normal direction and their inner boundaries approach each other. At $\alpha = 28^\circ$, the inner boundaries of the primary vortices touch each other, and thereafter at $\alpha = 30^\circ$ the primary vortices become asymmetric. The asymmetric response of the primary vortices at $\alpha = 30^\circ$ is believed to be due to a strong instability arising due to the strong interaction of the inner shear layers of the primary vortices.

At $\alpha = 30^\circ$, the injected mass-flow rate in the normal direction to the body surface is increased to $m_{\max} = 0.05, 0.06$ and 0.07 in order to recover the flow asymmetry. Figure 7 shows the results of these tests. Both the TPL contours and the SP-coefficient curves show that the flow is asymmetric and the side force does not vanish. It is seen that the flow asymmetry changes from the right to the left sides and so does the side force. Therefore, it is apparent that normal-injection control loses its effectiveness at high angles of attack for the considered conditions.

Hybrid Heating-Injection Control, $\alpha = 20^\circ - 42^\circ$

In this case, the surface-heating control is followed by normal-injection control. Figure 8 shows the results of this study. The control process is applied as follows: First, the whole surface is heated to $T_s = 5T_\infty$ and the heating control started at $\alpha = 20^\circ$, where the number of iterations is 12,000. Next, the angle of attack is increased 4° until symmetric flow is recovered at the 18,000 iterations. The angle of attack is then increased 2° each 1000 iteration until the angle of attack reaches 38° . The flow symmetry has been continuously recovered until the angle of attack of 36° where a slight flow asymmetry appears in the solution. At $\alpha = 38^\circ$, the flow asymmetry becomes stronger and the heating control loses its effectiveness for $T_s = 5T_\infty$.

At $\alpha = 38^\circ$, normal-injection control is applied with $m_{\max} = 0.05$ and $\theta = -67.5^\circ \rightarrow 67.5^\circ$. The angle of attack is then increased 2° each 3000 iterations. The history of the residual error and the corresponding zero side force is shown in Fig. 8. Figure 9 shows snapshots of the TPL contours and SP-coefficient curves at $\alpha = 38^\circ$, 40° and 42° . The TPL contours show asymmetric flows but the SP-coefficient curves show symmetry resulting in zero side force. Thus, it is concluded that a hybrid control of heating and normal injection is very effective in eliminating the side force at very high angles of attack.

Tangential-Injection Control, $m_{\max} = 0.2$

In this case, the circular section of the lower portion of the cone has a radius larger than that of the upper portion. The lower local radius is 1.05 that of the upper one. Flow is injected from the lip of the lower portion in a direction tangent to the surface of the upper portion. The maximum mass flow rate, m_{\max} , is 0.2 and the velocity profile at the lip exit is a parabolic one. Figure 10 shows the grid used for the thin-layer computations. Three grid blocks are used for the present computation. The first block is $121 \times 19 \times 2$, the second is $121 \times 63 \times 2$ and the third is $121 \times 63 \times 2$ all in the circumferential, normal and axial directions, respectively. The tangential flow control starts from the 20° angle of attack. The computations are carried out until a symmetric flow solution is obtained. Thereafter, the angle of attack is increased to 30° with a step of 2° . Figure 10 also shows the total pressure-loss contours for the controlled, symmetric flow solutions at $\alpha = 22^\circ$, 26° and 30° . It is noticed that as the angle of attack increases the inner shear layers of the controlled symmetric primary vortices approach each other and hence flow asymmetry might develop again.

CONCLUDING REMARKS

The computational solution of the unsteady, compressible, full Navier-Stokes equations has been used to study the effectiveness of two active control methods for asymmetric flows around circular pointed cones. Locally-conical flow assumptions have been used in order to reduce the computational cost of this study by an order of magnitude in comparison with that of three-dimensional flow solutions. The first active control method is applied by injecting air normal to the body surface from ports that are circumferentially distributed within a certain angle. The injected mass-flow rate is either constant or variable. The variable injected mass-flow rate is proportional to the surface-pressure difference between corresponding points on the right and left sides of the body surface. The results of this part of the study show that use of normal injection alone loses its effectiveness at very high angles of attack. The second active control method is applied by heating the body surface either partially or totally. The results of this part of the study show that surface-heating control is much more effective in comparison with normal-injection

control at very high angles of attack. Next, a hybrid control method which includes surface-heating control followed by normal-injection control is applied. The results of this part of the study shows the superior control effectiveness of the hybrid method. Active control using tangential flow injection is very promising. Work is still underway to exploit its effectiveness. Simultaneous application of passive control and the present active control methods is also investigated.

ACKNOWLEDGEMENT

For the first two authors, this research work has been supported by the NASA Langley Research Center under Grant No. NAG-1-994. The computational resources provided by the NASA Langley Research are appreciated.

REFERENCES

1. Kandil, O. A., Wong, T-C. and Liu, C. H., "Prediction of Steady and Unsteady Asymmetric Vortical Flow Around Cones," AIAA 90-0598, 1990. Also in AIAA Journal, Vol. 29, No. 12, pp. 1269-1278, 1991.
2. Kandil, O. A., Wong, T-C. and Liu, C. H., "Asymmetric Flow Around Cones with Noncircular Sections," AGARD Symposium on Missile Aerodynamics, AGARD CP No. 493, Friedrichshafen, Germany, pp. 16.1-16.11, 1990.
3. Kandil, O. A., Wong, T-C. and Liu, C. H., "Numerical Simulation of Steady and Unsteady Asymmetric Vortical Flows," ASME Symposium on Non-Steady Fluid Dynamics, FED-Vol. 92, Toronto, Canada, pp. 99-108, 1990. To appear in the Journal of Fluids and Structures, 1991.
4. Kandil, O. A., Wong, T-C., Kandil, H., A. and Liu, C. H., "Computation and Control of Asymmetric Vortex Flow Around Circular Cones Using Navier-Stokes Equations," ICAS Paper No. 3.5.3, Vol. 2, Stockholm, Sweden, pp. 883-893, 1990.
5. Kandil, O. A., Wong, T-C., Kandil, H. A. and Liu, C. H., "Thin-Layer and Full Navier-Stokes, Locally-Conical and Three-Dimensional Asymmetric Solutions," AIAA 91-0547, 1991.
6. Stahl, W., "Suppression of Asymmetry of Vortex Flow Behind a Circular Cone at High Incidence," Proceedings of the AIAA Atmospheric Flight Mechanics Conference, Boston, MA, AIAA 39-3372-CP, pp. 231-236, 1989.
7. Ng, T. T., "On Leading Edge Vortex and Its Control," Proceedings of the AIAA Atmospheric Flight Mechanics Conference, Boston, MA, AIAA 89-3346-CP, pp. 1-15, 1989.
8. Moskovitz, C., Hall, R. and DeJarnette, "Experimental Investigation of a New Device to Control the Asymmetric Flowfield on Forebodies at Large Angles of Attack," AIAA 90-0069, 1990.

9. Skow, A. M. and Peake, D. J., "Control of the Forebody Vortex Orientation by Asymmetric Air Injection, (Part B) — Details of the Flow Structure," AGARD-LS-121, High Angle-of-Attack Aerodynamics, pp. 10.1-10.22, 1982.
10. Ng, T. T., Suarez, C. J. and Malcolm, N., "Forebody Vortex Control Using Slot Blowing," Proceedings of the AIAA 9th Applied Aerodynamics Conference, Baltimore, Maryland, AIAA 91-3254-CP, pp. 412-421, 1991.
11. Gittner, M. N. and Chokani, N., "An Experimental Study of the Effects of Aft Blowing on a 3.0 Caliber Tangent Ogive Body at High Angles of Attack," Proceedings of the AIAA 9th Applied Aerodynamics Conference, Baltimore, Maryland, AIAA 91-3252-CP, pp. 390-399, 1991.
12. Font, G. I., Celik, Z. Z. and Roberts, L., "A Numerical and Experimental Study of Tangential Jet Blowing Applied to Bodies at High Angles of Attack," Proceedings of the AIAA 9th Applied Aerodynamics Conference, Baltimore, Maryland, AIAA 91-3253-CP, pp. 400-411, 1991.
13. Ng, T. T., "Aerodynamic Control of NASP-Type Vehicles Through Vortex Manipulation," AIAA 90-0594, 1990.
14. Tavella, D. A., Schiff, L. B. and Cummings, R. M., "Pneumatic Vortical Flow Control at High Angles of Attack," AIAA 90-0098, 1990.
15. Gee, K., Tavella, D. and Schiff, L. S., "Computational Optimization of a Pneumatic Forebody Flow Control Concept," Proceedings of the AIAA 9th Applied Aerodynamics Conference, Baltimore, Maryland, AIAA 91-3249-CP, pp. 370-380, 1991.

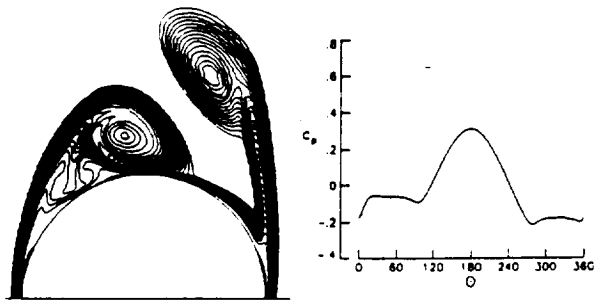


Figure 1. Asymmetric flow solution, TPL contours and SP coefficient; $\alpha = 20^\circ$, $M_\infty = 1.8$, $Re = 10^5$.

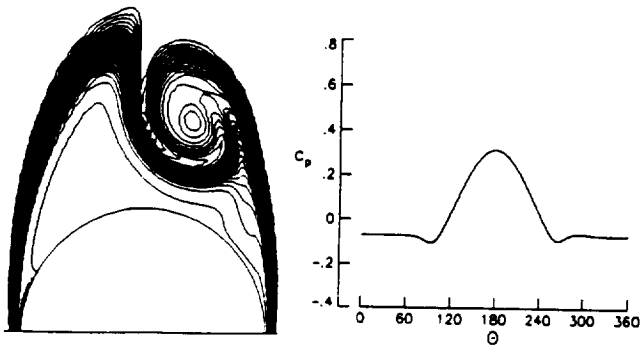
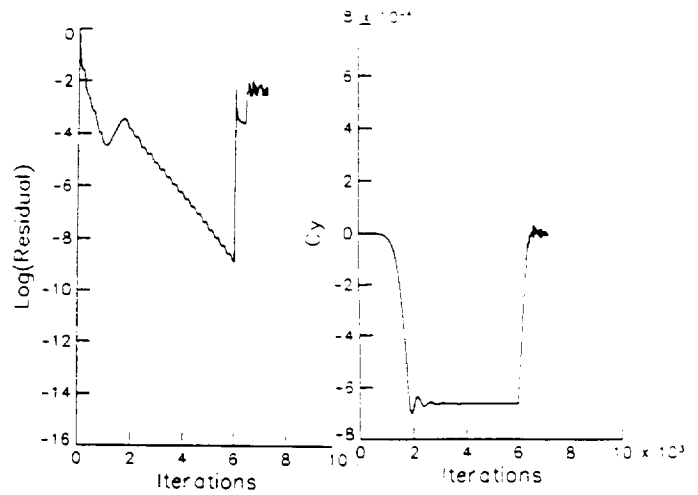


Figure 2. Normal-injection control, TPL contours and SP coefficient; $\alpha = 20^\circ$, $M_\infty = 1.8$, $Re = 10^5$, constant $m = 0.03$, $\theta = -22.5^\circ \rightarrow -67.5^\circ$.

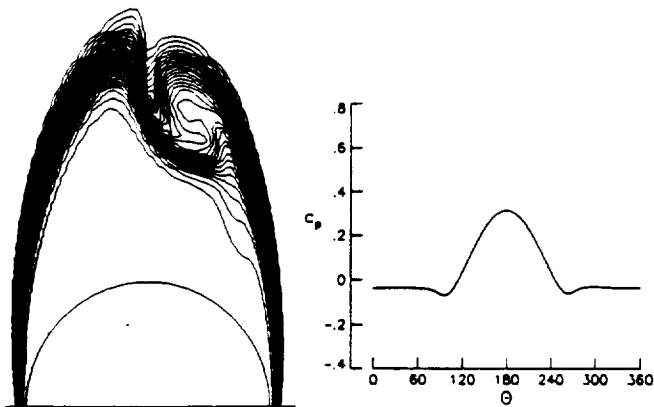
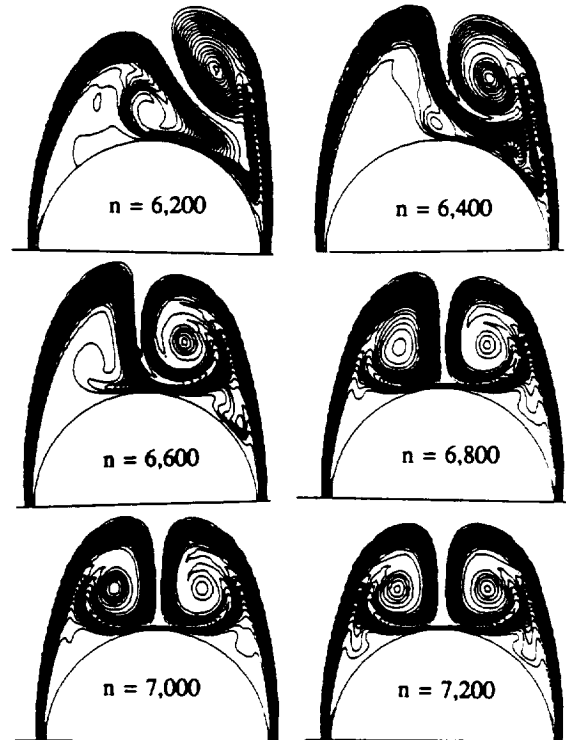


Figure 3. Normal-injection control, TPL contours and SP coefficient; $\alpha = 20^\circ$, $M_\infty = 1.8$, $Re = 10^5$, const $m = 0.03$, $\theta = 0^\circ \rightarrow -67.5^\circ$.

Figure 4. Normal-injection control; history of residual error and side force, TPL contours and SP coefficient; $\alpha = 20^\circ$, $M_\infty = 1.8$, $Re = 10^5$, variable m , $m_{max} = 0.03$, $\theta = -67.5^\circ \rightarrow +67.5^\circ$.

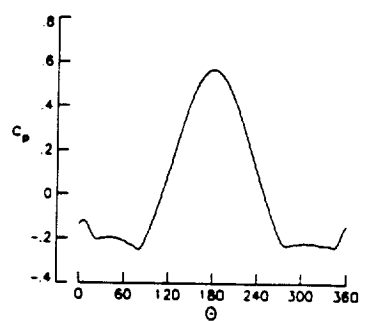
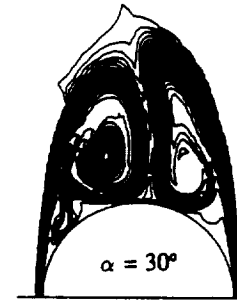
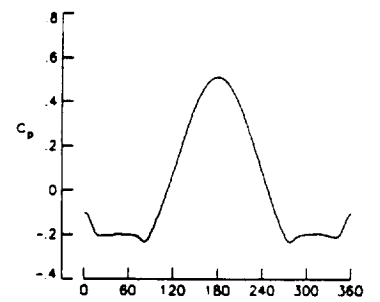
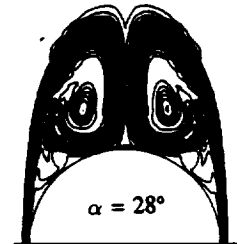
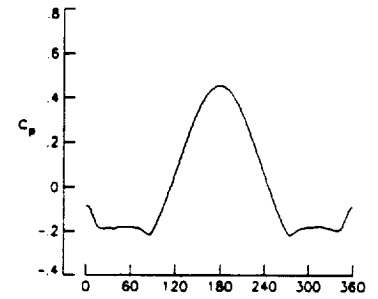
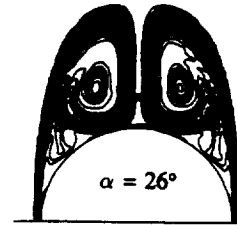
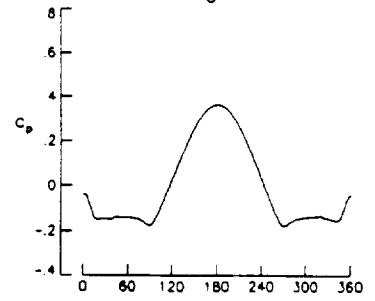
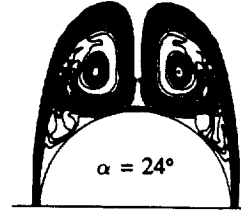
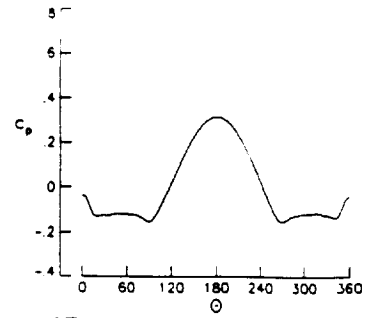
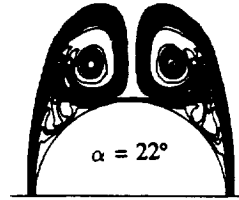
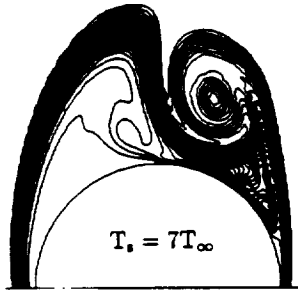
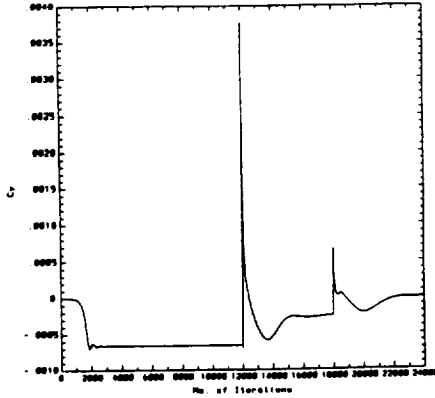
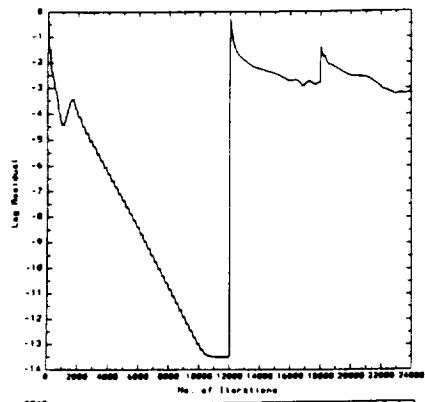


Figure 5. Surface-heating control, history of residual error and side force and TPL contours; $\alpha = 20^\circ$, $M_\infty = 1.8$, $R_e = 10^5$, $T_s = 5T_\infty \rightarrow 7T_\infty$, $\theta = 0 \rightarrow -180^\circ$.

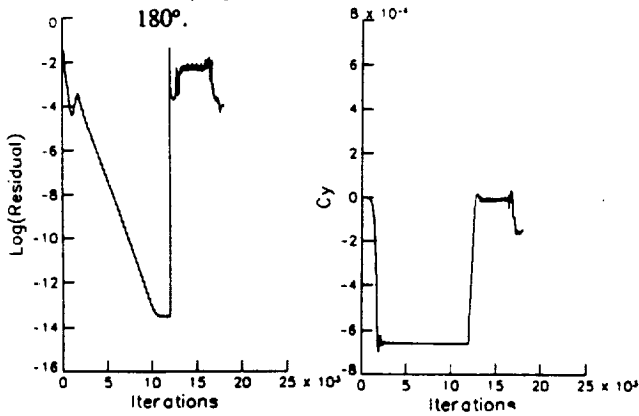


Figure 6. Normal-injection control; history of residual error and side force, TPL contours and SP coefficient; $\alpha = 22^\circ - 30^\circ$, $M_\infty = 1.8$, $R_e = 10^5$, variable m , $m_{max} = 0.03$, $\theta = -67.5^\circ - +67.5^\circ$.

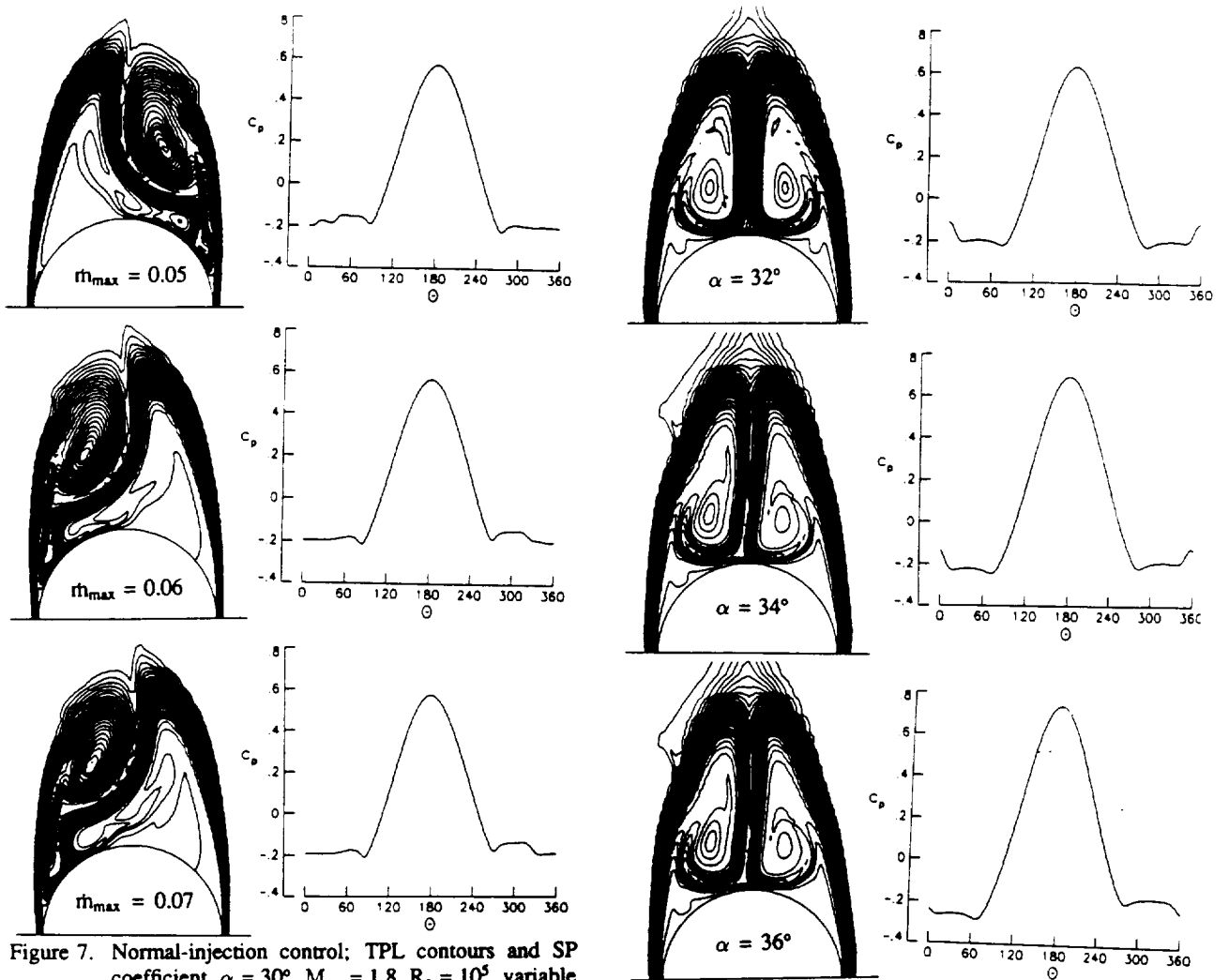


Figure 7. Normal-injection control; TPL contours and SP coefficient, $\alpha = 30^\circ$, $M_\infty = 1.8$, $Re = 10^5$, variable m , $m_{max} = 0.05, 0.06, 0.07$, $\theta = -67.5^\circ - +67.5^\circ$.

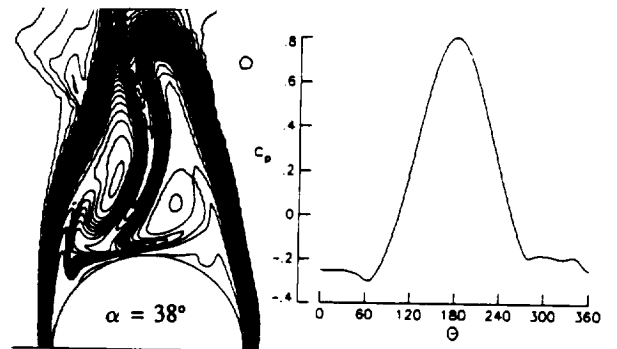
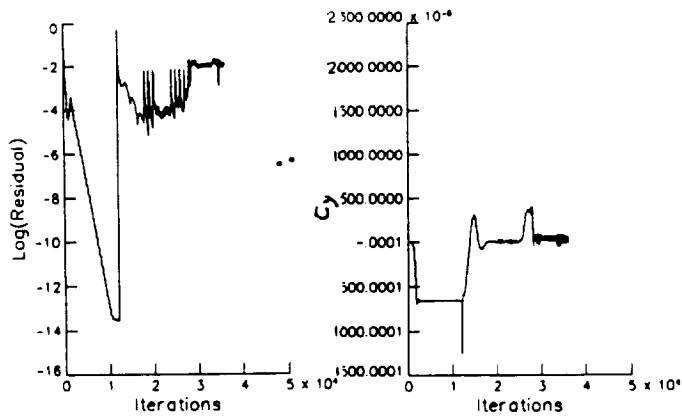


Figure 8. Hybrid heating-injection control (heating part); residual error and side force and TPL contours and SP coefficient; $\alpha = 20^\circ - 38^\circ$, $M_\infty = 1.8$, $Re = 10^5$, $T_s = 5 T_\infty$ on whole surface.

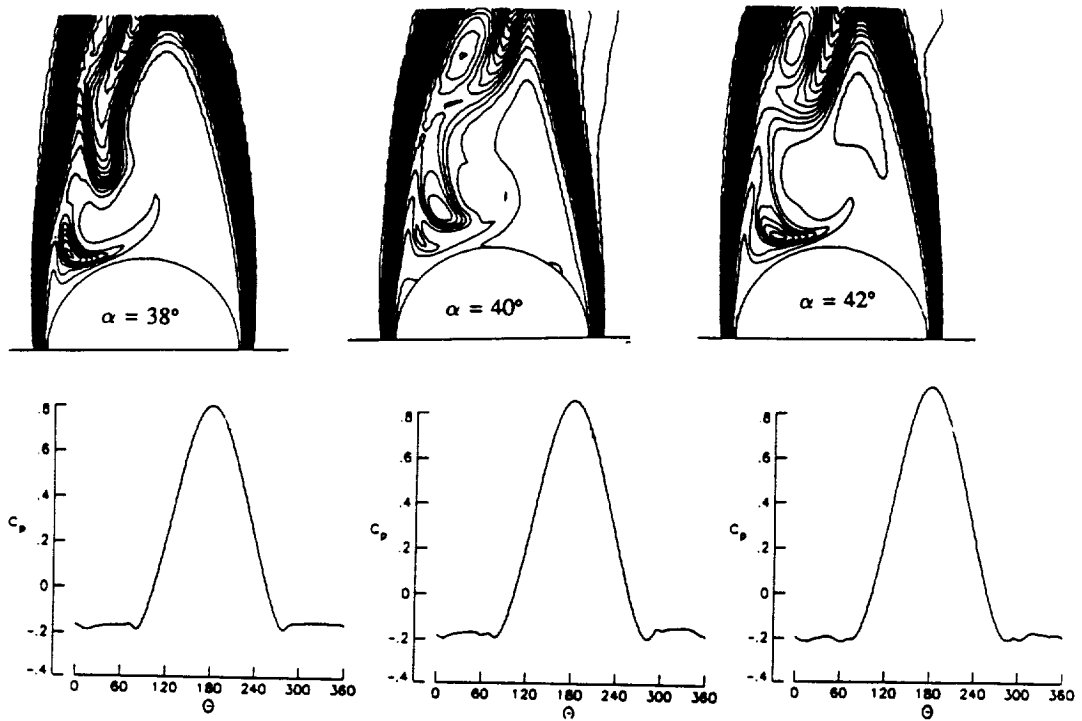


Figure 9. Hybrid heating-injection control (injection part); TPL contours and SP coefficient; $\alpha = 38^\circ - 42^\circ$, $M_\infty = 1.8$, $Re = 10^5$, variable m , $m_{max} = 0.05$, $\theta = -67.5^\circ - +67.5^\circ$.

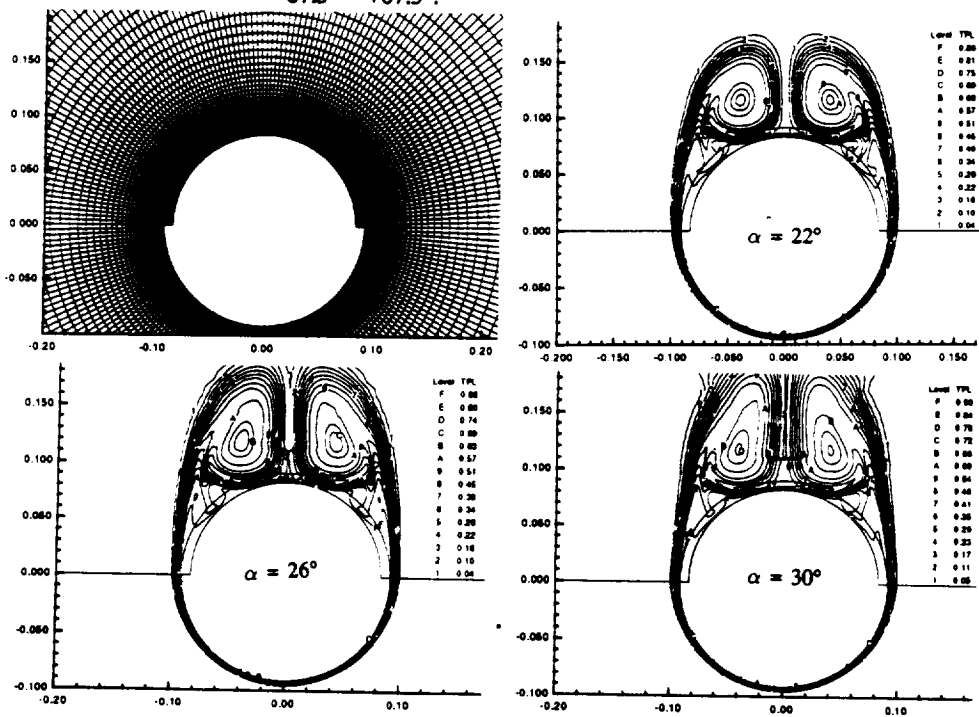


Figure 10. Typical multi-block grid and total pressure-loss contours for the tangential-flow injection control; $\alpha = 22^\circ, 26^\circ, 30^\circ$; $M_\infty = 1.8$, $Re = 10^5$, parabolic velocity profile at lip exit, $m_{max} = 0.2$



*1992 AIAA
92-2601-CP*

AIAA-92-2601-CP

**CRITICAL EFFECTS OF DOWNSTREAM
BOUNDARY CONDITIONS ON
VORTEX BREAKDOWN**

**Osama A. Kandil and Hamdy A. Kandil
Old Dominion University, Norfolk, VA 23529**

**C. H. Liu
NASA Langley Research Center, Hampton, VA 23665**

**AIAA 10th Applied
Aerodynamics Conference
Palo Alto, CA, June 22-25, 1992**



CRITICAL EFFECTS OF DOWNSTREAM BOUNDARY CONDITIONS ON VORTEX BREAKDOWN

Osama A. Kandil* and Hamdy A. Kandil**
Old Dominion University, Norfolk, VA 23529

and

C. H. Liu***

NASA Langley Research Center, Hampton, VA 23665

ABSTRACT

The unsteady, compressible, full Navier-Stokes (NS) equations are used to study the critical effects of the downstream boundary conditions on the supersonic vortex breakdown. The present study is applied to two supersonic vortex breakdown cases. In the first case, quasi-axisymmetric supersonic swirling flow is considered in a configured circular duct, and in the second case, quasi-axisymmetric supersonic swirling jet, that is issued from a nozzle into a supersonic jet of lower Mach number, is considered. For the configured duct flow, four different types of downstream boundary conditions are used, and for the swirling jet flow from the nozzle, two types of downstream boundary conditions are used. The solutions are time accurate which are obtained using an implicit, upwind, flux-difference splitting, finite-volume scheme.

INTRODUCTION

Numerical simulation of vortex breakdown has been focused in most of the existing literature on incompressible flows. Quasi-axisymmetric, vortex-breakdown simulations of incompressible swirling flows have been presented by Grabowski and Berger¹, Hafez, et al.², Salas and Kuruvilla³, Menne⁴, Wu and Hwang⁵ and Menne and Liu⁶. Three-dimensional, vortex-breakdown simulations of incompressible swirling flows have been presented by Spall, et al.⁷, Hänel⁸, and Krause^{9,10}. Discussion of the effects of side boundary conditions and downstream boundary conditions on vortex breakdown was presented by Krause in Ref. 10.

Longitudinal vortex/transverse shock-wave interactions are typical applications which appear in transonic and supersonic flows over a strake-wing configuration at moderate-high angles of attack, at a supersonic inlet ingesting a vortex and inside a supersonic combustor where fuel is injected in a swirling jet to enhance fuel-air mixing¹¹⁻¹³. For the strake-wing configuration, vortex breakdown is undesirable since it results in the stall phenomenon, and hence its occurrence need to be delayed. On the other hand, vortex breakdown for the other two applications is desirable since it enhances mixing and stability of the flame^{14,15}, and hence its occurrence need to be

controlled for the optimum performance. Unfortunately, the literature lacks this type of analysis with the exception of the preliminary work of Liu, Krause and Menne¹⁶, Copening and Anderson¹⁷, Delery, et al.¹¹, Kandil and Kandil¹⁸ and Meadows, Kumer and Hussaini¹⁹.

The first time-accurate NS solution for a supersonic vortex breakdown was developed by the present authors in Ref. 20. We considered a supersonic quasi-axisymmetric vortex flow in a configured circular duct. The time-accurate solution of the unsteady, compressible NS equations was obtained using an implicit, upwind, flux-difference splitting finite-volume scheme. A shock wave has been generated near the duct inlet and unsteady vortex breakdown has been predicted behind the shock. The predicted flow was characterized by the evolution, convection and shedding of vortex breakdown bubbles. The Euler equations were also used to solve the same problem. The Euler solution showed larger size and number of vortex-breakdown bubbles in comparison with those of the NS solutions. The time-accurate solution was carried out for 3,200 time steps which are equivalent to a dimensionless time of 16. Only one value of Reynolds number of 10,000 was considered in Ref. 20.

In a later paper²¹, we expanded our study of this flow using time-accurate computations of the NS equations with a fine grid in the shock-vortex interaction region and for long computational times. Several issues were addressed in that study. First, we showed the effect of Reynolds number on the temporal evolution and persistence of vortex-breakdown bubbles behind the shock. In that stage of computations, the conditions at the downstream exit were obtained by extrapolating the components of the flowfield vector from the interior cell centers. Although the flow was supersonic over a large portion of the duct exit, subsonic flow existed over a small portion of the exit around the duct centerline. Therefore, selected flow cases were computed using a Riemann-invariant-type boundary conditions at subsonic points of the duct exit. Finally, the effect of swirl ratio at the duct inlet was investigated.

In the present paper, we address the problem of specifying the downstream boundary conditions and their critical effects on the supersonic vortex breakdown problem for internal and external flows. For this purpose, the unsteady, compressible, full NS equations are used along with an implicit, upwind, flux-difference splitting, finite-volume scheme for the time-accurate solutions. For the

*Professor and Eminent Scholar, Department of Mechanical Engineering and Mechanics, Associate Fellow AIAA.

**Graduate Research Assistant, Member AIAA

***Group Leader, Theoretical Flow Physics Branch, Associate Fellow AIAA

internal flow case, supersonic swirling flow in a configured duct is considered along with four types of downstream boundary conditions. Keeping the duct geometry and the upstream flow conditions fixed, the exit boundary conditions are varied. The four exit boundary conditions include extrapolation of all the five variables from the interior cell centers, specifying the downstream pressure and extrapolating the other flow conditions from the interior cell centers, specifying the downstream pressure gradient and extrapolating the other four conditions from the interior cell centers, and using a disk of specified radius at the exit section. For the external flow case, supersonic swirling jet is issued from a nozzle into a supersonic non-swirling jet of Mach number lower than that of the swirling jet. Two types of downstream boundary conditions are considered. In the first type, extrapolation of all the five variables from the interior cell centers is used, while in the second type, the standard Riemann-invariant type boundary condition is used. All the results presented in this paper have been produced using our full NS solver which is known as the "FTNS3D" code. The CRAY-YMP computer of NASA Langley Research Center is used for the computations.

HIGHLIGHTS OF THE FORMULATION AND COMPUTATIONAL SCHEME

The conservative, unsteady, compressible, full Navier-Stokes equations in terms of time-independent, body-conformed coordinates ξ^1 , ξ^2 and ξ^3 are used to solve the problem. The equations are given in Ref. 21 and hence they are not shown here. Along with these equations, boundary conditions are specified at the computational-domain inlet, side wall and downstream exit. The downstream exit boundary conditions will be presented in the next section of the computational results. The initial conditions will also be presented in the next section.

The computational scheme used to solve the unsteady, compressible full NS equations is an implicit, upwind, flux-difference splitting, finite-volume scheme. It employs the flux-difference splitting scheme of Roe which is based on the solution of the approximate one-dimensional Riemann problem in each of the three directions. In the Roe scheme, the inviscid flux difference at the interface of a computational cell is split into left and right flux differences. The splitting is accomplished according to the signs of the eigenvalues of the Roe averaged-Jacobian matrix of the inviscid flux at the cell interface. The smooth limiter is used to eliminate oscillations in the shock region. The viscous and heat-flux terms are linearized and the cross-derivative terms of the viscous Jacobians are dropped in the implicit operator. These terms are differenced using second-order spatially accurate central differencing. The resulting difference equation is approximately factored and is solved in three sweeps in the ξ^1 , ξ^2 and ξ^3 directions. The scheme is used for third-order spatial accuracy and first-order temporal accuracy.

The scheme is coded in the computer program which is called "FTNS3D".

The quasi-axisymmetric solutions are obtained using the three-dimensional code by forcing the flowfield vector to be equal on two axial planes, which are in close proximity of each other.

COMPUTATIONAL RESULTS AND DISCUSSION

I. Vortex Breakdown in Configured Circular Duct

Figure 1 shows a configured circular duct which consists of a short, straight cylindrical part at the inlet which is followed by a short divergent cylindrical part until the axial length of 0.74. The divergence angle is 6° . The duct radius is then kept constant and a convergent-divergent nozzle with a throat radius of 0.95 is attached. The duct exit radius is 0.98 and its total length is 2.9. The divergent part of the duct ensures the stability of the formed shock in the inlet region. The configuration of the duct is intended to ensure that the supersonic inflow will become supersonic at the exit. As the computations will show, a small portion of the duct exit near its centerline becomes subsonic at certain times for the specified inflow conditions. This configured duct has also been used by Delery, et al. ¹¹ for their Euler equations computations of supersonic vortex breakdown in an attempt to computationally model an experimental set up.

The NS solver is used to compute all the following flow cases by using a grid of 221×51 on two axial planes, where 221 points are in the axial direction and 51 points are in the radial direction. In the inlet region up to the 0.74 axial station, 100 grid points are used and the remaining 121 points are used in the remaining part of the duct. The grid is also clustered at the centerline (CL) and the wall. The minimum radial grid size at the CL is 0.002. The two axial planes are spaced circumferentially at a certain angle so that the aspect ratio of the minimum grid size will be less than 2. The upstream Mach number is kept at 1.75 and the Reynolds number is kept at 100,000. The initial profile for the tangential velocity is given by

$$\frac{w}{U_\infty} = \frac{k_e}{r} \left[1 - \exp\left(-\frac{r^2}{r_m^2}\right) \right] \quad (1)$$

where $U_\infty = 1.74$, $r_m = 0.2$ and $k_e = 0.1$. The maximum $\frac{w}{U_\infty}$, swirl ratio β , is at $r = 0.224$ and its value is kept at 0.32. The radial velocity, v , at the initial station is set equal to zero and the radial momentum equation is integrated to obtain the initial pressure profile. Finally, the density ρ is obtained from the definition of the speed of sound for the inlet flow. With these compatible set of profiles, the computations are carried out accurately in time with $\Delta t = 0.0025$. The wall boundary conditions follow the typical Navier-Stokes solid-boundary conditions. These computations have been carried out on the CRAY YMP of the NASA Langley Research Center. The CPU time is 40 μ s/grid point/iteration for the NS calculation.

Next, we present the results of the computational study of this case which covers four types of exit boundary conditions.

1.1. Extrapolation from Interior Cell Centers

Figure 2 shows snapshots of the streamlines and Mach contours for this case. The downstream boundary conditions are obtained by extrapolating all the flow variables from the cell centers at the exit. The streamlines snapshots show multi-bubble vortex breakdown evolution, convection, merging and shedding. The time-accurate integration was carried out up to $t = 200$ and the solution showed periodic multi-frequency cycles of vortex-breakdown bubbles²¹. An example of the merging of vortex breakdown bubbles of same sign of vorticity is shown at $t = 17$. An example of convection and shedding of vortex breakdown bubbles is shown at $t = 25$. Comparing the streamlines solutions at $t = 25$ and $t = 89$, it is seen that the solutions are almost the same which conclusively show that the breakdown process is periodic. The Mach-contours show the dynamics of inlet shock motion. In the time range of $t = 3-8$, the inlet shock moves upstream toward the inlet and its central portion exists outside the inlet section at $t = 8$. In the time range of $t = 8-25$, the inlet shock moves downstream with corresponding evolution, convection, merging and shedding of breakdown bubbles. In the time range of $t = 25-45$, the inlet shock maintains its motion in the downstream direction at a slower rate than before, while another shock, which is downstream of the inlet shock, appears and also moves in the downstream direction. The evolution, convection and shedding slowly continues until $t = 66$. In the time range of $t = 66-78$, the downstream shock disappears and a large vortex-breakdown bubble appears and moves upstream. This motion of the bubble is accompanied by upstream motion of the inlet shock ($t = 78$). Later the inlet shock again moves in the downstream direction and the process is repeated. An animation movie has been produced for the total dimensionless time of $t = 200$. Figure 3 shows a blow-up of two snapshots of the streamlines solutions at $t = 84$ and $t = 87$. At $t = 84$, we recognize five vortex breakdown bubbles which spatially alternate in their sign of vortex strength. It is also noticed that six stagnation points exist at the axis. At $t = 87$, we recognize seven vortex breakdown bubbles and seven stagnation points. The figure shows the merging of two bubbles of same vorticity sign.

1.2. Riemann Invariant Boundary Conditions

with $p_b = p_\infty$

In this case, the back pressure at the subsonic points of the duct exist, p_b , is specified to be equal to p_∞ and the other four variables are extrapolated from the interior cell centers. The computations have repeated on the same grid and for the same flow conditions as that of the previous case. Figure 4 shows snapshots of the streamlines and Mach contours of the solution. Comparing the

present solution with the previous case (Fig. 2), it is seen that the two solutions are the same until $t = 35$. Thereafter, for $t > 35$, the inlet shock continuously moves in the downstream direction with the vortex-breakdown bubbles moving ahead of the shock. The shock and vortex bubbles are shed and disappears from the duct at advanced levels of time. The breakdown mode is termed as "a transient multi-bubble vortex breakdown." The reason behind disappearance of the shock-vortex-breakdown-bubble system is that the back pressure is so low that it cannot support the inlet shock keeping it in the inlet region. Moreover, the Riemann-invariant type conditions at subsonic points let the downstream effects propagate upstream as time increases.

1.3. Riemann Invariant Boundary Conditions

with $p = 2p_\infty$

In this case, the back pressure at the subsonic points of the duct exit is specified to be $p_b = 2p_\infty$ and the other four variables are extrapolated from the interior cell centers. Figure 5 shows snapshots of the streamlines and Mach contours of the solution. Comparing the present solution with the solution of the first case (Fig. 2), it is seen that the two solutions are similar with the exception that the present solution lags that of the first case in time. The reason behind this behavior is that the back pressure p_b is larger than that of the first case. Moreover, the Riemann invariant type conditions at subsonic points let the downstream effects propagate upstream as time increases. The existence of the large back pressure which is felt upstream supports the inlet shock and keeps it in the inlet region.

1.4. Riemann Invariant Boundary Conditions

with $\frac{\partial p}{\partial x} = \text{constant}$

In this case, the back pressure is obtained from the condition $\frac{\partial p}{\partial x} = \text{constant}$ at the subsonic points of the duct exit. The other flow variables are extrapolated from the interior cell centers. Figure 6 shows snapshots of the streamlines and Mach contours of the solution. Comparing the present solution with the solution of the first case (Fig. 2), it is seen that the two solutions are similar until $t = 22$. Thereafter, for $t > 22$, the inlet shock continuously moves in the downstream direction with the vortex-breakdown bubbles moving ahead of the shock. Again, as in the case of Fig. 4, the shock and vortex bubbles are shed and disappear from the duct at advanced levels of time. The breakdown is termed as "a transient multi-bubble vortex breakdown." The reason behind disappearance of the shock-vortex-breakdown-bubble system is that the back pressure obtained from $\frac{\partial p}{\partial x} = \text{constant}$ condition is so low that it cannot support the inlet shock keeping it in the inlet region. Moreover, the Riemann-invariant type conditions at subsonic points let the downstream effects propagate upstream as time increases.

1.5. Placing a Disk at the Exit with $r = 0.333$

In this case, a circular solid disk of radius $r = 0.333$ is placed at the duct exit and solid-boundary conditions are applied on the disk surface. For the remaining portion of the exit, the boundary conditions are obtained by extrapolation from the interior cell centers. Figure 7 shows snapshots of the streamlines and Mach contours of the solution. It is noticed from the Mach contours that most of the exit points are subsonic. The streamlines show that the shock-vortex-breakdown-bubble system first appears behind the duct exit. Thereafter, they move upstreams until the inlet shock moves outside of the inlet. The vortex-breakdown bubbles are then locked between the shock outside of the inlet and the circular disk at the exit.

II. Supersonic Swirling Jet from a Nozzle

Figure 8 shows the computational domain and a typical grid for this external flow case. The dimensions of the computational domain is 7×3.5 in the axial and radial directions, respectively. The grid is $221 \times 51 \times 2$ points in the axial, radial and tangential directions, respectively. The grid is clustered at the nozzle exit ($x = 0.0$) and at the domain centerline. The dimensionless nozzle radius is unity, where a supersonic jet of $M_\infty = 3.0$ is issued, and outside the nozzle another jet is issued at $M_\infty = 2.0$. The freestream Reynolds number is 296,000.

Figure 9 shows the inlet flow profiles of the axial velocity, swirl velocity, radial velocity, pressure and density, which are taken from the experimental data of Ref. 12. The initial profiles are used as quasi-axisymmetric profiles for the present computations. On the cylindrical boundary (side wall) of the flow at $r = 3.5$, freestream conditions are imposed corresponding to $M_\infty = 2.0$. The initial conditions in the computational domain are also taken as those corresponding to the freestream conditions at $M_\infty = 2.0$. The problem is solved using two types of exit boundary conditions at $x = 7.0$; first extrapolation of all five variables from the interior cell center and second using the Riemann-invariant-type boundary conditions.

II.1. Extrapolation from Interior Cell Centers

Figure 10 shows snapshots of streamlines and Mach contours of the solution. The streamlines show multi-bubble breakdown at the early levels of time. These bubbles develop due to the shock system formed at the nozzle exit in the vicinity of the centerline. It is noticed that a strong portion of the shock exists at the centerline which splits into two oblique shocks, one is a weak shock and the other is a strong shock. Behind the strong shock, the vortex breakdown bubbles exist. Thereafter, for $t > 5$, the oblique shocks move slowly in the downstream direction and breakdown the vortex bubble stays in its place. At $t > 55$, the shock system moves upstream and so does the vortex breakdown bubble. The slow motion of the shock

system and the vortex breakdown bubble continues back and forth between these two locations. No vortex shedding has been captured during the computations of this case. It is also noticed that most of the exit points are continuously supersonic and hence no downstream effects exist with the exception of a very thin-layer around the centerline.

II.2. Riemann Invariant Boundary Conditions

Next, the boundary conditions at the exit are replaced by using the Riemann-invariant-type boundary conditions with $p_b = p_\infty$ at the subsonic points. Figure 11 shows snapshots of the streamlines and Mach contours of the solution. By comparing the present solution with the previous case of Fig. 10, we see that there is very slight effect of the present boundary condition on the solution. This is understood since the subsonic region at the exit is very small and moreover, the exit boundary is far from the nozzle exit.

Figure 12 shows a blow-up of the Mach contours at $t = 55$ for the flow case of Fig. 10. The shock system near the nozzle exit is clearly seen.

Concluding Remarks

The unsteady, compressible full Navier-Stokes equations are used to study the critical effects of the downstream boundary conditions on the supersonic vortex breakdown. In the present study, two supersonic swirling flow cases are considered. The first one is for a supersonic swirling flow in a configured circular duct, where four types of exit boundary conditions are used. The second one is for a supersonic swirling jet issued from a nozzle into another supersonic jet of lower Mach number. This flow case is a computational simulation to the experimental case of Ref. 12.

In the first flow case, we have shown that the downstream exit boundary conditions produce substantial changes in the vortex breakdown modes, particularly at advanced time levels. This is due to the effect of the subsonic downstream points on the flow upstream. In the second flow case, we have shown that the downstream exit boundary conditions do not produce substantial changes in the vortex breakdown modes. This is due to the very thin subsonic region at the exit and the large distance of the downstream exit from the nozzle exit.

Acknowledgement

For the first two authors, this research work has been supported by NASA Langley Research Center under Grant No. NAG-1-994.

References

1. Grabowski, W. J. and Berger, S. A., "Solutions of the Navier-Stokes Equations for Vortex Breakdown," *Journal of Fluid Mechanics*, Vol. 75, Part 3, 1976, pp. 525-544.
2. Hafez, M., Kuruvila, G. and Salas, M. D., "Numerical Study of Vortex Breakdown," *Journal of Applied Numerical Mathematics*, No. 2, 1987, pp. 291-302.
3. Salas, M. D. and Kuruvila, G., "Vortex Breakdown Simulation" A Circumspect Study of the Steady, Laminar, Axisymmetric Model," *Computers and Fluids*, Vol. 17, No. 1, 1989, pp. 247-262.
4. Menne, S., "Vortex Breakdown in an Axisymmetric Flow," AIAA 88-0506, January 1988.
5. Wu, J. C. and Hwang, S., "Computational Study of Vortex Breakdown in Circular Tube," AIAA 91-1820, June 1991.
6. Menne, S. and Liu, C. H., "Numerical Simulation of a Three-Dimensional Vortex Breakdown," *Z. Flugwiss. Weltraumforsch.* 14, 1990, pp. 301-308.
7. Spall, R. E., Gatski, T. B. and Ash, R. L., "The Structure and Dynamics of Bubble-Type Vortex Breakdown," *Proc. R. Soc., London*, A429, 1990, pp. 613-637.
8. Breuer, M. and Hänel, D., "Solution of the 3-D Incompressible Navier-Stokes Equations for the Simulation of Vortex Breakdown," Eight GAMM Conference, Delft, Netherlands, September 27-29, 1989.
9. Krause, E., "Vortex Breakdown: Physical Issues and Computational Simulation," Third International Congress of Fluid Mechanics, Cairo, Egypt, January 1990, Vol. 1, pp. 335-344.
10. Krause, E., "The Solution of the Problem of Vortex Breakdown," Invited paper, International Conference on Numerical Methods for Fluid Dynamics, Oxford, England, June 1990.
11. Delery, J., Horowitz, E., Leuchter, O. and Solignac, J. L., "Fundamental Studies of Vortex Flows," *La Recherche Aéronautique*, No. 1984-2, 1984, pp. 1-24.
12. Metwally, O., Settles, G. and Horstman, C., "An Experimentally Study of Shock Wave/Vortex Interaction," AIAA 89-0082, January 1989.
13. Cutler, A.D. and Levey, B. S., "Vortex Breakdown in a Supersonic Jet," AIAA 91-1815, June 1991.
14. Rhode, D. L., Lilley, D. G. and McLaughlin, D. K., "On the Prediction of Swirling Flowfields Found in Axisymmetric Combustor Geometries," *Transactions of ASME*, Vol. 104, September 1982, pp. 378-384.
15. Altegeld, H., Jones, W. P. and Wilhelmi, "Velocity Measurements in a Confined Swirl Driven Recirculating Flow," *Experiments in Fluids*, Springer Verlag, Vol. 1, 1983, pp. 73-78.
16. Liu, C. H., Krause, E. and Menne, S., "Admissible Upstream Conditions for Slender Compressible Vortices," AIAA 86-1093, 1986.
17. Copening, G. and Anderson, J., "Numerical Solutions to Three-Dimensional Shock/Vortex Interaction at Hypersonic Speeds," AIAA 89-0674, January 1989.
18. Kandil, O. A. and Kandil, H. A., "Computation of Compressible Quasi-Axisymmetric Slender Vortex Flow and Breakdown," IMACS 1st International Conference on Computational Physics, University of Colorado, Boulder, June 1990, pp. 46-51. Also in *Computer Physics Communications*, Vol. 65, North-Holland, March 1991, pp. 164-172.
19. Meadows, K., Kumar, A. and Hussaini, M., "A Computational Study on the Interaction Between a Vortex and a Shock Wave," AIAA 89-1043, April 1989.
20. Kandil, O. A., Kandil, H. A. and Liu, C. H., "Computation of Steady and Unsteady Compressible Quasi-Axisymmetric Vortex Flow and Breakdown," AIAA 91-0752, January 1991.
21. Kandil, O. A., Kandil, H. A. and Liu, C. H., "Supersonic Quasi-Axisymmetric Vortex Breakdown," AIAA 91-3311-CP, September 1991, pp. 851-863.

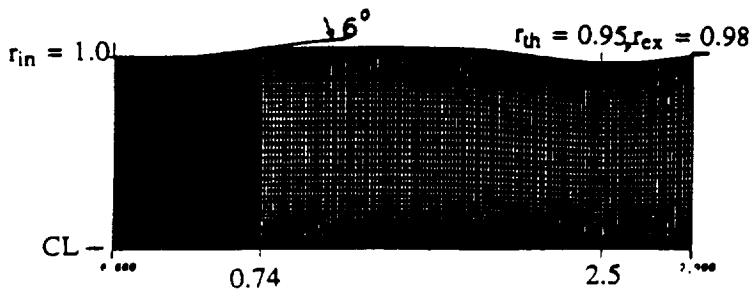


Figure 1. Typical grid for a supersonic configured circular duct; 221x51x2

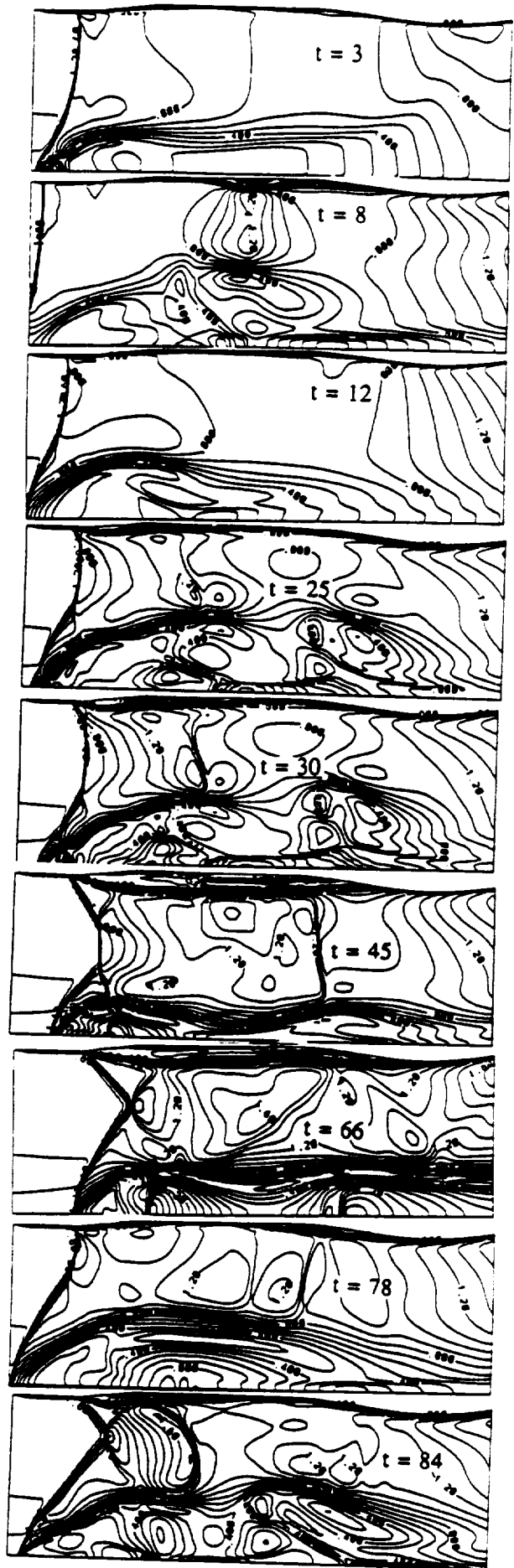
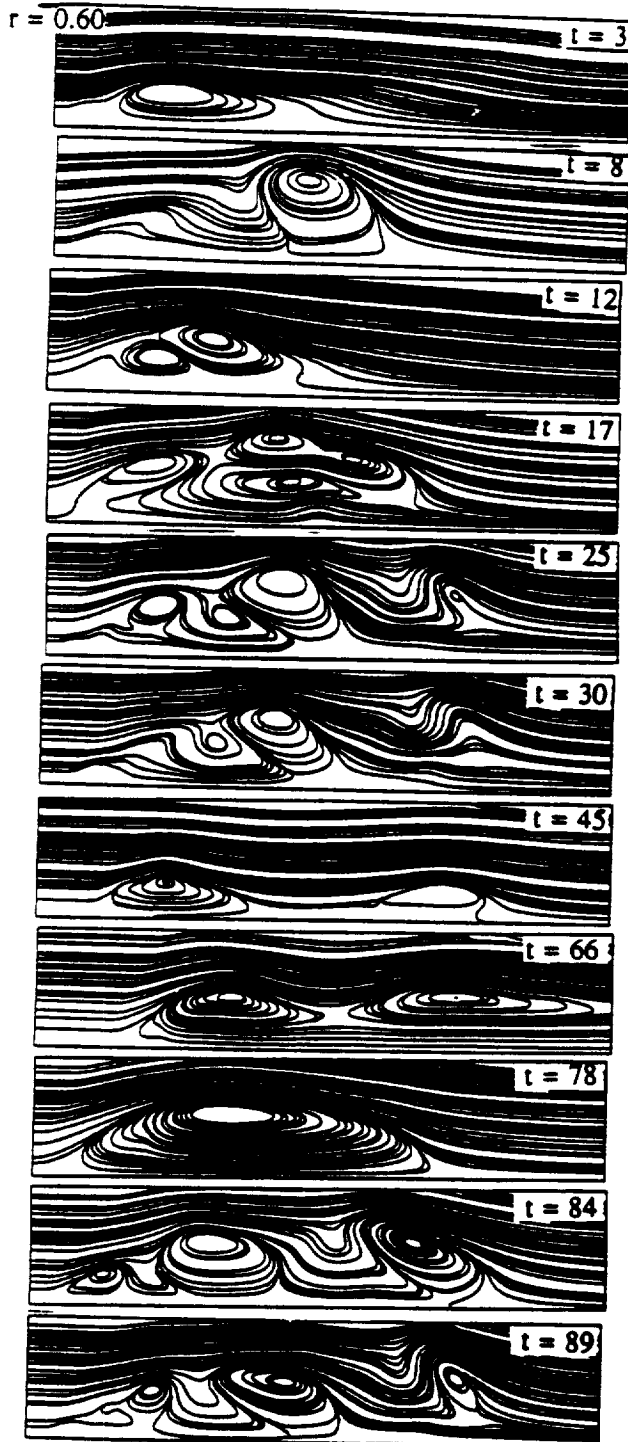


Figure 2. Streamlines and Mach contours for a swirling flow with periodic multibubble, multifrequency vortex breakdown, extrapolation from interior.

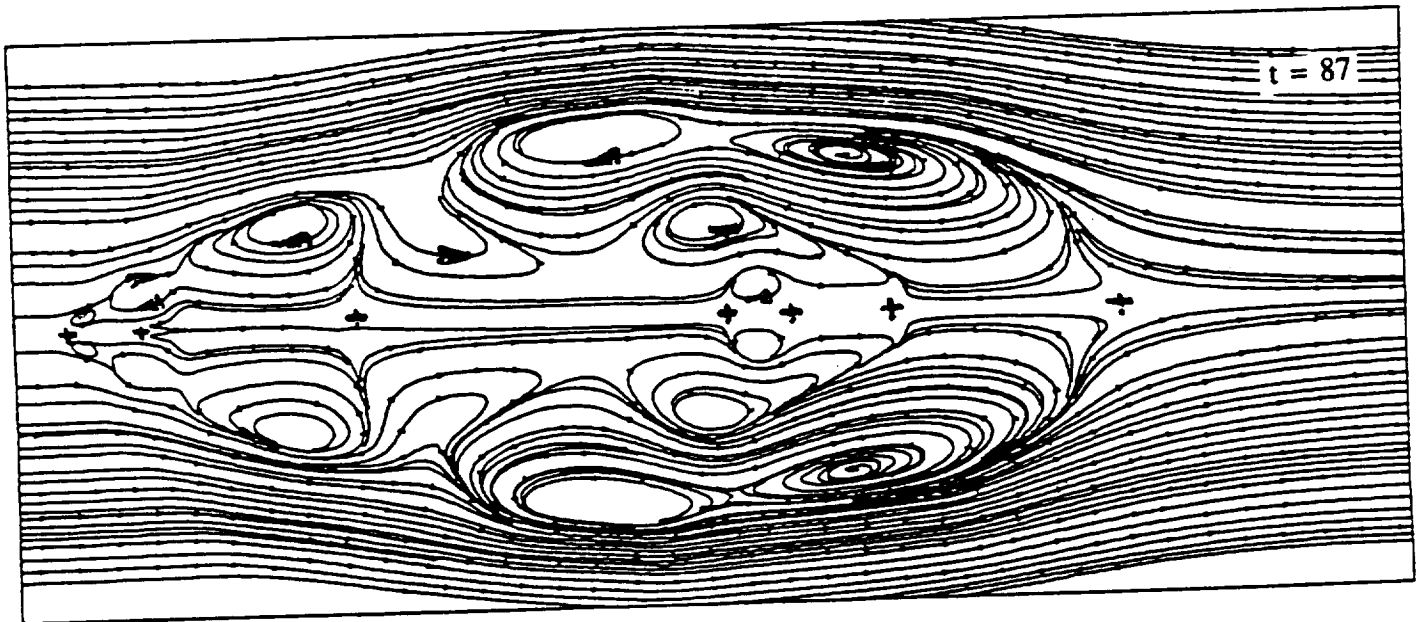
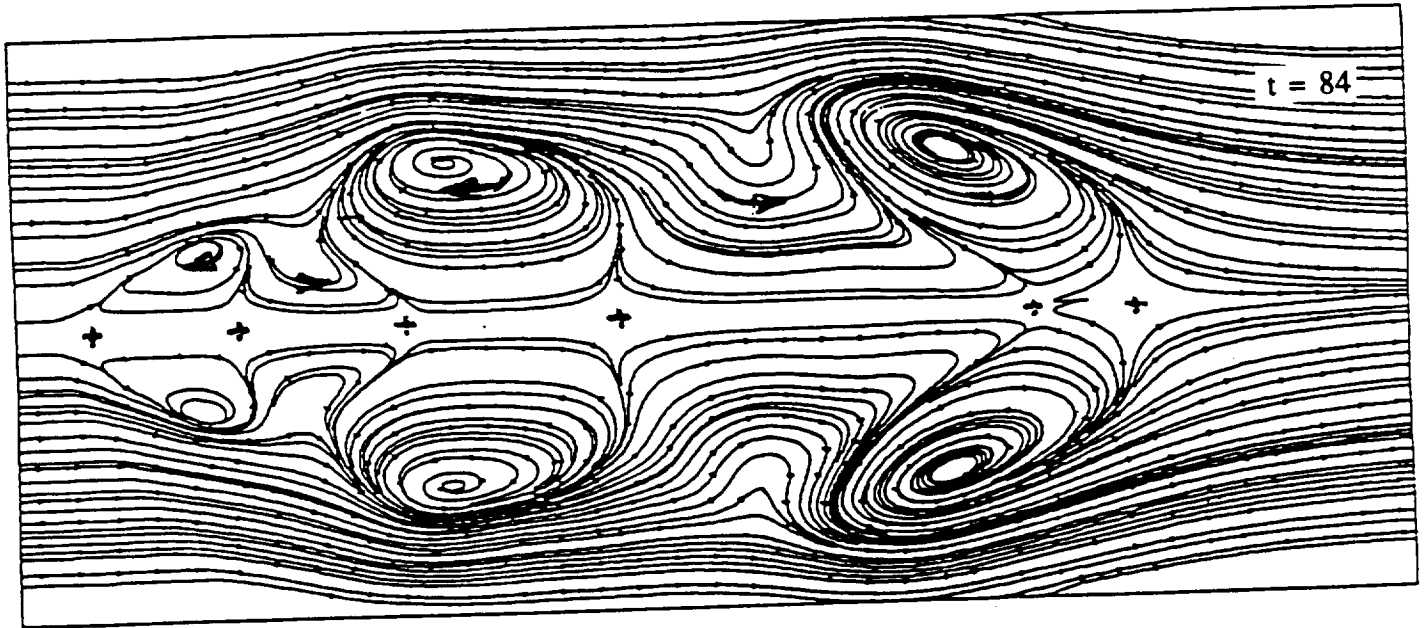


Figure 3. Blow-up of streamlines of periodic multibubble, multi-frequency vortex breakdown, extrapolation from interior B.C.

$r = 0.6$

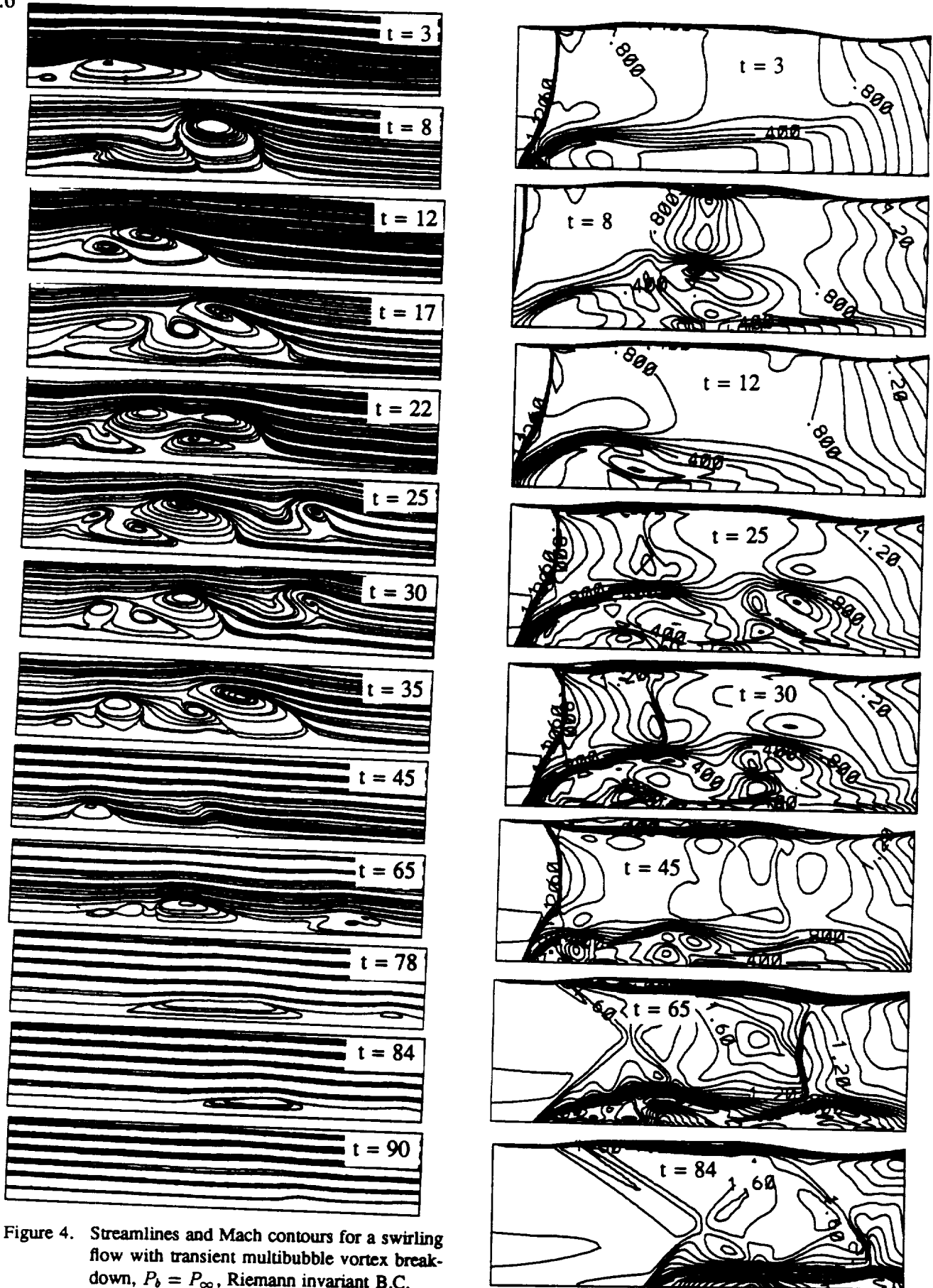


Figure 4. Streamlines and Mach contours for a swirling flow with transient multibubble vortex breakdown, $P_b = P_\infty$, Riemann invariant B.C.

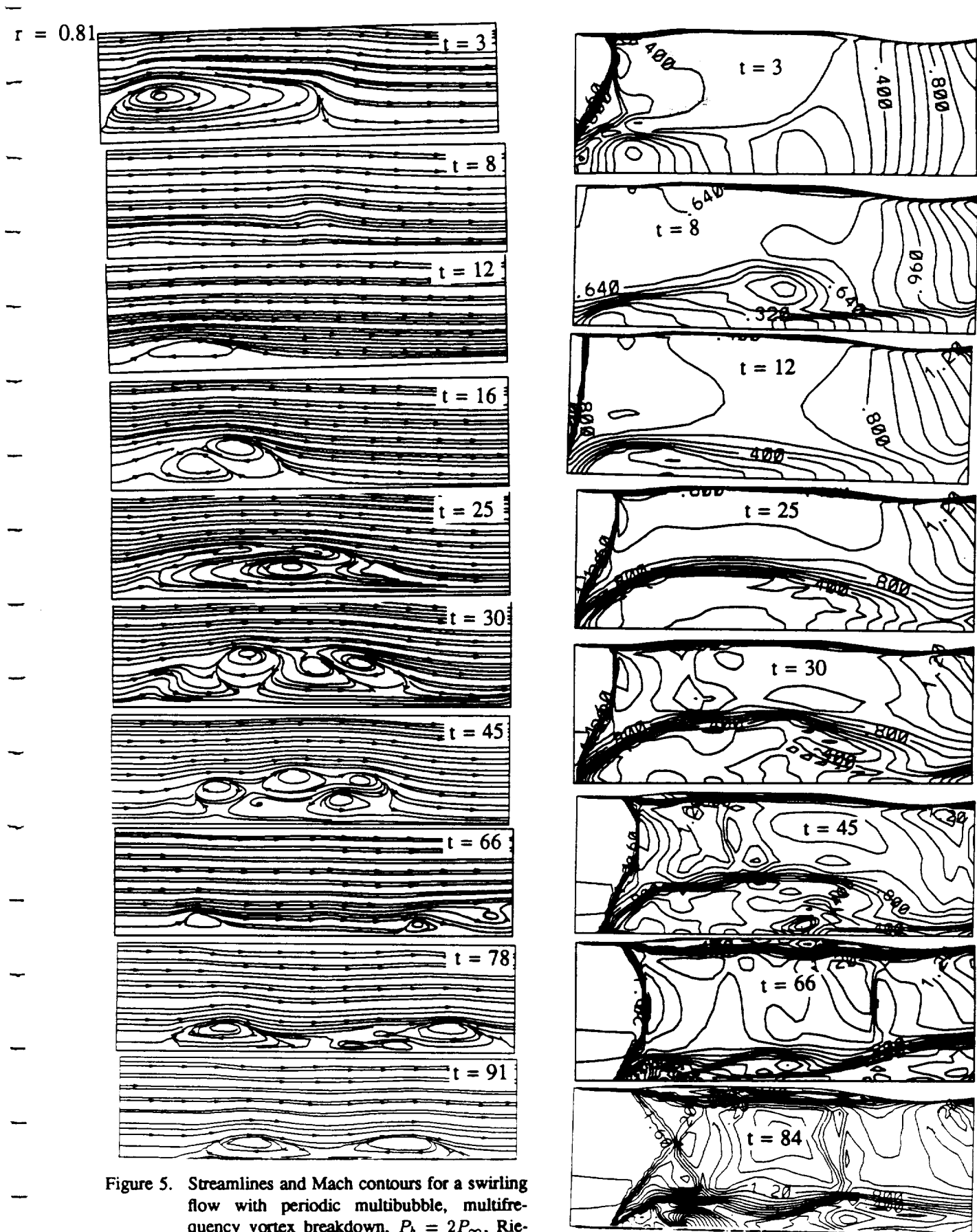


Figure 5. Streamlines and Mach contours for a swirling flow with periodic multibubble, multifrequency vortex breakdown, $P_b = 2P_\infty$, Riemann invariant B.C.

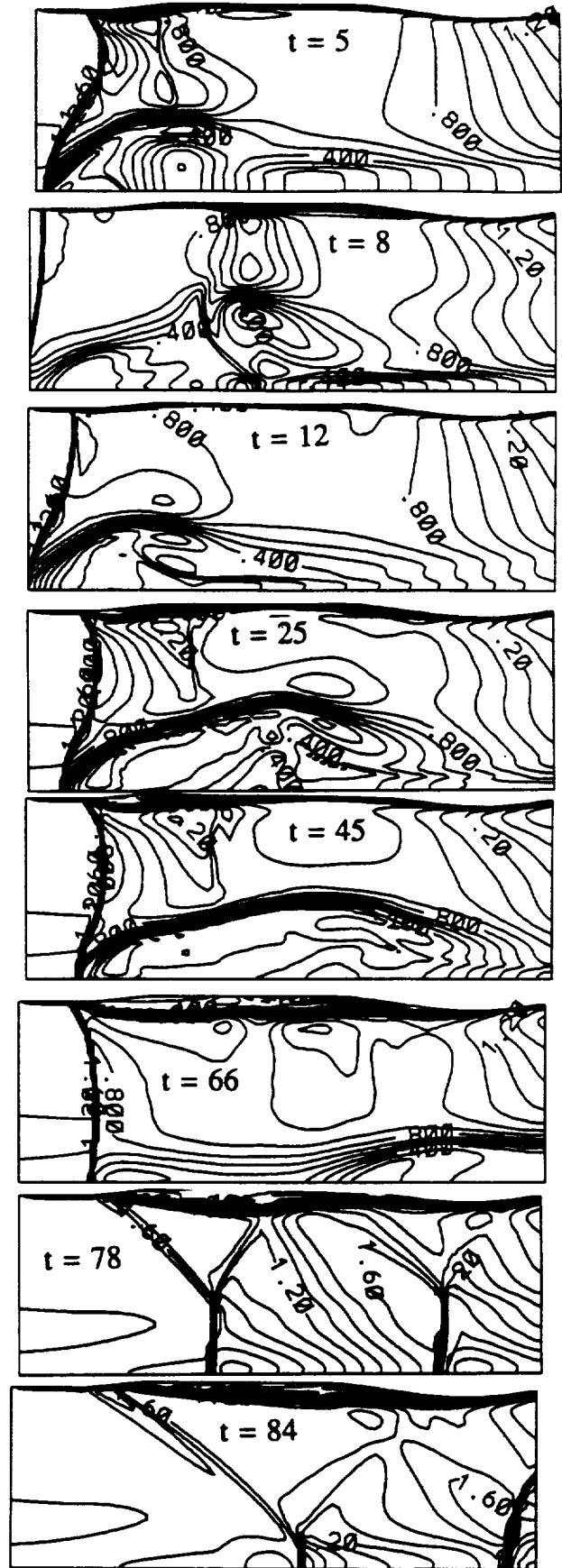
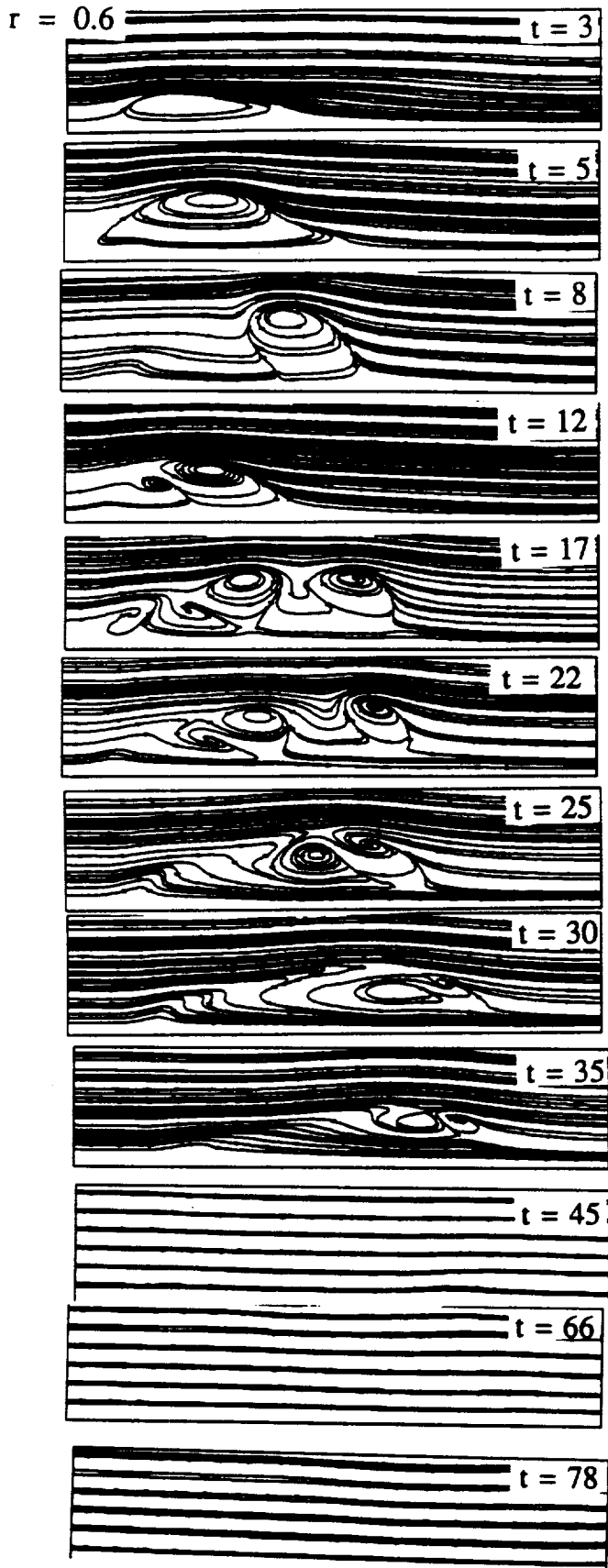


Figure 6. Streamlines and Mach contours for a swirling flow with transient multibubble vortex breakdown, $\frac{\partial p}{\partial x} = c$, Riemann invariant B.C.

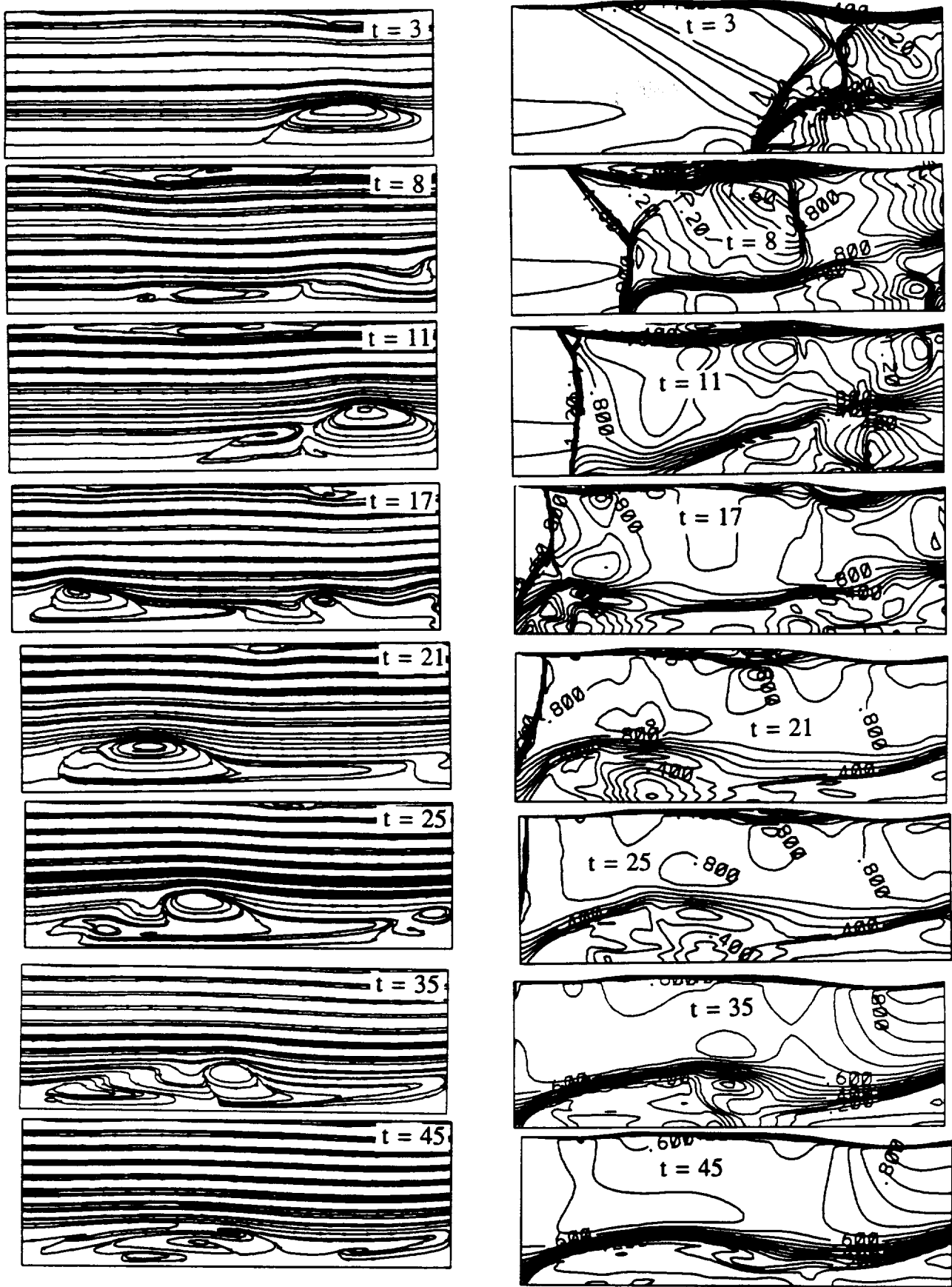


Figure 7. Streamlines and Mach contours for a swirling flow with quasi-steady multibubble vortex breakdown, downstream disk of $r = 0.333$.

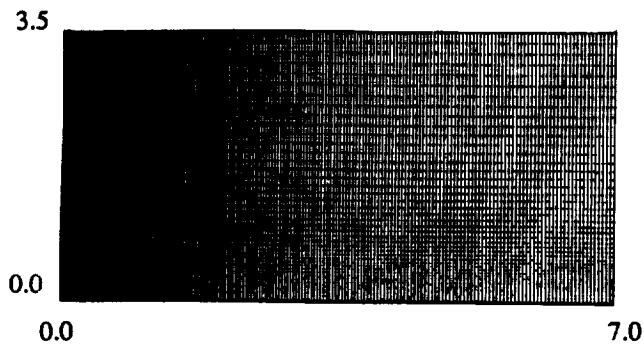


Figure 8. Typical grid for supersonic swirling jet from a nozzle, $221 \times 51 \times 2$

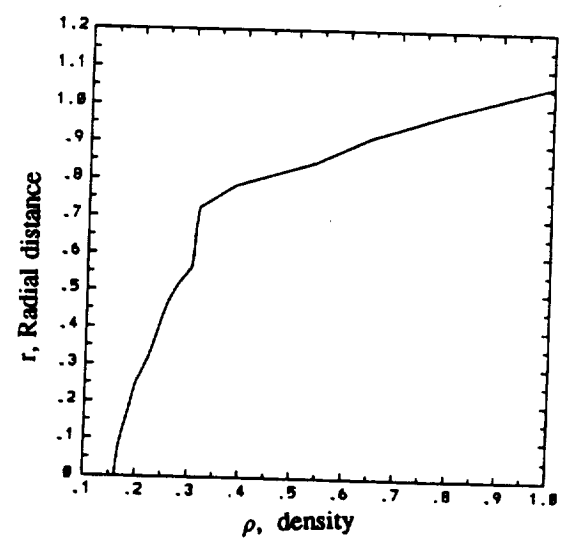
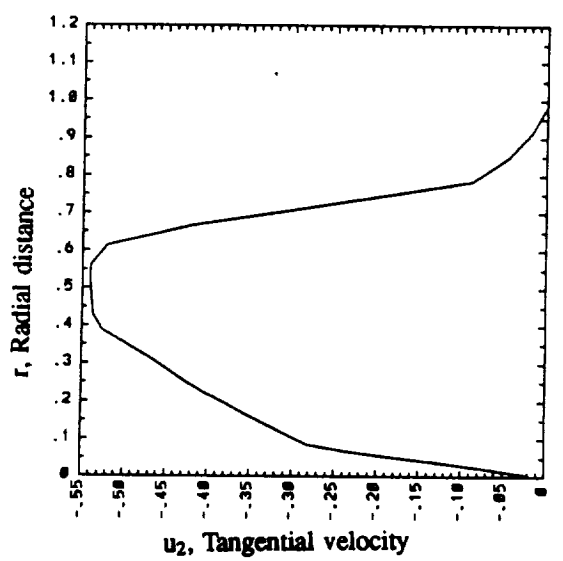
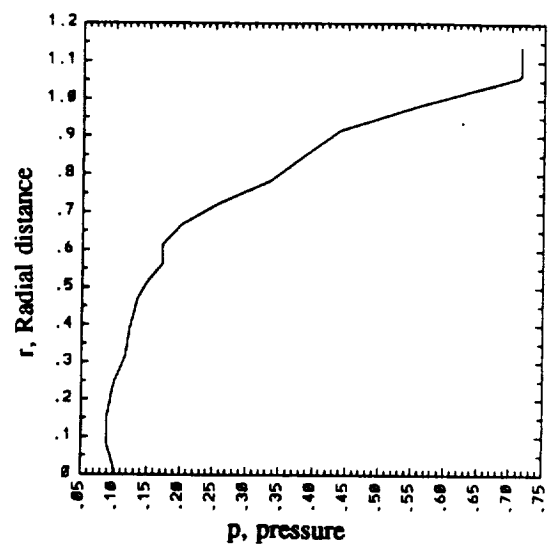
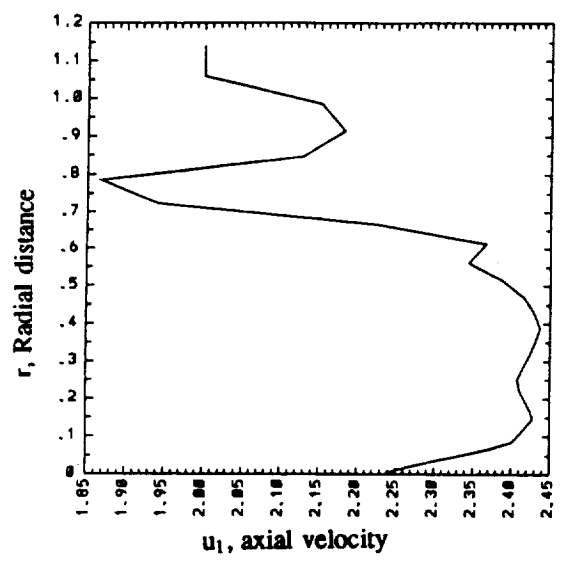
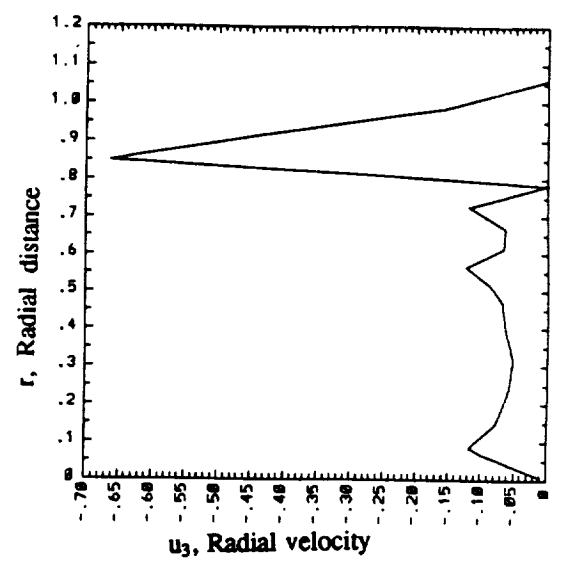


Figure 9. Quasi-axisymmetric flow profiles at $x = 0.0$ for supersonic swirling jet from a nozzle.

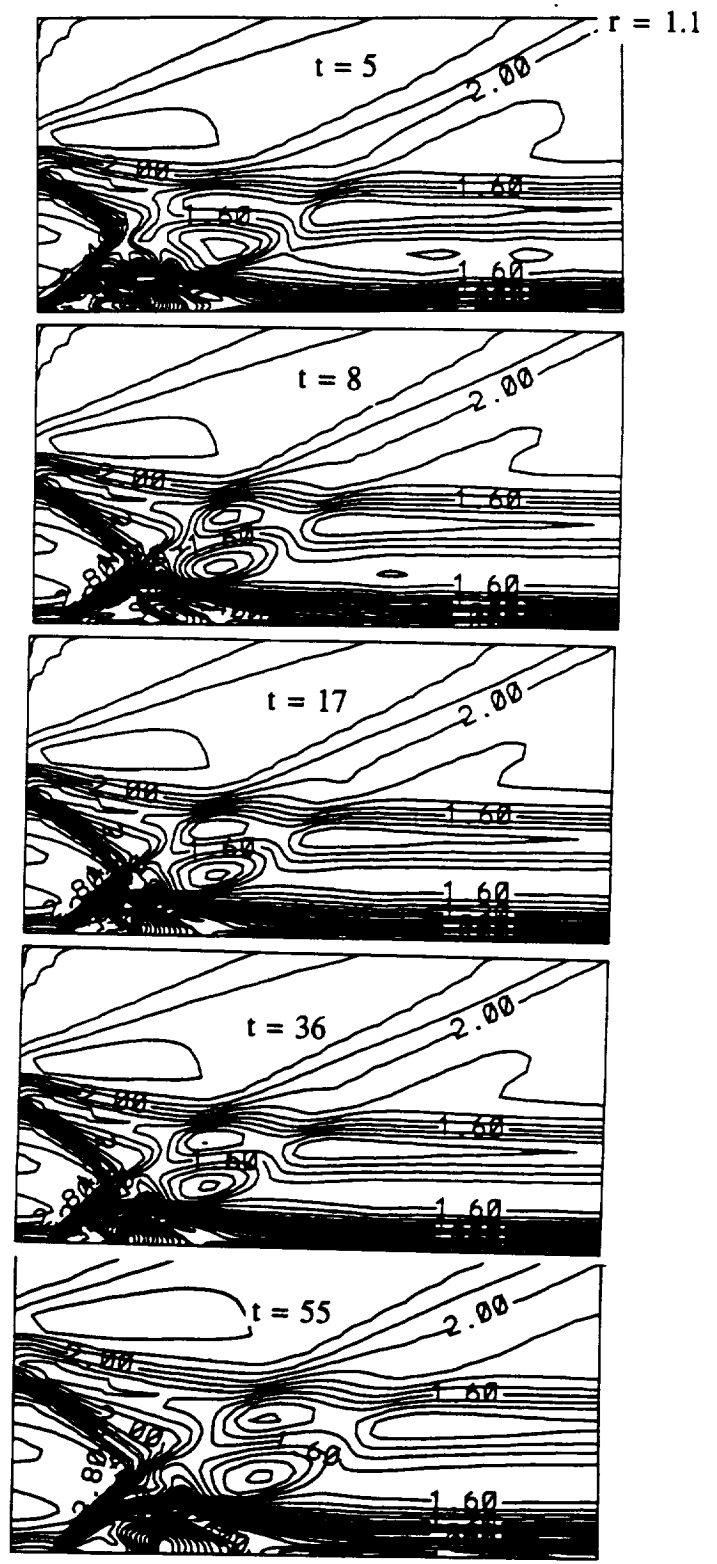
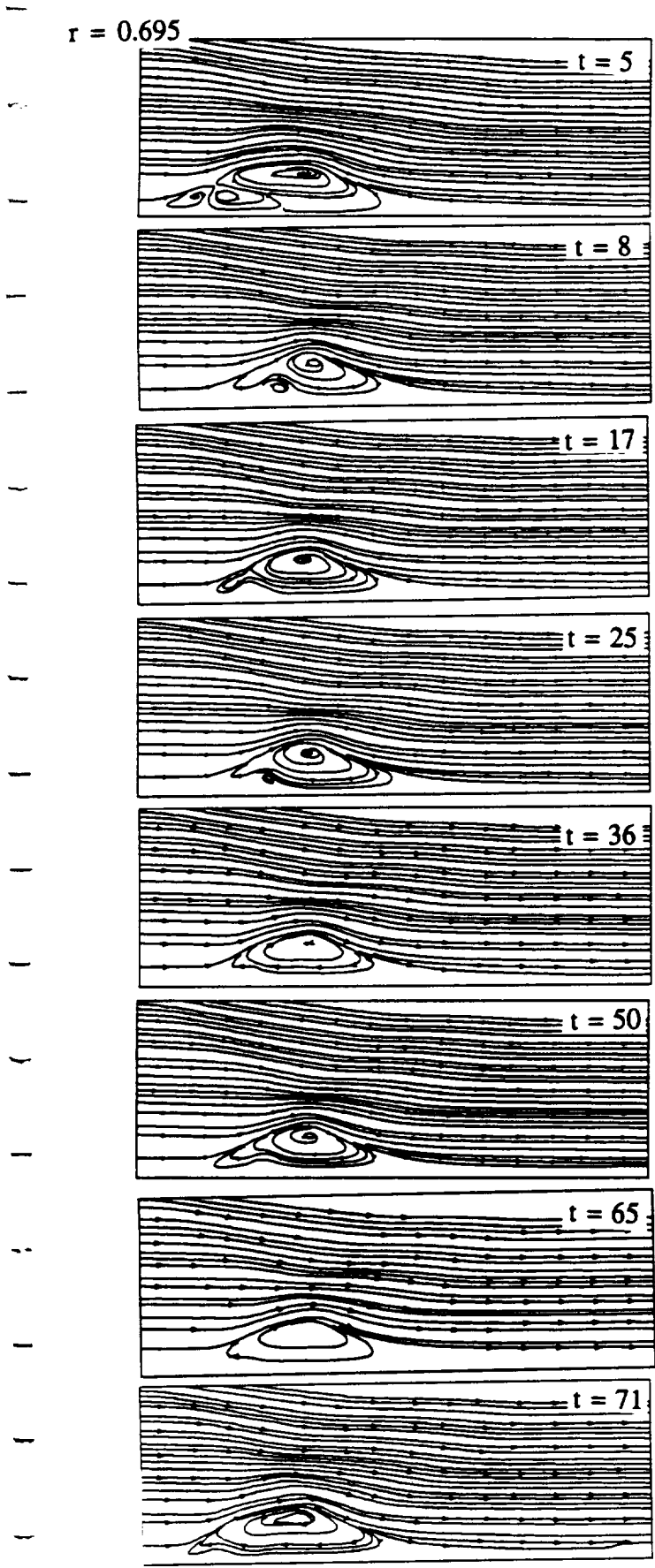


Figure 10. Streamlines and Mach contours for supersonic swirling jet from a nozzle with low-frequency almost single bubble vortex breakdown, extrapolation from interior B.C.

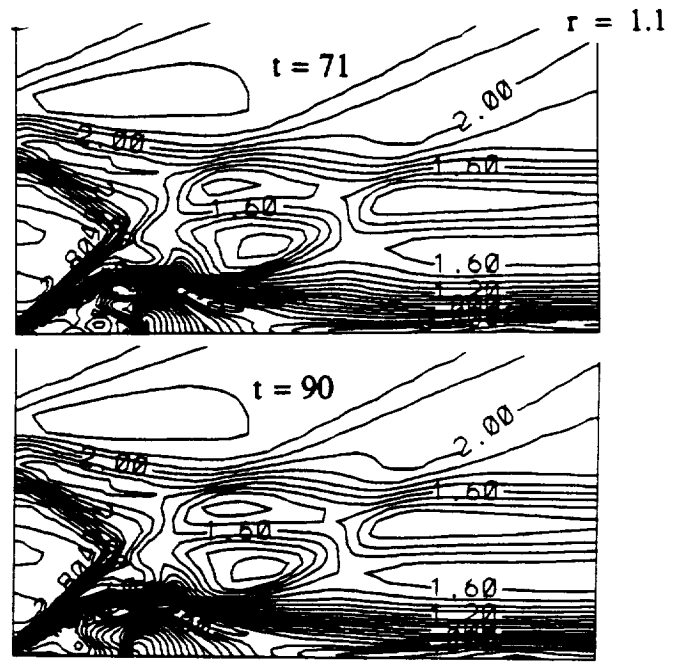
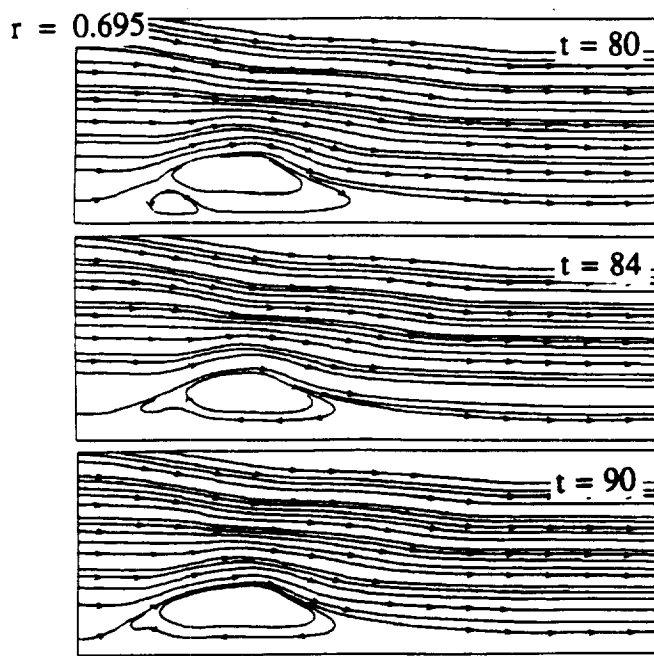


Figure 10. Continued

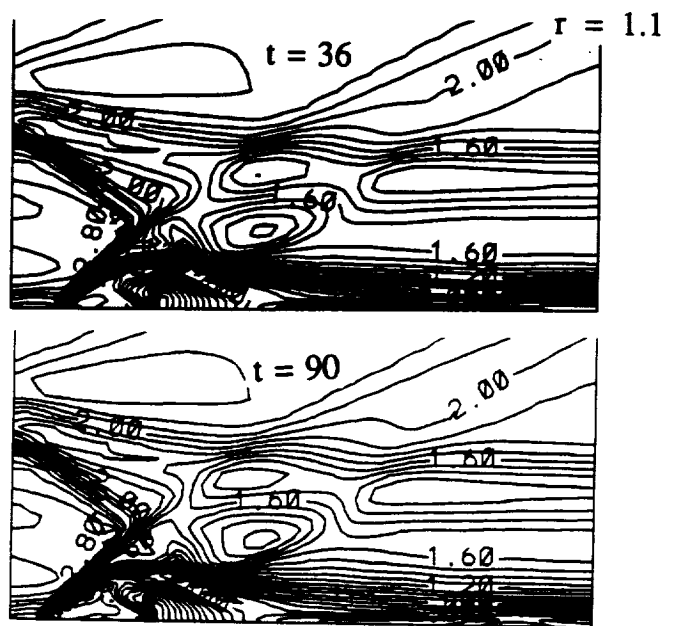
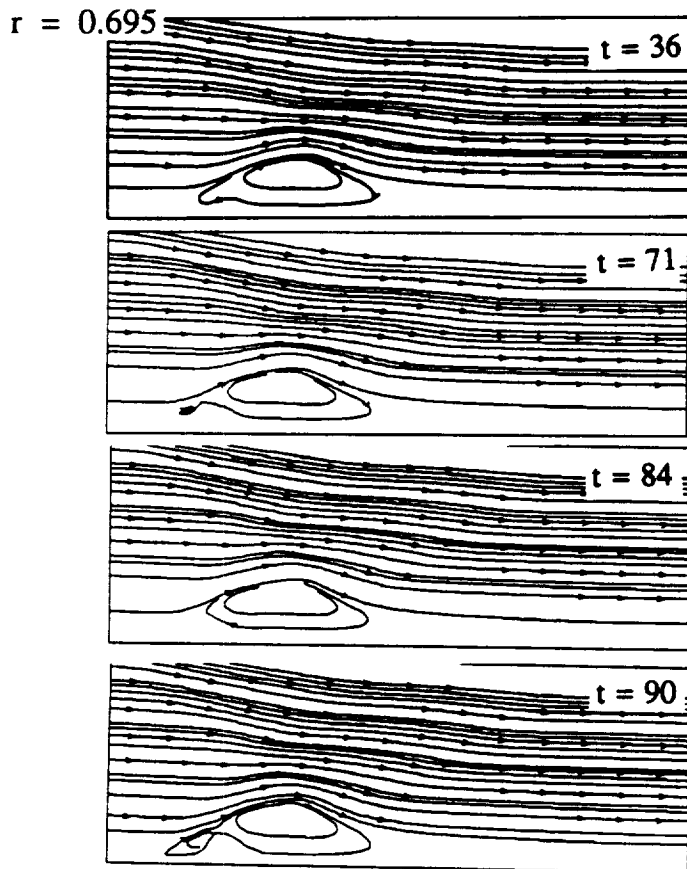
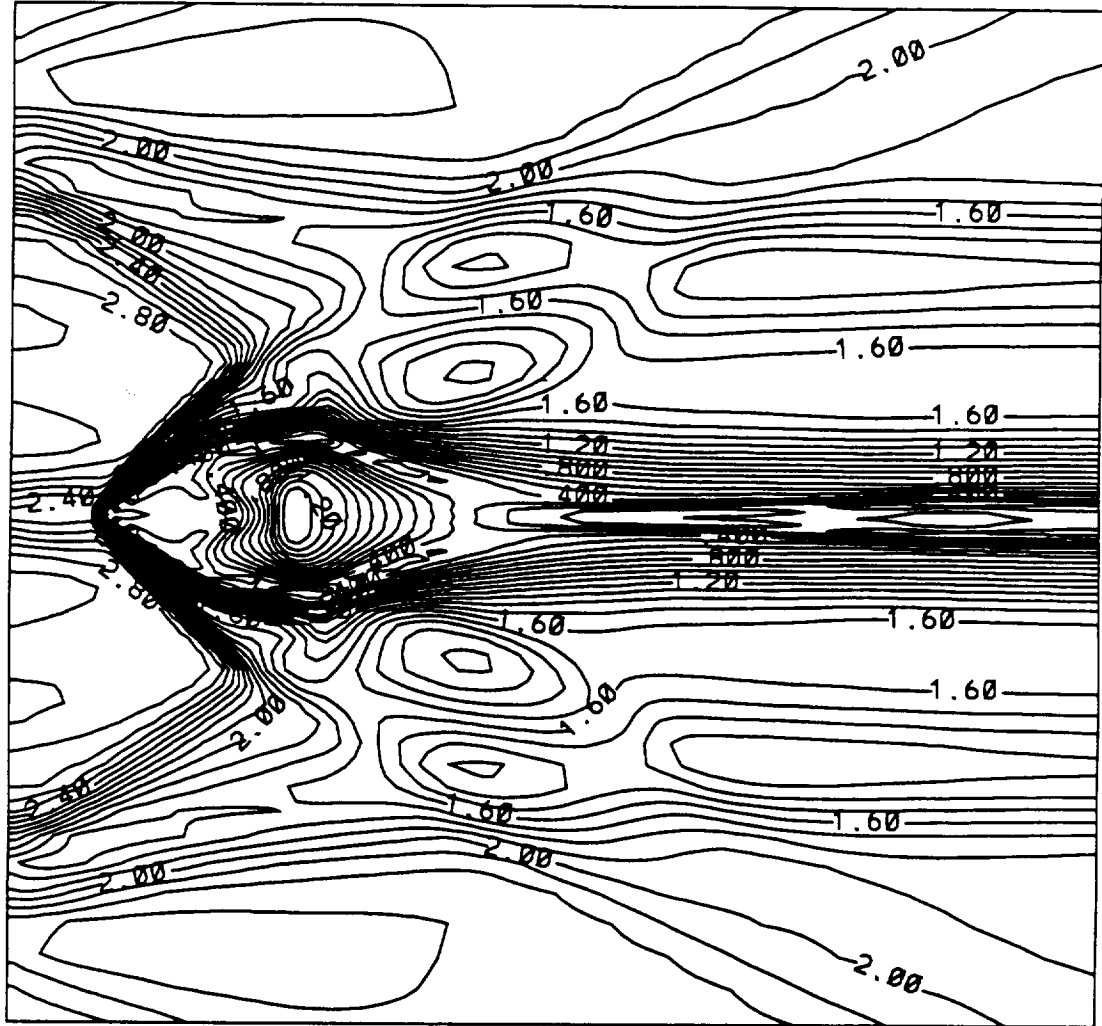


Figure 11. Streamlines and Mach contours for supersonic swirling jet from a nozzle with low frequency almost single bubble vortex breakdown, Riemann invariant B.C.

0.110E+01

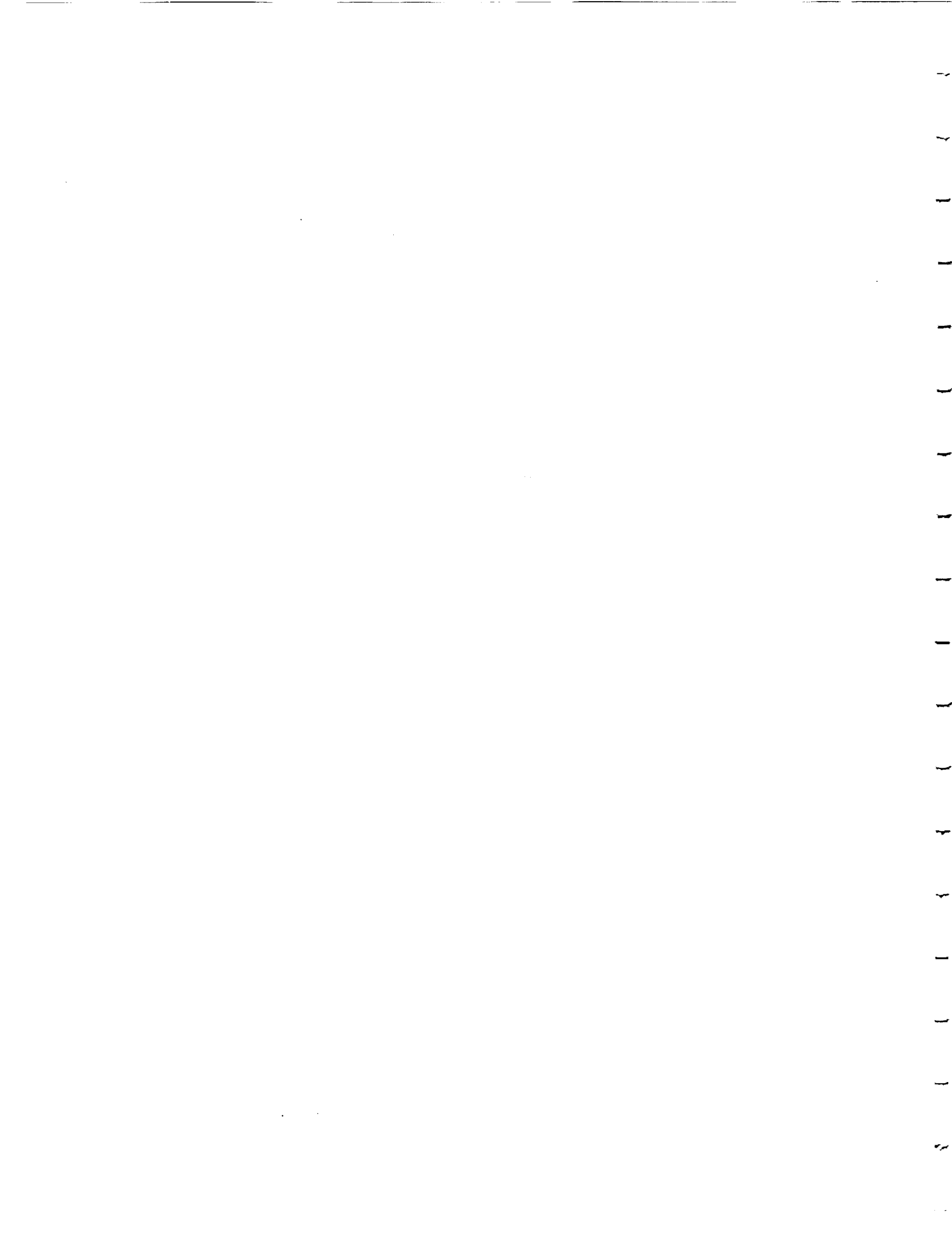


-0.110E+01

0.000E+00

0.231E+01

Figure 12. Blow-up of Mach contours at $t = 55$ for supersonic swirling jet from a nozzle with low frequency almost single bubble vortex breakdown, Riemann invariant B.C.



483674

10p

PROCEEDINGS OF THE ASIAN PACIFIC CONFERENCE ON COMPUTATIONAL
MECHANICS / HONG KONG / 11-13 DECEMBER 1991

N 93 - 14690

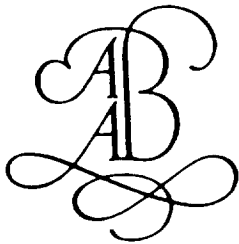
Computational Mechanics

Edited by

Y.K.CHEUNG, J.H.W.LEE & A.Y.T.LEUNG

University of Hong Kong

OFFPRINT



A.A. BALKEMA / ROTTERDAM / BROOKFIELD / 1991



Three-dimensional computational study of asymmetric flows using Navier-Stokes equations

T.-C. Wong & O.A. Kandil
Department of Mechanical Engineering and Mechanics, Old Dominion University, Norfolk, Va., USA

C.H. Liu
Theoretical Flow Physics Branch, NASA Langley Research Center, Hampton, Va., USA

ABSTRACT: The unsteady, compressible, thin-layer Navier-Stokes equations are used to obtain three-dimensional, asymmetric, vortex-flow solutions around cones and cone-cylinder configurations. The equations are solved using an implicit, upwind, flux-difference splitting, finite-volume scheme. The computational applications cover asymmetric flows around a 5° semi-apex angle cone of unit length at various Reynolds number. Next, a cylindrical afterbody of various length is added to the conical forebody to study the effect of the length of cylindrical afterbody on the flow asymmetry. All the asymmetric flow solutions are obtained by using a short-duration side-slip disturbance.

1. INTRODUCTION

The problem of asymmetric vortex-flow around slender bodies has received considerable attention by researchers in the computational fluid dynamics area [1-3] and by researchers in the experimental fluid dynamics area [4-6]. The problem is of vital importance to the dynamic stability and controllability of missiles and fighter aircraft. When flow asymmetry develops, it produces side forces, asymmetric lifting forces and corresponding yawing, rolling and pitching moments that might be larger than those available by the control system of the vehicle.

In several recent papers by the present authors [1, 2], the unsteady, thin-layer, compressible Navier-Stokes equations have been used to simulate steady and unsteady, asymmetric vortex flows, including their passive control, around cones with different cross-sectional shapes. The emphasis of these papers was extensive computational studies of the parameters which influence the asymmetric flow phenomenon and its passive control. Since the computational cost associated with the solution of three-dimensional-flow problems with reasonable flow resolution is very expensive, all the computational solutions were obtained using a locally-conical flow assumption. Such an assumption reduces the problem solution to that on two conical planes, which are in close proximity of each other, and hence it reduces the computational cost by an order of magnitude. Moreover, such solutions still provide extensive understanding of the flow physics since one can use very fine grids for reasonable flow resolution. In the present paper, we focus on the three-dimensional asymmetric flow problem using a very fine grid with high resolution near the solid boundary.

2. FORMULATION AND COMPUTATIONAL SCHEME HIGHLIGHTS

The conservative form of the dimensionless, unsteady, compressible, thin-layer Navier-Stokes equations in terms of time-independent, body-conformed coordinates are used. The implicit, upwind, flux-difference splitting finite-volume scheme is used to solve the unsteady, compressible, thin-layer Navier-Stokes equations. The scheme uses the flux-difference splitting scheme of Roe which is based on the solution of the approximate Riemann problem. Boundary conditions are explicitly implemented. At the plane of geometric symmetry, periodic conditions are used. Freestream



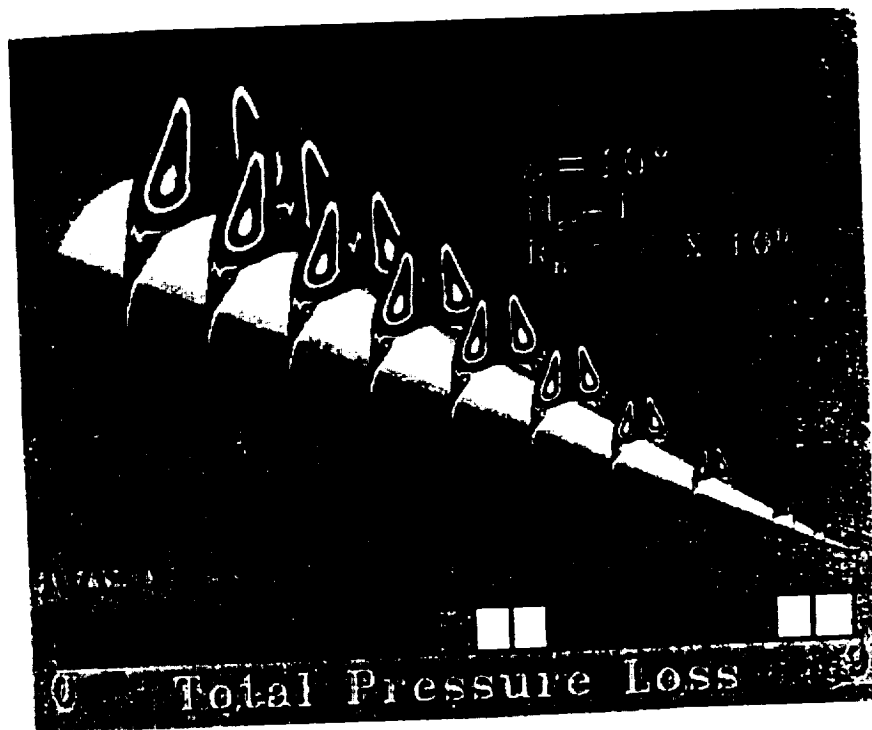


Figure 1. Asymmetric flow solution around a cone of unit length, short-duration side slip.

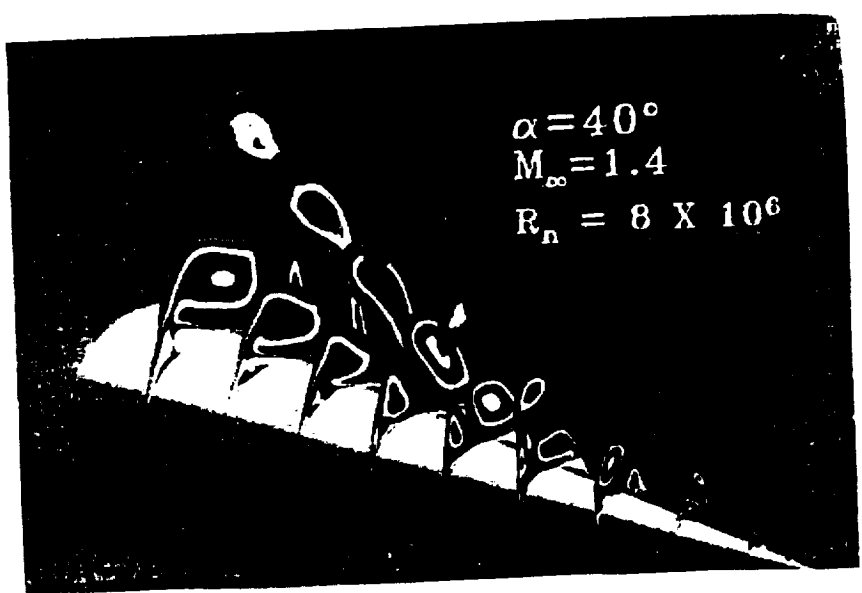


Figure 2. Asymmetric flow solution around a cone of unit length, short-duration side slip.

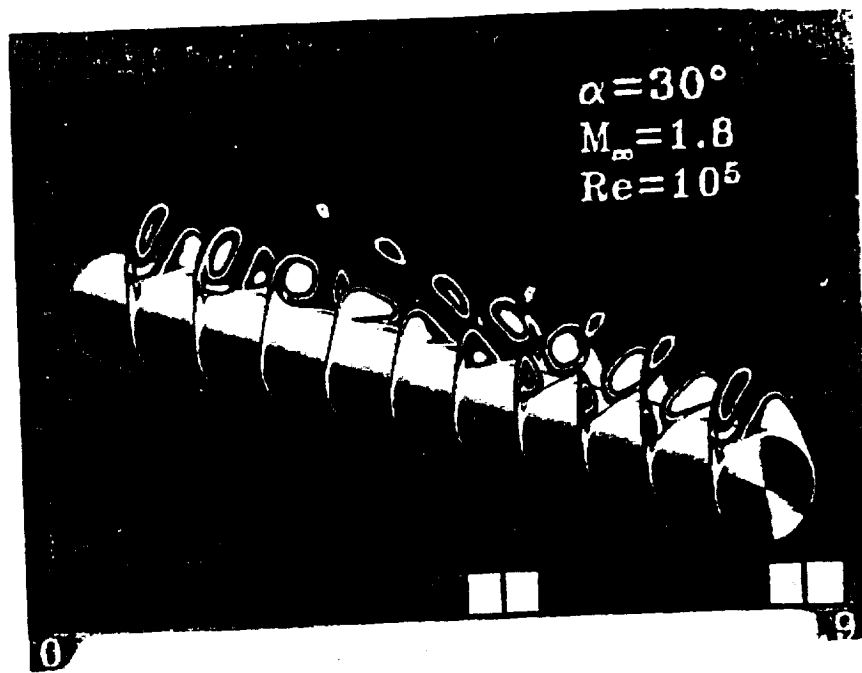


Figure 3. Unsteady asymmetric locally-conical flow solution at different time steps within one cycle (cylinder axis is a time axis), $\Delta t = 10^{-3}$.

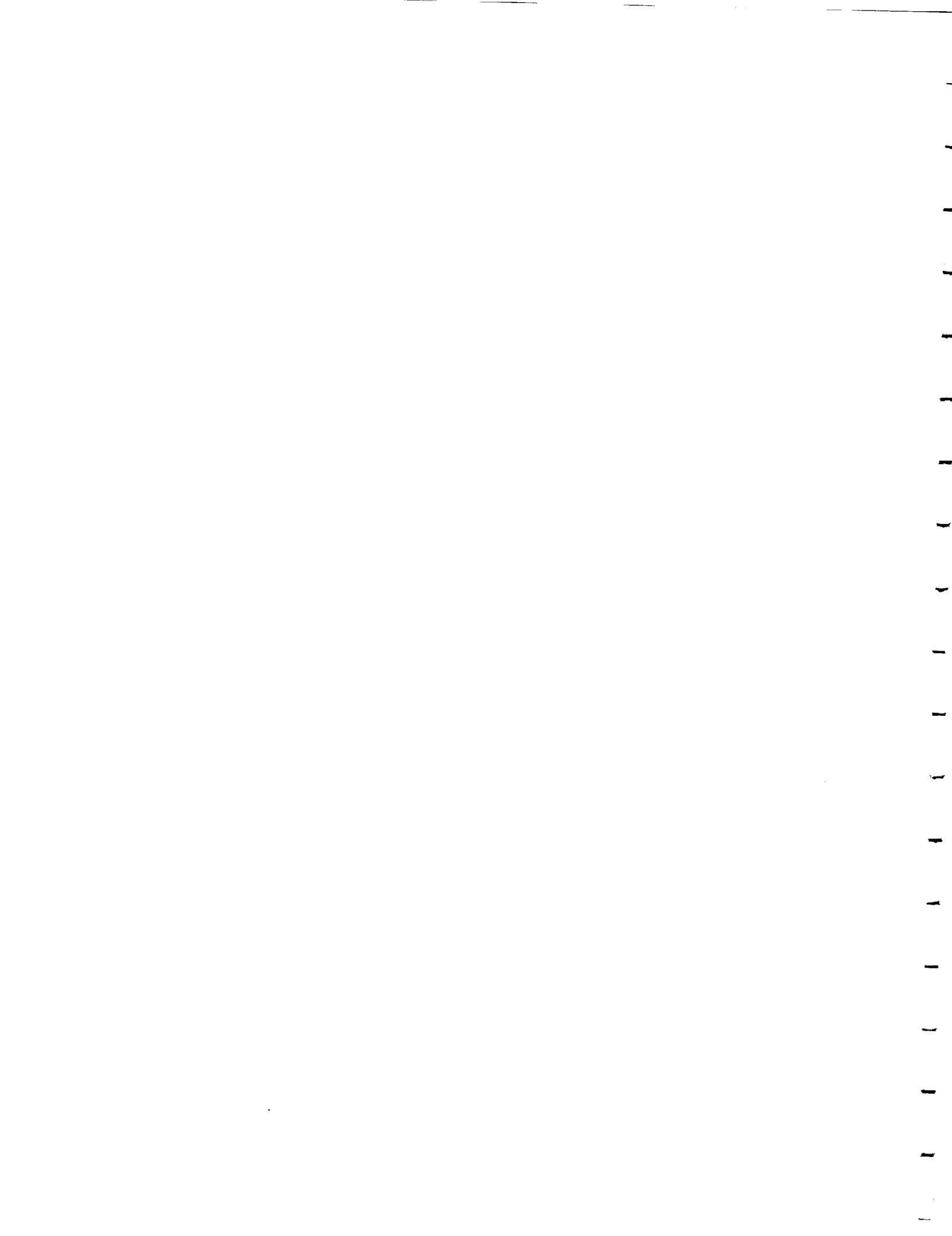
conditions are specified at the inflow boundaries and first-order extrapolation of the flow variables is used at the outflow boundaries. The conical shock enclosing the body is captured as part of the solution. On the solid boundary, the no-slip and no-penetration conditions are enforced and the normal pressure gradient is set equal to zero. For the temperature, the adiabatic boundary condition is enforced at the solid boundary. The initial conditions correspond to the freestream conditions with the no-slip and no-penetration conditions on the solid boundary.

3. COMPUTATIONAL APPLICATIONS AND DISCUSSIONS

Circular Cone

A 5° -semi-apex angle circular cone of unit length (cone length is the characteristic length) is considered. This is the same circular cone which was considered by the authors in Ref. 1 for the locally-conical flow solutions. A three-dimensional grid of $161 \times 81 \times 65$ in the wrap around, normal and axial directions, respectively, is generated by using a modified Joukowski transformation at axial stations. The grid is clustered algebraically in the normal direction of the body using a geometric series with minimum grid spacing of 10^{-6} at the cone vertex and 10^{-5} at the axial station of unit length. The cross-flow grid size of 161×81 is the same grid size which was used for the locally-conical flow solutions of Ref. 1.

With the flow conditions set at $\alpha = 20^\circ$, $M_\infty = 1.8$ and $Re = 10^5$, which are the same conditions as those of the locally-conical flow of Ref. 1, the three-dimensional solution produces a symmetric steady flow, unlike the locally-conical solution which produces asymmetric steady flow. Next, the search is directed at obtaining asymmetric flow solutions for the three-dimensional cone flow. In Fig. 1, we show the solution in the form of total-pressure loss for the same cone at $\alpha = 40^\circ$, $M_\infty = 1.4$ and $Re = 4 \times 10^6$. It is seen that the solution is asymmetric and is nearly self-similar over a long axial distance of the cone length. This solution is obtained using a short-duration side-slip



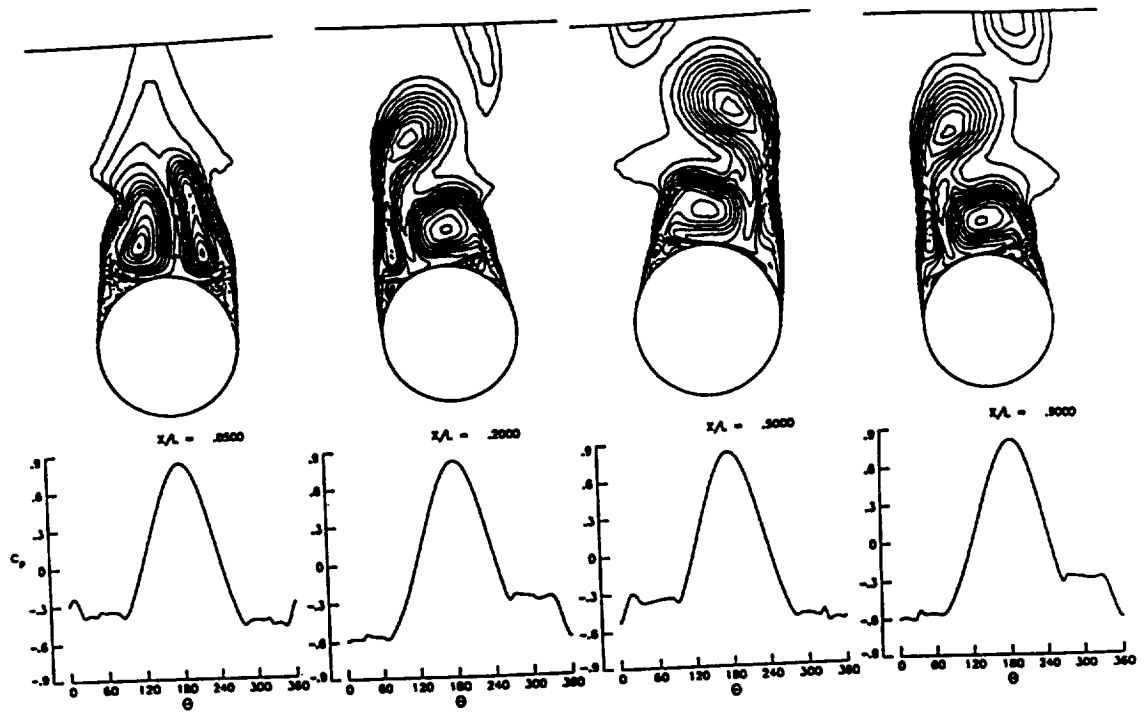


Figure 4. Total-pressure-loss contours and surface-pressure coefficient at different axial stations, a cone of unit length, $\alpha = 40^\circ$, $M_\infty = 1.4$, $Re = 8 \times 10^6$.

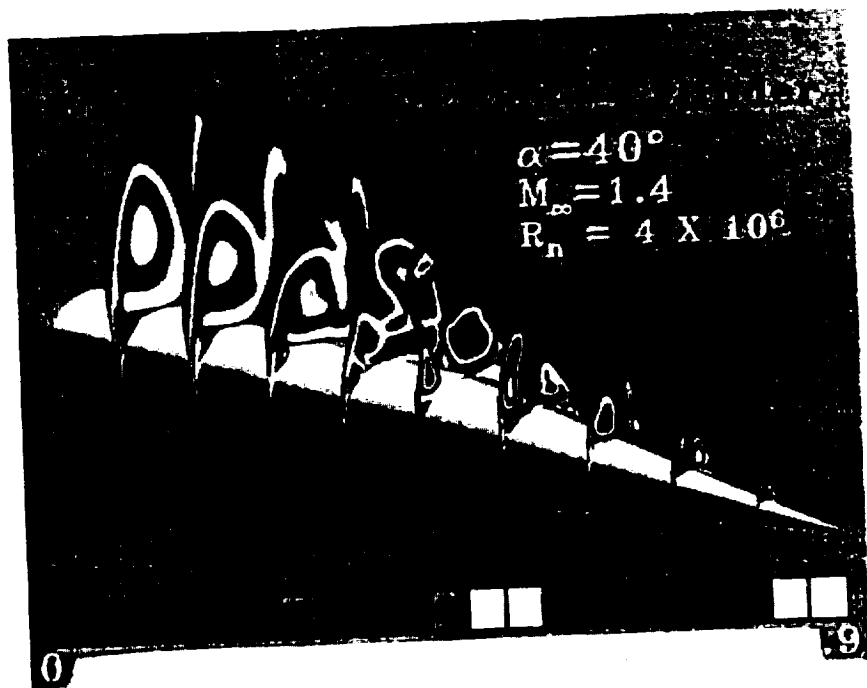
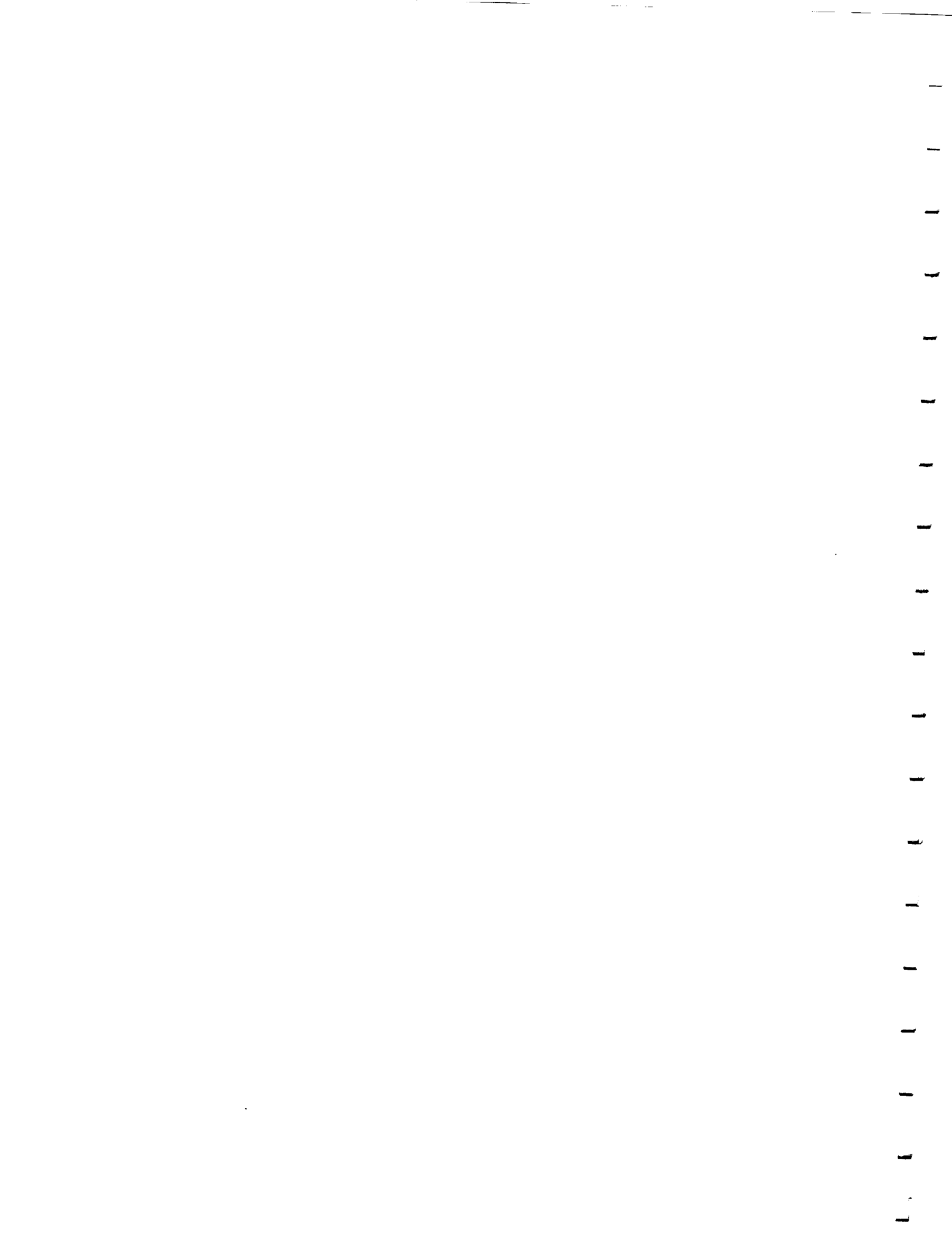


Figure 5. Asymmetric flow solution around a cone-cylinder configuration 1:1.



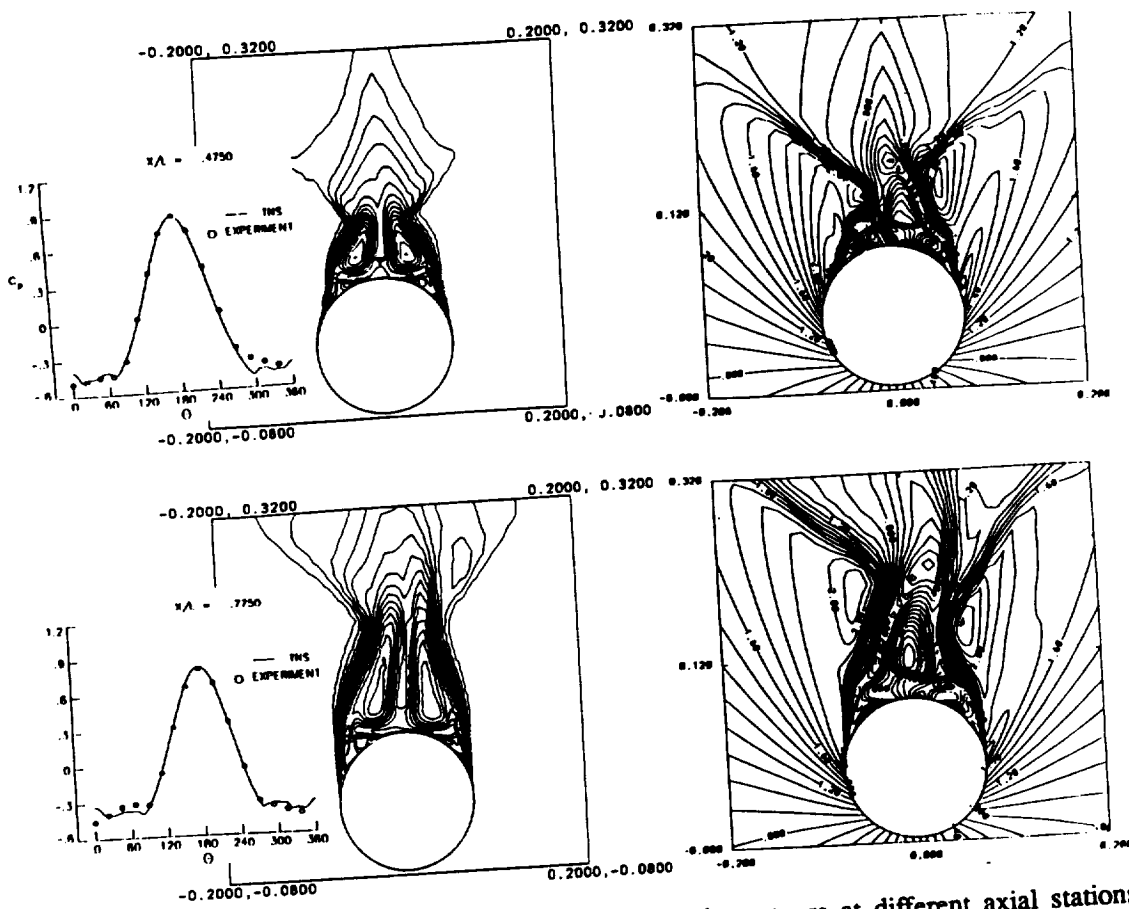


Figure 6. Surface pressure, total-pressure-loss and Mach contours at different axial stations, cone-cylinder configuration 0.5:0.5, $\alpha = 46.1^\circ$, $M_\infty = 1.6$, $Re = 6.6 \times 10^6$, comparison with experimental data (Ref. 5).

disturbance. When the residual error drops four orders of magnitude, a 2° -side-slip disturbance is applied for 100 iteration steps, then it is removed. Thereafter, the pseudo time stepping is continued until the residual error drops again four to five orders of magnitude and a stable asymmetric solution is obtained.

Figure 2 shows the total-pressure-loss solution for the same cone for a higher Reynolds number, $Re = 8 \times 10^6$. The asymmetry of the vortex flow becomes much stronger as compared with the previous case. The flow asymmetry of this case changes sides along the axial distance and a complete wave length of flow asymmetry is formed between the third and ninth cross-flow planes. Strong spatially shed vortices exist in the flowfield. This solution is qualitatively similar to the unsteady asymmetric locally-conical flow solution at different time steps [1] which is depicted in Fig. 3 on a cylinder with the axis of the cylinder representing time. The behavior of the flow asymmetry over one period in Fig. 3 is qualitatively similar to the behavior of the flow asymmetry over one wave length in Fig. 2. Figure 4 shows the total-pressure-loss contours and surface-pressure coefficient at different axial stations for the case of Fig. 2. The solutions at axial stations of $X/L = 0.2$ and 0.9 are almost the same (the total pressure losses are drawn to a scale given by the ratio of the circular diameters at $X/L = 1$ station and the local axial station). The flow asymmetry between these two stations represents a full wave length.



Circular Cone-Cylinder Configurations

To address the issue of the effect of cylindrical afterbody length on the flow asymmetry a cylindrical afterbody of different lengths is added to the unit-length conical forebody. The flow around the resulting cone-cylinder configurations is solved with the flow conditions of $\alpha = 40^\circ$, $M_\infty = 1.4$ and $Re = 4 \times 10^6$, which are the same flow conditions of the isolated unit-length cone of Fig. 1. The lengths of the cylindrical afterbody are chosen as 1, 1.5 and 2. The source of flow disturbance is the same short-duration 2° -side-slip disturbance. For the cone-cylinder configuration of 1:1 (cone length: cylinder length), Fig. 5 shows a very strong asymmetric flow on the cone, in comparison with the flow asymmetry of the isolated cone of Fig. 1, and on the cylindrical afterbody as well. It should be noted that inside the conical shock surrounding the cone-cylinder configuration, subsonic flow regions exist and hence the downstream cylindrical-afterbody boundary has an upstream effect. The cylindrical afterbody has dual effects which increases the flow asymmetry; the first is due to the cone-cylinder juncture and the second is due to the increase of the local angle of attack of the leeward side of the cylinder. Both of these effects increase the spatial growth of the flow asymmetry. For the cone-cylinder configurations of 1:1.5 and 1:2, the asymmetry is strong and the flow becomes unsteady [Ref. 3].

Next, we show a comparison of the computed results with available experimental data. For this purpose, we consider the cone-cylinder configuration of 0.5:0.5 which was experimentally tested by Landrum⁵. The configuration angle of attack is 46.1° , the Mach number is 1.6 and the Reynolds number based on the total configuration length (cone + cylinder) is 6.6×10^6 . The cone semi-apex angle is 9.5° . The problem is solved using a grid size of $161 \times 81 \times 65$. Figure 6 shows the surface-pressure coefficient along with the experimental data, the total-pressure-loss contours and the total Mach-number contours at the axial stations of 0.475 and 0.775. The computed and measured surface-pressure coefficient are in good agreement on all the axial stations. The asymmetry changes sides in the downstream direction as it is shown by the results of axial stations at 0.475 and 0.775. This comparison conclusively validates our computed results and the grid size.

4. CONCLUDING REMARKS

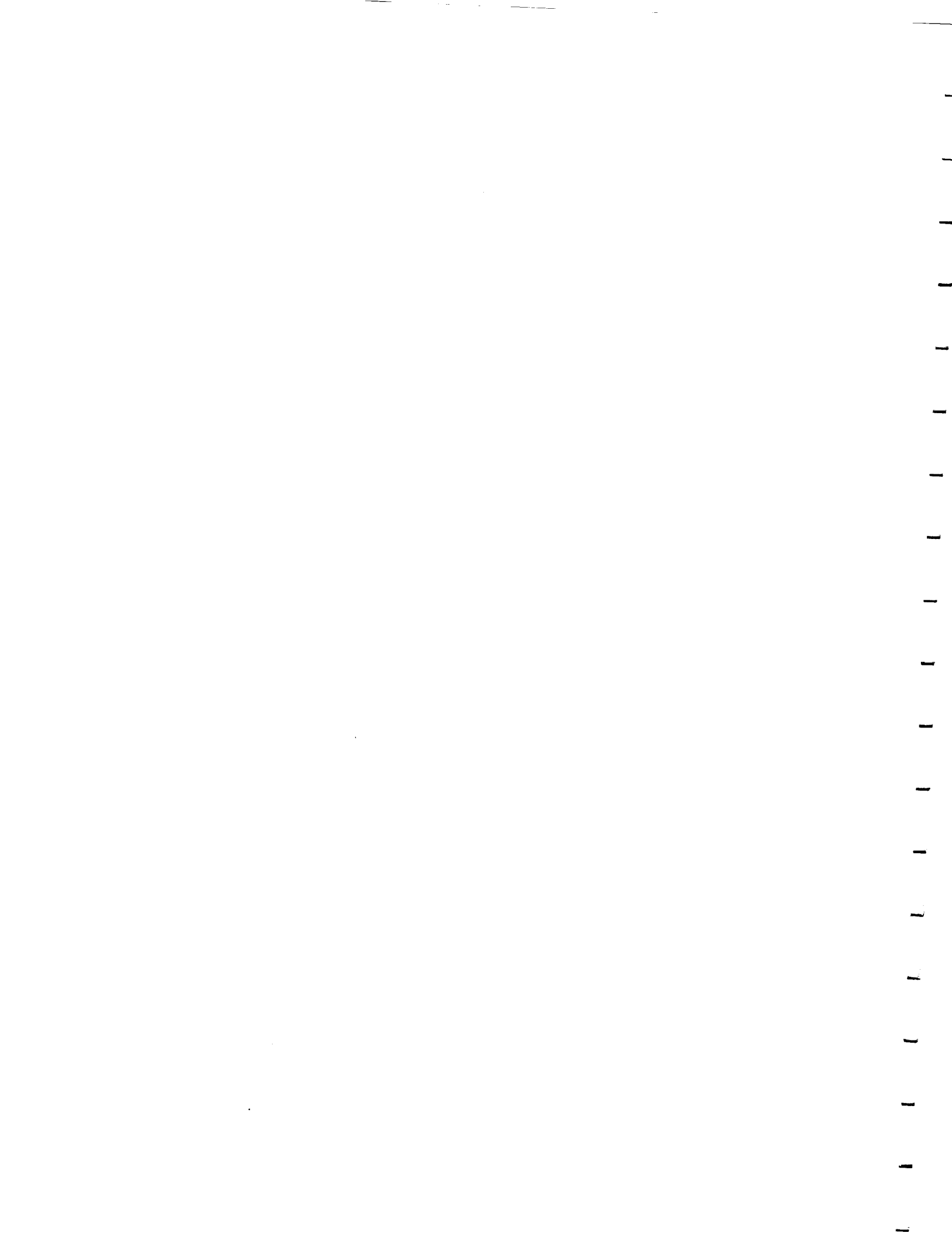
Several important issues are addressed in the present study. By increasing the flow Reynolds number for flows around a cone, we have shown that the flow asymmetry becomes strong and changes sides in the downstream direction. For the high-Reynolds flows, the spatial asymmetric flow develops in a wavy manner, which is qualitatively similar to the temporal asymmetric flow development of the locally-conical solutions, where the flow asymmetry develops in a periodic manner. By adding a cylindrical afterbody to the conical forebody, the flow asymmetry becomes stronger in comparison with that of the isolated cone. As the length of the cylindrical afterbody is increased, the flow asymmetry becomes stronger and unsteady. Finally, the computed results and grid used are conclusively validated.

ACKNOWLEDGEMENT

This research work is supported by the NASA Langley Research Center under Grant No. NAG-1-994. The computations have been carried out using the CRAY 2 (Voyager) of the NASA Langley Research Center.

REFERENCES

- [1] Kandil, O. A., Wong, T-C. and Liu, C. H., (1990) "Prediction of Steady and Unsteady Asymmetric Vortical Flow Around Cones," AIAA 90-0598. Also to appear in AIAA Journal, Vol. 29, No. 9, 1991.



- [2] Kandil, O. A., Wong, T-C. and Liu, C. H., (1990) "Numerical Simulation of Steady and Unsteady Asymmetric Vortical Flows," ASME Symposium on Non-Steady Fluid Dynamics, FED-Vol. 92, Toronto, Canada, pp. 99-108. To appear in the Journal of Fluids and Structures, 1991.
- [3] Kandil, O. A., Wong, T. C., and Liu, C. H., (1991) "Three-Dimensional Navier-Stokes Asymmetric Solution for Cones-Cylinder Configurations," AIAA 91-1732.
- [4] Keener, E. R. and Chapman, G. R., (1977) "Similarity in Vortex Asymmetries Over Slender Bodies and Wings," AIAA Journal, Vol. 15, No. 9, pp. 1370-1372.
- [5] Landrum, E. J., (1977) "Wind-Tunnel Pressure Data at Mach Numbers from 1.6 to 4.63 for a Series of Bodies of Revolution at Angles of Attack from -4° to 60° ," NASA Technical Memorandum, NASA TM-X-3558.
- [6] Lamont, P. J., (1980) "Pressure Around an Inclined Ogive Cylinder with Laminar, Transitional, or Turbulent Separation," AIAA Journal, Vol. 20, No. 11, pp. 1492-1499.



1720-1111
2-A-10-12

Prediction of Steady and Unsteady Asymmetric Vortical Flows Around Circular Cones

O. A. Kandil, T.-C. Wong, C. H. Liu

Reprinted from

AIAA Journal

Volume 29, Number 12, December 1991, Pages 2169-2178



A publication of the
American Institute of Aeronautics and Astronautics, Inc.
The Aerospace Center, 370 L'Enfant Promenade, SW
Washington, DC 20024-2518



Prediction of Steady and Unsteady Asymmetric Vortical Flows Around Circular Cones

Osama A. Kandil* and Tin-Chee Wong†
Old Dominion University, Norfolk, Virginia 23529

and
 C. H. Liu‡

NASA Langley Research Center, Hampton, Virginia 23665

Steady and unsteady, supersonic asymmetric vortical flows and their passive control around circular cones are considered in this paper. These problems are formulated by using the unsteady, compressible, single and double, thin-layer, Navier-Stokes equations. The equations are solved by using an implicit, upwind, flux-difference splitting, finite-volume scheme, either in a pseudotime stepping or in an accurate time stepping. An implicit, approximately factored, central-difference, finite-volume scheme has also been used to validate some applications of the upwind scheme. Local conical flows are assumed for the computational applications presented in this paper. Steady asymmetric vortical flows have been predicted by using random and controlled disturbances. Unsteady asymmetric vortex-shedding flows have also been predicted, for the first time, using time-accurate solutions with two different computational schemes. Control of flow asymmetry has been demonstrated computationally by inserting a vertical fin in the leeward plane of geometric symmetry.

Introduction

IN the high angle of attack (AOA) range, the separated vortical flow from forebodies of missiles and fighter aircraft may become asymmetric, producing large abrupt changes in force and moment coefficients. These abrupt changes may exceed the available controllability and lead to missile and aircraft spin. Experimental studies of several researchers¹⁻¹¹ have identified four distinct flow patterns about slender bodies through a wide AOA range and zero-degree side slip. The first pattern develops in the very small AOA range, where the flow is attached and the axial flow is dominant. In the intermediate AOA range, the crossflow becomes of the same order of magnitude as that of the axial flow, the flow separates on the leeward side, and a symmetric vortex pair is formed. As the AOA reaches a high range, the symmetric vortex pair becomes asymmetric, and the flows stay steady. For this asymmetric vortex-flow pattern to occur, it is not a necessary condition to have asymmetric separation lines on the leeward side of the body. The fourth flow pattern develops at a very high AOA range, where asymmetric time-dependent vortex shedding occurs either randomly or periodically, similar to the von Kármán vortex street in two-dimensional flows around cylinders.

For isolated pointed forebodies, the onset of vortical flow asymmetry occurs when the relative incidence (ratio of AOA to nose semi-apex angle) exceeds a certain value; e.g., for a pointed circular cone, the relative incidence must be higher

than two. However, the relative incidence value is not the only determinable parameter for the onset of vortical flow asymmetry. The onset of vortical flow asymmetry is also a function of the freestream Mach number and Reynolds number and the shape of the body cross-sectional area as well. Asymmetric vortical flow and vortex shedding have also been documented for delta wings^{12,13} at very high relative incidences and low subsonic regimes.

For the critical values of the relative incidence, Mach number and Reynolds number, and the shape of cross-sectional area, the symmetric flow is unstable. Any small flow disturbance in the form of a transient side slip, acoustic disturbance, or similar source of disturbance causes flow instability that produces, depending on the flow conditions, either a steady asymmetric vortical flow or an unsteady asymmetric flow with vortex shedding. In this paper, we present an extensive computational study of the steady asymmetric vortical flow and unsteady asymmetric flow with vortex shedding to address some of the influential parameters as the relative incidence and Mach number.

As the experimental work shows, the mechanisms that lead to asymmetric vortex wake are not well understood. However, two mechanisms have been established for explaining the evolution of flow asymmetry.^{5,6,9,10} The first mechanism applies to both laminar and fully turbulent flows. It suggests that flow asymmetry occurs due to instability of the velocity profiles in the vicinity of the enclosing saddle point that exists in the crossflow planes above the body primary vortices.^{2,7,10} The second mechanism suggests that flow asymmetry occurs due to asymmetric transition of the boundary-layer flow either at the nose in the axial direction or on both sides of the body in the crossflow planes. For pointed slender bodies, the first mechanism produces higher side forces than those produced by the second mechanism. These results have conclusively been shown through the experimental work of Lamont^{8,9} on 2-diam and 3.5-diam tangent ogive noses with cylindrical afterbody. An extensive review of the steady and unsteady vortex-induced asymmetric loads is given by Ericsson and Reding in Ref. 11.

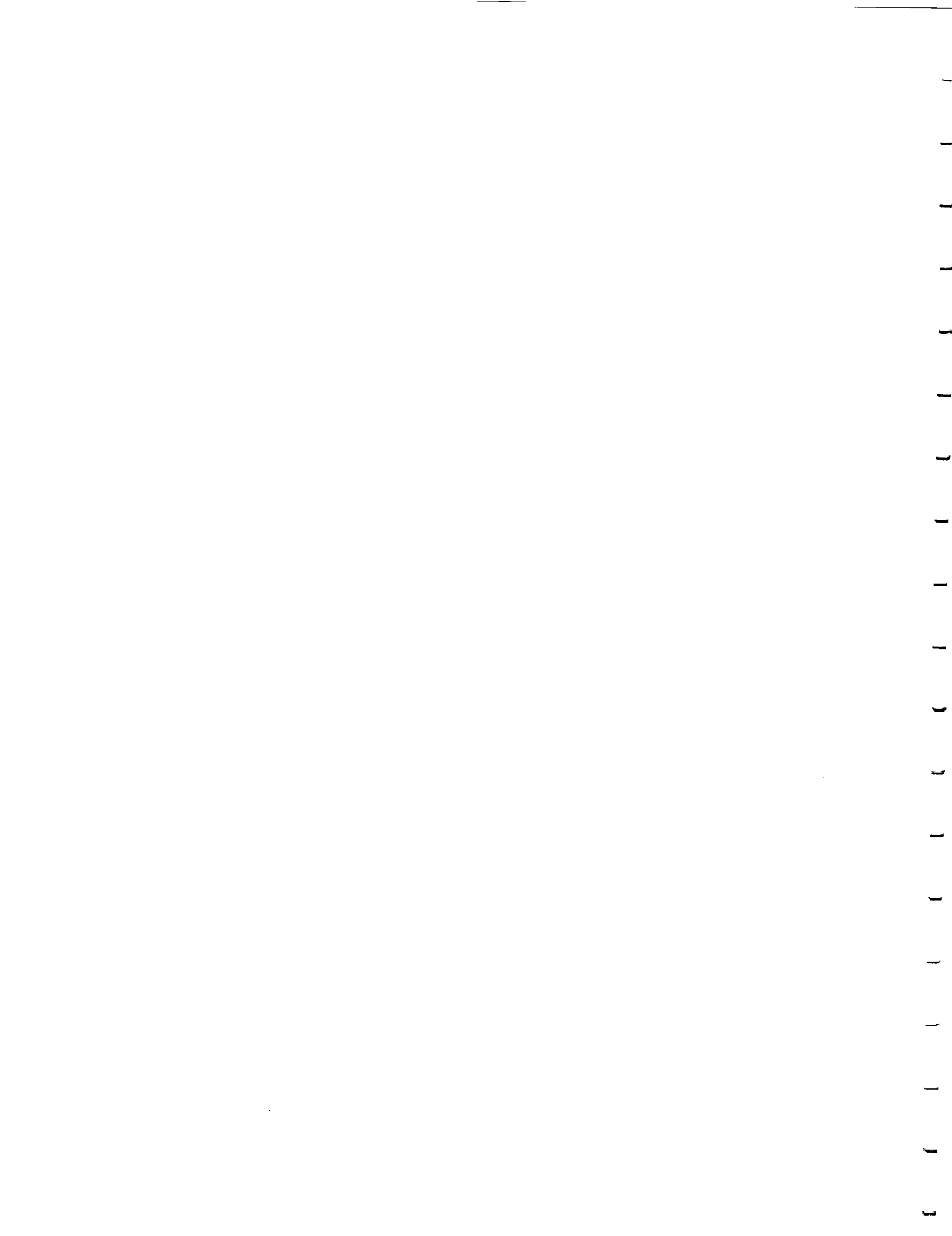
Several attempts have been carried out to computationally simulate asymmetric vortical flows around slender bodies of revolution. Early computational work on conical flows has been published in Refs. 14 and 15. Graham and Hankey¹⁶ presented the first three-dimensional Navier-Stokes computations for asymmetric flow around a cone-cylinder body at 30-

Received Jan. 2, 1990; presented as Paper 90-0598 at the AIAA 28th Aerospace Sciences Meeting, Reno, NV, Jan. 8-11, 1990; revision received Sept. 13, 1990; accepted for publication Sept. 17, 1990. Copyright © 1990 by the American Institute of Aeronautics and Astronautics, Inc. No copyright is asserted in the United States under Title 17, U.S. Code. The U.S. Government has a royalty-free license to exercise all rights under the copyright claimed herein for Governmental purposes. All other rights are reserved by the copyright owner.

*Professor and Eminent Scholar, Department of Mechanical Engineering and Mechanics, Associate Fellow AIAA.

†Research Assistant, Department of Mechanical Engineering and Mechanics, Member AIAA.

‡Senior Research Scientist, Theoretical Flow Physics Branch, Senior Member AIAA.



deg angle of attack, 1.6 freestream Mach number, and 0.4×10^6 Reynolds number. The MacCormack explicit finite difference scheme was used for the computations on a relatively coarse grid of $26 \times 30 \times 60$. A very small perturbation is induced by the truncation error of finite difference algorithm that triggers an instability of the saddle point above the body (first mechanism for asymmetry). Hence, the instability is induced by numerical bias that is physically amplified to produce flow asymmetry. By switching the order of spatial differencing in the predictor and corrector sweeps, the asymmetry was reversed.

Degani and Schiff¹⁷ used the thin-layer, Reynolds-averaged, Navier-Stokes equations to compute asymmetric vortical flow around an ogive-cylinder body. They found that flow asymmetry can be obtained by introducing an asymmetric disturbance very close to the body nose. The disturbance they used was in the form of a small jet that was blown from one side of the body near the nose. However, when the jet was turned off, the numerical solution unfortunately showed that the flow recovered its symmetry. The authors of the present paper believe that the problem is attributed to the smallest scale of the grid at the solid boundary and the damping effect of the numerical dissipation in the axial direction, in addition to the grid-fineness distribution.

Marconi¹⁸ used the Euler equations to solve for supersonic flow past a circular cone in conjunction with a "forced separation model," which was used by Dyer, et al.¹⁹ The pseudotime stepping was carried out until the residual error reached machine zero while the flow was symmetric. Proceeding with the time stepping, vortex-flow asymmetry was obtained and stayed stable thereafter. It is believed that the asymmetry was triggered by the machine round-off error, which acted as a disturbance to the saddle point in the flowfield. In a later paper, Siclari and Marconi²⁰ used the full Navier-Stokes equations to solve for supersonic asymmetric flows around a 5-deg semiapex angle cone over a wide range of angles of attack.

Very recently, Stahl²¹ conducted experimental studies of the low-speed flow around a circular cone of 8-deg semiapex angle circular cone in the angle of attack range of 15–50 deg at a Reynolds number of 7800 based on the base diameter. The onset of flow asymmetry was observed at 35-deg angle of attack. He has shown that the flow asymmetry can be suppressed by inserting a fin along the leeward plane of geometric symmetry with its edge along a ray through the apex. The minimum fin height for this purpose was found to be equal to the local radius of the cone.

In this paper, the supersonic, steady and unsteady, asymmetric vortical flows around circular cones are studied using the unsteady, compressible, single thin-layer, Navier-Stokes equations. Two computational schemes are used to solve the equations. The first, which is the main scheme used in this paper, is an implicit, upwind, flux-difference splitting, finite-volume scheme. The second, which is used to validate certain cases of the upwind scheme, is an implicit, approximately factored, central-difference, finite-volume scheme. Pseudotime stepping is used for steady flows and time-accurate stepping is used for unsteady flows. Some of the influential parameters for flow asymmetry, such as the relative incidence and Mach number, are addressed. A flow case of passive control of flow asymmetry is also studied using the unsteady, compressible, double thin-layer, Navier-Stokes equations.

Formulation

The three-dimensional compressible viscous flow around the body is governed by the conservative form of the dimensionless, unsteady, compressible, double thin-layer, Navier-Stokes equations. In terms of time-independent, body-conformed coordinates ξ^1 , ξ^2 , and ξ^3 , the equations are given by

$$\frac{\partial \bar{Q}}{\partial t} + \frac{\partial \bar{E}_s}{\partial \xi^s} - \frac{\partial (\bar{E}_v)_2}{\partial \xi^2} - \frac{\partial (\bar{E}_v)_3}{\partial \xi^3} = 0, \quad s = 1, 2, 3, \quad (1)$$

where

$$\bar{Q} = \frac{\bar{q}}{J} = \frac{1}{J} [\rho, \rho u_1, \rho u_2, \rho u_3, \rho e]^T \quad (2)$$

$$E_m \equiv \text{inviscid flux}$$

$$= (1/J) [\partial_k \xi^m \bar{E}_k]^T$$

$$= (1/J) [\rho U_m, \rho u_1 U_m + \partial_1 \xi^m p, \rho u_2 U_m + \partial_2 \xi^m p, \rho u_3 U_m + \partial_3 \xi^m p, (\rho e + p) U_m]^T, \quad m = 1, 2, 3 \quad (3)$$

$(\bar{E}_v)_2 \equiv$ viscous and head-conduction flux in ξ^2 direction

$$= (1/J) [0, \partial_k \xi^2 \tau_{k1}, \partial_k \xi^2 \tau_{k2}, \partial_k \xi^2 \tau_{k3}, \partial_k \xi^2 (u_n \tau_{kn} - q_k)]^T \quad (4)$$

$(\bar{E}_v)_3 \equiv$ viscous and head-conduction flux in ξ^3 direction

$$= (1/J) [0, \partial_k \xi^3 \tau_{k1}, \partial_k \xi^3 \tau_{k2}, \partial_k \xi^3 \tau_{k3}, \partial_k \xi^3 (u_n \tau_{kn} - q_k)]^T \quad (5)$$

$$U_m = \partial_k \xi^m u_k \quad (6)$$

The first element of the three momentum elements of Eq. (5) is given by

$$\partial_k \xi^3 \tau_{k1} \equiv \frac{M_\infty \mu}{Re} \left(\psi \partial_1 \xi^3 + \phi \frac{\partial u_1}{\partial \xi^3} \right) \quad (7)$$

where

$$\phi = \partial_k \xi^3 \partial_k \xi^3, \quad \psi = \frac{1}{2} \partial_k \xi^3 \frac{\partial u_k}{\partial \xi^3} \quad (8)$$

The second and third elements of the momentum elements are obtained by replacing the subscript 1, everywhere in Eq. (7), with 2 and 3, respectively. The last element of Eq. (5) is given by

$$\partial_k \xi^3 (u_n \tau_{kn} - q_k) \equiv \frac{M_\infty \mu}{Re} \left\{ \psi W + \phi \left[\frac{1}{2} \frac{\partial}{\partial \xi^3} (u_1^2 + u_2^2 + u_3^2) + \frac{1}{(\gamma - 1) Pr} \frac{\partial (a^2)}{\partial \xi^3} \right] \right\} \quad (9)$$

where

$$W = \partial_n \xi^3 u_n \quad (10)$$

For Eq. (4), in the case of double thin-layer, Navier-Stokes equations, the elements are given by equations similar to Eqs. (7–10) with the exception of replacing ξ^3 by ξ^2 . The double thin-layer, Navier-Stokes equations are used only for the passive control of flow asymmetry since the existence of the fin creates a second thin layer that is perpendicular to the cone thin layer. The reference parameters for the dimensionless form of the equations are L , a_∞ , L/a_∞ , ρ_∞ , and μ_∞ for the length, velocity, time, density, and molecular viscosity, respectively. The Reynolds number is defined as $Re = \rho_\infty V_\infty L / \mu_\infty$, and the pressure p is related to the total energy per unit mass and density by the gas equation

$$p = (\gamma - 1) \rho [e - \frac{1}{2}(u_1^2 + u_2^2 + u_3^2)] \quad (11)$$

The viscosity is calculated from the Sutherland law

$$\mu = T^{3/2} \left(\frac{1 + C}{T + c} \right), \quad C = 0.4317 \quad (12)$$

and the Prandtl number $Pr = 0.72$.

In Eqs. (1–10), the indicial notation is used for convenience. Hence, the subscript k and n are summation indices, the superscript or subscript s is a summation index, and the super-

script or subscript m is a free index. The range of k, n, s , and m is 1-3, and $\partial_k \equiv (\partial/\partial x_k)$.

Boundary conditions are explicitly implemented. They include inflow-outflow conditions and solid-boundary conditions. At the plane of geometric symmetry, periodic conditions are used for symmetric or asymmetric flow applications on the whole computational domain (right and left domains). At the far-field inflow boundaries, freestream conditions are specified since we are dealing with supersonic flows, whereas at the far-field outflow boundaries, first-order extrapolation from the interior points is used. On the solid boundary, the no-slip and no-penetration conditions are enforced; $u_1 = u_2 = u_3 = 0$, and the normal pressure gradient is set equal to zero. For the temperature, the adiabatic boundary condition is enforced on the solid boundary. The initial conditions correspond to the uniform flow with $u_1 = u_2 = u_3 = 0$ on the solid boundary.

For the passive control applications using a vertical fin in the leeward plane of geometric symmetry, solid-boundary conditions are enforced on both sides of the fin.

Highlights of Computational Schemes

The first computational scheme used to solve the unsteady compressible, single or double thin-layer, Navier-Stokes equa-

tions is based on the Roe inviscid flux-difference splitting scheme. In this scheme, the Jacobian matrices of the inviscid fluxes, $A_s = (\partial E_s / \partial q)$, $s = 1-3$, are split into left and right fluxes according to the signs of the eigenvalues of the inviscid Jacobian matrices. Flux limiters are used to dampen the numerical oscillations in regions of large changes of the gradients of the flowfield vector. The viscous and heat transfer terms are centrally differenced. The resulting equation is solved by using approximate factorization in the ξ^1, ξ^2 , and ξ^3 directions. The computational scheme is coded in the computer program CFL3D.

The second computational scheme is an implicit, approximately factored, centrally differenced, finite-volume scheme.²² Added second-order and fourth-order dissipation terms are used in the difference equation on its right-hand side terms, which represent the explicit part of the scheme. The Jacobian matrices of the implicit operator on the left-hand side of the difference equation are centrally differenced in space, and implicit second-order dissipation terms are added for the scheme stability. The left-hand side operator is approximately factored, and the difference equation is solved in three sweeps in the ξ^1, ξ^2 , and ξ^3 directions, respectively. The computational scheme is coded in the computer program ICF3D. The ICF3D code is used to verify some of the applications of the

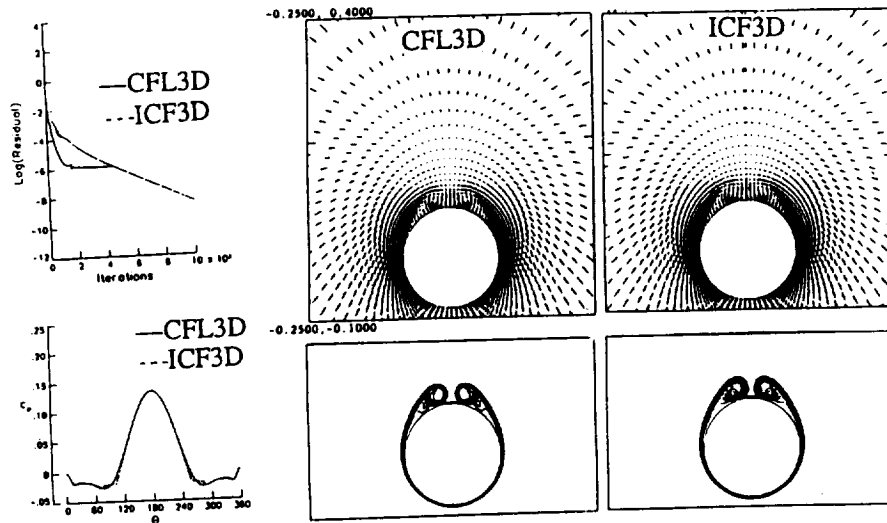


Fig. 1 Symmetric flow solutions for a circular cone, $\alpha = 10$ deg, $M_\infty = 1.8$, $Re = 10^5$ (validation case).

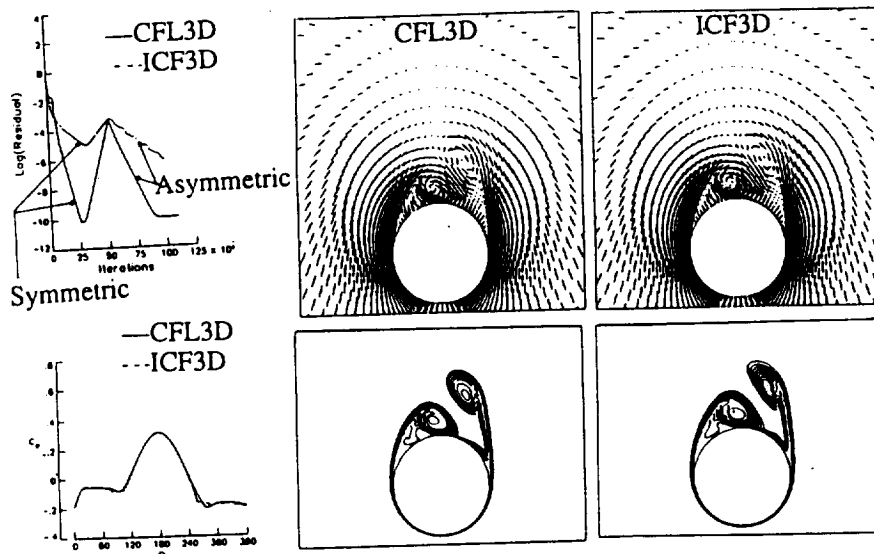


Fig. 2 Steady asymmetric flow solutions for a circular cone due to random disturbances, $\alpha = 20$ deg, $M_\infty = 1.8$, $Re = 10^5$ (validation case).

CFL3D code; namely the cases of Figs. 1 and 2. For the problem of passive control of flow asymmetry, the double thin-layer, Navier-Stokes equations have been solved using the CFL3D code.

Since the applications in this paper cover local-conical flows only, the three-dimensional scheme is used to solve for locally conical flows. This is achieved by forcing the conserved components of the flow vector field to be equal at two planes of $x = 0.95$ and 1.0 . The validity of local-conical-flow assumption is discussed in the next section.

Validity of the Local-Conical-Flow Assumption

The solutions presented in this paper are called local-conical solutions, which are obtained by equating the conserved components of the flowfield vector, in the three-dimensional scheme, on two crossflow planes that are in close proximity to each other at a selected location. Once this location is specified ($x = 1.0$ in the present applications), the flow Reynolds number is determined and the time scale, for time-accurate solutions, is also determined. The resulting solution is a local-conical solution at the specified location. It is not a global-conical solution. The locally conical equations can be shown by considering the conservative form of the Navier-Stokes equations in the Cartesian system

$$\frac{\partial q}{\partial t} + \frac{\partial(E - E_v)_i}{\partial x_i} = 0, \quad i = 1 - 3 \quad (13)$$

By introducing the conical coordinates

$$\eta_1 = \frac{x_1}{x_3}, \quad \eta_2 = \frac{x_2}{x_3}, \quad \eta_3^2 = x_1 x_1 \quad (14)$$

and using the chain rule to express Eq. (13) in terms of the conical coordinates, we get

$$\begin{aligned} \frac{\eta_3}{\theta} \frac{\partial q}{\partial t} + \frac{\partial}{\partial \eta_1} (\bar{E} - \bar{E}_v)_1 + \frac{\partial}{\partial \eta_2} (\bar{E} - \bar{E}_v)_2 \\ + \frac{\eta_3}{\theta^2} \frac{\partial}{\partial \eta_3} (\bar{E} - \bar{E}_v)_3 + 2(\bar{I} - I_v) = 0 \end{aligned} \quad (15)$$

where

$$\begin{aligned} \theta &= \sqrt{1 + \eta_1^2 + \eta_2^2} \\ \bar{E}_1 &= E_1 - \eta_1 E_3, \quad \bar{E}_2 = E_2 - \eta_2 E_3 \\ \bar{E}_3 &= E_3 + \eta_1 E_1 + \eta_2 E_2 \\ \bar{I} &= \bar{E}_3 \\ \bar{E}_{v1} &= E_{v1} - \eta_1 E_{v3} \\ \bar{E}_{v2} &= E_{v2} - \eta_2 E_{v3} \\ \bar{E}_{v3} &= E_{v3} + \eta_1 E_{v1} + \eta_2 E_{v2} \\ I_v &= \bar{E}_{v3} \end{aligned} \quad (16)$$

The conical flow condition requires that the flow variables be independent of the coordinate η_3 . If this condition is imposed in Eq. (15), by dropping the derivatives with respect to η_3 , the equation reduces to

$$\frac{\eta_3}{\theta} \frac{\partial q}{\partial t} + \frac{\partial}{\partial \eta_1} (\bar{E} - \bar{E}_v)_1 + \frac{\partial}{\partial \eta_2} (\bar{E} - \bar{E}_v)_2 + 2(\bar{I} - I_v) = 0 \quad (18)$$

It is clearly seen that Eq. (18) still has η_3 dependence in the unsteady term and the viscous and heat-flux terms (one can see the explicit dependence of the viscous and heat-flux terms on η_3 by transforming the elements of these vectors to the conical

coordinates). Hence, Eq. (18) is not self-similar, and therefore it does not represent a global-conical flow. However, if η_3 is set equal to a constant c , then one can consider Eq. (18) to represent a local-conical flow around $\eta_3 = c$. The resulting solution using Eq. (18) with $\eta_3 = c$ represents a local-conical solution with a Reynolds number and a time that are scaled by the constant c . It should be noted that if the flow is steady and inviscid, then Eq. (18) becomes self-similar, and hence it represents a global-conical flow. In the present paper, we indirectly solve Eq. (18) at a fixed location of unity. This is achieved in the three-dimensional flow equation, Eq. (1), by equating the elements of the flowfield vector at two planes in close proximity to each other. In this paper, we selected these planes to be located at $x = 0.95$ and 1.0 . In other numerical experiments, we use the plane locations at $x = 0.995$ and 1.0 . The results of these experiments were in excellent agreement with those of the present paper.

Computational Studies

Supersonic flows about a 5 deg semiapex angle circular cone at a Reynolds number of 10^5 have been considered. A grid of 161×81 points in the circumferential and normal directions is used throughout the present applications. The grid is generated by using a modified Joukowski transformation with a geometric series for the grid clustering near the solid boundary. The minimum grid length is 10^{-4} at the solid boundary, and the maximum radius of the computational domain is $21r$, where r is the radius of the circular cone at the axial station of unity.

Steady Symmetric Flows

Figure 1 shows steady symmetric vortical-flow solutions for the circular cone at 10 deg angle of attack and 1.8 freestream Mach number. In the figure, we show comparisons of the results of the CFL3D and ICF3D codes. The results include the residual error versus the number of iterations, the crossflow velocity, the total-pressure-loss contours, and the surface-pressure coefficients. It should be noted here that the angle θ in the C_p figure is measured from the leeward plane of geometric symmetry in the clockwise direction. The agreement of the results of the two code is excellent, and the results are in full agreement with those of Siclari and Marconi.²⁰

Steady Asymmetric Flow

Round-Off and Truncation Error Disturbances

The cone angle of attack is increased to 20 deg while all the other flow conditions are kept fixed. Figure 2 shows the results of the CFL3D and ICF3D codes. In the residual error figure, the CFL3D code shows that the residual error drops 10 orders of magnitude within 2500 iteration steps. Thereafter, the error increases by six orders of magnitude. The flow is symmetric during this 5000 iteration steps. Next, the error drops down by another six orders of magnitude and stays constant for 2500 iteration steps. The flow becomes asymmetric and stable. The ICF3D code shows that the residual error drops five orders of magnitude in the first 3000 iteration steps, increases two orders of magnitude in the next 2000 iteration steps, and then drops down by three orders of magnitude within the next 5000 iterations. The flow solution goes through a symmetric unstable solution and then to an asymmetric stable solution. The pressure-coefficient figure for the two codes is the same over the full range of the circumferential angle θ . The suction pressure in the range of $\theta = 0-90$ deg is lower than that of the range of $\theta = 270-360$ deg. The crossflow velocity and total-pressure-loss contours for the two codes are also in excellent agreement. They show the nature of the flow asymmetry and its details. The results are in complete agreement with those of Ref. 20.

Since the residual error of the CFL3D code is much smaller than that of the ICF3D code after the first 2500 iterations, the disturbance that triggered the asymmetry in the first code is attributed to the machine round-off error, while the distur-

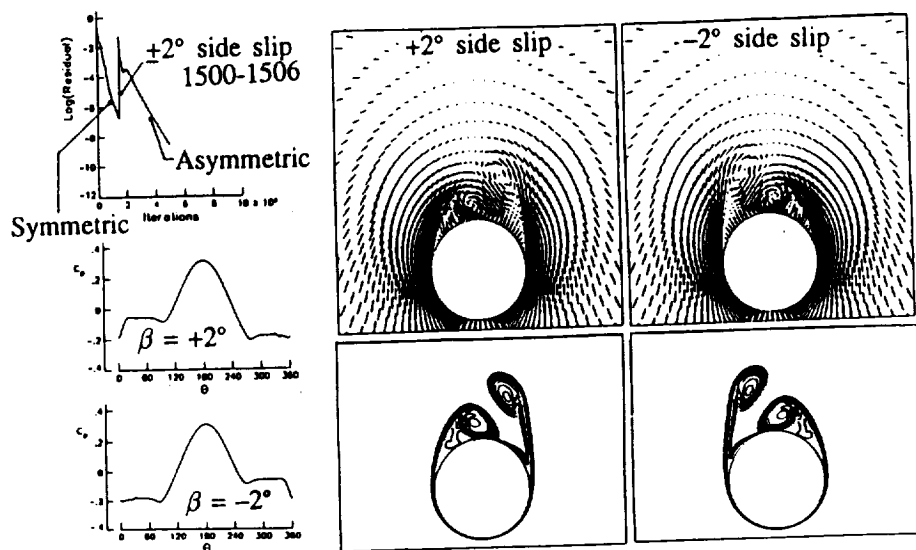


Fig. 3 Steady asymmetric flow solutions for a circular cone due to ± 2 deg transient side slip, $\alpha = 20$ deg, $M_\infty = 1.8$, $R_e = 10^5$.

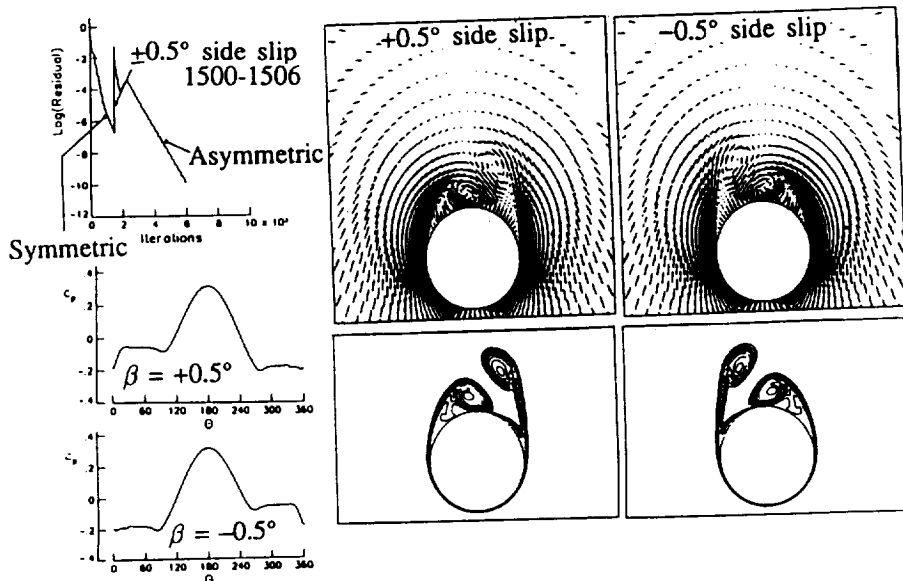


Fig. 4 Steady asymmetric flow solutions for a circular cone due to ± 0.5 deg transient side slip, $\alpha = 20$ deg, $M_\infty = 1.8$, $R_e = 10^5$.

bance that triggered the asymmetry in the second code is attributed to the truncation error of the scheme (since there is a bias due to the spatial marching direction). Both disturbances are random in nature. However, irrespective of the source of disturbance, the final asymmetric stable solution is the same.

Controlled Transient Side-Slip Disturbances

In Figs. 3 and 4, we show steady asymmetric flow solutions due to transient side-slip disturbances of ± 2 and ± 0.5 deg. The residual-error figures show a drop of seven orders of magnitude in the first 2000 iterations. At this step, a side-slip disturbance is imposed for six iteration steps, then it is removed. Irrespective of the magnitude or the sign of the side-slip disturbance, the residual error increases by six orders of magnitude, then it drops down very rapidly. A stable asymmetric flow solution is obtained. The asymmetric solutions corresponding to the ± 2 deg side-slip disturbances are mirror images of each other, as can be seen from the figures of the surface-pressure coefficient, crossflow velocity, and total-pressure-loss contours. The corresponding asymmetric solutions with the ± 0.5 deg side-slip-disturbances are exactly the same as those of the ± 2 deg side-slip disturbances. Moreover,

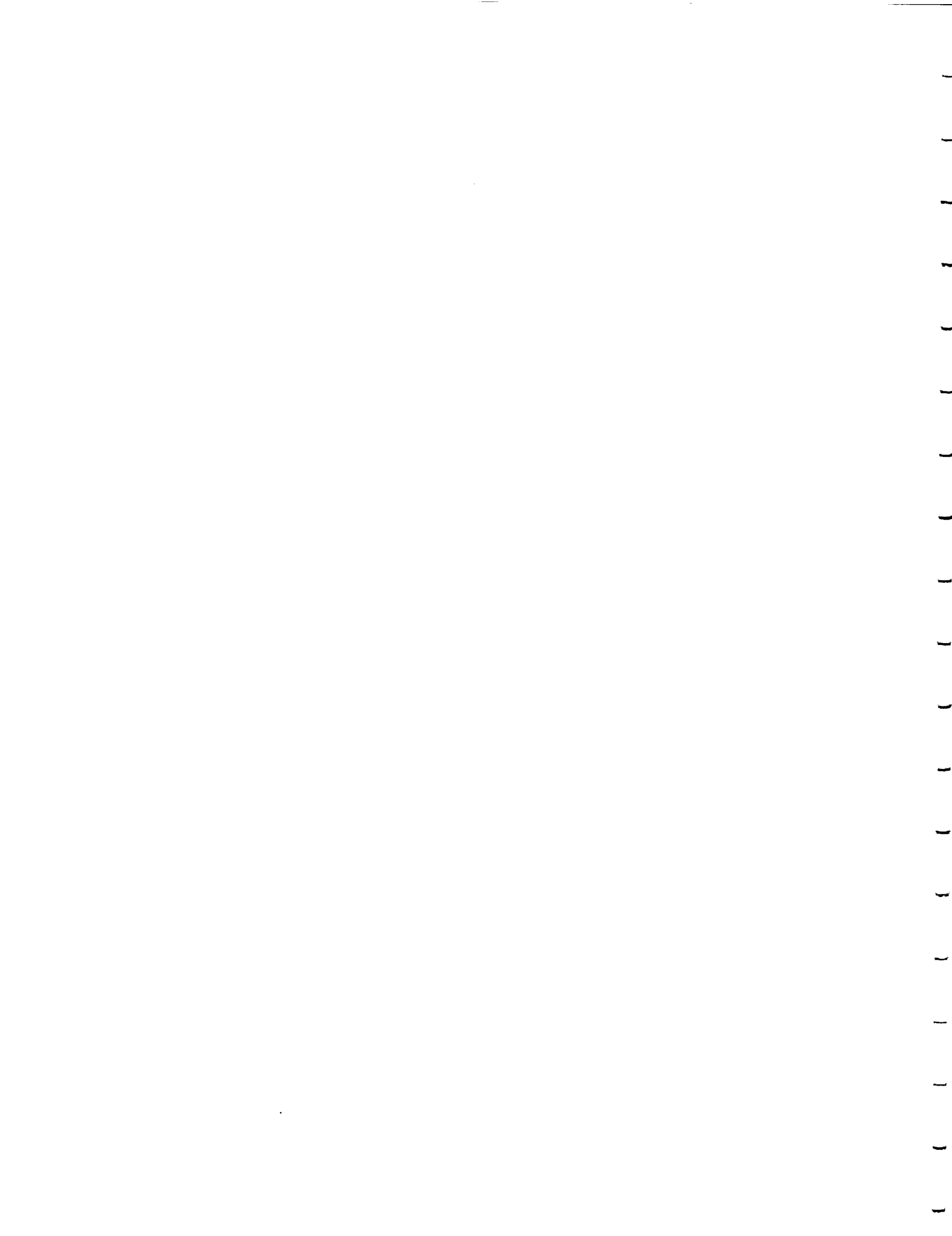
the final asymmetric solutions of the ± 2 deg and ± 0.5 deg side-slip disturbances are the same as those of Fig. 2.

Again, this numerical experiment shows that the same physical flow asymmetry is obtained.

Unsteady Asymmetric Vortex Shedding

In the present case, the angle of attack is increased to 30 deg and all the other flow conditions are kept the same as those of the cases above. Figure 5 shows the results of this case.

Here, we show the history of the residual error and the lift coefficient up to the 15,700 time step. First, pseudo-time stepping was used up to 10,000 iterations, and the solution was monitored every 500 iterations. The solution showed that the asymmetry was changing from the left side to the right side, which indicated a possibility of unsteady asymmetric vortex shedding. The residual error was also oscillating. The computations were repeated starting from the 3,500 iteration step using time-accurate calculations with $\Delta t = 10^{-3}$. The residual-error and lift-coefficient figures show the time history of the solution. It is seen that the residual error and the lift coefficient show a transient response that is followed by a periodic response. Figure 5 shows also snapshots of the time history of the solution for the total-pressure-loss contours and surface-



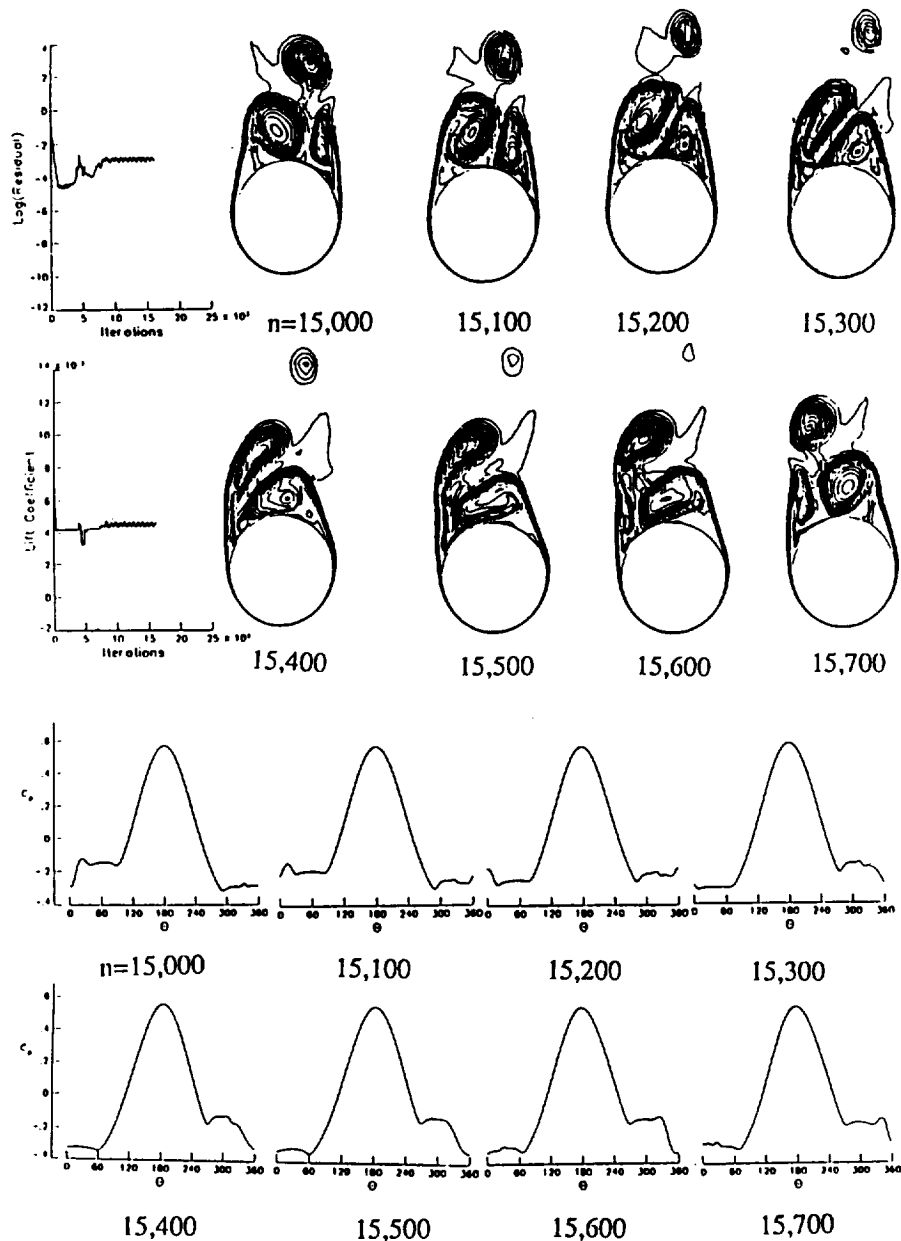


Fig. 5 Unsteady asymmetric flow solution (using flux-difference splitting) with vortex shedding for a circular cone during periodic flow responses: $\alpha = 30$ deg, $M_\infty = 1.8$, $R_\tau = 10^5$, $\Delta t = 10^{-3}$.

pressure coefficient. The solutions are shown every 100 time steps starting from the time step of 15,000. At $n = 15,000$, the asymmetric flow is seen with an already shed vortex from the right side. As time passes, the shed vortex is convected in the flow and the primary vortex on the left side stretches upwards while the primary vortex on the right gets stronger, as it is seen from the surface pressure figures. At $n = 15,600$, the primary vortex on the left side is about to be shed. At $n = 15,700$, the primary vortex on the left side is shed in the flowfield. It should be noticed that the solution at $n = 15,700$ is exactly a mirror image to that at $n = 15,000$. The solution from 15,000–15,700 represents the first one-half the cycle of shedding. The solution from 15,700–16,400 (not shown) represents the second one-half the cycle. The periodicity of the shedding motion is conclusively captured. The period of oscillations is $10^{-3} \times 1,400$ steps = 1.4 that produces a shedding frequency of 4.400 (Strouhal number). This solution is obtained by using the flux-difference splitting (FDS) scheme.

Very recently, a researcher in the computational simulation area of asymmetric flows claimed that he had applied the flux-vector splitting (FVS) scheme of the CFL3D code to the present flow case. His solution showed that the flow was

steady and symmetric. A statement of his results was communicated to us and we were asked to respond. Therefore, we recomputed the present flow case using the FVS scheme of the same CFL3D code. In Fig. 6, we show the results of the time-accurate solutions using the FVS scheme using the same grid. Using the FVS scheme, the flux limiters were turned on, and as can be seen from the logarithmic-residual curve, the solution becomes symmetric and steady after 5000 time steps. Next, the flux limiters are turned off, and the solution shows a transient response up to 12,000 time steps. Thereafter, the solution becomes periodic with periodic asymmetric vortex shedding. The solution was monitored every 100 time steps, and the results from $n = 13,900$ –14,600 are shown. Although the process of adjusting the time instants is difficult to match those of the FDS solution, it is seen that the captured snapshots of the FVS solution almost match those of the FDS solution. Comparing the FVS solutions at $n = 13,900$ and 14,600, it is seen that they are mirror images of each other. Hence, periodic flow response has been achieved with a period of $1400 \times 10^{-3} = 1.4$, which is exactly the same period of shedding as that of the FDS solution. This pinpoints the high numerical dissipation effect of the FVS scheme when the flux

limiters are turned on. The resulting numerical dissipation in the FVS is large enough to dampen the random disturbances of the flow solution. By turning off the flux limiters in the FVS scheme, the random disturbances can grow, producing the asymmetric unsteady vortex shedding. This also shows that the FDS scheme, even with the flux limiters turned on, is less dissipative than the FVS scheme. These results conclusively explain the erroneous claim of steady flow made by the previously mentioned researcher.

Steady Asymmetric Flow at Different Mach Numbers (Effect of M_∞)

Figure 7 shows the effect of the freestream Mach number ($M_\infty = 2.2, 2.6, \text{ and } 3.0$) on the convergence history, surface pressure, crossflow velocity, and total-pressure-loss contours for the circular cone at 20 deg angle of attack. At $M_\infty = 2.2$, the residual error shows that the stable asymmetric flow is obtained within the same number of iterations as that of the $M_\infty = 1.8$ case. At $M_\infty = 2.6$, the residual error shows that the stable asymmetric flow is obtained after a large number of iterations. And at $M_\infty = 3.0$, no asymmetric flow was captured, the flow stayed symmetrically stable. The surface pres-

sure figures show that the asymmetry gets weaker as the Mach number is increased. This conclusion is clearly seen from the crossflow velocity and the total-pressure-loss figures. It should be noted that since the nature of disturbance is random, flow asymmetry changes sides as the Mach number increases until it disappears.

Passive Control of Flow Asymmetry

Figure 8 shows the passive control of flow asymmetry by inserting a vertical fin in the leeward plane of geometric symmetry. The fin height is equal to the cone local radius r . Here, the double thin-layer, Navier-Stokes equations are used to obtain these results. The flow Mach number is kept at 1.8 and the angle of attack is 20 deg. The flow is completely symmetric as can be seen from the figures of the surface-pressure coefficient, total-pressure-loss contours, and crossflow velocity. A blow-up of the cross-flow velocity at the fin-cone juncture shows two corner recirculating bubbles of exactly the same size. This case has been obtained after 24,000 iteration steps. Again, this is the first time such a computational simulation of

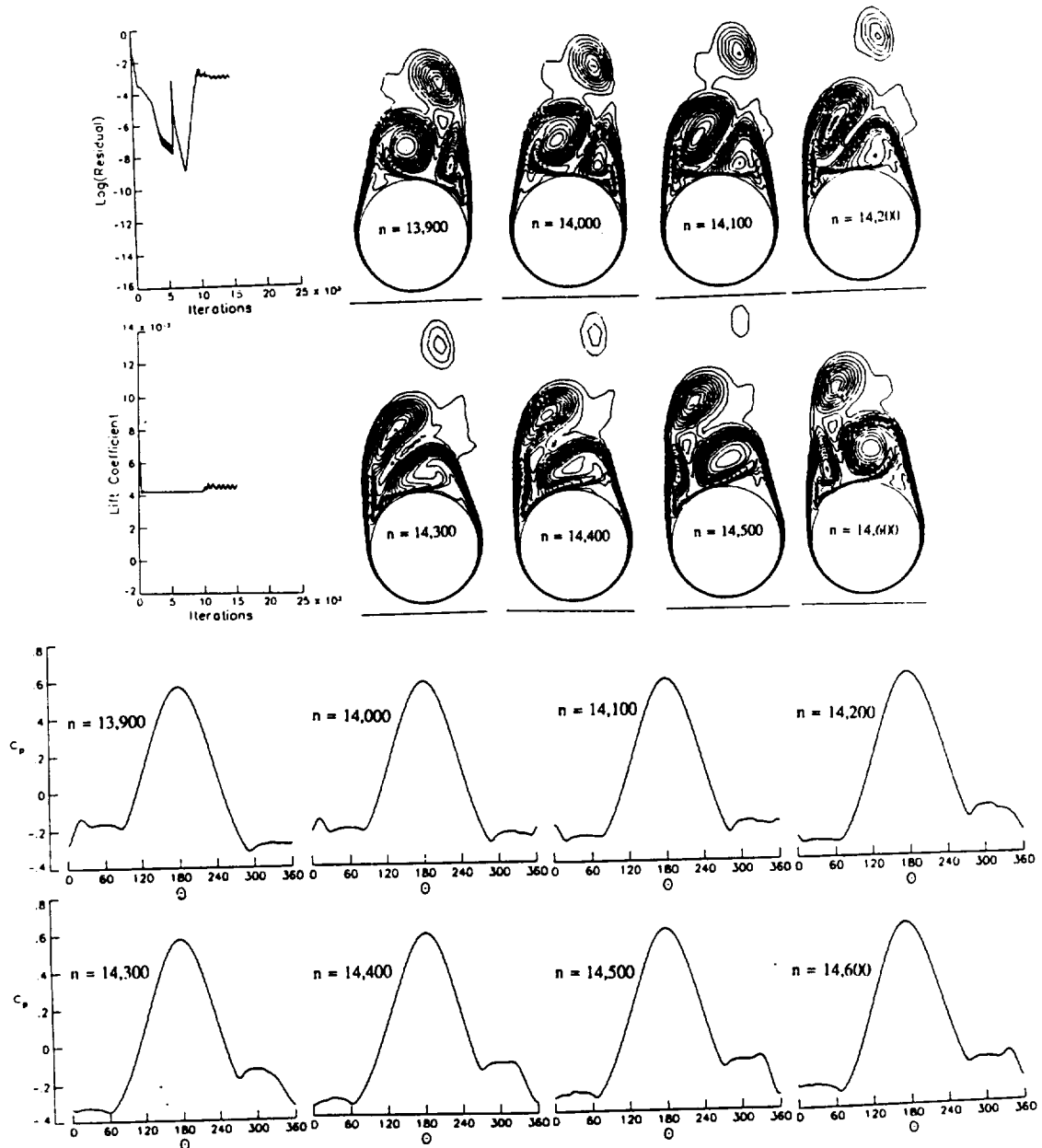


Fig. 6 Unsteady asymmetric flow solution (using flux-vector splitting) with vortex shedding for a circular cone during periodic flow response: $\alpha = 30$ deg, $M_\infty = 1.8$, $R_e = 10^5$, $\Delta t = 10^{-3}$.

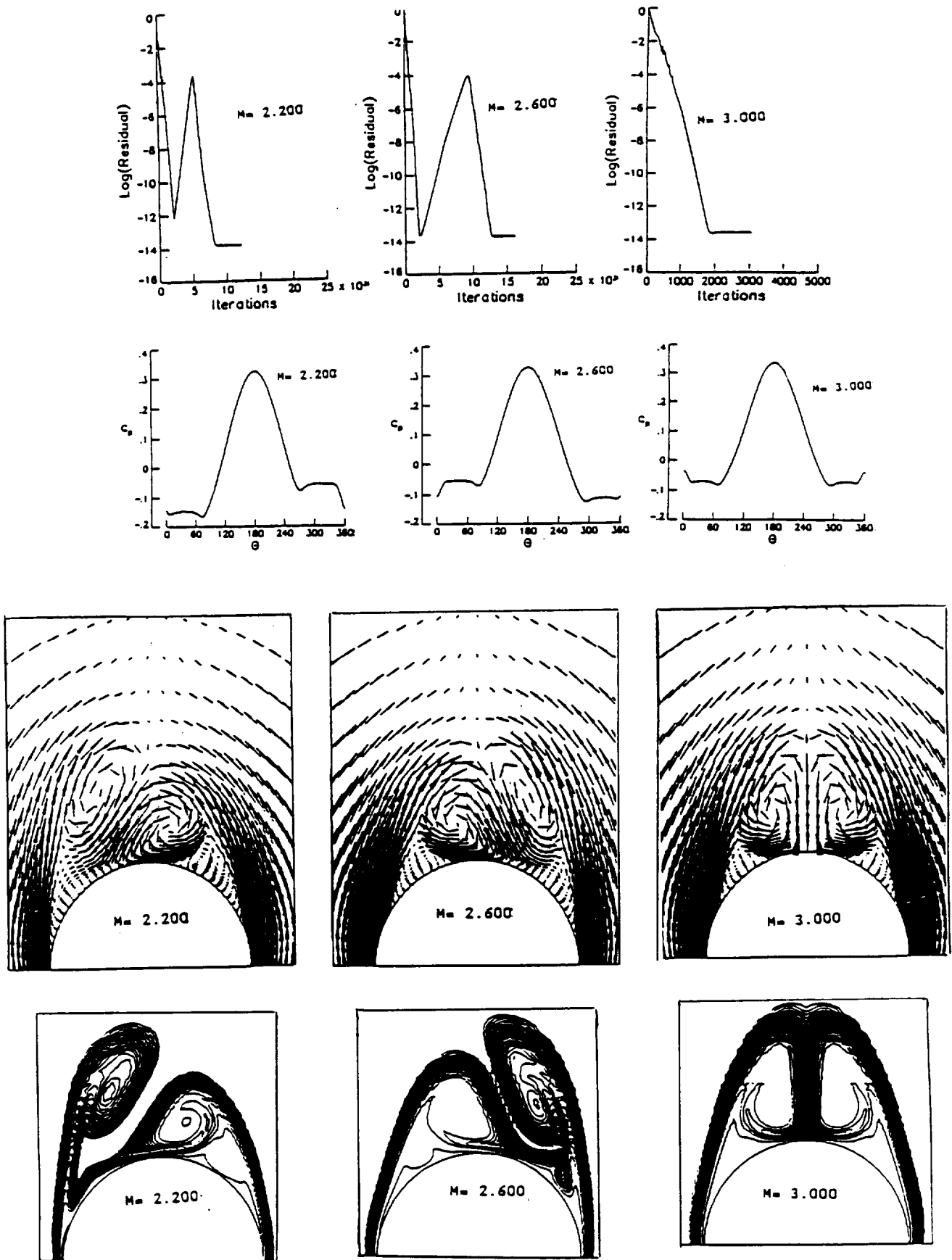


Fig. 7 Effect of the freestream Mach number on the flow asymmetry for a circular cone, $\alpha = 20$ deg; $M_\infty = 2.2, 2.6, 3.0$; $R_r = 10^5$.

1
2
3
4
5
6
7
8
9
10
11
12
13
14
15
16
17
18
19
20
21
22
23
24
25
26
27
28
29
30
31
32
33
34
35
36
37
38
39
40
41
42
43
44
45
46
47
48
49
50
51
52
53
54
55
56
57
58
59
60
61
62
63
64
65
66
67
68
69
70
71
72
73
74
75
76
77
78
79
80
81
82
83
84
85
86
87
88
89
90
91
92
93
94
95
96
97
98
99
100

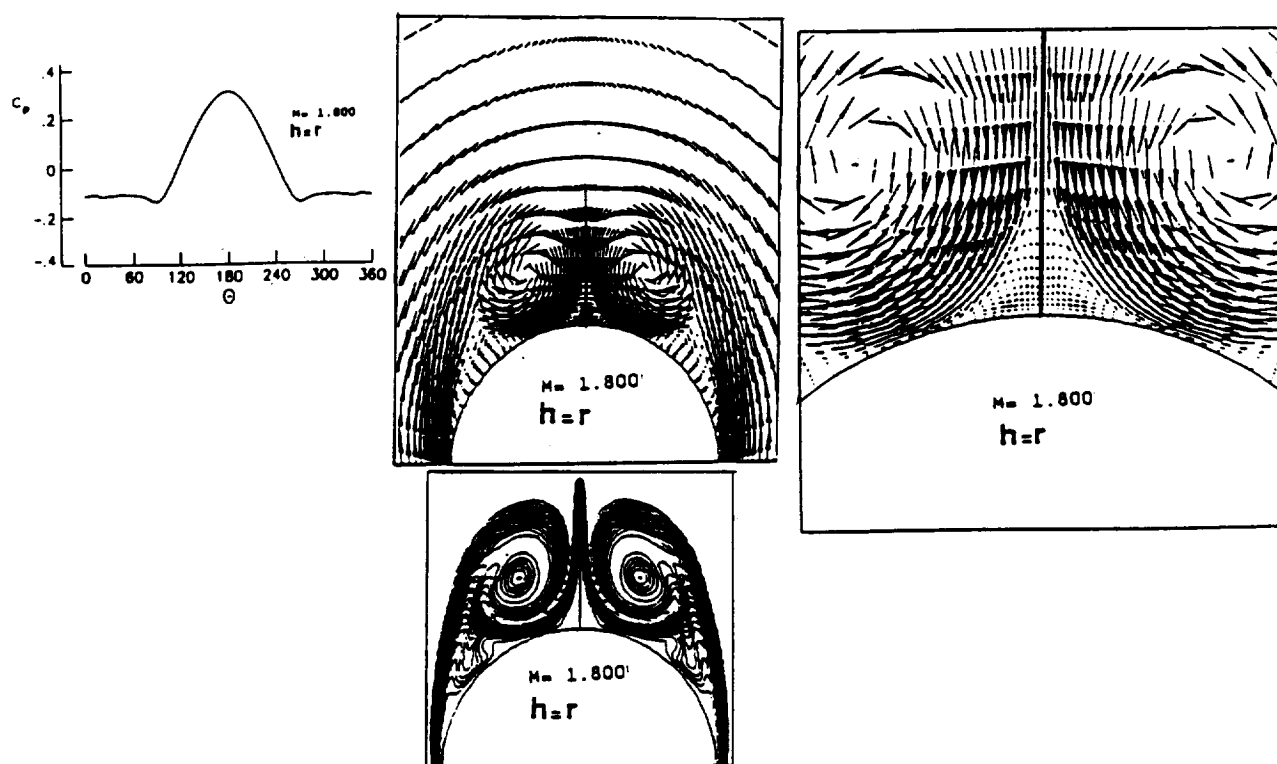


Fig. 8 Control of asymmetric flow of a circular cone using a vertical fin in the leeward geometric plane of symmetry, $\alpha = 20$ deg, $M_\infty = 1.8$, $Re = 10^5$, $h = r$ ($r =$ radius of circular section).

the passive control of the flow asymmetry has been presented. The results are in full agreement with Stahl's experimental study.²¹

Concluding Remarks

This paper presents extensive computational study and simulation of steady and unsteady asymmetric vortex flow around circular cones. A systematic study has been carried out to show the effects of angle of attack and Mach number. The study shows that the flow asymmetry is independent of the type or level of the disturbance. For the controlled transient side-slip disturbance, the solution is unique. For the uncontrolled random disturbance, the solution is also unique with the exception of having the same asymmetry changing sides on the cone. It conclusively shows that periodic vortex shedding has been captured at larger angles of attack. The unsteady asymmetric vortex-shedding solution has been substantiated by using two different computational schemes. It also shows that as the Mach number increases, the vortex flow asymmetry gets weaker until it disappears. The possibility of passive control of flow asymmetry has also been demonstrated. Many of the cases presented here are obtained for the first time, in particular, the asymmetric vortex shedding cases and the cases of passive control of flow asymmetry.

Acknowledgment

This research is supported by the NASA Langley Research Center under Grant NAS1-18584-08 for the first two authors.

References

- Thomas, K. D., and Morrison, D. F., "The Spacing, Position and Strength of Vortices in the Wake of Slender Cylindrical Bodies at Large Incidence," *Journal of Fluid Mechanics*, Vol. 50, No. 4, 1971, pp. 751-783.
- Keener, E. R., and Chapman, G. R., "Similarity in Vortex Asymmetries Over Slender Bodies and Wings," *AIAA Journal*, Vol. 15, No. 9, 1988, pp. 1370-1372.
- Peake, D. J., Owen, F. K., and Higuchi, H., "Symmetrical and Asymmetrical Separations About a Yawed Cone," AGARD-CP-247, Jan. 1979, pp. 16.1-16.27.
- Peak, D. J., Fisher, D. F., and McRae, D. S., "Flight, Wind Tunnel and Numerical Experiments with a Slender Cone at Incidence," *AIAA Journal*, Vol. 20, No. 10, 1979, pp. 1338-1345.
- Peake, D. J., and Tobak, M., "Three-Dimensional Flows About Simple Components at Angle of Attack," *High Angle-of-Attack Aerodynamics*, AGARD LS-121, Aug. 1982, pp. 2.1-2.56.
- Skow, A. M., and Peake, D. J., "Control of the Forebody Vortex Orientation by Asymmetric Air Injection, (Part B)—Details of the Flow Structure," *High Angle-of-Attack Aerodynamics*, AGARD-LS-121, Aug. 1982, pp. 10.1-10.22.
- Nishioka, M., and Sato, H., "Mechanism of Determination of the Shedding Frequency of Vortices Behind a Cylinder at Low Reynolds Numbers" *Journal of Fluid Mechanics*, Vol. 89, Part 1, 1978, pp. 49-60.
- Lamont, P. J., "Pressures Around an Inclined Ogive Cylinder with Laminar, Transitional, or Turbulent Separation," *AIAA Journal*, Vol. 20, No. 11, November 1980, pp. 1492-1499.
- Lamont, P. J., "The Complex Asymmetric Flow Over a 3.5D Ogive Nose Cylindrical Afterbody at High Angles of Attack," *AIAA Paper* 82-0053, Jan. 1982.
- Yanta, W. J., and Wardlaw, A. B., Jr., "The Secondary Separated Region on a Body at High Angles-of-Attack," *AIAA Paper* 82-0343, January 1982.
- Ericsson, L. E., and Reding, J. P., "Vortex-Induced Asymmetric Loads, in 2-D and 3-D Flows," *AIAA Paper* 80-0181, Jan. 1980.
- Shanks, R. E., "Low Subsonic Measurements of Static and Dynamic Stability Derivatives of Six Flat Plate Wings Having Leading-Edge Sweep Angles of 70°-84°," NASA TN D-1822, July 1963.
- Rediniotis, O., Stapountzis, H. and Telionis, D. P., "Vortex Shedding Over Nonparallel Edges," Virginia Polytechnic Institute and State University, Blacksburg, VA, Engineering Rept. VPI-88-39, Dec. 1988.
- McRae, D., "Numerical Study of Supersonic Viscous Cone Flow at High Angle of Attack," *AIAA Paper* 76-0097, Jan. 1976.
- Blutford, G., and Hankey, W., "Numerical Solutions of Supersonic and Hypersonic Viscous Flow Around Thin Delta Wings," *Proceedings of the AIAA 22nd Structural Dynamics Conference*, AIAA, New York, 1979, pp. 793-810.
- Graham, J. E., and Hankey, W. L., "Computation of the Asymmetric Vortex Pattern for Bodies of Revolution," *AIAA Journal*,

Vol. 23, No. 11, 1983, pp. 1500-1504.

¹⁷Degani, D., and Schiff, L. B., "Numerical Simulation of the Effect of Spatial Disturbances on Vortex Asymmetry," AIAA Paper 89-0340, Jan. 1989.

¹⁸Marconi, F., "Asymmetric Flows About Sharp Cones in a Supersonic Stream," *Proceedings of the 11th International Conference on Numerical Methods in Fluid Dynamics*, Williamsburg, VA, June 1988.

¹⁹Dyer, D., Fiddes, S. P., and Smith, J. H. B., "Asymmetric Vortex Formation from Cones at Incidence—A Simple Inviscid

Model," *Aeronautical Quarterly*, Vol. 33, June 1982, pp. 293-312.

²⁰Siclari, M. J., and Marconi, F., "The Computation of Navier-Stokes Solutions Exhibiting Asymmetric Vortices," AIAA Paper 89-1817, June 1989.

²¹Stahl, W., "Suppression of Asymmetry of Vortex Flow Behind a Circular Cone at High Incidence," AIAA Paper 89-3372-CP, Aug. 1989.

²²Kandil, O. A., and Chuang, H. A., "Unsteady Navier-Stokes Computations Past Oscillating Rolling Delta Wings at High Incidences," AIAA Paper 89-081, Jan. 1989.



10034
10017
N93-14691

NUMERICAL SIMULATION OF STEADY AND UNSTEADY ASYMMETRIC VORTICAL FLOW

O. A. KANDIL AND T.-C. WONG

*Department of Mechanical Engineering and Mechanics, Old Dominion University
Norfolk, VA 23529, U.S.A.*

AND

C. H. LIU

*Theoretical Flow Physics Branch, NASA Langley Research Center,
Hampton, VA 23665, U.S.A.*

Reprinted from

Journal of Fluids and Structures (1992) **6**, 249-265

453078

NUMERICAL SIMULATION OF STEADY AND UNSTEADY ASYMMETRIC VORTICAL FLOW

O. A. KANDIL AND T.-C. WONG

*Department of Mechanical Engineering and Mechanics, Old Dominion University
Norfolk, VA 23529, U.S.A.*

AND

C. H. LIU

*Theoretical Flow Physics Branch, NASA Langley Research Center,
Hampton, VA 23665, U.S.A.*

(Received 7 August 1990 and in revised form 1 August 1991)

The unsteady, compressible, thin-layer, Navier–Stokes (NS) equations are solved to simulate steady and unsteady, asymmetric, vortical laminar flow around cones at high incidences and supersonic Mach numbers. The equations are solved by using an implicit, upwind, flux-difference splitting (FDS), finite-volume scheme. The locally conical flow assumption is used and the solutions are obtained by forcing the conserved components of the flowfield vector to be equal at two axial stations located at 0.95 and 1.0. Computational examples cover steady and unsteady asymmetric flows around a circular cone and its control using side strakes. The unsteady asymmetric flow solution around the circular cone has also been validated using the upwind, flux-vector splitting (FVS) scheme with the thin-layer NS equations and the upwind FDS with the full NS equations. The results are in excellent agreement with each other. Unsteady asymmetric flows are also presented for elliptic- and diamond-section cones, which model asymmetric vortex shedding around round- and sharp-edged delta wings.

1. INTRODUCTION

AT HIGH ANGLES OF ATTACK, flow separations from the forebodies of missiles and fighter aircraft may become asymmetric resulting in side forces, yawing moments and rolling moments which are, in many instances, sufficiently large to trigger missile and aircraft spin. Experimental studies have shown that it is not necessary for the separation lines to be asymmetric in order for the separated flow to be asymmetric (Kenner & Chapman 1977; Peak *et al.* 1979; Lamont 1980, 1982). These studies have also shown that unsteady asymmetric flow with vortex shedding may be either random or periodic, where the latter is similar to the Kármán vortex street in two-dimensional flows around cylinders.

The onset of flow asymmetry occurs when the relative incidence (ratio of angle of attack to semi-apex angle) of pointed forebodies exceeds certain critical values. At the critical values of relative incidence, flow asymmetry develops due to natural and/or forced disturbances. The origin of natural disturbances may be a transient side slip, an acoustic disturbance, or similar disturbance of short duration. The origin of forced disturbances is geometric perturbations due to imperfections in the nose geometric symmetry or similar disturbances of permanent nature. In addition to the relative incidence as one of the determinable parameters for the onset of flow asymmetry, the free-stream Mach number, Reynolds number and shape of the body cross-sectional area are important determinable parameters. Asymmetric flow and vortex shedding

have also been documented for sharp-edged delta wings at very high relative incidences (Shanks 1963; Rediniotis *et al.* 1988).

The mechanisms which lead to steady and unsteady asymmetric vortical flows past wings and bodies at high angles of attack and zero side slip are not well understood. The experimental studies of these phenomena by several investigators (e.g. Keener & Chapman 1977; Lamont 1982; Skow & Peake 1982; Peake & Tobak 1982) propose two mechanisms for explaining the origin of flow asymmetry. The first mechanism suggests that the asymmetry occurs due to instability of the velocity profiles in the vicinity of the enclosing saddle point which exists in the cross-flow planes above the body primary vortices. The second mechanism suggests that the asymmetry occurs due to asymmetric transition of the boundary-layer flow at the apex, either in the axial direction or on both sides of the body in the cross-flow plane.

Very recently, several attempts have been carried out to computationally simulate asymmetric vortical flows around slender bodies of revolution. In a paper by Marconi (1988), the Euler equations are used along with a "forced separation model", which is introduced by Fiddes (1989), to solve for supersonic flow past a circular cone. The pseudo-time stepping is carried out until the residual error reaches machine zero while the flow is symmetric. Proceeding with the time stepping, vortex-flow asymmetry is obtained and stays stable thereafter. It is believed that the asymmetry is triggered by the machine round-off error, which acts as a disturbance to the saddle point in the flowfield. This work shows that the first mechanism of asymmetric vortex flow is basically an inviscid mechanism. In a recent paper by Siclari & Marconi (1989), the full Navier-Stokes equations are used to solve for supersonic asymmetric flows around a 5°-semi-apex angle cone over a wide range of angles of attack.

Kandil *et al.* (1990a) used the unsteady, thin-layer Navier-Stokes equations along with two different implicit schemes to simulate asymmetric vortex flows around cones with different cross-sectional shapes. The numerical investigation focuses on a 5°-semi-apex angle circular cone and locally conical flow is assumed. The first scheme is an implicit, upwind, flux-difference splitting, finite-volume scheme and the second one is an implicit, approximately factored central-difference, finite-volume scheme. Keeping the Mach number and Reynolds number constant at 1.8 and 10^5 , respectively, the angle of attack is varied from 10 to 30°. At $\alpha = 10^\circ$, a steady symmetric solution is obtained and the results of the two schemes are in excellent agreement. At $\alpha = 20^\circ$ and irrespective of the type or level of the disturbance, a unique steady asymmetric solution is obtained and the results of the two schemes are in excellent agreement. Two types of flow disturbances are used: a random round-off error or a random truncation-error disturbance, and a controlled transient side-slip disturbance with short duration. For the controlled transient side-slip disturbance the solution is unique, and for the uncontrolled random disturbance the solution is also unique with the exception of having the same asymmetry changing sides on the cone. At $\alpha = 30^\circ$, an unsteady asymmetric solution with vortex shedding is obtained, and the vortex shedding is perfectly periodic. Next, the angle of attack is kept fixed at 20° and the Mach number is increased from 1.8 to 3.0 with a step of 0.4. The solutions show that the asymmetry becomes weaker as the Mach number is increased. The flow recovers its symmetry when the Mach number reaches 3.0. Passive control of the flow asymmetry has also been tentatively demonstrated by using a fin on the leeward side of the body along the plane of geometric symmetry.

Experimental research efforts have also been directed to control asymmetric flows for eliminating or attenuating the asymmetric forces and the resulting moments by using either passive-control or active-control methods. Passive-control methods include

the use of a vertical fin on the leeward side along the plane of geometric symmetry (Stahl 1989), the use of fixed or movable forebody strakes (Skow & Peak 1982; Ng 1989), or the use of a rotatable forebody tip having variable cross-section, from a circular shape at its base to an elliptic shape at its tip (Moskovitz *et al.* 1990). Active-control methods primarily include the use of blowing ports with various blowing rates and directions on the forebody surface (Ng 1990). Computational simulations have also been used to study the effectiveness of both passive (Kandil *et al.* 1990a) and active control methods (Travella *et al.* 1990).

In this paper, the unsteady, compressible, laminar, thin-layer, Navier–Stokes equations are used, along with an implicit, upwind, flux-difference splitting, finite-volume scheme to solve for steady and unsteady, asymmetric vortex flows around cones. The steady results include asymmetric flow around a circular cone and its control using side strakes. The unsteady results include the asymmetric vortex shedding around circular, elliptic- and diamond-section cones. The unsteady results for the circular cone are verified by using the FVS with the thin-layer Navier–Stokes equations and the FDS with the full Navier–Stokes equations.

2. FORMULATION

2.1. GOVERNING EQUATIONS

The three-dimensional compressible viscous flow around the body is governed by the conservative form of the dimensionless, unsteady, compressible, thin-layer Navier–Stokes equations. In terms of time-independent body-conformed coordinates ξ^1 , ξ^2 and ξ^3 , the equations are

$$\frac{\partial Q}{\partial t} + \frac{\partial E_s}{\partial \xi^s} - \frac{\partial (E_v)}{\partial \xi^3} = 0, \quad (1)$$

where

$$Q = \frac{\bar{q}}{J} = \frac{1}{J} [\rho, \rho u_1, \rho u_2, \rho u_3, \rho e]^T; \quad (2)$$

$$\begin{aligned} E_m &\equiv \text{inviscid flux} = \frac{1}{J} [\partial_k \xi^m \hat{E}_k]^T \\ &= \frac{1}{J} [\rho U_m, \rho u_1 U_m + \partial_1 \xi^m p, \rho u_2 U_m + \partial_2 \xi^m p, \rho u_3 U_m \\ &\quad + \partial_3 \xi^m p, (\rho e + p) U_m]^T, \quad m = 1, 2, 3; \end{aligned} \quad (3)$$

$(E_v)_3 \equiv$ viscous and heat-conduction flux in ξ^3 direction

$$= \frac{1}{J} [0, \partial_k \xi^3 \tau_{k1}, \partial_k \xi^3 \tau_{k2}, \partial_k \xi^3 \tau_{k3}, \partial_k \xi^3 (u_n \tau_{kn} - q_k)]^T; \quad (4)$$

$$U_m = \partial_k \xi^m u_k. \quad (5)$$

The first element of the three momentum elements of equation (4) is given by

$$\partial_k \xi^3 \tau_{k1} = \frac{M_\infty \mu}{\text{Re}} \left(\psi \partial_1 \xi^3 + \frac{\partial u_1}{\partial \xi^3} \right), \quad (6)$$

where

$$\phi = \partial_k \xi^3 \partial_k \xi^3, \quad \psi = \frac{1}{3} \partial_k \xi^3 \frac{\partial u_k}{\partial \xi^3}. \quad (7)$$

The second and third elements of the momentum elements are obtained by replacing the subscript 1, everywhere in equation (6), with 2 and 3, respectively. The last element of equation (4) is given by

$$\partial_k \xi^3 (u_n \tau_{kn} - q_k) \equiv \frac{M_\infty \mu}{\text{Re}} \left\{ \psi W + \phi \left[\frac{1}{2} \frac{\partial}{\partial \xi^3} u_s u_s + \frac{1}{(\gamma - 1) \text{Pr}} \frac{\partial (a^2)}{\partial \xi^3} \right] \right\}, \quad (8)$$

where

$$W = \partial_n \xi^3 u_n. \quad (9)$$

The reference parameters for the dimensionless form of the equations are L , a_∞ , L/a_∞ , ρ_∞ and μ_∞ for the length, velocity, time, density and molecular viscosity, respectively. The Reynolds number is defined as $\text{Re} = \rho_\infty V_\infty L / \mu_\infty$, and the pressure, p , is related to the total energy per unit mass, e , and density, ρ , by the gas equation

$$p = (\gamma - 1) \rho (e - \frac{1}{2} u_n u_n). \quad (10)$$

The viscosity, μ , is calculated from the Sutherland law

$$\mu = T^{3/2} \left(\frac{1 + C}{T + C} \right), \quad C = 0.4317, \quad (11)$$

and the Prandtl number $\text{Pr} = 0.72$.

In equations (1)–(10), the indicial notation is used for convenience. The subscripts k and n are summation indices, the superscript or subscript s is a summation index and the superscript or subscript m is a free index. The range of k , n , s and m is 1–3, and $\partial_k \equiv \partial / \partial x_k$. In equations (1)–(11), u_n is the Cartesian velocity component, U_m the contravariant velocity component, τ_m the Cartesian component of the shear stress tensor, q_k the Cartesian component of heat flux vector, a the local speed of sound and M_∞ the free-stream Mach number.

2.2. BOUNDARY AND INITIAL CONDITIONS

Boundary conditions are explicitly implemented. They include inflow-outflow conditions and solid-boundary conditions. At the plane of geometric symmetry, periodic conditions are used for symmetric or asymmetric applications on the whole computational domain (right and left domains). Since we are dealing with supersonic flows, at the far-field inflow boundaries, free-stream conditions are specified, and the conical shock is captured as part of the solution. At the far-field outflow boundaries first-order extrapolation from the interior points is used. On the solid boundary, the no-slip and no-penetration conditions are enforced, $u_1 = u_2 = u_3 = 0$, and the normal pressure gradient is set equal to zero. For the temperature, the adiabatic boundary condition is enforced on the solid boundary. The initial conditions are set equal to the free-stream conditions with $u_1 = u_2 = u_3 = 0$ on the solid boundary.

For the passive control application using side strakes, solid-boundary conditions are enforced on both sides of the strake.

3. COMPUTATIONAL SCHEMES

The principal computational scheme used to solve the governing equations is an implicit, upwind, flux-difference splitting, finite-volume scheme. It employs the



flux-difference splitting scheme of Roe. The Jacobian matrices of the inviscid flux-differences are split into left and right flux differences according to the signs of the eigenvalues of the inviscid Jacobian matrices. The smooth flux limiters are used to eliminate oscillations in the shock region. The viscous and heat-flux terms are centrally differenced. The resulting difference equation is solved using approximate factorization along the ξ^1 , ξ^2 and ξ^3 directions, respectively. The scheme is third-order accurate in space and first-order accurate in time. The computational scheme is coded in the computer program "CFL3D." Details of the scheme are given by Rumsey & Anderson (1988).

The second scheme is an implicit, approximately factored, central-difference, finite-volume scheme. Added second-order and fourth-order dissipation terms are used in the difference equation on its right-hand side terms, which represent the explicit part of the scheme. The Jacobian matrices of the implicit operator on the left-hand side of the difference equation are centrally differenced in space, and implicit second-order dissipation terms are added for the numerical stability. The left-hand side operator is approximately factored, and the difference equation is solved in three sweeps along the ξ^1 , ξ^2 and ξ^3 directions, respectively. The computational scheme is coded in the computer program "ICF3D". Details of the scheme are given by Kandil & Chuang (1989). The ICF3D code is used to verify some cases which are solved by the CFL3D code. In this paper, the ICF3D code is used to validate the steady asymmetric flow case.

A third computational scheme is used to validate the unsteady asymmetric vortex flow around the circular cone at a 30° angle of attack. This scheme is the flux-vector splitting scheme which is based on the van Leer flux-vector splitting scheme (Rumsey & Anderson 1988). This optional scheme is also coded in the computer program "CFL3D".

Since the applications in this paper cover locally conical flows only, the three-dimensional codes are used to solve for locally conical flows at the axial station $x_1 = 1$. This is achieved by forcing the conserved components of the flowfield vector, \hat{q} , to be equal at two planes located at $x_1 = 0.95$ and 1.0 . The concept of locally conical flow is explained in the next section.

4. LOCALLY CONICAL FLOWS

Locally conical solutions of the thin-layer or full Navier-Stokes equations are obtained using one of two methods. In the first method, the governing equations are transformed using the conical-coordinate transformation. Invoking the conical flow condition which requires that the flow variables be independent of the radial distance (or axial distance, depending on the transformation) from the cone apex, equating the radial distance (or axial distance) which appears in the transformed equations to a constant (equals to unity in most of the present locally conical solutions), the resulting equations are solved on one spherical (or cross-flow) surface. In the second method, the three-dimensional flow equations are solved on two spherical (or cross-flow) surfaces which are located in the very near proximity of a constant radial (or axial) distance.

During the pseudo-time or accurate-time stepping, the flowfield vector is forced to be equal at the corresponding grid centers on the two surfaces. This method is used in the present paper to obtain locally conical solutions. The resulting solutions from these two methods are the same locally conical solutions. These solutions correspond to the specified radial (or axial) distance and hence they change as the radial (or axial)

distance is changed. The reason behind that is simply because the transformed equations, according to the first method, are not self-similar and hence they are not globally conical. This is shown below by developing the transformed equations of the first method. Considering the unsteady, compressible, Navier–Stokes equations in the Cartesian coordinates,

$$\frac{\partial q}{\partial t} + \frac{\partial(\mathbf{E} - \mathbf{E}_v)_i}{\partial x_i} = 0, \quad i = 1-3, \quad (12)$$

introducing the conical coordinates,

$$\eta_1 = \frac{x_1}{x_3}, \quad \eta_2 = \frac{x_2}{x_3}, \quad \eta_3^2 = x_i x_i, \quad (13)$$

and using the chain rule, equation (12) is transformed to

$$\frac{\eta_3}{m} \frac{\partial q}{\partial t} + \frac{\partial}{\partial \eta_1} (\bar{\mathbf{E}} - \bar{\mathbf{E}}_v)_1 + \frac{\partial}{\partial \eta_2} (\bar{\mathbf{E}} - \bar{\mathbf{E}}_v)_2 + \frac{\eta_3}{m^2} \frac{\partial}{\partial \eta_3} (\bar{\mathbf{E}} - \bar{\mathbf{E}}_v)_3 + 2(\bar{\mathbf{I}} - \bar{\mathbf{I}}_v) = 0, \quad (14)$$

where

$$\begin{aligned} m &= \sqrt{1 + \eta_1^2 + \eta_2^2}, & \bar{\mathbf{E}}_1 &= \mathbf{E}_1 - \eta_1 \mathbf{E}_3, \\ \bar{\mathbf{E}}_2 &= \mathbf{E}_2 - \eta_2 \mathbf{E}_3, & \bar{\mathbf{E}}_3 &= \mathbf{E}_3 + \eta_1 \mathbf{E}_1 + \eta_2 \mathbf{E}_2, \\ \bar{\mathbf{I}} &= \bar{\mathbf{E}}_3, & \bar{\mathbf{E}}_{v1} &= \mathbf{E}_{v1} - \eta_1 \mathbf{E}_{v3}, \\ \bar{\mathbf{E}}_{v2} &= \mathbf{E}_{v2} - \eta_2 \mathbf{E}_{v3}, & \bar{\mathbf{E}}_{v3} &= \mathbf{E}_{v3} + \eta_1 \mathbf{E}_{v1} + \eta_2 \mathbf{E}_{v2}, \\ \bar{\mathbf{I}}_v &= \bar{\mathbf{E}}_{v3}. \end{aligned} \quad (15)$$

The conical flow condition requires that the flow variables be independent of the coordinate η_3 (radial distance). Invoking this condition in equation (14) by dropping the derivatives with respect to η_3 , equation (14) reduces to

$$\frac{\eta_3}{m} \frac{\partial q}{\partial t} + \frac{\partial}{\partial \eta_1} (\bar{\mathbf{E}} - \bar{\mathbf{E}}_v)_1 + \frac{\partial}{\partial \eta_2} (\bar{\mathbf{E}} - \bar{\mathbf{E}}_v)_2 + 2(\bar{\mathbf{I}} - \bar{\mathbf{I}}_v) = 0. \quad (16)$$

It is obvious that the unsteady term includes η_3 . Moreover, the viscous terms $\partial \bar{\mathbf{E}}_{v1} / \partial \eta_1$, $\partial \bar{\mathbf{E}}_{v2} / \partial \eta_2$ and $\bar{\mathbf{I}}_v$ include η_3 , and hence equation (16) is not self-similar. The explicit dependence of the viscous terms on η_3 can be shown through one of the elements of these vectors. For example, we consider

$$\begin{aligned} \frac{\partial}{\partial \eta_1} (\tau_{xx} - \eta_1 \tau_{xz}) &= \frac{M_\infty}{R_3} \frac{\partial}{\partial \eta_1} \left[\mu \left(2 \frac{\partial u_1}{\partial x} - \frac{2}{3} \left(\frac{\partial u_1}{\partial x} + \frac{\partial u_2}{\partial y} + \frac{\partial u_3}{\partial z} \right) - \eta_1 \left(\frac{\partial u_1}{\partial z} + \frac{\partial u_3}{\partial x} \right) \right) \right] \\ &= \frac{M_\infty m}{\text{Re} \eta_3} \frac{\partial}{\partial \eta_1} \left[\mu \left(\left(\frac{4}{3} - \eta_1^2 \right) \frac{\partial u_1}{\partial \eta_1} + \eta_1 \frac{\partial u_1}{\partial \eta_2} - \frac{2}{3} \frac{\partial u_2}{\partial \eta_2} - \frac{\eta_1}{3} \frac{\partial u_3}{\partial \eta_1} + \frac{2}{3} \eta_2 \frac{\partial u_3}{\partial \eta_2} \right) \right]. \end{aligned} \quad (17)$$

Thus, the unsteady term and viscous terms are scaled by the radial distance η_3 and equation (16) does not represent a globally conical flow. The best to be done to make use of this equation is to select a constant value for η_3 , and solve the resulting equation for what we call “locally conical flow”. If η_3 is assigned another constant value, the resulting equation will have another scale for the unsteady term and viscous terms. It is concluded that equation (16) becomes globally conical if the unsteady term and viscous terms vanish, and hence only the steady Euler equations are globally conical.

5. COMPUTATIONAL APPLICATIONS

5.1. STEADY ASYMMETRIC FLOW AROUND A CIRCULAR CONE

A grid of 161×81 points in the circumferential and normal directions, respectively is used. The grid is generated by using a modified Joukowski transformation with a geometric series for the grid clustering near the solid boundary. The minimum grid spacing at the solid boundary in the normal direction is 10^{-4} (the characteristic length is the conical station at $x_1 = 1$). A 5° -semi-apex angle cone at angle of attack, α , of 20° , free-stream Mach number, M_∞ , of 1.8 and Reynolds number, Re , of 10^5 is used. The maximum radius of the computational domain is $21r$, where r is the cone cross-section radius at the axial station $x_1 = 1$.

Figure 1 shows the residual error versus the number of iterations, the surface-pressure coefficient, the cross-flow velocity and the total-pressure-loss contours for the CFL3D and ICF3D codes. In the residual error figure, the CFL3D code shows that the residual error drops ten orders of magnitude, to machine zero, within 2,500 iteration steps and the solution is still symmetric. Thereafter, the error increases by six-orders of magnitude and slightly asymmetric solutions are obtained. The flow is symmetric during the first 5,000 iteration steps. Next, the error drops down by another six orders of magnitude, to machine zero again, and stays constant, and a stable steady asymmetric solution is obtained. It should be noted here that when the residual error first reaches machine zero, the machine-round-off error acts as a random asymmetric disturbance to the critically symmetric solution. Thereafter, the disturbance grows spatially, producing the asymmetric solution. The ICF3D code shows that the residual error drops five orders of magnitude in the first 3,000 iteration steps, increases two orders of magnitude in the next 2,000 iteration steps, and then drops down by three orders of magnitude within the next 5,000 iterations. The flow solution goes through a

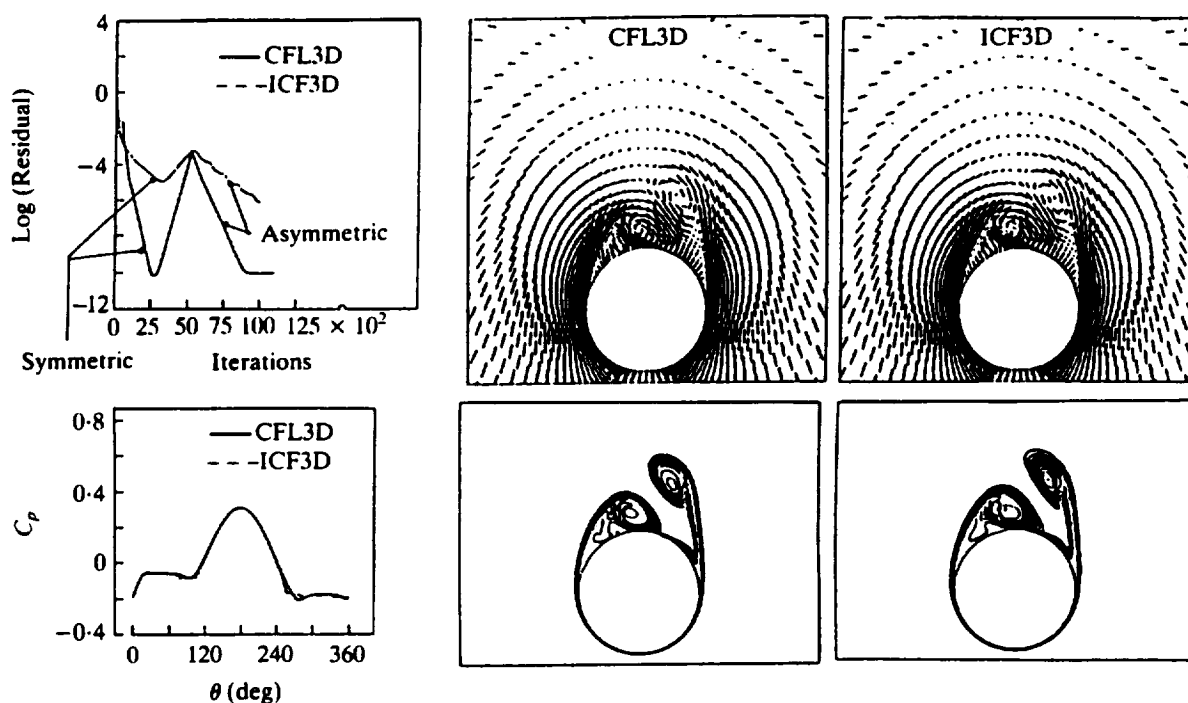


Figure 1. Comparison of steady asymmetric flow solutions around a circular cone, $\alpha = 20^\circ$, $M_\infty = 1.8$, $Re = 10^5$.



symmetric unstable solution and then to the asymmetric stable solution. The pressure coefficient curves for the two codes are in excellent agreement over the circumferential angle θ , which is measured from the leeward plane of symmetry. The suction pressure in the range of $\theta = 0-90^\circ$ is lower than that in the range of $\theta = 270-360^\circ$. The cross-flow velocity and total-pressure-loss contours for the two codes are in excellent agreement. They show the nature of the flow asymmetry and its details.

Since the residual error of the CFL3D code is much smaller than that of the ICF3D code, the disturbance which triggered the asymmetry in the first code is attributed to the machine round-off error, while the disturbance which triggered the asymmetry in the second code is attributed to the truncation error of the scheme. Both disturbances are random in nature. However, irrespective of the source of disturbance, the final asymmetric stable solution is unique. Kandil *et al.* (1990a) have shown that the solution is still unique if another source of disturbance is applied for the same critical flow

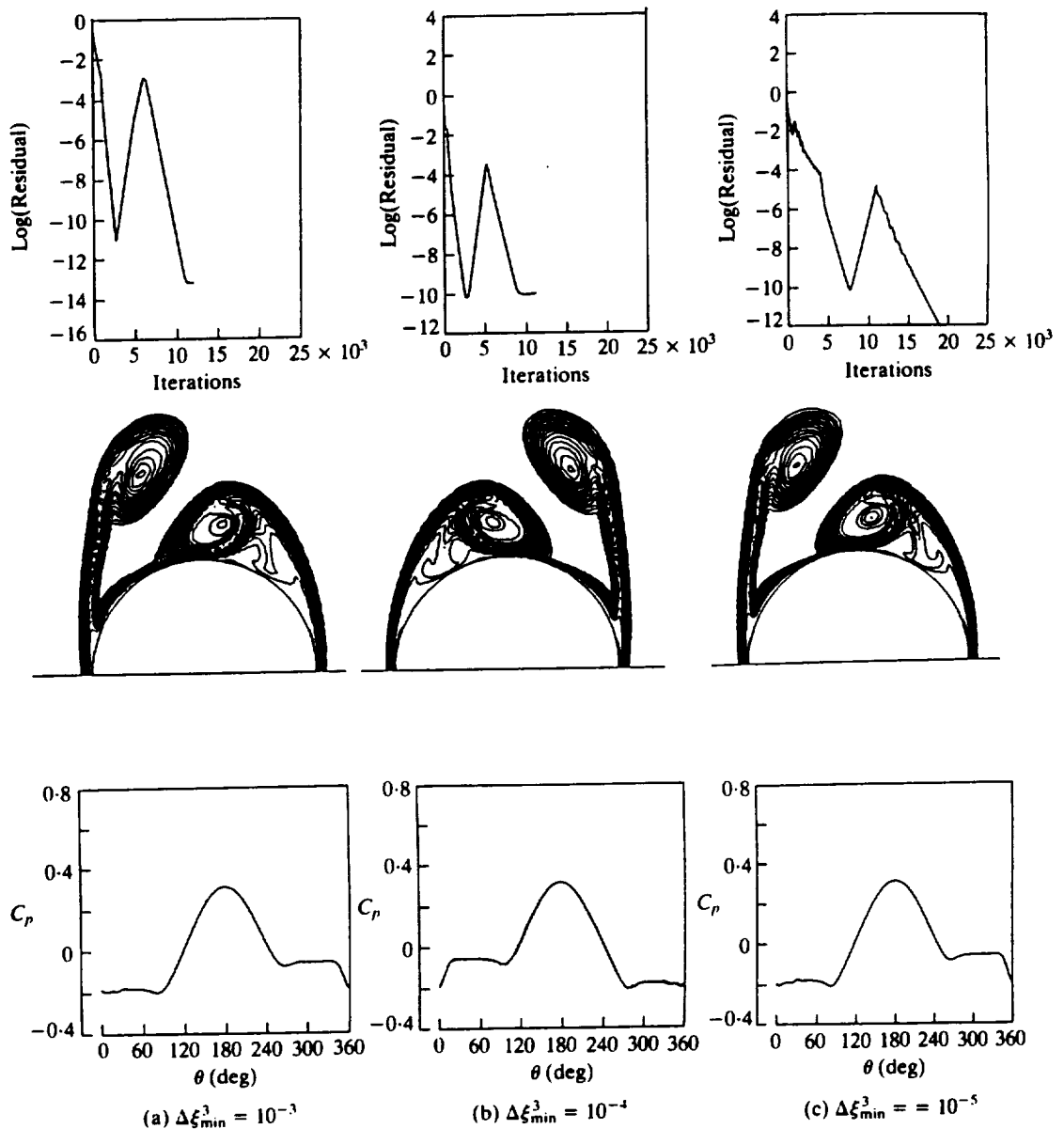


Figure 2. Effect of minimum grid size on the asymmetric flow solution; $\alpha = 20^\circ$, $M_\infty = 1.8$, $Re = 10^5$.



conditions; e.g., a 2° or 0.5° short-duration side-slip disturbance produces the same flow asymmetry.

In Figure 2, we show the effect of the minimum grid size on the flow asymmetry for the same flow conditions of the previous case. The figure shows the residual error versus the number of iterations, the total-pressure-loss contours and the surface-pressure coefficient for $\Delta\xi_{\min}^3 = 10^{-3}$, 10^{-4} and 10^{-5} at the cone surface. The histories of the residual errors are qualitatively of similar behavior. The total-pressure-loss contours show unique solutions with the exception of having the asymmetry changing sides. This is understood due to the random nature of the disturbance—a machine round-off error. The surface-pressure-coefficient curves also show unique solutions.

With all the numerical experiments given above, it is conclusively proven that the asymmetric solution is not scheme-, numerics- or disturbance-dependent.

5.2. PASSIVE CONTROL OF ASYMMETRIC FLOW USING SIDE STRAKES

Figure 3 shows the results of passive control of flow asymmetry around the circular cone of Figure 1 by using side strakes of height equal to $0.3r$. The iteration histories of the residual error, lift coefficient and side-force coefficient show the attenuation of the flow asymmetry and the final stable symmetric solution. The surface-pressure-coefficient curve, the cross-flow velocity and the total-pressure-losses contours show the final symmetric solution and the symmetric vortices associated with this controlled flow.

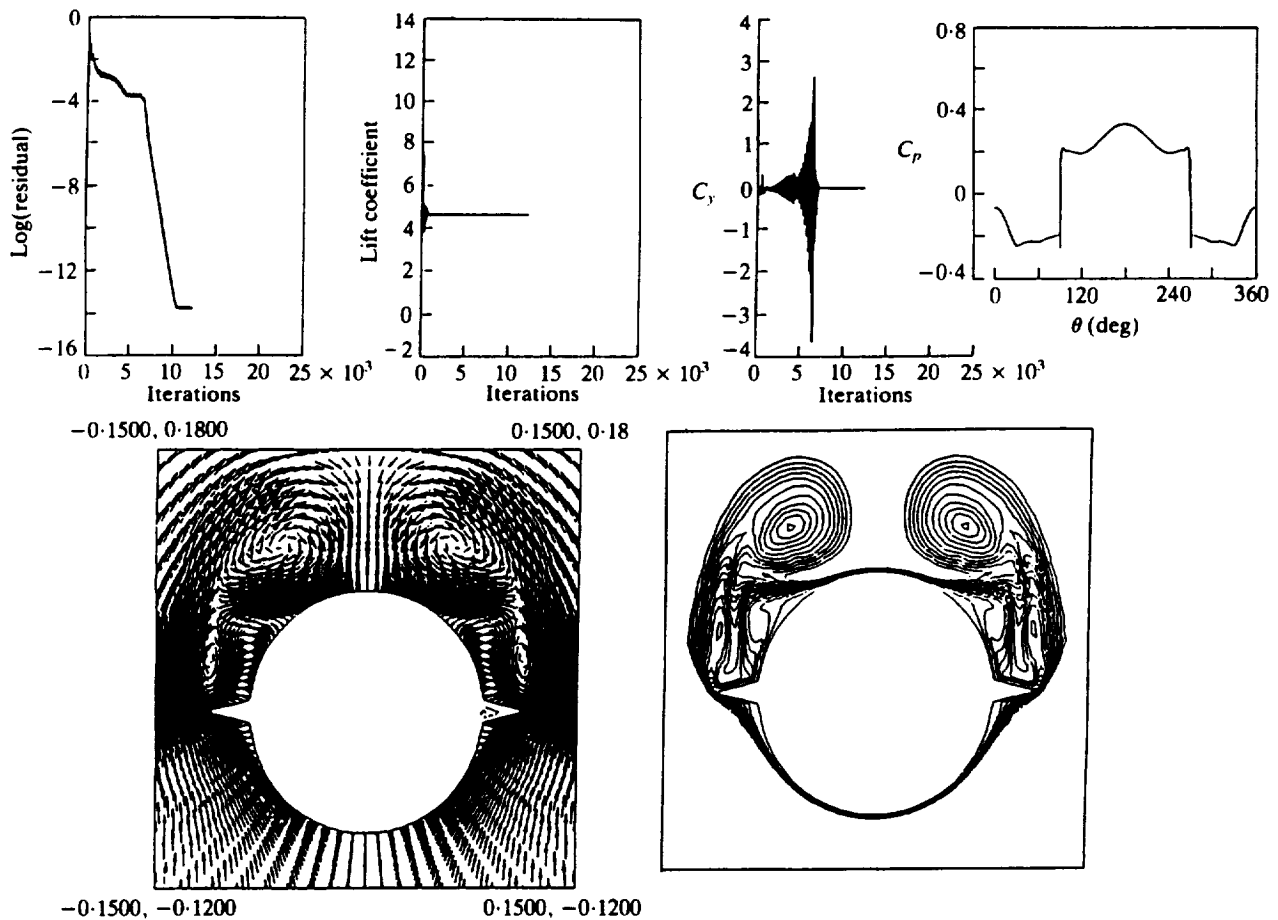
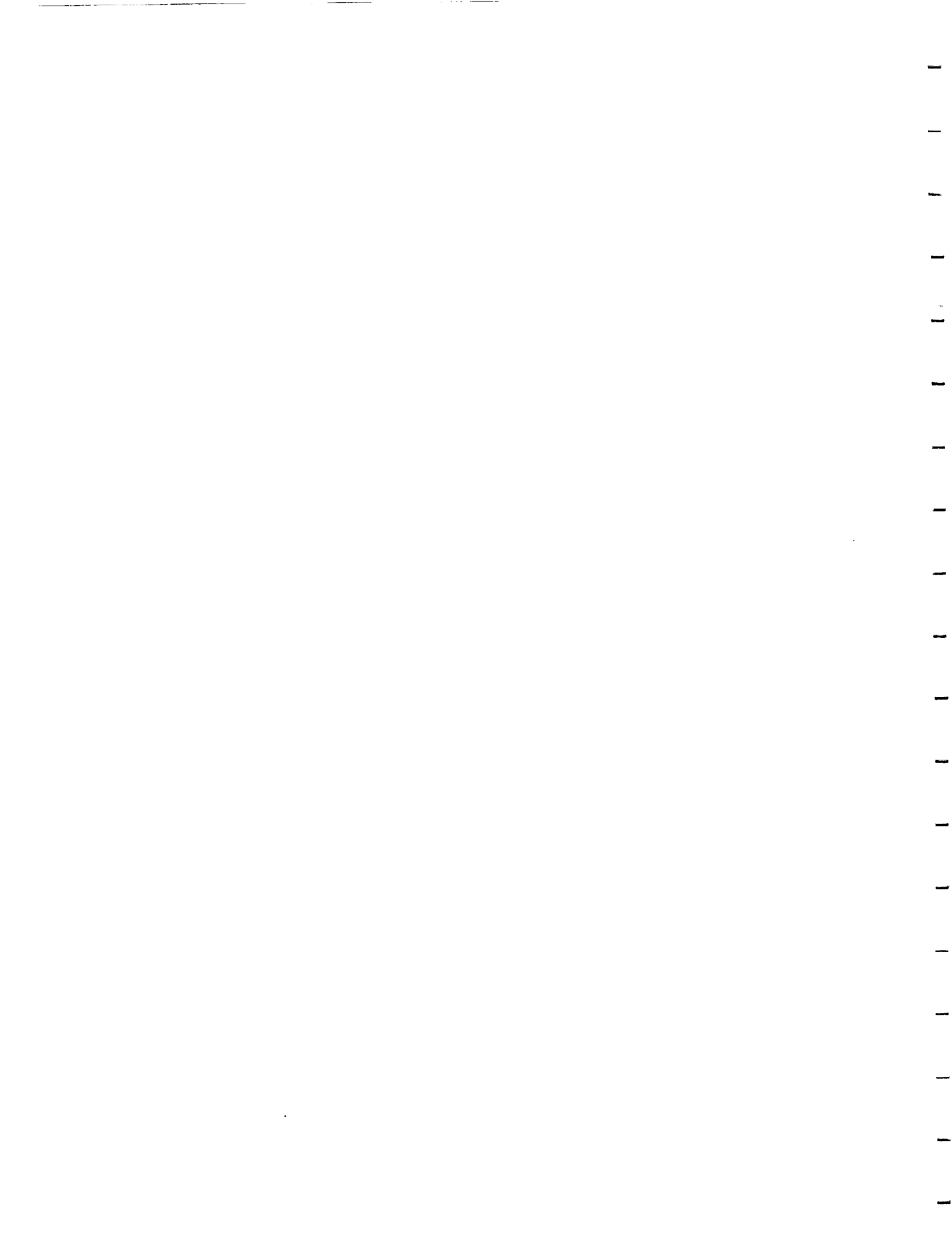


Figure 3. Passive control of asymmetric flow around a circular cone using strakes, $\alpha = 20^\circ$, $M_\infty = 1.8$, $Re = 10^5$, $h = 0.3r$ (h and r are local strake height and cone radius, respectively.).



The side strakes push the primary vortices away from the leeward plane of geometric symmetry, and hence they prevent communication of the flow disturbance from the two sides. It should also be noticed that the C_p curves of Figures 1 and 3 show that the side strakes provide additional lift besides their function of controlling the flow asymmetry.

5.3. UNSTEADY ASYMMETRIC FLOW AROUND A CIRCULAR CONE

Keeping the Mach number at 1.8 and Reynolds number at 10^5 , the angle of attack is increased to 30° for the flow around the circular cone of Figure 1. Figure 4 shows the results of this case using the FDS scheme with the thin-layer NS equations, FVS-scheme with the thin-layer NS equations and the FDS scheme with the full NS equations. Here, we show the history of the residual error, the lift coefficient and the total-pressure-loss contours. For the first solution, pseudo-time stepping was used up to

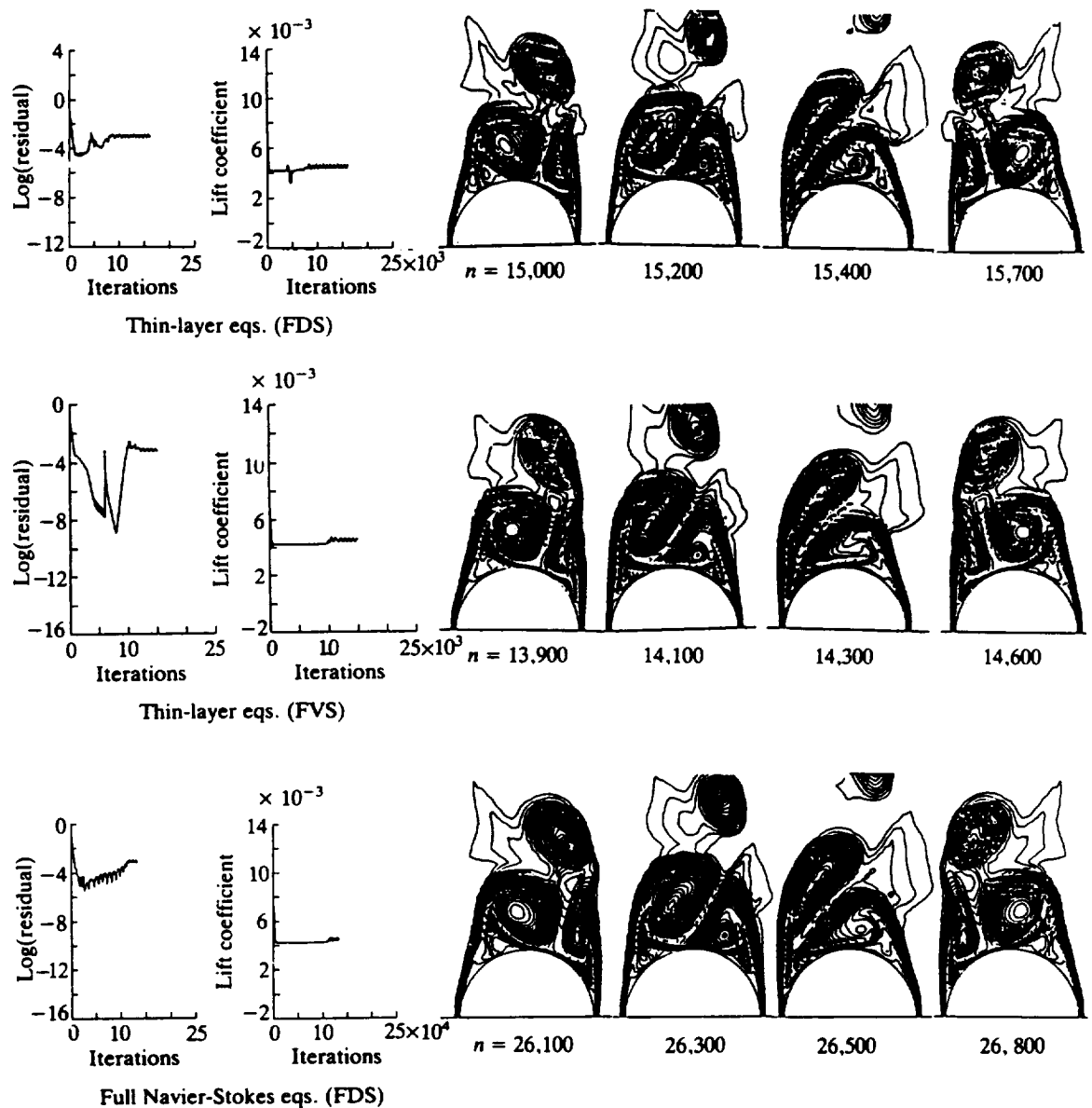


Figure 4. Comparison of unsteady asymmetric flow solutions with vortex shedding around a circular cone; periodic flow response; $\alpha = 30^\circ$, $M_\infty = 1.8$, $Re = 10^5$, $\Delta t = 10^{-3}$.



10,000 iterations and the solution was monitored every 500 iterations. The solution showed that the asymmetry was changing from the left side to the right side, which indicated a possibility of unsteady asymmetric vortex shedding. The residual error was also oscillating. The computations were repeated starting from the 3,500 iteration step using time-accurate calculations with $\Delta t = 10^{-3}$. The residual-error and lift-coefficient curves show the time history of the solution. It is seen that the residual error and the lift coefficient show a transient response which is followed by a periodic response. Snapshots of the total-pressure-loss contours are shown at time steps of $n = 15,000$; 15,200; 15,400 and 15,700. At $n = 15,000$, the asymmetric flow is seen with an already shed vortex from the right side. As time progresses, the shed vortex is convected in the flow and the primary vortex on the left side stretches upwards, while the primary vortex on the right gets stronger and expands to the left side. At $n = 15,700$, the primary vortex from the left side is shed in the flow field. It should be noticed that the solution at $n = 15,700$ is exactly a mirror image of that at $n = 15,000$. The solution from 15,000–15,700 represents one half the cycle of shedding. The solution from 15,700–16,400 represents the second one half of the cycle (not shown). The periodicity of the shedding motion is conclusively captured. The period of oscillation is $10^{-3} \times 1,400 \text{ steps} = 1.4$ which corresponds to a shedding frequency of 4.488.

Figure 4 also shows the results of the FVS scheme with the thin-layer NS equations for one-half cycle of oscillation. Using the FVS scheme, the flux limiters are turned on initially and, as can be seen from the logarithmic-residual curve, the solution becomes symmetric and steady after 5,000 time steps. Next, the flux limiters are turned off, and the solution shows a transient response up to 12,000 time steps. Thereafter, the solution becomes periodic with periodic asymmetric vortex shedding. The solution was monitored every 100 time steps, and we show snapshots of the total-pressure-loss contours between $n = 13,900$ and $n = 14,600$. Although the process of adjusting the time instants in order to match those of the FDS solution is difficult, it is seen that the captured snapshots of the FVS solution almost match those of the FDS solution. Comparing the FVS solutions at $n = 13,900$ and 14,600, it is seen that they are mirror images of each other. Hence, periodic flow response has been achieved with a period of $1,400 \times 10^{-3} = 1.4$; which is exactly the same period of shedding as that of the FDS solution. This pinpoints the high numerical dissipation effect of the FVS scheme when the flux limiters are also turned on. The resulting numerical dissipation in the FVS scheme is large enough to dampen the random disturbances of the flow solution. By turning off the flux limiters in the FVS scheme, the random disturbances grow, producing the asymmetric unsteady vortex shedding. This also shows that the FDS scheme, even with the flux limiters turned on, is less dissipative than the FVS scheme. Finally, we show the results of the FDS-scheme with the full NS equations. The solution conclusively confirms the previous solutions and hence the unsteady solution is not scheme- or equation-dependent.

Figure 5 shows snapshots of the surface-pressure coefficient using the FDS and FVS schemes with the thin-layer NS equations. They are in excellent agreement with each other. The oscillation of the side force is clearly seen in this figure.

5.4. UNSTEADY ASYMMETRIC FLOW AROUND AN ELLIPTIC SECTION CONE, $f_r = 0.8$

Figure 6 shows the solution for an elliptic-section cone with fineness ratio of 0.8. The residual-error curve shows that the solution produces a symmetric flow through the first 5,000 time steps. Afterwards, the solution shows a transient unsteady flow response for 2,500 time steps which is followed by an unsteady, perfectly periodic, vortex-shedding



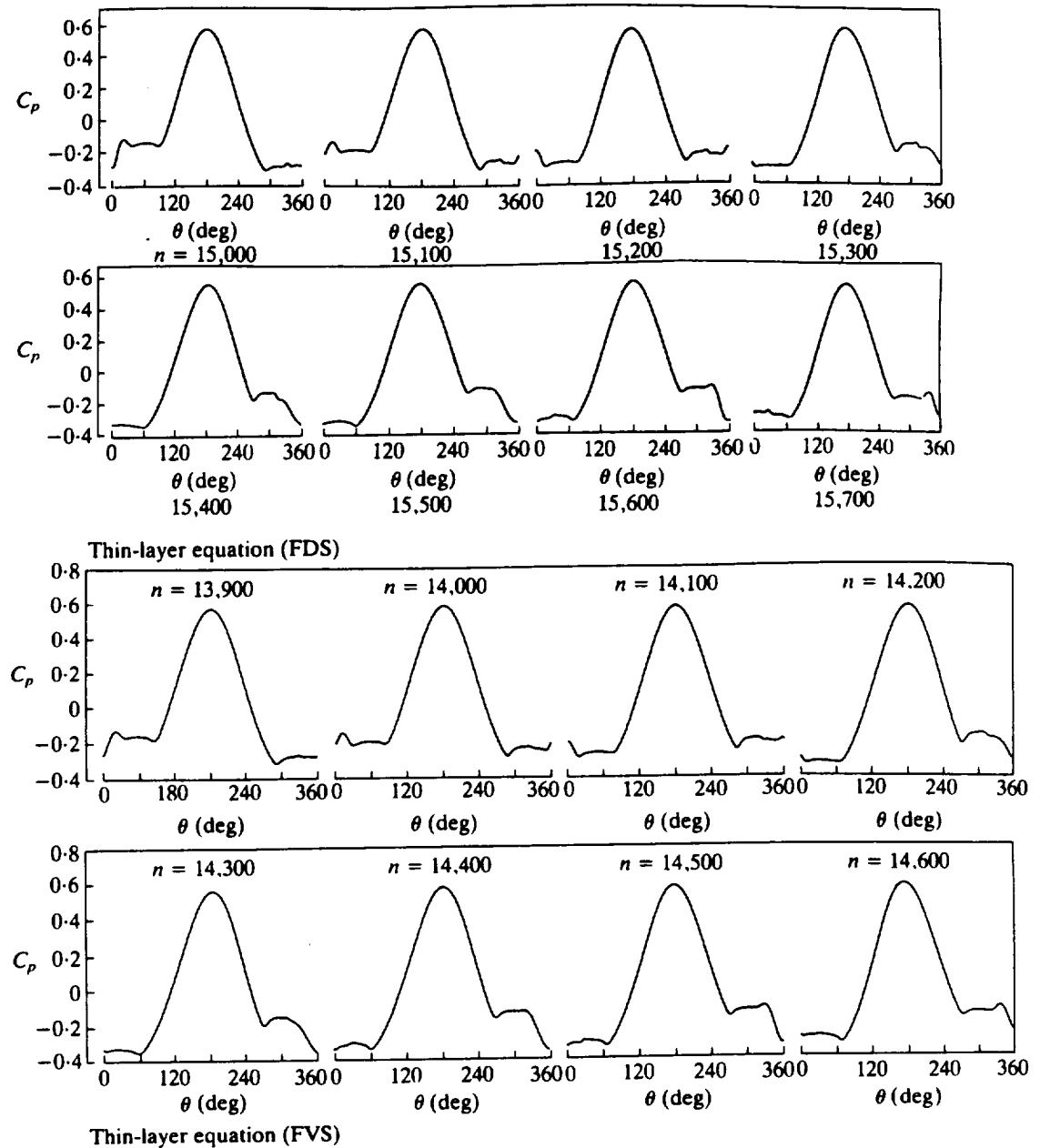


Figure 5. Comparison of snapshots of surface-pressure coefficients around a circular cone; $\alpha = 30^\circ$, $M_\infty = 1.8$, $Re = 10^5$, $\Delta t = 10^{-3}$.

solution. The lift-coefficient curve shows the same nature of the solution as that of the residual-error curve. This case is carried out using time-accurate stepping with $\Delta t = 10^{-3}$.

We also show snapshots of the total-pressure-loss contours and surface-pressure coefficients at the time steps of 12,000, 12,500, 13,000, 13,500, 14,000 and 14,500. The solutions at $n = 12,000$ and $14,500$ are mirror images of each other which confirm that the solution is periodic. The period of oscillation is $5,000 \times 10^{-3} = 5$ which corresponds to a shedding frequency of 1.257. At $n = 12,000$, the total-pressure-loss contours show that the right-side vortex is stretched, having two vortices; one at the top and the second one below it. In addition, a secondary vortex is seen at the surface. The left-side vortex has expanded to the right with two vortices beneath it. At $n = 12,500$,

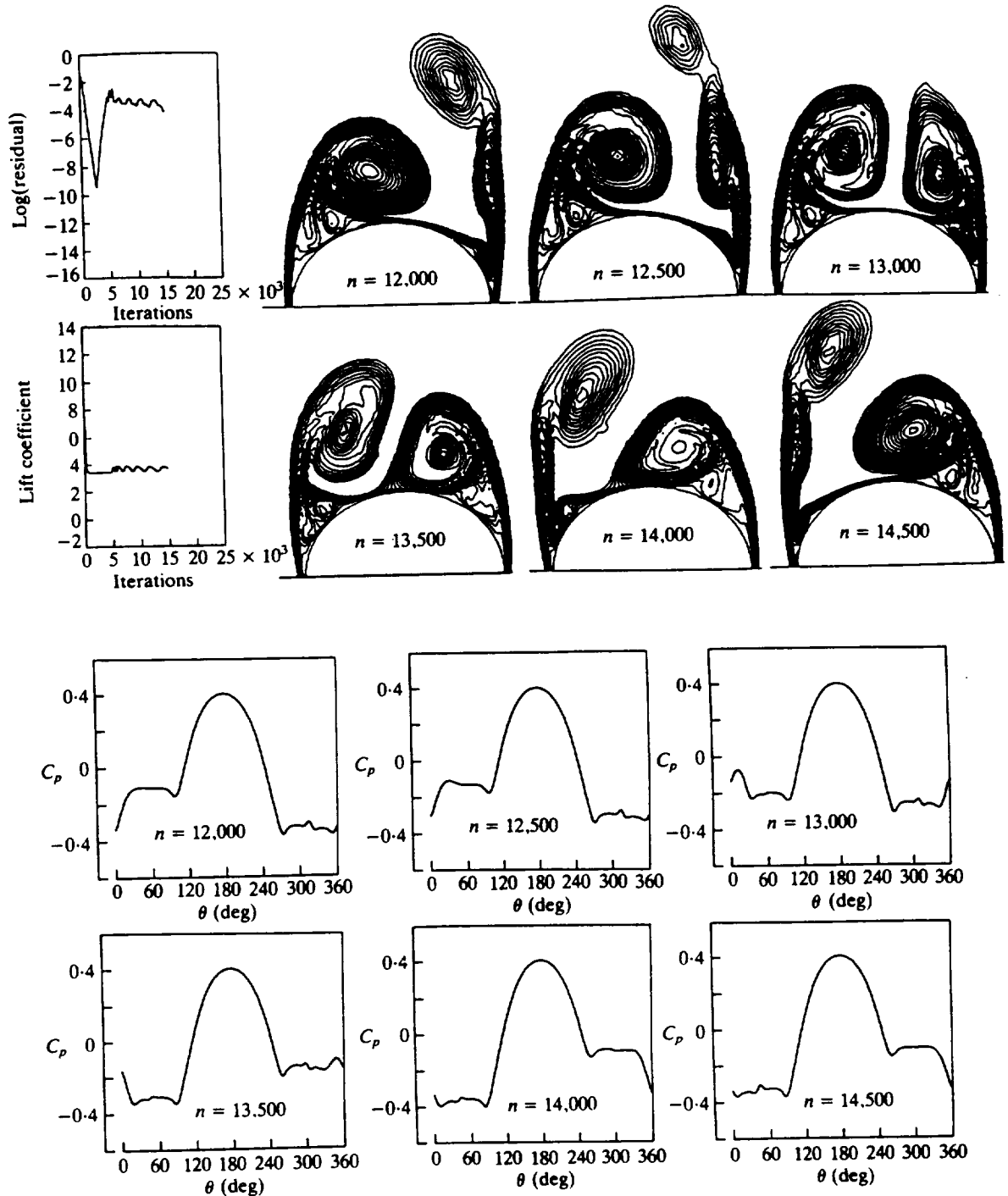


Figure 6. Unsteady asymmetric flow solution with vortex shedding around an elliptic-section cone; periodic flow response; $\alpha = 25^\circ$, $M_\infty = 1.5$, $Re = 10^5$, $f_r = 0.8$, $\Delta t = 10^{-3}$.

the top vortex on the right side has been almost shed while the one below it is expanding. At $n = 13,000$, the top vortex on the right side has been shed and convected with the flow, while the vortex below it is expanding to the left. As time passes, the vortex on the left side is stretching upwards and the vortex on the right side is expanding to the left, as seen from the snapshots at 13,000, 13,500 and 14,000. At $n = 14,500$, the vortices on the left side and right side become mirror images of those on the right side and left side, respectively, at $n = 12,000$. Again, this case conclusively shows that unsteady vortex-shedding flows are captured.

5.5. UNSTEADY ASYMMETRIC FLOW AROUND AN ELLIPTIC-SECTION CONE, $f_r = 0.2$ (THICK WING CASE)

This case is presented to show that asymmetric vortex shedding also exists for wing-like sections. Here, the elliptic-section fineness ratio is reduced to 0.2. To obtain this impressive flow case, we have to decrease the free-stream Mach number to 1.4, increase the angle of attack to 34° and increase the free-stream Reynolds number to 2×10^6 . These adjustments have been made to enhance the critical flow conditions for flow asymmetry. For the same section fineness ratio, same angle of attack and same free-stream Mach number and for free-stream Reynolds number range of 10^5 – 1.5×10^6 , the flow is either symmetric or steady asymmetric. It is unsteady only when the Reynolds number is increased to 2×10^6 .

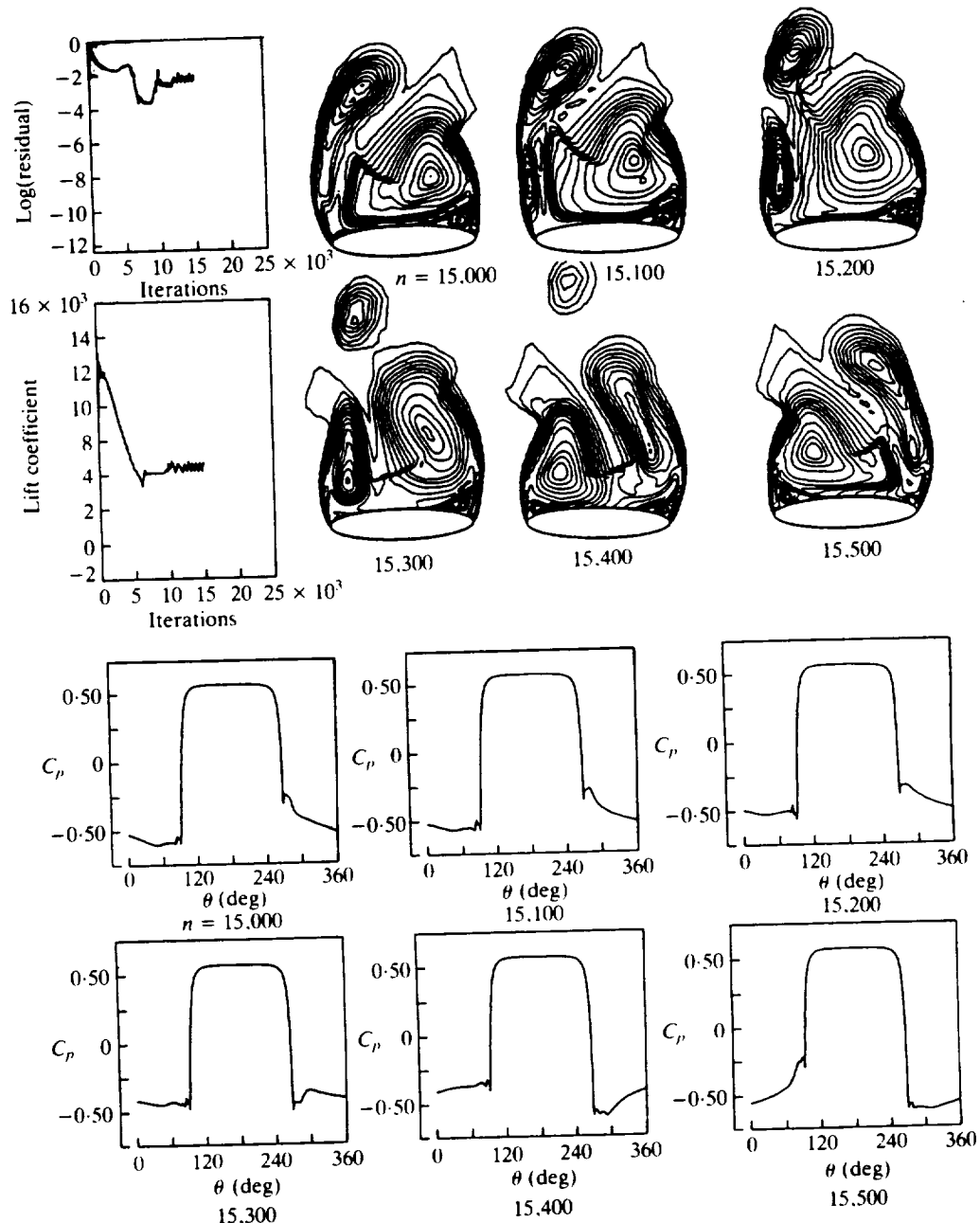


Figure 7. Unsteady asymmetric flow solution with vortex shedding around an elliptic-section cone (a thick wing); periodic flow response; $\alpha = 34^\circ$, $M_\infty = 1.4$, $Re = 2 \times 10^6$, $f_r = 0.2$, $\Delta t = 2 \times 10^{-3}$.

Figure 7 shows the time-accurate ($\Delta t = 2 \times 10^{-3}$) results of this case which includes the time-history of residual error, the time-history of the lift coefficient, snap shots of the total-pressure-loss contours and snapshots of the surface-pressure coefficients. The snapshots at $n = 15,000, 15,100, 15,200, 15,300, 15,400$ and $15,500$ represent approximately one-half the cycle of the periodic flow response. The total-pressure-loss contour at $n = 15,000$ shows that the left-side vortex is stretched, while the right-side vortex has expanded, covering a large region of the left side of the flow domain over the wing. Under the right-side vortex, a strong secondary vortex is formed. At $n = 15,100$, the left-side vortex shows two regions of vortical flows; one at the top and another one below it. Both vortex regions of the left vortex rotate in the same clockwise direction. At $n = 15,200$, the top vortex is shed into the flow field, while the one below it gets stronger and stretches upwards. At $n = 15,300$ and $15,400$, the shed vortex from the left side is convected in the flow, the left vortex is expanding to the right and convecting vorticity to the right vortex. The right vortex is getting stronger, shrinking in thickness and stretching upwards. A secondary vortex is forming under the left vortex, and the secondary vortex under the right vortex is diminishing, at $n = 15,500$, the flow is approximately a mirror image of that at $n = 15,000$. The number of time steps for one cycle of periodic response is 1050, which gives a period of oscillation of $2 \times 10^{-3} \times 1,050 = 2.1$ corresponding to a frequency of 2.992.

5.6. UNSTEADY ASYMMETRIC FLOW AROUND A DIAMOND-SECTION CONE, $f_4 = 0.2$ (THICK WING CASE)

Figure 8 shows the results of the time-accurate ($\Delta t = 5 \times 10^{-4}$) results for this case which include snapshots of the total-pressure-loss contours and snapshots of the surface-pressure coefficients. The snapshots are given at $n = 11,500, 12,000, 12,500, 13,000, 13,500$ and $14,000$. The number of time steps for one cycle of periodic response is 4,500, which gives a period of oscillation of $5 \times 10^{-4} \times 4,500 = 2.25$ corresponding to a frequency of 2.793. It should be noted here that the angle of attack is 38° , which is higher than that of the elliptic-section cone of Figure 7, where the angle of attack is 34° and all the other flow conditions are the same. Comparing the surface pressure curves of the elliptic-section wing (Figure 7) and the diamond-section wing (Figure 8), we conclude that the diamond-section wing has less asymmetric strength and higher lift coefficient than those of the elliptic-section wing.

6. CONCLUDING REMARKS

The unsteady, compressible, thin-layer, Navier–Stokes equations are used along with several computational schemes to numerically simulate steady and unsteady asymmetric vortex flows around cones. The concept of the locally conical flow assumption has been developed and discussed. A steady asymmetric flow solutions has been presented and verified for a circular cone. Passive control of the flow asymmetry has been demonstrated for the circular cone by using side strakes. Unsteady, asymmetric vortex flows with periodic vortex shedding have been presented for cones with a circular section, an elliptic section of fineness ratio of 0.8, an elliptic section of fineness ratio of 0.2 and a diamond section of fineness ratio of 0.2. The unsteady asymmetric flow solution for the circular cone has been verified using two schemes with the thin-layer and full NS equations. The present study shows that, for the same flow conditions, circular section cones produce the strongest flow asymmetry while the diamond section cones produce the weakest flow asymmetry. It is conclusive that unsteady flow asymmetry with vortex shedding has been captured. It should be noted

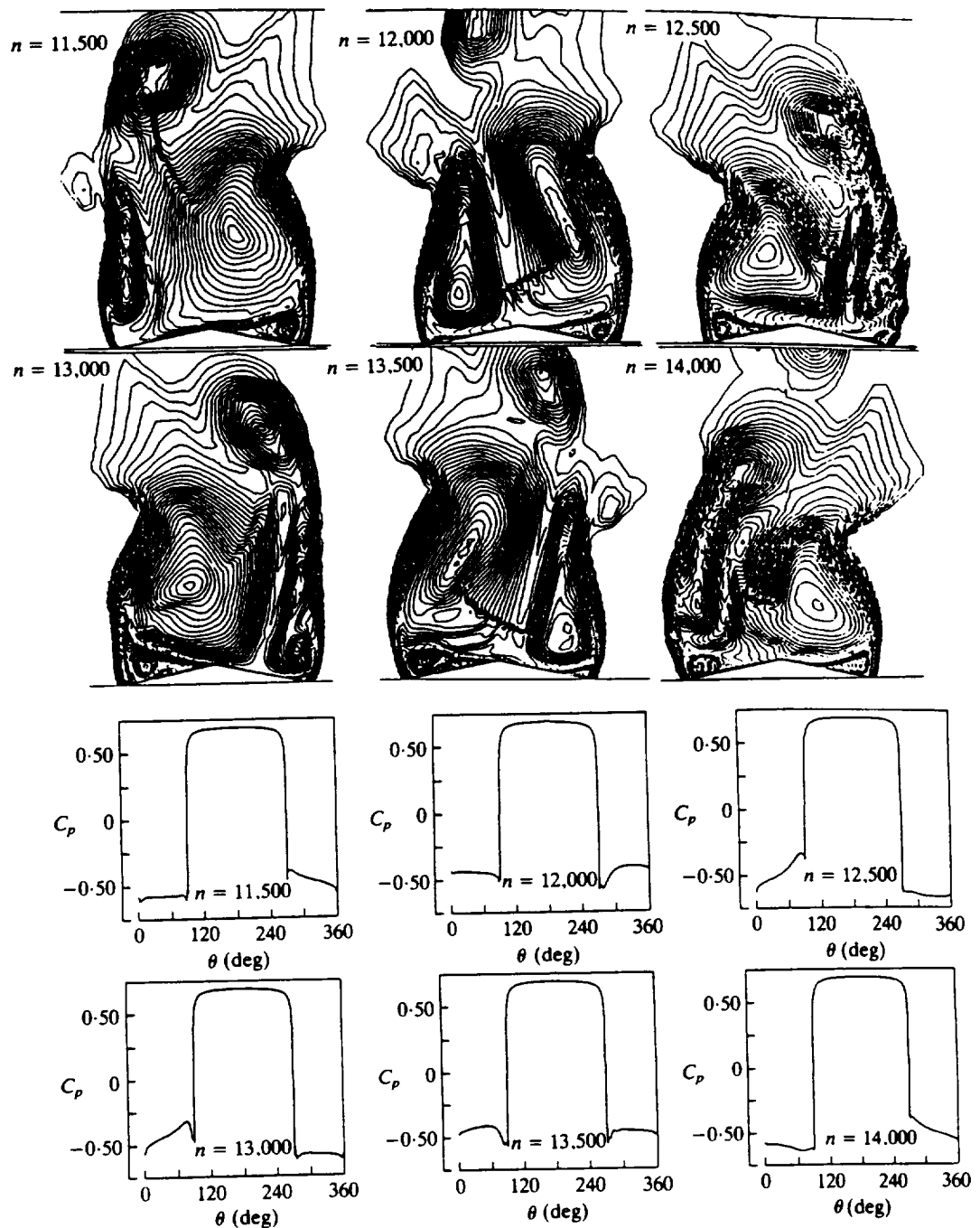


Figure 8. Unsteady asymmetric flow solution with vortex shedding around a diamond-section cone (a thick wing), periodic flow response, $\alpha = 38^\circ$, $M_\infty = 1.4$, $Re = 2 \times 10^6$, $f_r = 0.2$, $\Delta t = 5 \times 10^{-4}$.

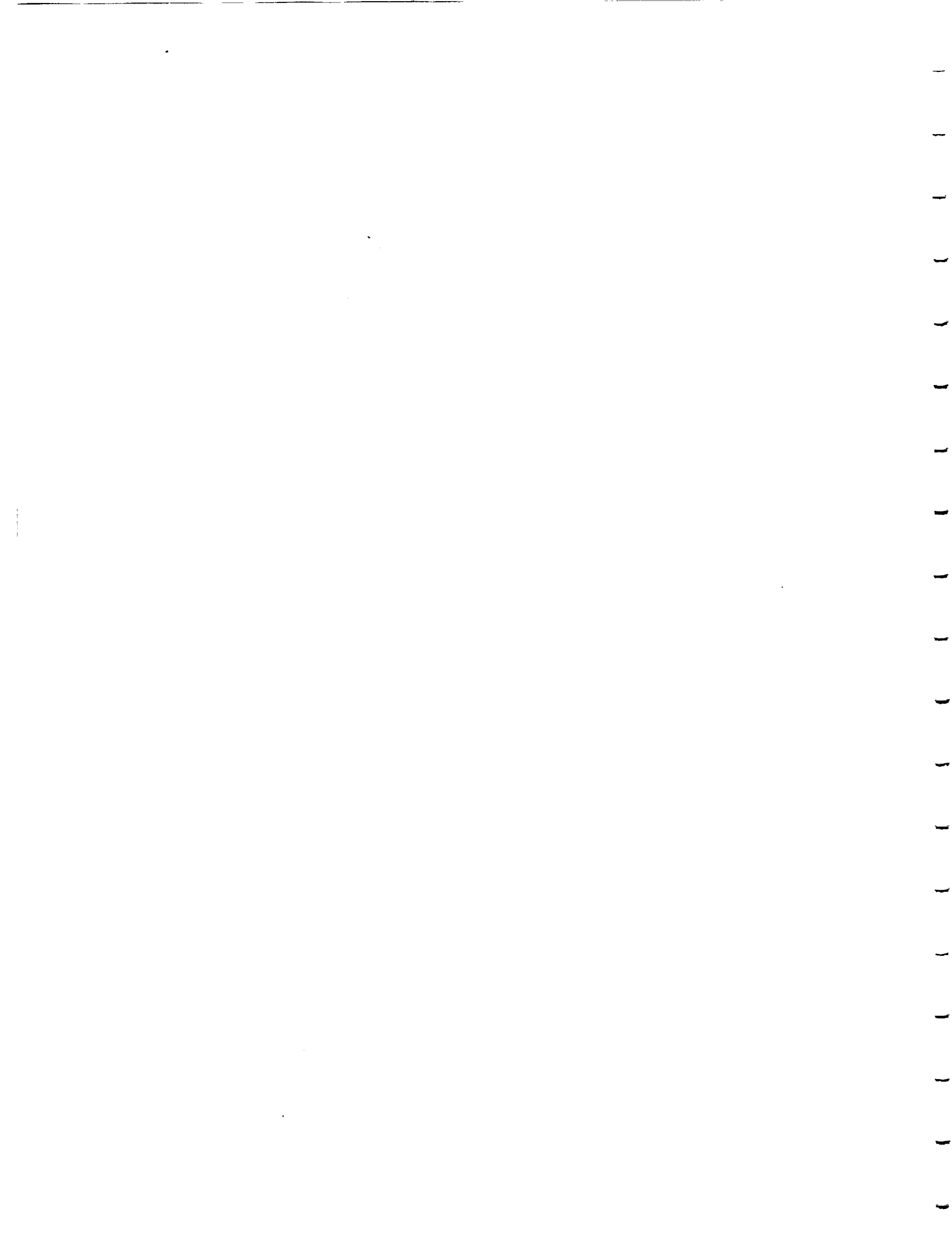
that these solutions are based on the locally conical flow assumption and hence they must not be used for quantitative comparisons with three-dimensional flow results. The reason behind such a restriction is the length scale involved with the unsteady and viscous terms of the locally conical NS equations. However, the solutions are computationally economical for qualitative and parametric studies of asymmetric flows.

ACKNOWLEDGEMENT

This research work is supported by the NASA Langley Research Center under Grants No. NAS1-18584-71 and NAG-1-994.

REFERENCES

- FIDDLES, S. P. 1989 Recent developments in the production of separated flow past slender bodies at incidence. In *Proceedings Royal Aeronautical Society Conferences on Prediction and Exploitation of Separated Flows*, pp. 31.1–31.17, London, U.K.
- KANDIL, O. A. & CHUANG, H. A. 1989 Unsteady Navier–Stokes computations past oscillating delta wings at high incidence. AIAA Paper No. 89-081. Also *AIAA Journal* **28**, 1565–1572.
- KANDIL, O. A., WONG, T.-C. & LIU, C. H. 1990a. Prediction of steady and unsteady asymmetric flows around cones. AIAA Paper No. 90-0598.
- KANDIL, O. A., WONG, T.-C. & LIU, C. H. 1990b Asymmetric supersonic flow around cones with noncircular sections. *AGARD Conference Proceedings No. 493, Missile Aerodynamics*, pp. 16.1–16.11.
- KEENER, E. R. & CHAPMAN, G. R. 1977 Similarity in vortex asymmetries over slender bodies and wings. *AIAA Journal* **15**, 1370–1372.
- LAMONT, P. J. 1980 Pressure around an inclined ogive cylinder with laminar, transitional and turbulent separation. *AIAA Journal* **20**, 1492–1499.
- LAMONT, P. R. 1982 The complex asymmetric flow over a 3.5D ogive nose and cylindrical afterbody at high angles of attack. AIAA Paper No. 82-0053.
- MARCONI, F. 1988 Asymmetric flows about sharp cones in a supersonic stream. In *Proceedings of 11th International Conference on Numerical Methods in Fluid Dynamics*, Williamsburg, VA, U.S.A.
- MOSKOVITZ, C., HALL, R. & DEJARNETTE, F. 1990 Experimental investigation of a new device to control asymmetric flowfield on forebodies at large angles of attack. AIAA Paper No. 90-0069.
- NG, T. T. 1989 On leading edge vortex and its control. AIAA Paper no. 89-3346-CP.
- NG, T. T. 1990 Aerodynamic control of NASP-type vehicles through vortex manipulation. AIAA Paper No. 90-0594.
- PEAKE, D. J., OWEN, F. K. & HIGUCHI, H. 1979 Symmetrical and asymmetrical separations about a yawed cone. *AGARD CP-247*, 16.1–16.27.
- PEAKE, D. J. & TOBAK, M. 1982 Three-dimensional flows about simple components at angle of attack. *AGARD LS-121, High angle-of-attack aerodynamics*, 2.1–2.56.
- REDINIOTIS, O., STAPOUNTZIS, H. & TELIONIS, D. P. 1988 Vortex shedding over nonparallel edges. VPI & SU Engineering Report, VPI-88-39.
- RUMSEY, L. C. & ANDERSON, W. K. 1988 Some numerical aspects of unsteady Navier–Stokes computations over airfoils using dynamic meshes. AIAA Paper No. 88-0329.
- SHANKS, R. E. 1963 Low subsonic measurements of static and dynamic stability derivatives of six flat plate wings having leading-edge sweep angles of 70°–84°. NASA TND-1822.
- SICLARI, M. J. & MARCONI, F. 1989 Computations of Navier–Stokes solutions exhibiting asymmetric vortices. AIAA Paper No. 89-1817.
- SKOW, A. M. & PEAKE, D. J. 1982 Control of forebody vortex orientation by asymmetric air injection (Part B)—Details of the flow structure. *AGARD LS-121, High angle-of-attack aerodynamics*, 10.1–10.22.
- STAHL, W. 1989 Suppression of asymmetry of vortex flow behind a circular cone at high incidence. AIAA Paper No. 89-3372-CP.
- TRAVELLA, D. A., SCHIFF, L. B. & CUMMINGS 1990 Pneumatic vortical flow control at high angles of attack. AIAA Paper No. 90-0098.



15-34

N 9 3 - 1 2 9 9 7

Passive Control of Supersonic Asymmetric Vortical Flows around Cones

C. H. LIU

*Theoretical Flow Physics Branch, NASA Langley Research Center,
Hampton, Virginia 23665-5225*

AND

OSAMA A. KANDIL AND TIN-CHEE WONG

*Department of Mechanical Engineering and Mechanics, Old Dominion University,
Norfolk, Virginia 23529-0247*

Received November 27, 1990

C. H. Liu, Osama A. Kandil, and Tin-Chee Wong, Passive Control of Supersonic Asymmetric Vortical Flows around Cones. *IMPACT of Computing in Science and Engineering* 4, 80-96 (1992).

The unsteady, compressible, thin-layer Navier-Stokes equations are used to numerically study the passive control of steady and unsteady supersonic asymmetric flows around circular and noncircular cones. The main computational scheme of the present study is an implicit upwind, flux-difference splitting, finite-volume scheme. Passive control of flow asymmetry is studied by using a vertical fin in the leeward plane of geometric symmetry and side strakes with and without thickness at different orientations. The study focuses on circular-section cones since they are the most likely section-shapes for strong flow asymmetry. Side-strake passive control is shown to be more efficient and practical than vertical-fin passive control. © 1992 Academic Press, Inc.

INTRODUCTION

In the moderate to high angle-of-attack (AOA) ranges, which are typical flight conditions for highly maneuverable fighter aircraft and missiles, extensive regions of vortex-dominated flow develop on the vehicle.

Within these AOA ranges, the cross-flow velocity components and the gradients of other flow variables become of the same order of magnitude as or higher than those of the axial direction. Consequently, flow separation occurs and vortices emanate from the three-dimensional separation lines of boundary-layer flows on wings, strakes, and fuselage of the vehicle. If the vortices are symmetric and stable, their influence can be exploited favorably to provide high lift and maneuverability for the vehicle. On the other hand, if the vortices

4830-4
17P



become asymmetric or if vortex breakdown occurs, the useful influence of the vortices is terminated. Large side forces, asymmetric lifting forces, and corresponding yawing, rolling, and pitching moments, which may be larger than those provided by the vehicle control system, develop and jeopardize flight safety. The onset of buffeting due to vortex breakdown is another unfavorable vortex-induced phenomenon.

Highly swept, round- and sharp-leading-edge wings, and pointed slender bodies are common aerodynamic components of fighter aircraft and missiles. The study of vortex-dominated flow around these isolated aerodynamic components adds to our basic understanding of vortex-dominated flows. The solution of asymmetric vortex flow about slender bodies in the high AOA range is vital to the dynamic stability and controllability of fighter aircraft and missiles. The onset of flow asymmetry occurs when the relative incidence (ratio of angle of attack to nose semiapex angle) of pointed forebodies exceeds certain critical values. At these critical values of relative incidence, flow asymmetry develops due to natural and/or forced disturbances. The origin of natural disturbances may be a transient sideslip, an acoustic disturbance, or a similar disturbance of short duration. Forced disturbances, however, are caused by geometric perturbations due to imperfections in the nose geometric symmetry or similar disturbances of a permanent nature. In addition to the relative incidence as one of the determinable parameters for the onset of flow asymmetry, the freestream Mach number, Reynolds number, and body cross-section shape are important determinable parameters.

Several computational attempts have been made to simulate asymmetric vortical flows around slender bodies [1-7]. Kandil, Wong, and Liu [5] used the unsteady thin-layer Navier-Stokes equations along with two different implicit schemes to simulate asymmetric vortex flows around cones with different cross-section shapes. The numerical investigation was focused on a 5° -semi-apex angle circular cone under locally conical flow assumption. The first computational scheme was an upwind, flux-difference splitting, finite-volume scheme and the second one was an implicit, central-difference, finite-volume scheme. The Mach number and Reynolds number being held constant at 1.8 and 10^5 , respectively, the angle of attack (α) was varied from 10° to 30° . At $\alpha = 10^\circ$, a steady symmetric solution was obtained and the results of the two schemes were in excellent agreement. At $\alpha = 20^\circ$ and irrespective of the type or level of the disturbance, a steady asymmetric solution was obtained and the results of the two schemes were in excellent agreement. Two types of flow disturbances were used; a random round-off error or a random truncation-error disturbance, and a controlled transient sideslip disturbance with short duration. For the controlled transient sideslip disturbance the solution was unique, and for the uncontrolled random disturbance the solution was also unique with the exception of having the same asymmetry changing sides on the cone. At $\alpha = 30^\circ$, an unsteady asymmetric solution with vortex shedding was obtained, and the vortex shedding was perfectly periodic. Next, the angle

of attack was kept fixed at 20° and the Mach number was increased from 1.8 to 3.0 in increments of 0.4. The solutions showed that the asymmetry became weaker as the Mach number was increased. The flow recovered its symmetry when the Mach number reached 3.0. Selected solutions of steady and unsteady asymmetric flows were also presented for cones with elliptic and diamond cross-sectional areas.

In a later paper by the present authors [6], several issues related to the asymmetric flow solutions were addressed. It was shown that a unique asymmetric flow solution is obtained irrespective of the size of the minimum grid spacing at the solid boundary. The asymmetry could reverse sides due to the random nature of the disturbance. It was also shown that for the same flow conditions and same section fineness ratio, diamond-section cones with sharp edges have less flow asymmetry than elliptic-section cones. Again, it was also shown that unsteady periodic asymmetric flow with vortex shedding is predicted. In Ref. [7] by Kandil, Wong, and Liu, several unsteady, asymmetric vortex flows with periodic vortex shedding for circular and noncircular-section cones were presented and studied.

Experimental research efforts have also been made to control asymmetric flows for eliminating or attenuating the asymmetric forces and the resulting moments by using either passive-control [8-10] or active-control [11-13] methods. Passive-control methods include the use of a vertical fin on the leeward side along the plane of geometric symmetry [8], the use of fixed or movable forebody strakes [9-12], or the use of a rotatable forebody tip having variable cross section (from a circular shape at its base to an elliptic shape at its tip [10]). Active control methods primarily include the use of blowing ports with various blowing rates and directions on the forebody surface [11, 12]. Computational simulations have also been used to study the effectiveness of both passive [5] and active control methods [13].

In the present paper, we present a computational study for passive control of supersonic asymmetric vortical flows around cones using a vertical fin in the leeward plane of geometric symmetry and side strakes with and without thickness at different orientations. Although the present study has been focused on passive control of circular-section cones, a few applications have been considered for noncircular-section cones.

FORMULATION

Governing Equations

The three-dimensional, compressible, viscous flow around the body is governed by the conservative form of the dimensionless, unsteady, compressible Navier-Stokes equations. Introducing the time-independent body-conforming coordinates ξ^1 , ξ^2 , and ξ^3 , and applying thin-layer approximations to the governing equations in ξ^2 and ξ^3 directions yields the transformed equations



$$\frac{\partial \bar{Q}}{\partial t} + \frac{\partial \bar{E}_s}{\partial \xi^s} - \frac{\partial (\bar{E}_v)_2}{\partial \xi^2} - \frac{\partial (\bar{E}_v)_3}{\partial \xi^3} = 0; \quad s = 1, 2, 3, \quad (1)$$

where

$$\bar{Q} = \frac{\hat{q}}{J} = \frac{1}{J} [\rho, \rho u_1, \rho u_2, \rho u_3, \rho e]^t \quad (2)$$

$\bar{E}_s \equiv$ inviscid flux

$$= \frac{1}{J} [\rho U_s, \rho u_1 U_s + \partial_1 \xi^s p, \rho u_2 U_s + \partial_2 \xi^s p, \rho u_3 U_s + \partial_3 \xi^s p, (\rho e + p) U_s]^t; \quad s = 1, 2, 3 \quad (3)$$

$(\bar{E}_v)_2 \equiv$ viscous and heat-conduction flux in the ξ^2 direction

$$= \frac{1}{J} [0, \partial_k \xi^2 \tau_{k1}, \partial_k \xi^2 \tau_{k2}, \partial_k \xi^2 \tau_{k3}, \partial_k \xi^2 (u_n \tau_{kn} - q_k)]^t \quad (4)$$

$(\bar{E}_v)_3 \equiv$ viscous and heat-conduction flux in the ξ^3 direction

$$= \frac{1}{J} [0, \partial_k \xi^3 \tau_{k1}, \partial_k \xi^3 \tau_{k2}, \partial_k \xi^3 \tau_{k3}, \partial_k \xi^3 (u_n \tau_{kn} - q_k)]^t \quad (5)$$

$$U_s = \partial_k \xi^s u_k. \quad (6)$$

The first of the three momentum elements of Eq. (5) is given by

$$\partial_k \xi^3 \tau_{k1} \equiv \frac{M_\infty \mu}{\text{Re}} \left(\psi \partial_1 \xi^3 + \phi \frac{\partial u_1}{\partial \xi^3} \right), \quad (7)$$

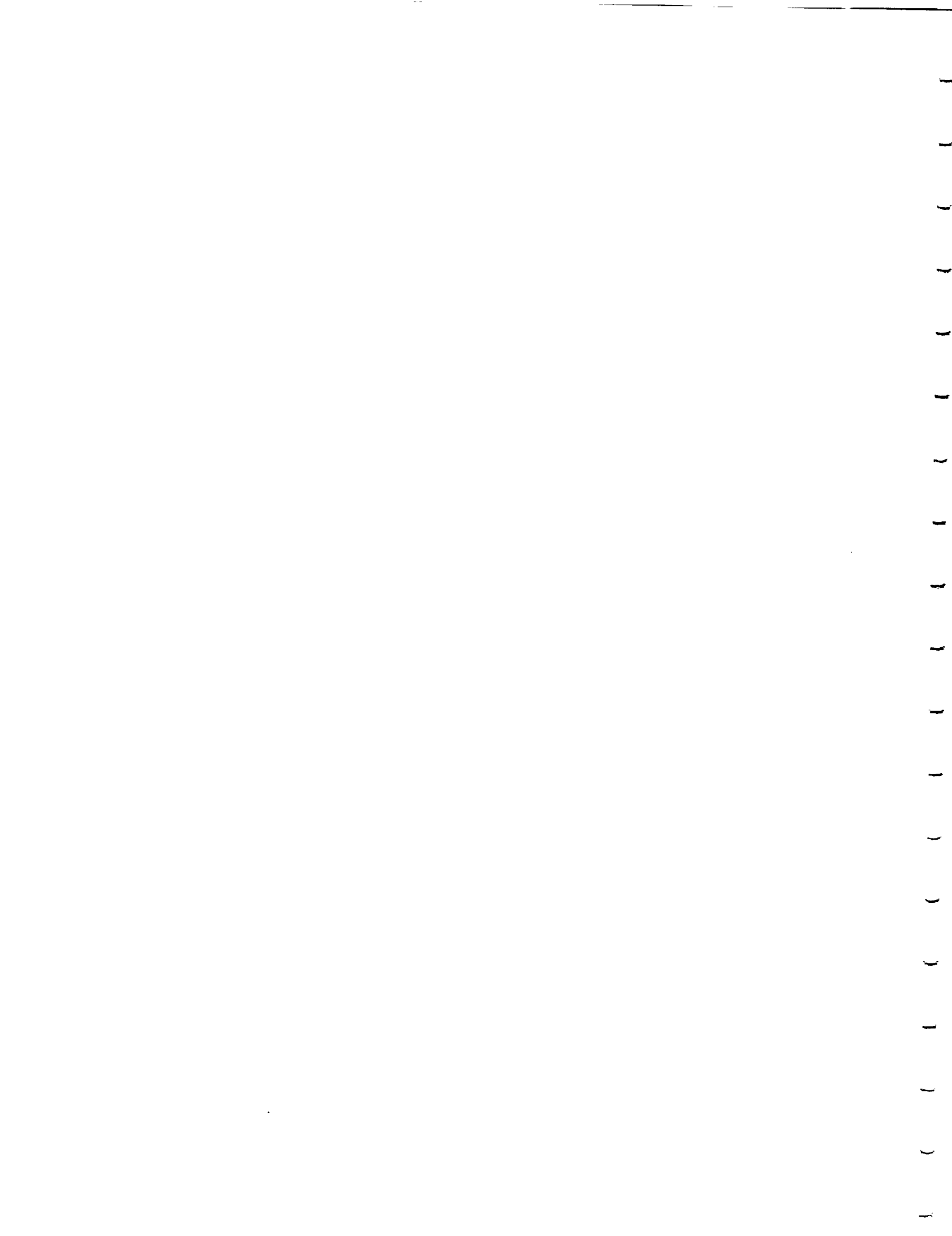
where

$$\phi = \partial_k \xi^3 \partial_k \xi^3, \quad \psi = \frac{1}{3} \partial_k \xi^3 \frac{\partial u_k}{\partial \xi^3}. \quad (8)$$

The second and third momentum elements are obtained by replacing the subscript 1, everywhere in Eq. (7), with 2 and 3, respectively. The last element of Eq. (5) is given by

$$\begin{aligned} & \partial_k \xi^3 (u_n \tau_{kn} - q_k) \\ & \equiv \frac{M_\infty \mu}{\text{Re}} \left\{ \psi \partial_n \xi^3 u_n + \phi \left[\frac{1}{2} \frac{\partial}{\partial \xi^3} (u_1^2 + u_2^2 + u_3^2) + \frac{1}{(\gamma - 1) \text{Pr}} \frac{\partial (a^2)}{\partial \xi^3} \right] \right\}. \quad (9) \end{aligned}$$

For Eq. (4), in the case of thin-layer approximations applied to the ξ^2 direction, the elements are given by equations similar to Eqs. (7)–(9) with the exception



of replacing ξ^3 by ξ^2 . This set of thin-layer Navier-Stokes equations is used only for the passive control cases using a vertical fin since the existence of the fin creates a second viscous thin layer which is perpendicular to the cone's thin layer. This viscous layer on the fin is in the ξ^3 direction. For the passive control cases using side strakes, thin-layer equations in ξ^2 direction are used since the viscous layers on the strakes are in the ξ^2 direction due to the method used to construct the grid around the strakes. The reference parameters for the dimensionless form of the equations are L , a_∞ , L/a_∞ , ρ_∞ , and μ_∞ for the length, velocity, time, density, and molecular viscosity, respectively. The Reynolds number is defined as $Re = \rho_\infty V_\infty L / \mu_\infty$, and the pressure, p , is related to the total energy per unit mass and density by the gas equation

$$p = (\gamma - 1)\rho \left[e - \frac{1}{2}(u_1^2 + u_2^2 + u_3^2) \right]. \quad (10)$$

The viscosity is calculated from the Sutherland law

$$\mu = T^{3/2} \left(\frac{1 + C}{T + C} \right), \quad C = 0.4317, \quad (11)$$

and the Prandtl number $Pr = 0.72$.

In Eqs. (1)–(9), indicial notation is used for convenience. Hence, the subscripts k and n are summation indices, the superscript or subscript s is a summation index. The range for k , n , and s is 1–3, and $\partial_k \equiv \partial/\partial x_k$.

Boundary and Initial Conditions

Boundary conditions are explicitly implemented. They include inflow-outflow conditions and solid-boundary conditions. At the plane of geometric symmetry, periodic conditions are used. At the far-field inflow boundaries, freestream conditions are specified and the outer shock is captured as part of the solution. At the far-field outflow boundaries first-order extrapolation from the interior points is used. On the solid boundary, the no-slip and no-penetration conditions are enforced ($u_1 = u_2 = u_3 = 0$) and the normal pressure gradient is set equal to zero. For the temperature, the adiabatic boundary condition is enforced on the solid boundary. The initial conditions correspond to uniform flow with $u_1 = u_2 = u_3 = 0$ on the solid boundary.

For the passive control applications, solid-boundary conditions are enforced on both sides of the fin or the strakes.

HIGHLIGHTS OF THE COMPUTATIONAL SCHEME

The main computational scheme used to solve the governing equations is an implicit, upwind, flux-difference splitting, finite-volume scheme. It employs



the flux-difference splitting scheme of Roe, which is based on the solution of the approximate Riemann problem. The inviscid flux difference at the cell interface is split into left and right flux differences according to the signs of the eigenvalues of the Roe averaged-Jacobian matrices of the inviscid fluxes $A_s = \partial \bar{E}_s / \partial \hat{q}$; $s = 1-3$. Flux limiters are used to eliminate oscillations in the shock region. The viscous and heat-flux terms are centrally differenced. The resulting difference equation is solved using approximate factorization in the ξ^1 , ξ^2 , and ξ^3 directions. The computational scheme is coded in the computer program "CFL3D." In this program, an implicit, flux-vector splitting, finite-volume scheme, which is based on the Van Leer scheme [14], can also be used instead of the flux-difference splitting scheme. The flux-vector splitting scheme is also used to solve for the unsteady asymmetric flow application in this paper. This application is a validation of the solution obtained previously [5] for the same application using the flux-difference splitting scheme.

Since the applications in this paper cover conical flows only, the three-dimensional scheme is used to solve for locally conical flows. This is achieved by forcing the conserved components of the flow vector field to be equal at the two axial planes located at $x_1 = 0.95$ and 1.0 of the conical grid.

COMPUTATIONAL STUDIES

1. *Passive Control For a Circular Cone Using a Vertical Fin, $\alpha = 20^\circ$*

In this section, we consider the control of steady asymmetric flow around a 5° -semiapex angle circular cone at an angle of attack $\alpha = 20^\circ$, freestream Mach number $M_\infty = 1.8$, and freestream Reynolds number $Re = 10^5$. Two vertical fins of heights $h = 0.5r$ and r are placed in the leeward plane of geometric symmetry, where r is the cone local radius. Figure 1 shows the results of this study, which include the total-pressure-loss contours, the surface-pressure coefficient versus the angle θ (θ is measured from the leeward plane of geometric symmetry in the clockwise direction), and the lift coefficient versus the number of iterations. The figure also shows the results of the asymmetric flow without a vertical fin [5]. With $h = 0.5r$, the flow is still strongly asymmetric after 34,000 iterations. Comparing the case of no fin with the case of $h = 0.5r$, it is seen that the asymmetry changed sides. This is due to the random nature of the disturbance, which is a machine round-off error. With $h = 0.5r$, two vortex cores, which are connected to each other and to the body through free-shear layers, develop from the left side of the body. From the right side of the body, a free-shear layer develops and crosses over the fin to the left side of the body. It produces two vortex cores; one at each corner of the body-fin juncture with secondary separations below them. This case has been solved accurately in time but it does not show any vortex shed-



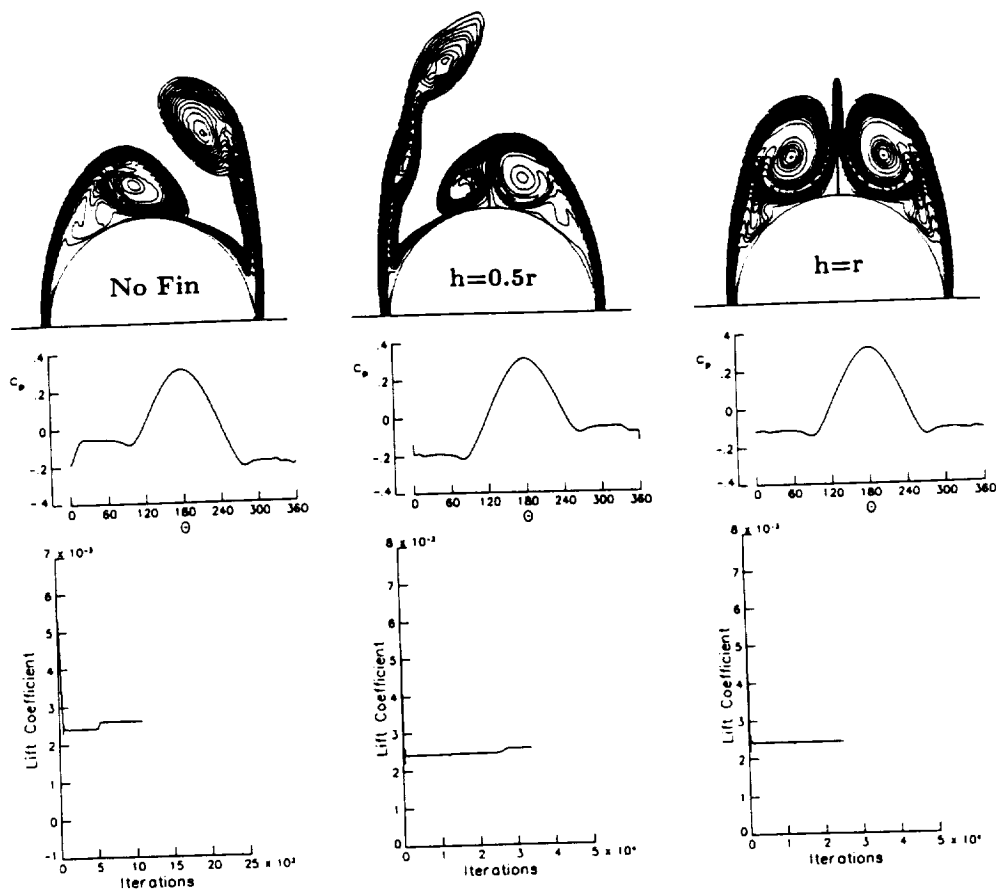


FIG. 1. Passive control of asymmetric flow around a circular cone using a vertical fin. $\alpha = 20^\circ$, $M_\infty = 1.8$, $Re = 10^5$, $h = 0.5r$ and r ($r =$ cone local radius).

ding or unsteadiness. When the fin height is increased to $h = r$, perfect flow symmetry is obtained. The lift-coefficient curves show that when flow asymmetry develops, the lift coefficient increases over a small number of iterations and remains constant thereafter. When the flow becomes symmetric, as with $h = r$, the lift coefficient does not increase. The reason behind the flow asymmetry with $h = 0.5r$ is that the free-shear layer from the right-hand side of the body is still higher than the fin height, which allows the flow disturbances from the right and left side to interact.

Figure 2 shows a typical grid for studying passive control using a vertical fin. It contains 161×81 grid points in the wrap-around and normal directions, respectively. The grid is generated by using a modified Joukowski transformation with clustering in the normal direction at the cone surface, and clustering in the wrap-around direction at the vertical fin surfaces. The maximum radius of the computational domain is $21r$. The figure also shows blow-ups of the cross-flow velocity in the cone-fin-juncture region for $h = 0.5r$ and r . It is noticed that two small recirculating bubbles exist under the vortex cores.



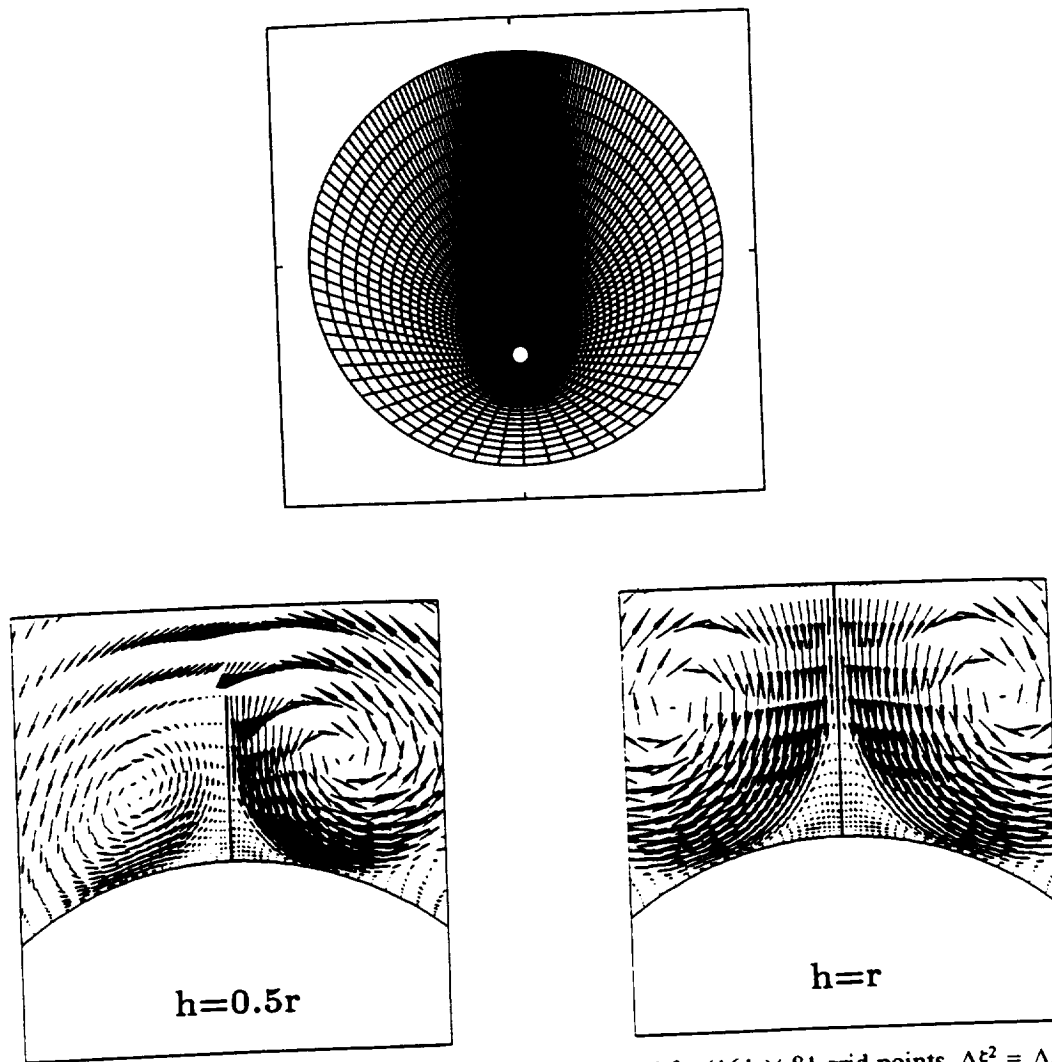


FIG. 2. A typical grid for passive control using a vertical fin (161×81 grid points, $\Delta\xi^2 = \Delta\xi^3 = 10^{-4}$) and blow-ups of cross-flow velocity in the cone-fin juncture ($\alpha = 20^\circ$, $M_\infty = 1.8$, $Re = 10^5$).

2. Passive Control For a Circular Cone Using Side Strakes, $\alpha = 20^\circ$

In Fig. 3, control of flow asymmetry for the same flow conditions as in the first application is considered using sharp-edged thick strakes of height $h = 0.3r$. The side-strakes render the flow perfectly symmetric since the two primary vortex cores, left and right, are pushed further apart preventing the flow disturbances of the two sides from interacting. It is easily seen that there are four vortices on each side; one is a primary vortex and three are secondary vortices. The pressure-coefficient curve shows jumps at $\theta = 90^\circ$ and 270° , where the strakes are located. These jumps change the shape of the C_p -curve in comparison with that of the vertical-fin-control case. Moreover, the lift coefficient of the side-strake-control case is double that of the vertical-fin-control case.

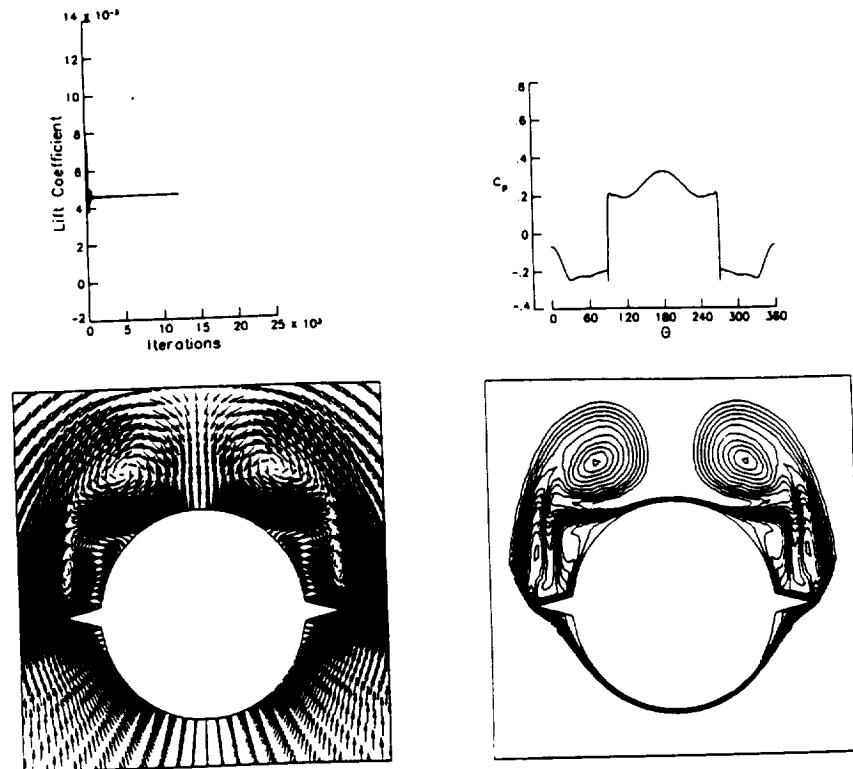


FIG. 3. Passive control of asymmetric flow around a circular cone using sharp-edged thick strakes. $\alpha = 20^\circ$, $M_\infty = 1.8$, $Re = 10^5$, $h = 0.3r$.

It is concluded that side-strake control in comparison with vertical-fin control not only is efficient in providing higher lift, but also is more practical due to the strake's shorter height, and hence lesser weight.

3. Passive Control For a Circular Cone Using Side Strakes with and without Thickness, $\alpha = 30^\circ$

In this case, the cone angle of attack is increased to 30° keeping all the other flow conditions fixed. This flow application has been solved previously in Ref. [5] by Kandil, Wong, and Liu using a flux-difference splitting (FDS) scheme. The results showed unsteady asymmetric flow with periodic vortex shedding. The total-pressure-loss contours of the time steps from 15,000 to 15,700, representing one-half the cycle during the periodic response, is shown in Fig. 4. Other unsteady asymmetric flows with periodic vortex shedding around elliptic-section and diamond-section cones have also been presented by the authors in Refs. [5, 7]. In all these applications, the FDS scheme was used. In order to show that the unsteady asymmetric solutions are not scheme dependent, the effect of computational methodologies and numerical dissipation on the solutions are examined in the present paper. The case of asymmetric flow around a circular cone has also been computed using the flux-



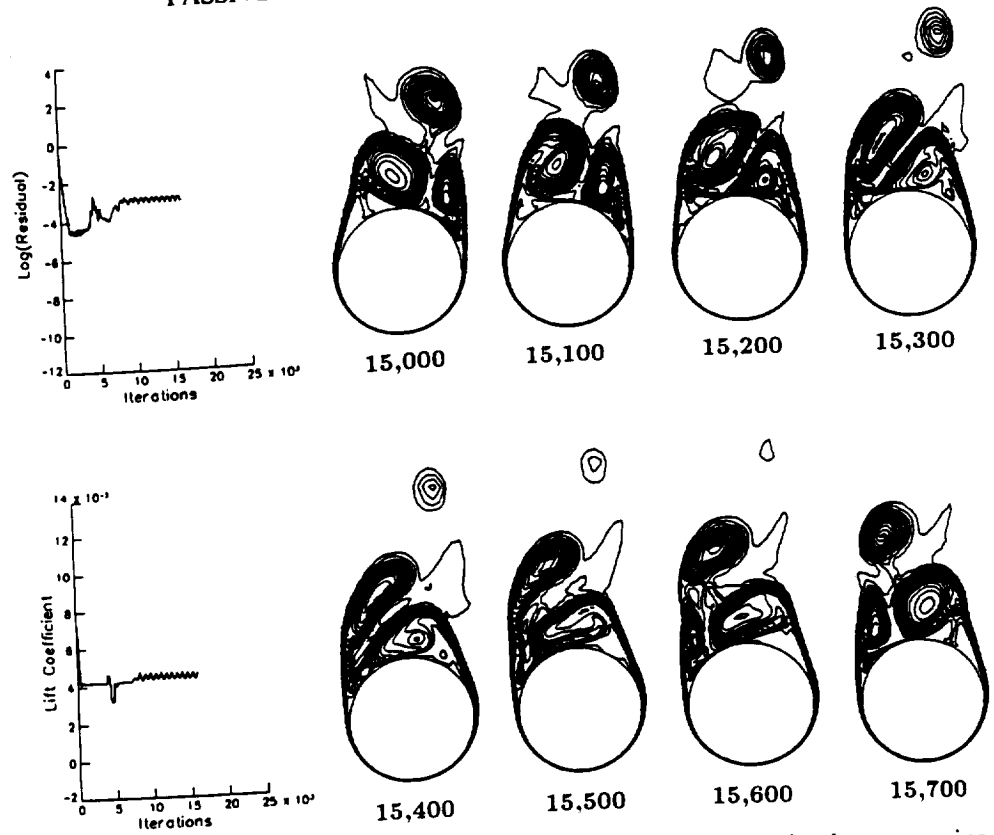


FIG. 4. Unsteady asymmetric flow with vortex shedding around a circular cone using FDS schemes. $\alpha = 30^\circ$, $M_\infty = 1.8$, $Re = 10^5$, $\Delta t = 10^{-3}$.

vector splitting (FVS) scheme of the same code. In Fig. 5, we show the time-accurate solutions using the FVS scheme on the same grid. Using the FVS scheme, the flux limiters are turned on, and as can be seen from the logarithmic-residual curve, the solution becomes symmetric and steady after 5000 time steps. Next, the flux limiters are turned off, and the solution shows a transient response up to 12,000 time steps. Thereafter, the solution becomes periodic with periodic asymmetric vortex shedding. The solution is shown every 100 time steps starting from time step 13,900 until time step 14,600. Although the process of adjusting the time instants to match those of the FDS solution is difficult, it is seen that the captured snapshots of the FVS solution almost match those of the FDS solution at time steps 15,000, 15,100, 15,200, 15,300, 15,400, 15,500, 15,600, and 15,700, respectively. Comparing the FVS solutions at time step of 13,900 with that of 14,600, it is seen that they are mirror images of each other. Hence, periodic flow response has been achieved with a period of $1,400 \times 10^{-3} = 1.4$, which is exactly the same period of shedding as that of the FDS solution. This pinpoints the high numerical dissipation effect of the FVS scheme when the flux limiters are turned on. The resulting numerical dissipation in the FVS is large enough to dampen the random disturbances of the flow solution. By turning off the flux limiters in

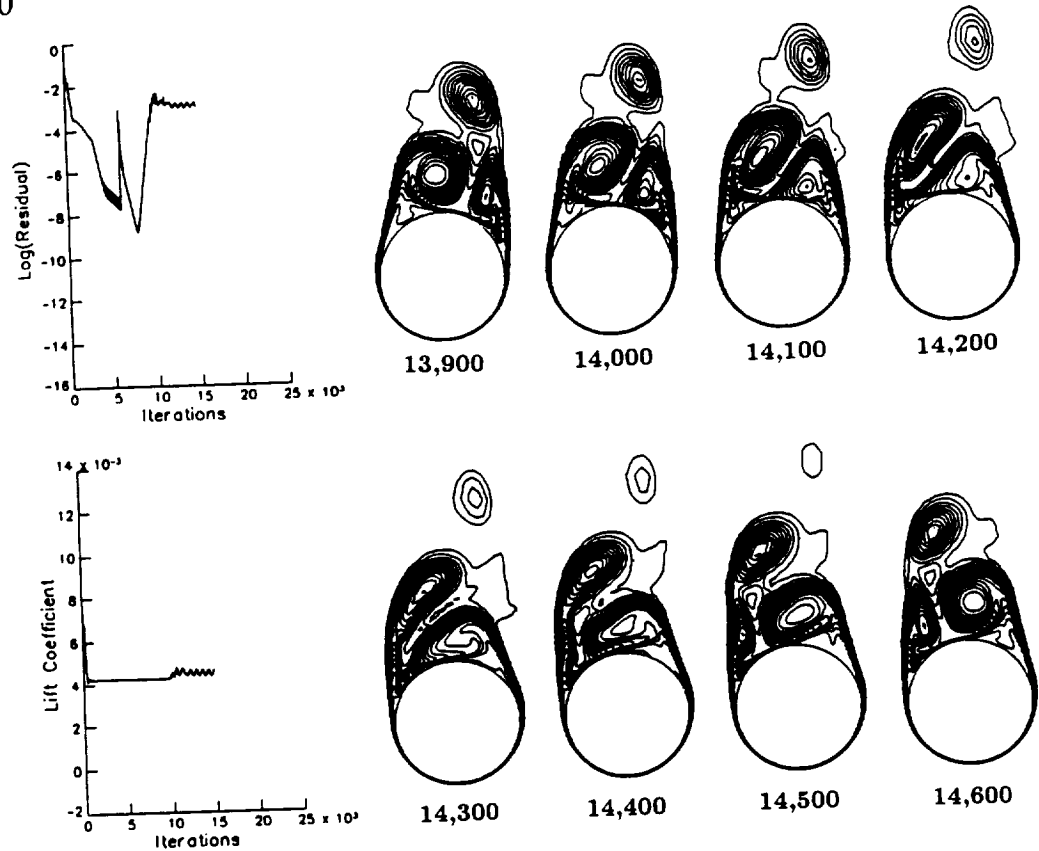


FIG. 5. Unsteady asymmetric flow with vortex shedding around a circular cone using FVS schemes. $\alpha = 30^\circ$, $M_\infty = 1.8$, $Re = 10^5$, $\Delta t = 10^{-3}$.

the FVS scheme, the random disturbances can grow producing the asymmetric unsteady vortex shedding. This also shows that the FDS scheme, even with the flux limiters turned on, is less dissipative than the FVS scheme. These results conclusively show that unsteady asymmetric flows are obtained irrespective of the numerical methodologies.

Next, we consider the control of this unsteady asymmetric flow using sharp-edged thick strakes and flat-plate strakes with different orientations. For all the strake shapes, the height is kept at $0.3r$. Figure 6 shows the results of this study using sharp-edged and flat-plate strakes at $\delta = 0^\circ$, 10° , and -10° , where δ is the angle measured in the counter-clockwise direction from the horizontal line at $\theta = 90^\circ$. For this angle of attack, all the strake orientations are still effective in eliminating the unsteady asymmetric vortex shedding and rendering the flow perfectly symmetric. Again the C_p -curves show jumps at the strakes leading edges at $\theta = 90^\circ$ and 270° . The lift coefficient of all controlled flow cases, Fig. 7, is higher than that of the asymmetric flow case. With slight differences in the lift coefficient, the highest lift is produced by the flat-plate strakes with $\delta = -10^\circ$, where the primary vortex cores are slightly closer to the body surface than for the other cases.

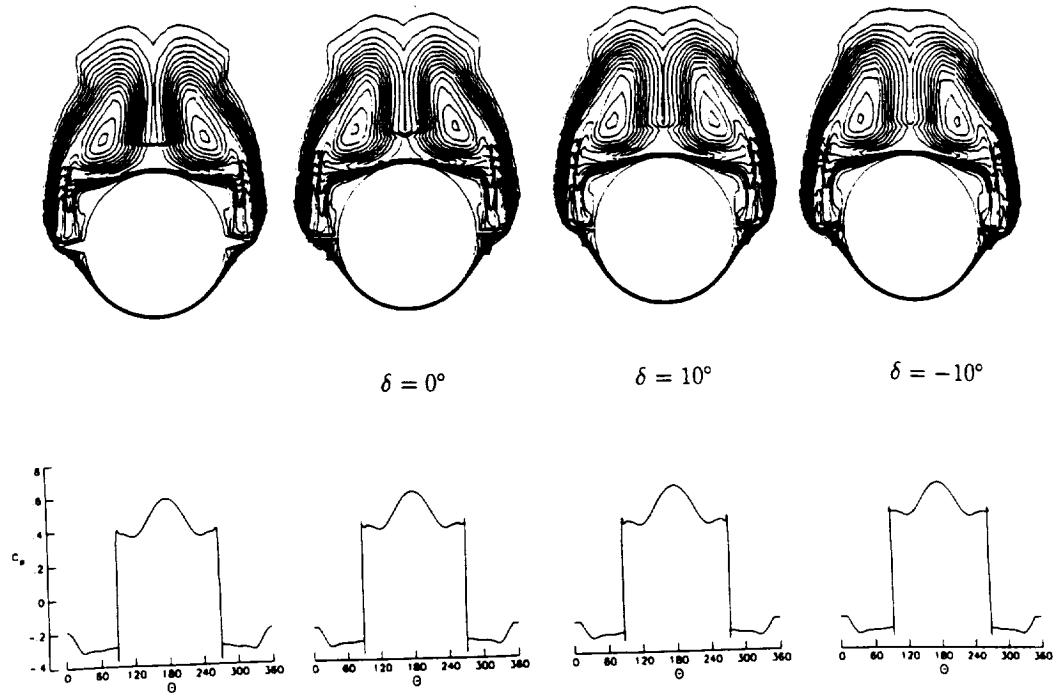


FIG. 6. Passive control of asymmetric flow around a circular cone using sharp-edged thick strakes and flat-plate strakes with different orientations. $\alpha = 30^\circ$, $M_\infty = 1.8$, $Re = 10^5$, $h = 0.3r$.

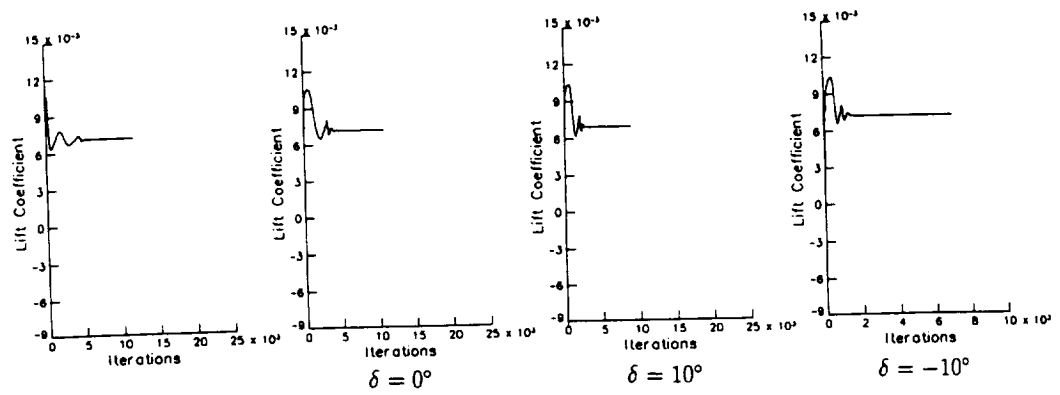


FIG. 7. Lift coefficients and typical grids for passive control using side strakes. $\alpha = 30^\circ$, $M_\infty = 1.8$, $Re = 10^5$, $h = 0.3r$.

Comparing the results of the sharp-edged thick strakes at $\alpha = 30^\circ$ with those of the sharp-edged thick strakes at $\alpha = 20^\circ$ (Fig. 3), we notice that the primary vortex cores of the former are closer to the plane of symmetry and higher above the cone surface than those of the latter.

In the bottom row of Fig. 7, we show typical grids for the cases of sharp-edged thick strakes and the flat-plate strakes with $\delta = 10^\circ$. The grids are generated by using a hyperbolic grid generator with transfinite grid interpolation to refine the grid in the strake region.

4. Passive Control For a Circular Cone Using Sharp-Edged Thick Strakes, $\alpha = 40^\circ$

For this case, the angle of attack is increased to $\alpha = 40^\circ$ keeping all the other flow conditions fixed. The same sharp-edged thick strakes of the previous case ($\alpha = 30^\circ$) have been used along with the same grid. Figure 8 shows the results of this case. It is seen that although the C_p -curve looks perfectly symmetric and although the lift coefficient curve does not show any increase after the time step 4,000, the total-pressure-loss contours show very slight asymmetry. This indicates that the current height of the strakes might not be suf-

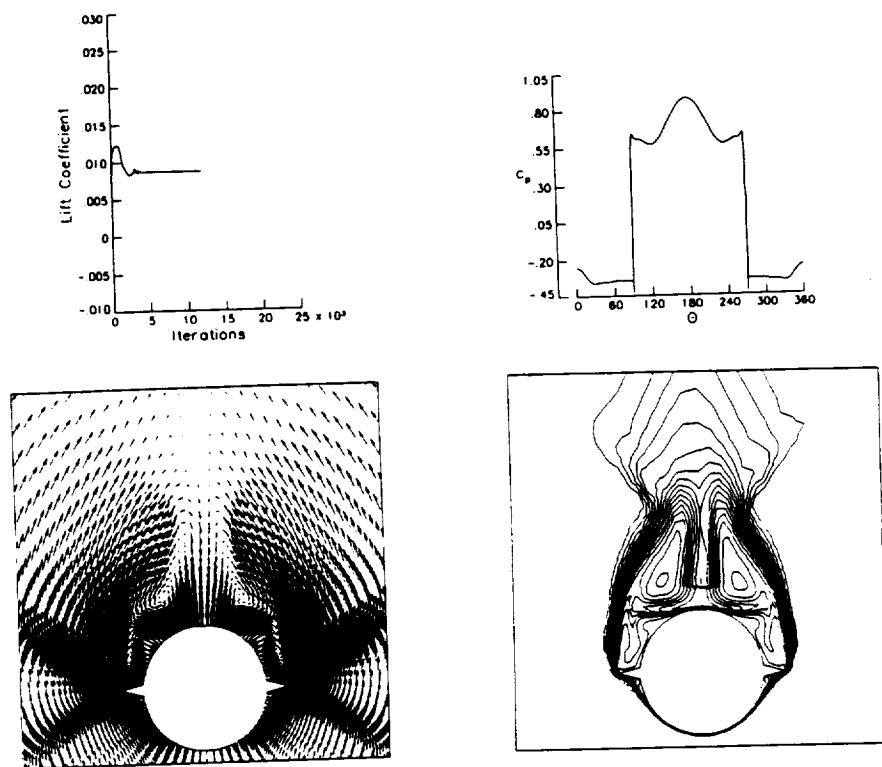


FIG. 8. Passive control of asymmetric flow around a circular cone using sharp-edged thick strakes. $\alpha = 40^\circ$, $M_\infty = 1.8$, $Re = 10^5$, $h = 0.3r$.

ficient to yield flow symmetry at higher angles of attack. The present solution shows that the vortical flow substantially stretches upwards.

5. *Passive Control For an Elliptic-Section Cone Using a Vertical Fin,*
 $\alpha = 25^\circ$

In order to produce a substantial flow asymmetry (of the same order as that of the circular cone of Fig. 1) for an elliptic-section cone of fineness ratio $fr = 0.6$, the angle of attack has been increased to $\alpha = 25^\circ$, and the freestream Mach number has been decreased to $M_\infty = 1.5$. Passive control of this flow has been tested using vertical fins of heights $h = 1.5a$ and $2a$, where $2a$ is the length of the cross-section minor axis. The grid is 161×81 in the wrap-around and normal directions, and was generated by a modified Joukowski transformation with minimum grid spacing of $\Delta\xi^2 = 10^{-4}$ and $\Delta\xi^3 = 10^{-4}$ (for the vertical-fin control). The results are shown in Figs. 9 and 10. For the case with no fin, the lift coefficient shows an increase near step 7,000, and it remains constant thereafter. For the case with $h = 1.5a$, the flow is still strongly asymmetric and the lift coefficient shows an increase near step 8000. The total-pressure-loss contours show a very long free-shear layer from the left side. From the right side, the free-shear layer becomes higher than the vertical fin and crosses over the fin to the left side. Two primary-vortex cores are

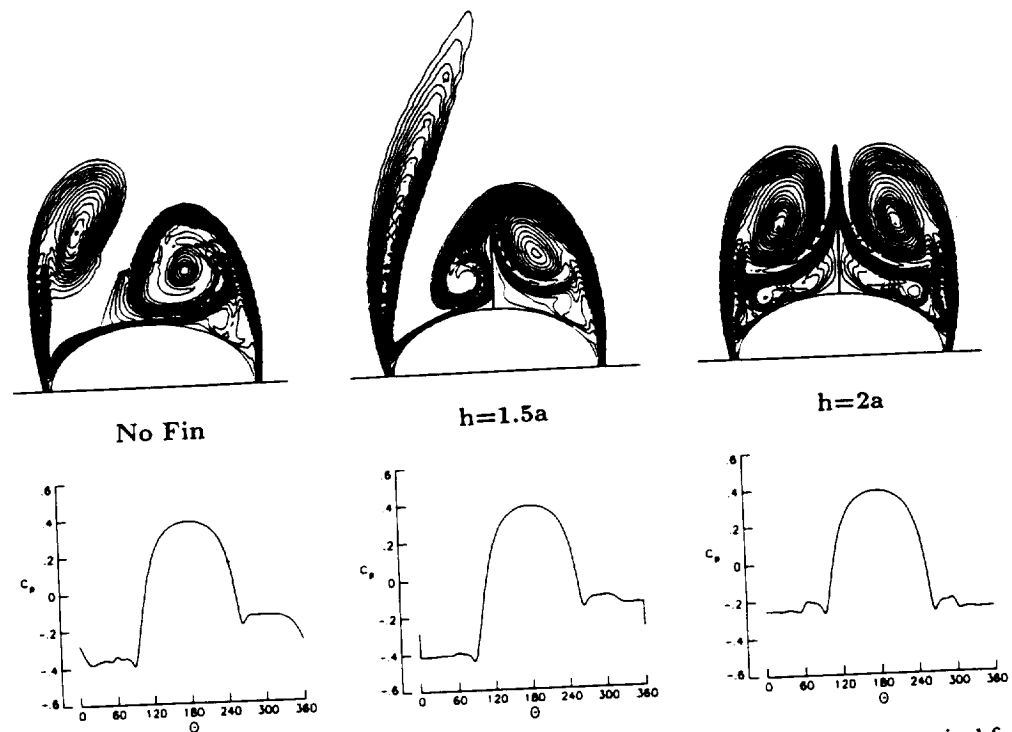


FIG. 9. Passive control of asymmetric flow around an elliptic-section cone using vertical fin. $\alpha = 25^\circ$, $M_\infty = 1.5$, $Re = 10^5$, $fr = 0.6$, $h = 1.5a$ and $2a$ ($2a =$ cone local minor-axis length).

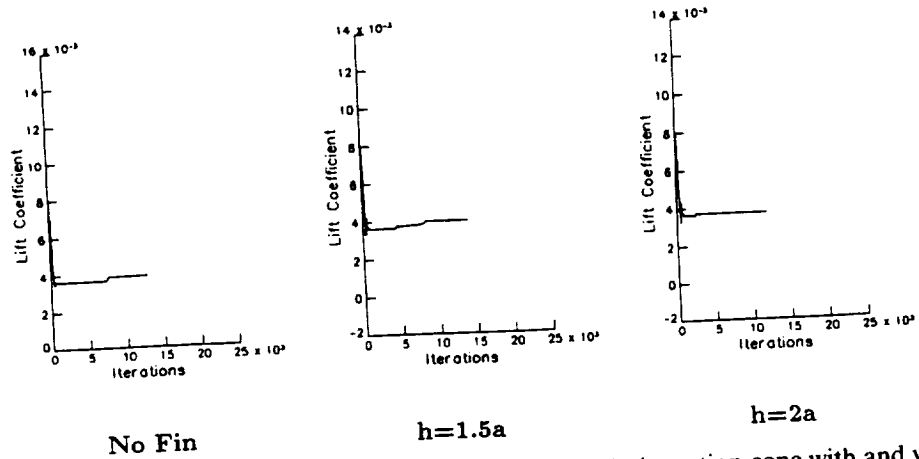


FIG. 10. Comparison of lift coefficients for flow over an elliptic-section cone with and without a vertical fin. $\alpha = 25^\circ$, $M_\infty = 1.5$, $Re = 10^5$, $fr = 0.6$, $h = 1.5a$ and $2a$.

formed at the cone-fin juncture with secondary separations below them. When the fin height is increased to $h = 2a$, perfect symmetric flow is obtained and the lift coefficient remains constant. The behavior of this vertical-fin control case is very similar to that of the circular cone. As long as the vertical fin is high enough as compared to the maximum height of the free-shear layer, flow symmetry is obtained. Obviously, if side-strakes are used, they will push the vortex cores further apart preventing disturbance interaction between the two sides, and flow symmetry will be achieved.

6. Passive Control For a Diamond-Section Cone Using a Vertical Fin, $\alpha = 25^\circ$

For this case, the section fineness ratio is 0.8, the angle of attack is $\alpha = 25^\circ$, and the freestream Mach number is 1.5. With the exception of the section fineness ratio, the flow conditions of this case are the same as those of the elliptic-section cone. This simply shows that for the same section fineness ratio and same flow conditions, diamond-section cones with sharp edges produce less flow-asymmetry strength than that of elliptic-section cones.

Figure 11 shows the results of the diamond-section cone flow with and without a vertical fin. For the flow-control case, a symmetric flow has been obtained using a vertical fin of height $h = 1.5a$, which is shorter than that required for the elliptic-section case.

CONCLUDING REMARKS

Computational studies for passive control of steady and unsteady, supersonic, asymmetric vortical flows have been carried out using vertical fins in the leeward plane of geometric symmetry, and using side strakes with and without thickness. The governing equations are the unsteady, compressible, thin-layer Navier-Stokes equations. The equations have been solved using



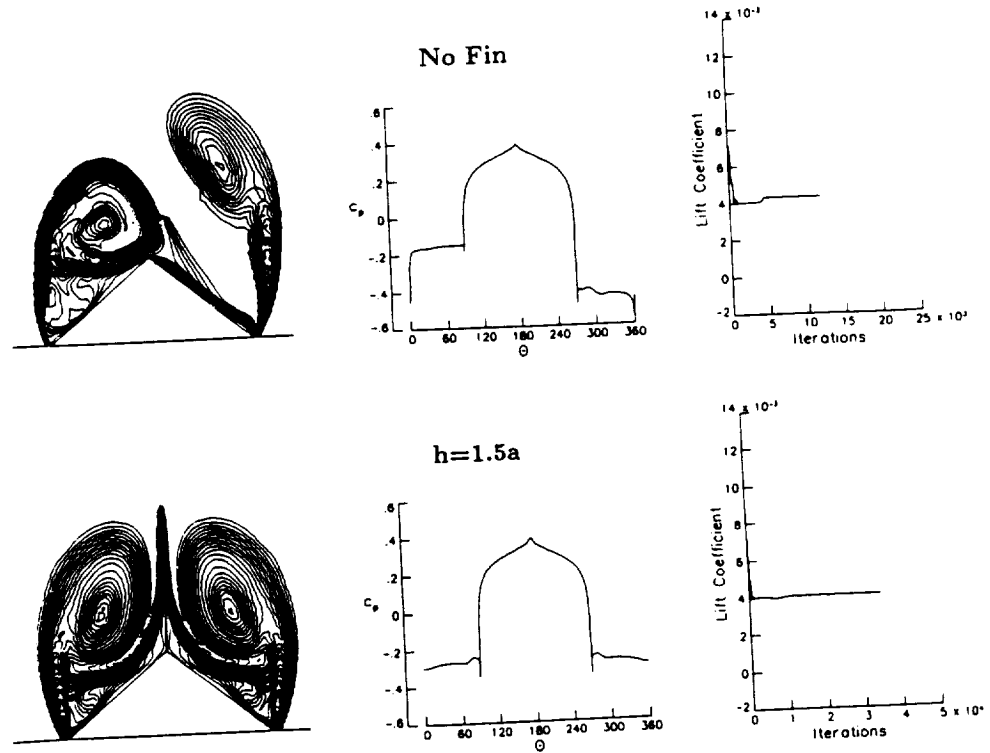


FIG. 11. Passive control of asymmetric flow around a diamond-section cone using a vertical fin. $\alpha = 25^\circ$, $M_\infty = 1.5$, $Re = 10^5$, $fr = 0.8$, $h = 1.5a$.

an implicit, upwind, flux-difference splitting, finite-volume scheme. The flow-control studies have focused on circular-section cones since they are the best potential section-shapes for strong flow asymmetry. It has been shown that side-strake passive control is very effective over a wide range of angle of attack. It has also been shown that side-strake control is more efficient than vertical-fin control in producing higher lift. Moreover, it is more practical since the strakes have shorter height and, hence, less weight in comparison with the vertical fin.

ACKNOWLEDGMENTS

This research work has been supported by the NASA Langley Research Center under Grant NAS1-18584-71 for the last two authors.

REFERENCES

1. J. E. Graham and W. L. Hankey, Computation of the asymmetric vortex pattern for bodies of revolution. *AIAA J.* **23**, 1500-1504 (1983).
2. D. Degani and L. B. Schiff, Numerical simulation of the effect of spatial disturbances on



- vortex asymmetry. In *AIAA 28th Aerospace Sciences Meeting, Reno, Nevada*. AIAA 89-0340 (1989).
3. D. Degani, Numerical investigation of the origin of vortex asymmetry. In *AIAA 28th Aerospace Sciences Meeting, Reno, Nevada*. AIAA 90-0593 (1990).
 4. M. J. Siclari, Asymmetric separated flows at supersonic speeds. In *AIAA 28th Aerospace Sciences Meeting, Reno, Nevada*. AIAA 90-0595 (1990).
 5. O. A. Kandil, T. C. Wong, and C. H. Liu, Prediction of steady and unsteady asymmetric flows around cones. In *AIAA 28th Aerospace Sciences Meeting, Reno, Nevada*. AIAA 90-0598 (1990).
 6. O. A. Kandil, T. C. Wong, and C. H. Liu, Asymmetric supersonic flow around cones with noncircular sections. AGARD Paper No. 16, in *Symposium on Missile Aerodynamics, Friedrichshafen, Germany* (1990).
 7. O. A. Kandil, T. C. Wong, and C. H. Liu, Numerical simulation of steady and unsteady asymmetric vortical flows. *ASME Symposium on Non-Steady Fluid Dynamics, Toronto, Ontario*. FED-Vol. 92, pp. 99-108, (1990).
 8. W. Stahl, Suppression of asymmetry of vortex flow behind a circular cone at high incidence. In *AIAA Atmospheric Flight Conference, Boston, Massachusetts*. AIAA 39-3372-CP, pp. 231-236 (1989).
 9. T. T. Ng, On leading edge vortex and its control. In *AIAA Atmospheric Flight Conference, Boston, Massachusetts*. AIAA 89-3346-CP, pp. 1-15 (1989).
 10. C. Moskovitz, R. Hall, and F. DeJarnette, Experimental investigation of a new device to control the asymmetric flowfield on forebodies at large angles of attack. In *AIAA 28th Aerospace Sciences Meeting, Reno, Nevada*. AIAA 90-0069 (1990).
 11. A. M. Skow and D. J. Peake, Control of the forebody vortex orientation by asymmetric air injection, Part B—Details of the flow structure. In AGARD-LS-121, *High Angle-of-Attack Aerodynamics*, pp. 10.1-10.22 (1982).
 12. T. T. Ng, Aerodynamic control of nasp-type vehicles through vortex manipulation. In *AIAA 28th Aerospace Sciences Meeting, Reno, Nevada*. AIAA 90-0594 (1990).
 13. D. A. Travella, L. B. Schiff, and R. M. Cummings, Pneumatic vortical flow control at high angles of attack. In *AIAA 28th Aerospace Sciences Meeting, Reno, Nevada*. AIAA 90-0098 (1990).
 14. L. C. Rumsey and W. K. Anderson, Some numerical aspects of unsteady Navier-Stokes computations over airfoils using dynamic meshes. In *AIAA 26th Aerospace Sciences Meeting, Reno, Nevada*. AIAA 88-0329 (1988).

